

Old Dominion University

ODU Digital Commons

Electrical & Computer Engineering Theses & Dissertations

Electrical & Computer Engineering

Spring 2024

Broadband Dielectric Spectroscopic Detection of Volatile Organic Compounds With Zinc Oxide and Metal-Organic Frameworks as Solid-State Sensor Materials

Papa Kojo Amoah

Old Dominion University, papakojoamoah08@gmail.com

Follow this and additional works at: https://digitalcommons.odu.edu/ece_etds



Part of the [Chemistry Commons](#), [Computer Engineering Commons](#), and the [Electromagnetics and Photonics Commons](#)

Recommended Citation

Amoah, Papa K.. "Broadband Dielectric Spectroscopic Detection of Volatile Organic Compounds With Zinc Oxide and Metal-Organic Frameworks as Solid-State Sensor Materials" (2024). Doctor of Philosophy (PhD), Dissertation, Electrical & Computer Engineering, Old Dominion University, DOI: 10.25777/896g-v847 https://digitalcommons.odu.edu/ece_etds/258

This Dissertation is brought to you for free and open access by the Electrical & Computer Engineering at ODU Digital Commons. It has been accepted for inclusion in Electrical & Computer Engineering Theses & Dissertations by an authorized administrator of ODU Digital Commons. For more information, please contact digitalcommons@odu.edu.

**BROADBAND DIELECTRIC SPECTROSCOPIC DETECTION OF VOLATILE
ORGANIC COMPOUNDS WITH ZINC OXIDE AND METAL-ORGANIC
FRAMEWORKS AS SOLID-STATE SENSOR MATERIALS**

by

Papa Kojo Amoah
B.S. December 2016, Frostburg State University

A Dissertation Submitted to the Faculty of
Old Dominion University in Partial Fulfillment of the
Requirements for the Degree of

DOCTOR OF PHILOSOPHY

ELECTRICAL AND COMPUTER ENGINEERING

OLD DOMINION UNIVERSITY
May 2024

Approved by:

Helmut Baumgart (Director)

Abdelmageed Elmustafa (Member)

Linda Vahala (Member)

Gon Namkoong (Member)

Yaw Obeng (Member)

ABSTRACT

BROADBAND DIELECTRIC SPECTROSCOPIC DETECTION OF VOLATILE ORGANIC COMPOUNDS WITH ZINC OXIDE AND METAL-ORGANIC FRAMEWORKS AS SOLID-STATE SENSOR MATERIALS

Papa Kojo Amoah
Old Dominion University, 2024
Director: Dr. Helmut Baumgart

The industrial revolution drove technological progress but also increased the release of harmful pollutants, posing significant risks to human health and the environment. Volatile organic compounds (VOCs), which have various anthropogenic and natural sources, are particularly concerning due to their impact on public health, especially in urban areas. Addressing these adverse effects requires comprehensive strategies for mitigation as traditional gas sensing techniques have limitations and there is a need for innovative approaches to VOC detection.

VOCs encompass a diverse group of chemicals with high volatility, emitted from various human activities and natural sources. These compounds play a crucial role in the formation of ground-level ozone and secondary pollutants, significantly impacting global climate and air quality. Anthropogenic sources dominate in urban areas, exacerbating air pollution and its associated health risks. Monitoring and controlling VOC emissions are imperative for public health, environmental sustainability, and industrial processes.

Gas sensors offer a promising solution for VOC monitoring, with advancements focusing on improving sensitivity, selectivity, and real-time detection capabilities. Broadband dielectric spectroscopy (BDS) emerges as a non-contact metrology method for probing material properties,

particularly suited for gas-sensitive materials like zinc oxide (ZnO) and metal-organic frameworks (MOFs). BDS provides detailed insights into gas sensing mechanisms, enabling the development of enhanced gas sensing devices.

This thesis explores the use of ZnO and MOFs as detection elements in gas sensing applications, aiming to advance understanding and application of gas sensing technologies. Objectives include investigating ZnO's oxidization mechanism, studying metal-doped ZnO for enhanced sensing, exploring MOF films for VOC detection, and conducting a comparative analysis between ZnO and MOF sensors. Experimental setups involve BDS measurements to monitor changes in material properties and gas-sensor interactions. Experimental investigations reveal unique mechanistic insights into ZnO gas sensing behavior, particularly in detecting aliphatic alcohols like ethanol. Metal doping of ZnO nanorods alters gas sensing responses, with different metals exhibiting distinct detection mechanisms. MOF films demonstrate high sensitivity to VOCs, showcasing potential applications in gas sensing technologies. Comparative analysis highlights the advantages of MOF films over ZnO nanorods for ethanol vapor detection at low temperatures.

Copyright, 2024, by Papa Kojo Amoah, All Rights Reserved.

This thesis is dedicated to my parents, Paul Amoah and Amma Twum-Amoah, and to my sisters,
Maame Amoah and Ewuradjoa Amoah.

ACKNOWLEDGMENTS

I extend my sincerest appreciation to Dr. Helmut Baumgart and Dr. Yaw Obeng, my esteemed mentors, for their patient guidance, enthusiastic encouragement, and valuable feedback during the course of this research endeavor. Dr. Baumgart's generosity in welcoming me into his research group at the Applied Research Center (ARC) at Jefferson Laboratory has provided me with a remarkable opportunity for growth. His unwavering support and genuine counsel have been invaluable to me. Similarly, I am indebted to Dr. Obeng for his guidance, which began during my undergraduate internship at the National Institute of Standards and Technology (NIST) and continued steadfastly throughout my graduate studies. I am profoundly grateful for his mentorship.

I also extend my gratitude to my committee members, Dr. Linda Vahala, Dr. Gon Namkoong, and Dr. Abdelmageed Elmustafa, for their engagement throughout this process.

Special thanks are extended to Dr. Wei Cao for his invaluable advice and support with various characterization tools throughout my research at ARC. Additionally, I am deeply thankful to Dr. Tarek Abdel-Fattah for his mentorship and for graciously allowing me access to the chemistry lab facilities at Christopher Newport University (CNU) for my research. Furthermore, I would like to thank Dr. Engelbert Redel from Karlsruhe Institute of Technology (KIT) Germany for graciously supplying the HKUST-1 SURMOF films for this study, Dr. Rhonda Franklin from the University of Minnesota for her help in generating the equivalent circuits and the model for the ZnO nanorods, and Dr. Tehseen Adel and Dr. Angela Hight Walker from NIST for help with the Raman characterization of the materials.

I am grateful for the camaraderie and collaboration with my fellow graduate students, Dr. Manish Ojha, Shakel Sharifuzzaman, Sadiya Tahsin, Najmin Sultana, and Qui Quach, whose presence enriched my doctoral journey.

My deepest gratitude goes to my parents, Paul Amoah and Amma Twum-Amoah, and my sisters, Maame Amoah and Ewuradjoa Amoah, and my extended family and friends for their unwavering love, encouragement, and support throughout my academic pursuit. Their constant support has been a source of strength and motivation for me.

TABLE OF CONTENTS

	Page
LIST OF TABLES	x
LIST OF FIGURES	xi
Chapter	
1 INTRODUCTION AND LITERATURE REVIEW	1
1.1 Background	1
1.2 Volatile Organic Compounds (VOCs)	2
1.3 VOC detection methods	9
1.4 Metal Oxide Semiconductor (MOS) Sensors	22
1.5 Dissertation Objectives	42
2 MATERIALS AND EXPERIMENTAL TECHNIQUES	52
2.1 Sensing Material: ZnO	52
2.2 Sensing Material: Metal Organic Frameworks (MOFs)	97
2.3 Characterization Techniques	109
3 BROADBAND DIELECTRIC SPECTROSCOPY (BDS).....	129
3.1 Electromagnetic Theory	129
3.2 Electromagnetic Radiation	131
3.3 Dielectric Theory	133
3.4 Dielectric Properties.....	137
3.5 Dielectric Relaxation.....	139
3.6 Dielectric Spectroscopy.....	142
3.7 Scattering Parameters	152
3.8 Practical Considerations for BDS	157
3.9 Some examples of BDS use in other studies	164
3.10 How BDS was used for this Research Work.....	165
4 THE USE OF ZnO AS SENSING MATERIAL.....	169
4.1 Introduction	169
4.2 Experimental	172
4.3 Results and Discussion	175
4.4 Conclusions	187
5 METAL-DOPED ZnO AS THE DETECTION ELEMENT	190
5.1 Introduction	190
5.2 Experimental Details	192
5.3 Results and Discussion	194
5.4 Conclusions	204

Chapter	Page
6 METAL-ORGANIC FRAMEWORK MOF FILMS AS SENSING MEDIA	206
6.1 Introduction	206
6.2 Experimental	210
6.3 Results and Discussion	216
6.4 Conclusions	229
7 SIDE BY SIDE COMPARISON - ZnO VS MOF FILMS AS SENSING MEDIA	236
7.1 Introduction	236
7.2 Experimental	244
7.3 Results and Discussion	246
7.4 Conclusions	257
8 SUMMARY AND FUTURE WORK	263
8.1 Summary	263
8.2 Contributions to Science	268
8.3 Outlook and Future work	269
9 APPENDIX	278
10 VITA.....	286

LIST OF TABLES

Table	Page
1.1.....	4
1.2.....	21
1.3.....	36
2.1.....	53
3.1.....	146
3.2.....	160
6.1.....	222

LIST OF FIGURES

Figure	Page
1.1 As part of a closed loop IoT network, there's a need for continuous monitoring of VOC emissions using smart sensing devices. The information obtained from this monitoring can be used to control and regulate industrial VOC generation or make decisions in healthcare regarding the existence of a disease and the need for treatment [21].	9
1.2. Gas sensors that monitor VOCs can be broadly categorized based on their functional materials and transduction mechanisms. This framework outlines the various families of gas sensors within these two basic principles [27]......	11
1.3. Schematic diagram illustrating the sensing mechanism of n-type and p-type MOS [67].	27
1.4. A schematic diagram of the reaction mechanism of a MOS sensor showing the band bending at the surfaced the material when exposed to a gas [69]......	29
1.5. Schematic representation of how the sensitivity of metal-oxide gas sensors is influenced by the size of crystallites [2].	30
1.6. Structural and band models of conductive mechanism upon exposure to reference gas. (a) with or (b) without CO [68].	34
1.7. An illustration that shows the response time and recovery time of a specific MOS gas sensor. The graph displays how fast the sensor reacts to changes in gas concentration and how long it takes to return to its initial state after the gas concentration has changed [71].	38
1.8. Dependence of the sensitivity of MOS gas sensors on the sensor operating temperature. Initially, an increase in temperature leads to an increase in the adsorption of gas species (both chemisorption and physisorption). However, this effect only persists up to a certain threshold, which varies depending on the specific MOS and the target gas molecule. Once this threshold is reached, the high thermal motion of the adsorbed species promotes desorption, leading to a decrease in sensor sensitivity [71].	39
2.1. The wurtzite unit cell of ZnO is illustrated, with Zn represented in yellow and O in grey [5].	53
2.2. Band structure of wurtzite ZnO [11]......	57
2.3. The creation of energy bands for electrons in a silicon crystal possessing a lattice structure similar to that of diamond [12].	59
2.4. A diagram illustrating the changes made to a face-centered-cubic host metal lattice by substitutional and interstitial atomic modifications using light elements. In (a), foreign light	

atoms are shown displacing the original atoms in a substitutional manner. In (b), the foreign light atoms are depicted as being inserted into vacant spaces within the lattice structure [20]..... 61

2.5. Lowest resistivities and highest free carrier concentrations achieved using various ion-assisted or thermal deposition methods [36]..... 65

2.6. In (a) n-type and (b) p-type semiconductors, impurities can create an energy band that can merge with the valence or conduction band. Unlike regular semiconductors, the Fermi level in degenerate semiconductors is within this energy band, not the band gap. As a result, degenerate semiconductors behave more like metals [43]. 69

2.7. The relationship between the growth rate of ZnO and the temperature at which it is grown when diethylzinc (DEZ) and water are utilized as precursors in the ALD process [94]. 86

2.8. The following is a schematic representation depicting the sequential procedure involved in the ALD process [94]. 87

2.9. Schematic representation of the suggested surface reaction of ALD ZnO using DEZ and water as the precursors [96]. 88

2.10. A diagram displaying the different types of ALD reactor systems. [98] 90

2.11. ALD flow type reactor [99]..... 91

2.12 Schematic diagram of the process steps for the hydrothermal solution growth of ZnO nanorods [133]. 96

2.13. The MOF structure is formed through the creation of chemical bonds between metal ions as nodes and organic molecules as linkers [108]. 98

2.14. Model depicting a portion of the crystal structure of the Metal-Organic Framework MOF Film (HKUST-1) showing an open pore structure without any loading. Green, gray, and red spheres represent Cu, C, and O atoms, respectively; H atoms are omitted for clarity [109]..... 99

2.15. Illustration of the SURMOF assembly process via Layer-by-Layer spray deposition where the substrate was pre-treated with MHDA (16-mercaptohexadecanoic acid) a Self-Assembled Monolayer (SAM) for surface functionalization [112]..... 104

2.16. Depiction of resolution through (a) Airy disk patterns and (b) wavefront peaks [123].....110

2.17. Illustration of the various kinds of signals generated upon impact of the primary beam with the surface specimen [123].113

3.1. The electromagnetic spectrum featuring wavelength, frequency, and energy [2]. 131

3.2. EM wave propagation showing electric (E) and magnetic field (B) [3]..... 133

3.3. Polarization mechanisms versus frequency range [5].....	135
3.4. Diagram of a microwave sensor system (adapted from [8]).....	143
3.5. Example of raw output data as a reflection coefficient from a VNA [3].	145
3.6. Schematic of a transmission line utilizing the waveguide technique (R = power reflected, T = power transmitted) [10].....	147
3.7. Network analyzer and dielectric probe measuring the permittivity of contaminated soil [6].	149
3.8. Measurement of sample using free space method [11].....	150
3.9. Measurement of thin film using cavity resonator [9].....	152
3.10. The S-parameter matrix of a two port system [14].	155
3.11. A Lecroy SPARQ analyzer connected to a pc with a USB cable [20].	161
3.12. Image of the top-down view of the grounded coplanar waveguide with end launchers....	163
3.13. A schematic cross section of a GSG coplanar waveguide with its dimensions shown [23].	163
4.1. Planar view and Cross-sectional FE-SEM images of intrinsic ZnO nanorods highlighting the fine grain polycrystalline ALD ZnO seed layer underneath and the resulting morphology of a dense array of ZnO nanorods (adapted from Reference 3).....	172
4.2. A schematic representation of experimental setup used in this study showing the ZnO sample on a ground-signal-ground (GSG) waveguide situated in a controlled environment (Pyrex tube).	173
4.3. Images of a) BDS instrumental arrangement, and b) a zoomed-in view of the waveguide with the cover slip on top of it.	174
4.4 The time evolution of the reactor temperature during the experiments described in this work.	177
4.5. A phenological model of a ZnO nanorod under microwave interrogation in a gaseous ambient during sensor preparation step, where adsorbed oxygen species cause a negative charge build-up on the nanorod surface as used in this study. E is an electric field fringe from the microwave emanating from the signal line and terminating on the ground line of the GSG coplanar waveguide, l_{ZnO} is the mechanical length of the nanorod, while ϕ_{bulk} is the diameter of the bulk, and ϕ_d is the depletion layer thickness of the ZnO nanorod, respectively. It is important to note that the seed ZnO layer thickness is exaggerated for illustrative purposes in Figure 4.5; it	

is very small compared to the length of the ZnO nanorods as seen in the cross-sectional SEM micrograph of Fig.1.1.	177
4.6. An electrical equivalent circuit model of the ZnO nanorod configuration in Figure 4.5 as used in this study. Note that inductance has been excluded from the seed layer representation.	178
4.7. Temperature dependence of microwave insertion loss (S_{21} amplitude) of ZnO on Si in air and in alcohol gaseous environments, monitored at 6 GHz as a function of elapsed time.....	180
4.8. Comparison of the temperature dependence of microwave insertion loss (S_{21} amplitude) of the waveguide-cover glass stack with / without the ZnO/Si sample in air monitored at 6 GHz.	182
4.9. Flow diagram illustrating the conversion process of raw data into RLGC values.	183
4.10. A comparison of the temperature dependence of microwave attenuation constant of ZnO on Si in air only and with air-ethanol vapor mixture present in the reactor environments, monitored at 6 GHz. The data suggest that the attenuation constant is independent of the gaseous environment in the temperature regime used in this work.....	184
4.11. The real part of the S_{21} data, denoted as the S_{21} amplitude, positioned on the left, and the imaginary part, known as the S_{21} phase, located on the right where the four data points at volume indicate measurements at the four temperatures (40, 60, 70, 80 °C in ascending order).....	185
5.1. a) SEM images and b) EDS spectra of Ag nanoparticles doped ZnO nanorods.....	194
5.2. a) SEM images and b) EDS spectra of ZnO nanorods doped with Au nanoparticles.....	195
5.3. a) SEM images and b) EDS spectra of ZnO nanorods doped with Co nanoparticles.....	195
5.4. A visualization of the movement of atoms associated with the active optical modes in the wurtzite structure of ZnO [10].	197
5.5. TEM image depicting Au nanoparticles decorating ZnO nanorods, with EDS spectra confirming the presence of Au [9].	198
5.6. Raman spectra of pure and metal-doped ZnO samples taken at room temperature in the range of 100–600 cm^{-1}	199
5.7. Contour plots of the amplitude and phase of Ethanol (EtOH) detection as a function of temperature with a) undoped ZnO nanorods and b) Ag doped ZnO nanorods. Each color on the legend to the right of each plot represents a mean S_{21} amplitude or phase value at .5 GHz.	201
5.8. Contour plots of the amplitude and phase of EtOH detection with a) Co-ZnO nanorods and b) Au-doped ZnO nanorods.	202

6.1. Schematic illustration depicting the structure of HKUST-1 SURMOF films, where the pores are loaded with TCNQ (TCNQ, tetracyanoquinodimethane) [14].	208
6.2 Schematic representation illustrating the HKUST-1 SURMOF film growth with MOF precursors Copper acetate inorganic solution (1.0 mM) and Benzene tricarboxylic acid BTC organic linker (0.2 mM). Copper atoms are depicted in green, oxygen atoms in red, and carbon atoms in gray [72].	211
6.3. A phenomenological model of a doped HKUST-1 SURMOF under microwave interrogation in a gaseous ambient. ECPW is an electric field fringe from the microwave emanating from the signal line and terminating on the ground line of the GSG CPW. Note that the figure is for illustration only, and not to scale. Some features important features have been deliberately exaggerated for illustrative purposes.	214
6.4. Planar view FE-SEM micrographs of HKUST-1 SURMOF thin films grown on borosilicate glass substrates displaying the differences in MOF morphology between undoped pristine MOFs versus TCNQ-doped MOFs of very loosely stacked MOF grains with very noticeable gaps between individual MOF grains, which are especially pronounced following TCNQ loading of thicker 40 deposition cycles of MOF films: (a) 10 cycles pristine MOF; (b) 10 cycles TCNQ; (c) 40 cycles MOF pristine; and (d) 40 cycles MOF with TCNQ-loaded MOF [adapted from Reference #35].	215
6.5. Temperature dependence of microwave insertion loss amplitude (S_{21}) of pristine and TCNQ-doped HKUST-1 SURMOF on Si in a N_2 -rich air environments, at 1 GHz. The error bars represent the standard deviation of at least three measurements on the same sample and are substantially smaller than the symbol sizes and are therefore not visible.	218
6.6. Methanol concentration dependence of the time-averaged microwave insertion loss amplitude (S_{21}) of a TCNQ-loaded HKUST-1 SURMOF film on Si substrate at 65 °C, purged with pure air, monitored at 0.5 GHz. The error bars represent the standard deviation of at least three five-minute measurements for each aliquot of methanol.	219
6.7. Comparison of analyte concentration dependence of microwave insertion loss amplitude (S_{21}) TCNQ-loaded HKUST-1 SURMOF on Si substrate at 65 °C in air, monitored at 0.5 GHz. The error bars represent the standard deviation of at least three measurements.	220
6.8. The dependence of the slope of the analyte volume dependence of insertion loss on the electrocatalytic oxidation potential of aliphatic alcohol analytes on a platinum-based catalyst, taken from Lammy et al. [47]. The blue dashed line is just a visual aid.	222
6.9. Surface roughness of HKUST-1 SURMOF films exposed to varying amounts of ethanol vapor at 65 °C showing initial surface plasticization and recovery with increasing volumes of solvent. The error bars represent the standard deviation of roughness measurements from at least three distinct areas on the sample surface.	224

6.10. Comparison of solvent concentration dependence of microwave insertion loss amplitude (S_{21}) TCNQ-loaded HKUST-1 on Si substrate at 65 °C, in air, for methanol (MeOH), ethanol (EtOH), and 1:1 mixture of ethanol and methanol, monitored at 0.5 GHz. The 1:1 mixture of MeOH-EtOH designated by black symbols completely overlap those for pure methanol (MeOH) blocking the visibility of the green symbols. The error bars represent the standard deviation of at least three measurements.	225
6.11. The relationship between the slope of the analyte volume dependence of insertion loss and the Gutmann Acceptor (AN). AN is a measure of hydrogen bond acidity, and the linear relationship suggests that the analyte molecules and/or the oxidation products form hydrogen bonds within the HKUST-1 structure.....	226
7.1. Schematic illustration depicting the structure of HKUST-1 SURMOF films, where the pores are loaded with TCNQ (TCNQ, tetracyanoquinodimethane) [25].	240
7.2. Temperature dependence of microwave insertion loss (S_{21} amplitude) of ZnO on Si substrate in nitrogen-rich air and gaseous ethanol environments, monitored at 6 GHz. Note that the symbol sizes are much larger than the error bars.....	248
7.3. Temperature dependence of microwave insertion loss (S_{21} amplitude) in TCNQ loaded HKUST-1 MOF film on Si substrate in N_2 -rich air, The error bars represent the standard deviation of at least three measurements on the same sample.....	253
7.4. Insertion loss (S_{21} Amplitude) monitored at 0.5 GHz as a function of volume of neat ethanol injected into vapor reactor (i.e., ethanol vapor concentration) environments at 80 C° in air.	254
7.5. Comparison of the microwave insertion loss (S_{21}) dependence on ethanol concentration on ZnO versus TCNQ-doped HKUST-1 MOF sensing media on Si in gaseous ethanol environments, monitored at 0.1 GHz. Note the error bars represent the standard deviation of at least 3 replicate measurements.....	257
8.1. Illustrates the ion implantation of ZnO with Cr at a concentration of 1%, delineating the associated parameters and the simulated Gaussian depth profile of Cr at 20 keV.....	271
8.2. Illustrates the implantation of ZnO with Ti at a concentration of 1%, delineating the associated parameters and the simulated Gaussian depth profile Ti at 20 keV.....	272
8.3. Illustrates the ion implantation of Ti into ZnO with Ti at a concentration of 2%.....	273

CHAPTER 1

INTRODUCTION AND LITERATURE REVIEW

1.1 Background

While the industrial revolution offered great technological progress, it also resulted in the creation of large amounts of harmful pollutants that pose risks to human health when they are released into the atmosphere. Human actions have a detrimental effect on the natural environment by contaminating our drinking water, polluting the air we breathe, and degrading the soil needed for plant growth. Human-caused air pollution stands out as one of the foremost public health risks worldwide, contributing to approximately 9 million fatalities annually [1]. Moreover, air pollution presents a major threat with a variety of adverse health impacts. Even at low levels, vulnerable individuals may suffer from short-term exposure in the form of conditions such as chronic obstructive pulmonary disease (COPD), asthma, respiratory diseases, and increased hospitalization rates. Prolonged exposure to air pollution is associated with long-term health conditions such as asthma, pulmonary issues, heart diseases, and a higher risk of death in general. Additionally, research suggests a relationship between extended exposure to poor air quality and the development of diabetes. Infants are especially vulnerable, as air pollution has been linked to respiratory issues, heart problems, mental disorders, and complications during childbirth that could lead to infant mortality or chronic illnesses as they grow up. National reports highlight the increased risks of both illness and death related to daily fluctuations in particulate matter levels.

Residents of large urban areas, where road emissions significantly contribute to the deterioration of air quality, bear the brunt of the impact of air pollution. Industrial accidents pose an additional threat, with the potential release of toxic fog leading to fatal consequences for nearby

populations. The dispersion of pollutants is contingent on various factors such as atmospheric stability and wind [1, 2]. Urban air pollution typically results from significant levels of sulfur dioxide, carbon oxides (carbon dioxide and carbon monoxide), nitrogen oxides, as well as fine and ultrafine particulate matter (PM) suspended in the air. Depending on other urban emission sources, there are also traces of heavy metals and volatile organic compounds (VOCs) [3]. These VOCs can infiltrate deep into the airways and reach the bloodstream and are associated with more severe illnesses.

Furthermore, overall, addressing these environmental challenges is imperative for public health and necessitates comprehensive strategies to alleviate the repercussions of both climate change and air pollution [1, 2].

1.2 Volatile Organic Compounds (VOCs)

Volatile organic compounds (VOCs) are a broad group of chemicals with high volatility that can cause significant harm to both human health and the environment when released into the atmosphere [4]. Practically all human activities in daily life result in the release of organic substances into the air. Everyday actions such as operating vehicles, cooking, and even breathing release natural compounds like alcohols, alkanes, alkenes, amides, aromatics, carbonyls, esters, and ethers into the atmosphere. Additionally, the use of pesticides, construction materials, lawn mowing, venting gases, industrial wastewater discharge, petroleum refining, natural gas processing, and painting are also important contributors to these emissions [1, 2]. Technically, VOCs can be defined as organic compounds with a Reid vapor pressure exceeding 10.3 Pa under normal temperature (293.15 K) and pressure (101.325 kPa) [5, 6]. VOCs can be classified

according to their chemical structure and properties, leading to several distinct categories [7].

These include, but are not limited to:

- *Aliphatic Compounds*: Straight-chain or branched nonaromatic organic compounds such as methane, ethane, propane, and butane.
- *Oxygenated Compounds*: Contain oxygen atoms in their structure with unsaturated bonds, such as alcohols (methanol, ethanol), ketones (acetone), and esters.
- *Aromatic Compounds*: Compounds with a cyclic (ring) structure such as benzene, toluene, and xylene.
- *Halogenated Compounds*: Hydrocarbons with halogen (fluorine, chlorine, bromine, or iodine) substitutions such as chloroform, carbon tetrachloride, and dichloromethane.
- *Esters*: Compounds formed by the condensation reaction between acids and alcohols such as ethyl acetate and butyl acetate.
- *Terpenes*: Found in essential oils from plants such as limonene and pinene [7].

Table 1.1 presents a compendium of the physical attributes of some VOCs, for example, immediately dangerous to life or health (IDLH) and threshold limit value (TLV) of some VOCs. The TLV refers to the highest concentration of a chemical that can be present in the air without causing harm to human health after prolonged exposure [2].

TABLE 0.1
Property and threshold limit values of some common VOCs [2]

VOC name and formula	Properties	IDLH	TLV
Acetone (C ₃ H ₆ O)	Colorless, pungent odor, sweetish taste, flammable	20,000 ppm	750 ppm
Acetylene (C ₂ H ₂)	Colorless, distinctive odor, low toxicity	N/A	N/A
Benzene(C ₆ H ₆)	Colorless, strong aroma, highly flammable, Chronic toxicity	500 ppm	1 ppm
Cyclohexene (C ₆ H ₁₀)	Colorless, mild solvent odor, Flammable, low acute toxicity	10,000 ppm	300 ppm
Ethanol (C ₂ H ₅ OH)	Colorless, alcoholic smell and taste, flammable, low toxicity	3300 ppm	1000 ppm

TABLE 1.1 CONTINUED

VOC name and formula	Properties	IDLH	TLV
Formaldehyde (HCHO)	Colorless, pungent odor, flammable, low acute toxicity	20 ppm	0.75 ppm
Methanol (CH ₃ OH)	Colorless, mild odor, flammable, high toxicity	25,000 ppm	200 ppm
Toluene(C ₇ H ₈)	Colorless, aromatic odor, highly flammable, slight acute toxicity	500 ppm	100 ppm
2-propanol (C ₃ H ₈ O)	Colorless, alcohol-like odor, bitter taste, Flammable low toxicity,	12,000 ppm	400 ppm
n-Butanol (C ₄ H ₉ OH)	Colorless, vinous odor, flammable, slightly toxic	8000 ppm	100 ppm

1.2.1 Sources of VOC emissions

The troposphere, or ground-level ozone, is a trace gas formed by the chemical reaction between nitrogen oxides and VOCs in the presence of sunlight. This ground-level ozone is a harmful air pollutant and is the main contributor to smog in the atmosphere in certain places. VOCs are key precursors of tropospheric ozone and can impact global climate and quality of life. Many volatile organic compounds and their resulting products contribute significantly to secondary pollutants in urban areas [8-10]. VOCs affect the oxidation (cleansing) potential of the troposphere through rapid reactions with hydroxyl radicals (OH) [11]. They are emitted from numerous anthropogenic and natural sources. Natural sources are responsible for about 90% of emission worldwide, and stem from vegetation, biomass burning, livestock, and volcanic activity. Anthropogenic sources dominate in urban areas and include the use and production of fossil fuels, industrial activity, and consumer products like adhesives, and coatings [8, 12, 13].

1.2.1.1 Natural emissions

Naturally occurring atmospheric fumes comprised of dust from the earth's crust, sea salt in coastal regions, and organic material such as pollen, spores, or plant and animal remnants. Volcanic activities can also release significant quantities of particles into the air. Other natural sources of air pollution include: thunderstorms emitting substantial amounts of nitrogen oxides, algae on the surface of oceans resulting in the release of hydrogen sulfide (H_2S), wind erosion injecting particles into the atmosphere, and humid areas like swamps, or shallow lakes generating methane [10].

1.2.1.2 Anthropogenic

The term anthropogenic refers to changes in nature which are caused by or influenced by human beings. In urban settings, most air pollution originates from human actions; this includes mobile emissions such as those from cars, trucks, airplanes, and marine engines, along with stationary sources like factories and power plants [10, 14]. The inadequate burning of carbon-based fuels during road traffic is a major factor in air pollution within large cities in developed nations, leading to the creation of carbon monoxide and hydrocarbons. Moreover, nitrogen oxides (NO_x) are produced by the interaction of nitrogen and oxygen during high-temperature combustion of fossil fuels. Furthermore, human activities have caused a rise in levels of VOCs from petroleum and chemical industries, as well as NO_x emissions from power stations and vehicles. This has resulted in higher concentrations of ozone, leading to the formation of smog in densely populated and industrial areas. The use of coal and fuel oils containing sulfur result to the formation of SO_2 , which is commonly used in transportation and energy generation in various industrial processes. Fluorine derivatives and aluminum are some specific pollutants that result from industrial waste. The processing of ores leads to the release of heavy metals such as cadmium, zinc, and lead, while mercury is generated through domestic waste incineration. Nitrogen fertilizers used in agriculture produce nitric oxide and ammonia, which also contribute to pollution. Additionally, methane, another greenhouse gas, is primarily released through animal respiration [10, 15].

It is essential to monitor VOCs as they have a significant impact on the quality of our environments, human health, and industrial processes. VOCs can be useful as biomarkers in disease diagnosis and health assessment [16-18]. The analysis of exhaled breath for VOCs is a non-invasive and potentially cost-effective method for monitoring human body chemistry and diagnosing diseases. The distinctive chemical signatures of VOCs in humans can be used for rapid

diagnosis, making their monitoring crucial for early disease detection and healthcare applications. Additionally, the monitoring of VOCs in urban air has been associated with respiratory diseases, emphasizing the significance of VOC monitoring for public health purposes [19-21]. Monitoring and controlling VOC emissions are also pivotal in different working environments for promoting occupational health and safety. It's also essential for assessing the role of VOCs in air quality, especially in the context of ongoing policy goals [22] [23].

These VOCs can contribute to the formation of ozone, leading to atmospheric pollution such as haze and photochemical smog. Therefore, it is crucial to effectively monitor and prevent VOCs in furniture production [24]. Monitoring volatile organic compounds is crucial for research and development across various fields. For instance, it is important in the study of plant evolution, as plants release VOCs in reaction to both living and non-living influences, and these substances have a notable impact on plant evolutionary processes. Plants produce a wide variety of secondary metabolites (produced during metabolism) over the course of their evolution to address specific needs. These specialized compounds, known as secondary metabolites, serve diverse functions in interacting with both living and non-living elements within ecosystems. Volatile organic compounds represent one significant group among these metabolites, with more than 1700 identified across various plant species. Released from different parts of the plants, VOCs play a vital role in shaping the chemical environment of ecosystems through complex interactions at different scales—from landscapes to individual flowers. They influence interactions between plants and pollinators, herbivores, and other flora [25].

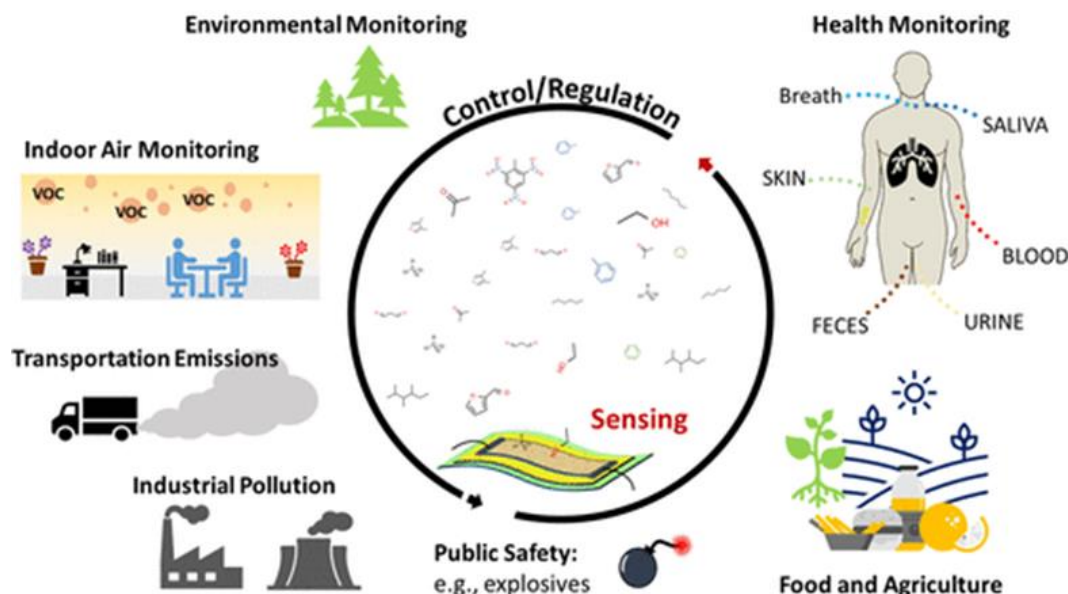


Figure 0.1 As part of a closed loop IoT network, there's a need for continuous monitoring of VOC emissions using smart sensing devices. The information obtained from this monitoring can be used to control and regulate industrial VOC generation or make decisions in healthcare regarding the existence of a disease and the need for treatment [21].

1.3 VOC detection methods

With this section starts a review of the state of the art in gas sensing detection.

A diverse range of consumer and personal care products can emit substantial amounts of VOCs into the air during usage. It is estimated that there may be 50-300 different types of VOCs present in the air of inhabited buildings at any given time. Therefore, VOC levels serve as a critical parameter to determine indoor ambient air quality, in conjunction with other metrics such as temperature and CO₂ levels [2, 14, 15]. There is active research aimed at developing technologies for both efficient and capable monitoring the stringent environmental regulations on VOCs in the environment around the world (figure 1.1) [5].

Gas sensors are a technology which can be used to monitor these VOCs. They consist of a transducer and an active layer that translates specific chemical reactions into a change in its intrinsic properties (e.g., optical, acoustic, electrical, etc.), volume, or mass once exposed to vapor analytes. The transducer is then responsible for detecting these changes and converting them into a measurable electric signal that corresponds to the nature and concentration of the analyte. To effectively monitor VOCs, it is essential to employ advanced sensing technologies that offer a range of factors such as high sensitivity, selectivity, precision, good limit of detection, good resolution, accuracy, reversibility, good recovery and response time, and real-time detection capabilities. Furthermore, the level of miniaturization and power consumption at the device level are also considered along with cost-effectiveness, longevity, and potential integration with wireless networks to determine its suitability for different applications [26, 27].

Gas sensors can be categorized based on two fundamental principles: (i) the type of transduction mechanism used, or (ii) the active layer utilized for interacting with vapor analytes. In terms of transduction mechanism, gas sensors can belong to four main families: electrochemical, optical, gravimetric/thermal, or calorimetric devices. Alternatively, gas sensors can be classified according to the type of active layer they utilize for sensing gas analytes VOCs and comprise various materials such as metal oxide semiconductors, polymers, carbon nanostructures, biomaterials, and hybrid composites which are among several functional material categories identified in studies examining interactions with VOCs (Figure 1.2) [27].

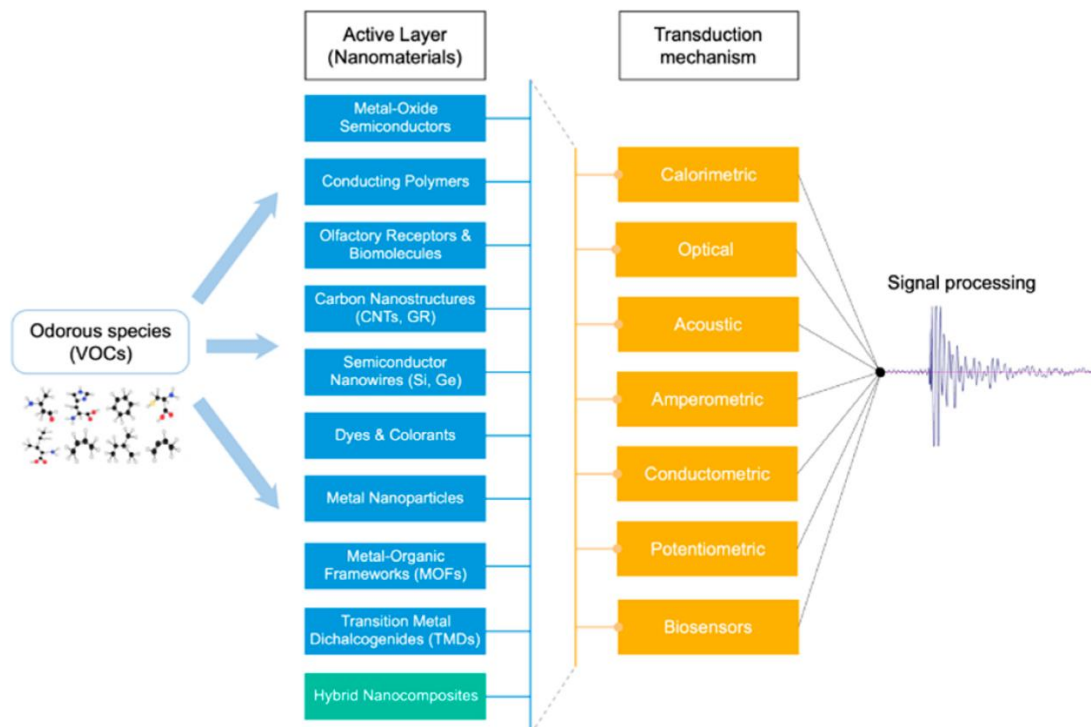


Figure 0.2. Gas sensors that monitor VOCs can be broadly categorized based on their functional materials and transduction mechanisms. This framework outlines the various families of gas sensors within these two basic principles [27].

1.3.1 Mass Spectrometry (e.g., proton-transfer-reaction mass spectrometry)

Proton-transfer-reaction mass spectrometry (PTR-MS) is a cutting-edge technique for real-time measurements of trace amounts of VOCs in the air, including various oxygenated VOCs. The technique works through the use of proton-transfer reactions involving hydronium ions (H_3O^+) to ionize VOCs, in conjunction with mass spectrometric identification of the resulting product ions. It proves to be an ideal tool for investigating the atmospheric chemistry of organic compounds as it enables the measurement of many crucial VOCs from both natural and anthropogenic sources alongside their oxidation products. Proton-transfer-reaction mass spectrometry (PTR-MS) has emerged as a useful tool for studying VOCs in the atmosphere, highlighting the significance of advanced analytical techniques for VOC monitoring [28].

1.3.2 Optical Sensors

Optical gas sensors operate based on a change in optical properties of specific gas species at specific optical wavelengths. An optical gas sensor comprises three vital components: a light-emitting element, a photodetection element, and a gas-sensing element [29]. The optical properties that are measured include light absorbance, fluorescence, polarization, color, wavelength, or reflectivity and then are converted into an electrical signal. This conversion process allows for the determination of analyte concentration and identification based on the proportional relationship between the electrical signal and the nature of the analytes [27]. Two frequently utilized optical sensors, fiber-optic gas sensors and photonic crystal cavity PhC gas sensors, are discussed.

1.3.2.1 Fiber-Optic

In the late 1980s, the fiber optic VOC gas sensor emerged and has since advanced significantly. It is now extensively used for detecting explosive gases, analyzing hazardous gases, monitoring environmental quality, and diagnosing diseases [26, 30]. This type of sensor is desirable due to its safe and dependable detection capabilities, resistance to electromagnetic interference and corrosion, compact size, lightweight nature, portability, and suitability for confined spaces.

A standard gas sensing system using fiber optics typically includes a light source, a probe for gas sensing using fiber optics, a chamber for the gas sample, a detector for measuring light intensity, and a demodulator. The light source may be a tunable or single-frequency laser, or a broadband light source. The photodetector could be a spectrometer, an optical spectrum analyzer, or a simple photodetector. Fiber optic sensors operate based on the transmission of light through

optical fibers, utilizing changes in the light signal to detect variations in the surrounding environment. For VOC sensing, these sensors often rely on the interaction between the analyte molecules and the optical properties of the sensor (such as intensity, wavelength, frequency, phase, polarization state etc.), leading to measurable changes in the transmitted or reflected light [30].

The optical fiber contains the transmitted light in its core using the total internal reflection principle, which restricts its potential for sensing applications. Therefore, a mix of different fiber optic structures is required to improve the interaction between light and the surrounding environment for sensing purposes. While fiber optic technology has proven to be effective in various fields, it still has limitations due to the fiber optic's lack of sensitivity and selectivity to gases, which greatly restricts its usefulness in sensing. Fiber optic sensors may also be limited due to their size of the optical fiber itself, which limits miniaturization [26, 30]. As a result, it is necessary to explore alternative methods to complement or replace fiber optic technology for gas detection.

The optical fiber utilizes the total internal reflection principle to contain transmitted light in its core. However, this limits its potential for sensing applications due to lack of sensitivity and selectivity to gases. To enhance the interaction between light and the surrounding environment for sensing purposes, a combination of different fiber optic structures is required. Several configurations of fiber optic sensors are used for VOC sensing, each with its unique advantages and applications. One common design involves the use of evanescent wave absorption, where a portion of the optical field extends beyond the core of the fiber, interacting with the surrounding environment. Alternatively, Fabry-Perot interferometers, surface plasmon resonance (SPR) sensors, Raman scattering, and distributed feedback (DFB) lasers are also utilized to enhance sensitivity and selectivity in VOC detection [30, 31].

1.3.2.2 Photonic Crystal Cavity (PhC)

Photonic crystal cavity sensors have emerged as a promising technology for VOC sensing due to their ability to provide highly sensitive and selective detection. Photonic crystals are dielectric materials with periodicity (e.g., polymers and semiconductors with alternating high and low refractive index), creating bandgaps that prevent certain wavelengths from propagating [32]. They influence the motion of photons similarly to how electron motion is affected by semiconductor crystals [31, 33]. By introducing defects or optical cavities into the crystal lattice, particular resonant dips/peaks are formed, allowing for highly confined optical fields. When VOCs interact with the sensor surface, changes in refractive index or absorption properties alter the resonant conditions, leading to detectable shifts in the optical spectrum [34]. The main characteristics in PhC gas sensing are the quality factor (Q) and sensitivity (S). The energy stored inside the cavity structure is proportional to Q, while the size of the cavity is linked to the mode volume. PhC gas sensors come in three variations: 1D, 2D, and 3D configurations. The fabrication process for the 3D structure is intricate with limited applications. Researchers commonly focus on developing the higher Q 2D configuration due to its favorable characteristics compared to other configurations [31].

PhC sensors have found applications in diverse areas of VOC sensing. In environmental settings, they can be used for real-time detection of pollutants and monitoring air quality. In industrial settings, they offer enhanced safety by detecting harmful VOC concentrations [35]. Moreover, in medical applications, photonic crystal cavity sensors show promise for diagnosing diseases through the detection of VOC biomarkers in breath samples [36]. Despite the promising capabilities of PhC sensors, challenges such as susceptibility to environmental conditions, long-

term stability, fabrication errors, coupling problem, temperature influence, and scalability need to be addressed for widespread adoption [37].

Ongoing research is focused on developing robust and cost-effective sensor platforms while exploring novel materials and fabrication techniques. Also being explored is the integration of artificial intelligence algorithms for real-time data analysis and the development of portable, miniaturized devices for on-site VOC sensing [38, 39].

1.3.3 Gravimetric Sensors

Gravimetric gas sensors operate on the principle that the mass of an active sensing material changes when it interacts with VOCs [27]. These sensors typically consist of a sensitive material, such as a polymer or a metal-organic framework (MOF), which adsorbs VOC molecules. The mass change is then measured using a variety of techniques, such as quartz crystal microbalance (QCM) or surface acoustic wave (SAW) devices [27, 40, 41].

1.3.3.1 Surface Acoustic Wave

Surface acoustic wave (SAW) sensors are a type of gravimetric devices that use piezoelectric crystals to detect VOCs. This technology was first introduced by Wohltjen and Dessy in 1979 for chemical sensing applications. SAW sensors are highly sensitive and can detect harmful gases like H_2S , NH_3 and NO_2 . They also offer several benefits, such as operability at ambient temperatures, rapid response times, cost-effectiveness, simple reproducibility, and strong stability [30].

These devices consist of two interdigitated transducers that generate and receive an acoustic wave propagating across the surface of the piezoelectric crystal located between the transducer electrodes. These electrodes are usually made of inert metals or alloys such as Au, Cr/Au/Cr, etc. When an AC voltage is applied to these electrodes, an acoustic wave is generated which travels across the crystal surface [42]. SAW sensors commonly use crystals like lithium niobate (LiNbO_3), gallium phosphate (GaPO_4), and quartz. When VOCs interact with the surface of the sensor, they induce changes in the mass of the entire sensing unit and in the acoustic wave propagation characteristics, leading to measurable changes in frequency, velocity, or amplitude. These changes are then correlated with the concentration of the target VOCs, providing a reliable and sensitive means of detection [27, 40].

SAW sensors find applications in diverse fields for VOC sensing. In environmental settings, they are used to monitor trace levels of VOCs [43]. Additionally, SAW sensors have potential applications in healthcare for detecting cancer biomarkers in breath samples for disease diagnosis [44].

Recent progress in surface acoustic wave sensor technology has concentrated on enhancing selectivity, miniaturization, integration with electronics, and improving signal analysis. Furthermore, there is a focus on optimizing advanced coatings and functionalization techniques to mitigate undesired effects and drifts originating from the devices themselves, the environment, and the measurement system [45].

1.3.3.2 Quartz Crystal Microbalance

Quartz Crystal Microbalance (QCM) -based sensors operate similarly to SAW sensors, but they have a different device structure. The sensor comprises a quartz chip coated with a sensing membrane with absorption capabilities, and a set of gold electrodes attached to the chip's bottom, one on each side. The sensor's sensitivity and selectivity depend on the type of sensing material and the interaction between the gas and film compounds. To enhance the sensor's sensitivity, specific sensing materials for specific VOCs biomarkers need to be developed [40]. These sensors were later modified for use as gas sensors, allowing intentional improvement of their sensing abilities by integrating different chemical sensing materials with the capacity to specifically interact with a specific target gas.[46].

QCMs detect resonance frequency shift of a piezoelectric quartz crystal coated with sensing materials like polymers and graphene. The resonance frequency shift has a linear relationship with the target gas properties and concentrations due to analyte adsorption and the mass change of the gas molecules. The QCM consists of a thin quartz crystal, typically made of a piezoelectric material like quartz, which generates an electric potential under mechanical stress. VOC molecules then get adsorbed onto the crystal's coating or directly onto its surface, leading to increased mass on its surface that causes a resonant frequency shift detectable through an electrical signal [46, 47].

QCM sensors have found applications in various fields for VOC sensing. In environmental monitoring, these sensors can be used for the detection of air pollutants. They can also be used for the detection of food-borne pathogens. Furthermore, QCM sensors have also been used in healthcare applications, for instance, in detecting VOC biomarkers for degenerative diseases like atherosclerosis, diabetes, retinal, and macular degeneration [48]. Recent advancements in QCM

sensor technology include the development of advanced analyzers for real-time calculation of equivalent electrical model parameters [49].

1.3.4 Calorimetric Sensors

Calorimetric gas sensors, also known as "pellistors," "catalytic beads," or "combustible gas sensors", detect VOCs by measuring heat changes caused by combustible gases on the sensor surface [50]. They operate based on enthalpy change or thermal conductivity and have been proven effective for monitoring a wide range of hydrogen peroxide (H_2O_2) concentrations. These sensors typically consist of a thermal element, often a micro-hotplate or microheater, and a temperature-sensitive material. The basic operation of these sensors involves the measurement of the heat released or absorbed during a chemical reaction between the target gas and a catalyst, resulting in a change in temperature that can be quantitatively measured [51, 52].

Calorimetric sensors commonly lack selectivity due to their intrinsic physical mechanisms. This is because many pure gases or gas mixtures can have similar combustion enthalpies or thermal conductivities. However, many industrial uses of commercial calorimetric sensors rely on the prior knowledge of known or limited gas constituents with sufficiently different physical characteristics. In this way, the sensors can be appropriately selected and calibrated for the analytes for the intended VOC. In order to enhance the effectiveness of currently used calorimetric sensors, future focus is being directed towards decreasing power consumption, enhancing the sensors' resilience against poisoning and mechanical impact, and the development of "flame-resistant" sensors that include an enclosure to protect the sensing beads from igniting nearby gases, thereby preventing explosions [53].

2.1.1 Electrochemical Sensors

Electrochemical sensors can detect low concentrations of VOCs by analyzing the electrical response. Three primary categories of electrochemical sensors include amperometric, potentiometric, and conductometric devices [27]. Within each of these categories, there are several types of sensors.

Electrochemical sensors based on the use of **amperometric** techniques (i.e., current magnitude at constant applied voltage) are the most common methods for gas detection [54]. The magnitude of the current is determined by the properties and quantity of the analytes present. These devices function through a chemical reaction at the interface of the active electrode [27, 55]. Common amperometric electrochemical sensors include those for detecting gases such as carbon monoxide, ammonia, acetaldehyde, ethanol, ethylene, sulfur dioxide, nitrogen oxide, and nitrogen dioxide. Furthermore, these sensors are affordable, easy to use, and can often be miniaturized [56].

Potentiometric gas sensors measure changes in potential or electric field when interacting with vapor gases. Unlike amperometric sensors, they do not require a current flow to operate but are based on an open-circuit voltage measurement. Typically using solid-state electrolytes like yttria-stabilized zirconia, these devices contain an electrolyte sealed in a tube with electrodes on both the inner and outer sides, referred to as the reference electrode (RE) and sensing electrode (SE). The SE establishes an equilibrium potential influenced by the concentration of the targeted gas, while a standard potential is maintained at the RE as a reference. Coated with catalysts such as platinum or palladium for enhanced performance, potentiometric gas sensors exhibit exceptional selectivity towards specific constituents within gases, enduring stability over extended periods, and rapid response times on the millisecond scale without needing regular maintenance

[27, 55, 57]. Field effect transistors fall under this category of gas sensors and have been developed using various materials including carbon nanotubes, silicon thin films or nanowires, and polymers - particularly garnering attention due to their seamless integration capability with existing electronic platforms [27, 58].

Conductometric or chemiresistive gas sensors are widely used for detecting VOCs because of their simple design, ease of operation, low fabrication cost, compact size, and ability to be miniaturized [27]. They are based on a conducting polymer and/or metal oxide semiconductor (MOS), which both work on the principle of changing conductivity or resistance when exposed to vapor analytes. The response mechanisms may vary, but the physical components of conductive sensors, including sensing materials, electrodes, and substrates, remain largely consistent. Additionally, MOS-based sensors require an additional heating element. [40]. They also exhibit quick response and recovery times at low concentrations and display high sensitivity across a wide range of volatile compounds. While traditional chemiresistors typically have sensitivities at the parts per million (ppm) level with response and recovery times varying from several seconds to a few minutes depending on the application, recent progress in micromachining techniques and nanomaterials has resulted in devices with heightened sensitivities that can achieve limits of detection at sub-ppm levels (e.g., 10 parts per billion (ppb)) within just a few minutes (i.e., 2–3 min). Additionally, due to their simple design and compact nature, these sensors can be easily miniaturized and implemented onto flexible substrates—promising a potential for wearable applications. However, like potentiometric gas sensors, main concerns regarding chemiresistors include sensitivity to environmental factors like humidity as well as lack of selectivity, potentially leading to baseline drift or ineffective performance in complex gas mixtures [27]. Table 1.2 compares some of the common gas sensor technologies.

TABLE 0.2
Comparison of some gas detection sensor technologies [29].

No.	Sensor Type	Advantages	Disadvantages
1	Catalytic	Simple, measures flammability of gases and low-cost technology	Requires air or oxygen to work. Can be poisoned by lead, chlorine, and silicones.
2	Thermal	Robust but simple construction. Easy to operate in absence of oxygen. Measuring range is very wide.	Reaction due to heating wire.
3	Electrochemical	Measures toxic gases in relatively low concentrations. Wide range of gases can be detected.	Failures are unrevealed
4	Optical	Easy to operate in absence of oxygen. Not affected by electromagnetic interference. Monitoring area is very wide.	Affected by ambient light interference.
5	Semiconductors	Mechanically robust, works well at constant high humidity condition.	Susceptible to contaminants and changes due to environmental conditions. Non-linear response effects complexity.
6	Surface Acoustic Wave	Detect nerve and blister agents. Battery-less and could be used for wireless applications. Could be placed in harsh and rotating parts.	Due to its small size, there is difficulty in handling during fabrication process.

1.4 Metal Oxide Semiconductor (MOS) Sensors

Semiconducting oxides are materials that possess unique sensing properties, which make them ideal for use in various sensing applications. These materials have the ability to detect changes in their electrical conductivity when exposed to different gases when heated up. Metal oxides are the most commonly used sensing material in this class, as they exhibit excellent sensitivity and selectivity towards various gases [59]. Based on their oxygen ionosorption behavior, they can be classified as either n-type or p-type semiconductors. N-type semiconductors have excess electrons that move around freely, while p-type semiconductors have a deficiency of electrons, creating "holes" that can move around [75].

In 1953, Bardeen and Brattain first demonstrated the gas sensing property of semiconductors. They showed how specific gases affected the conductivity of a n-type Ge semiconductor [60]. In 1954, Heiland [61] conducted a study on the semiconducting properties of zinc oxide (ZnO) and discovered that changes in the partial pressure of oxygen or other atmospheric gases can have an impact on these properties. Specifically, he found that when the partial pressure of oxygen decreased, the conductivity of zinc oxide increased. This observation was a significant step in understanding the sensitivity of zinc oxide to changes in the environment. Later in 1962, a group led by Seiyama [62] conducted further research ZnO thin films and discovered a phenomenon related to the adsorption and desorption of gas on the surface of an oxide material. This phenomenon led to changes in the conductivity of the material, which could be measured and analyzed. This discovery opened new possibilities for the use of ZnO in various applications such as gas sensors and catalysis. A wide variety of oxide materials have been studied and described in the literature, including but not limited to ZnO, tin oxide (SnO_2), titanium oxide (TiO_2), and tungsten oxide (W_2O_3). Each of these materials has its own unique sensing properties

and can be tailored to specific sensing applications. As such, they remain a popular choice for researchers and engineers working in the field of gas sensing [63].

1.4.1 Advantages and disadvantages of MOS Sensors

MOS are widely used as gas sensing materials due to their unique properties. One of the primary advantages of these materials is their low cost, which makes them an attractive option for various applications. Additionally, metal oxide semiconductors are relatively easy to fabricate, allowing them to be produced in large quantities without significant expense. Another advantage of MOS sensors is their simplicity of use. They are easy to operate and can detect different types of gases, including flammable and toxic ones, which is essential for ensuring safety in various environments. However, there are also some limitations associated with these sensing materials.

One of the main disadvantages of metal oxide semiconductors is their poor selectivity and cross-sensitivity. This means that they might not be able to distinguish between different gases effectively, which can lead to false alarms or inaccurate readings. Additionally, they have a low sensitivity to lower gas concentrations, making their detection limit a concern. Another limitation of these materials is their high-power consumption, which can be a significant concern for portable devices. Furthermore, they are prone to baseline resistance drift, which can affect the accuracy of the readings. Finally, metal oxide semiconductors require high operating temperatures, which can limit their use in some applications [63].

1.4.2 Gas sensing mechanism

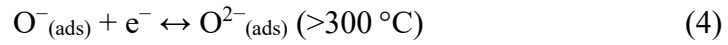
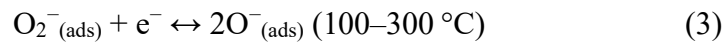
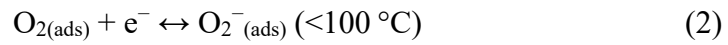
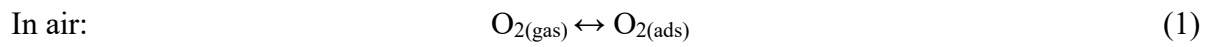
MOS-based sensors are a type of gas sensor that use a conductometric (resistive) mechanism to measure the concentration of VOCs in the air. The sensing mechanism of MOS-based gas sensors is not yet fully understood. However, the most widely accepted theory is the oxygen adsorption and desorption model, which can be explained in several steps [64].

The sensitivity of MOS gas sensors is highly dependent on the operating temperature, and to achieve the optimum operating temperature, the semiconducting metal oxide active sensing material is typically deposited directly on top of a heating layer. This heating layer, often made of a thin film of a metal such as platinum or gold, is responsible for providing a stable and controlled temperature to the active sensing material, enabling it to accurately detect and measure the concentration of gases [65, 66].

When MOS sensing materials are exposed to the air, they undergo a series of surface chemical reactions. Oxygen molecules in the air get adsorbed on the surface of these materials, leading to the formation of various chemisorbed ionic oxygen species. These oxygen species may include O_2^- , O^- , and O^{2-} ions. However, chemisorption is a process that requires activation energy, and different oxygen species require different temperatures to occur on the surface of the MOS sensing material. The O_2^- species requires higher activation energy to be chemisorbed and is usually present at higher temperatures, while other species are more likely to be ionic species at lower temperatures. At temperatures below 400°C, which is where most metal oxide-based VOC sensors operate, O_2^- is the predominant species [2].

When these negatively charged oxygen ion species are formed on the surface of n-type MOS sensing materials (having electrons as majority carriers), they lead to the creation of electron depletion regions underneath the surface of the material. This depletion region is generated due to charge transfer when the adsorbed Oxygen removes electrons from the n-type MOS material and

thereby becomes negatively ionized and thus builds a negative surface charge as depicted in the chemical reaction equations 1–4 below. The surface adsorbed Oxygen acts as electron acceptor. The formation of these ion species can be described by a set of related equations (equations 1-4), which are crucial for understanding the charge transfer mechanism between an n-type semiconductor and an electron depleting gas.



In MOS, an electron-depleted surface layer is formed in the presence of atmospheric oxygen under normal atmospheric conditions and typical operating temperatures. This oxygen is either adsorbed or chemisorbed onto the surface. When the surface layer is initially exposed to air, the MOS surface consumes the oxygen, and the oxygen ionic species get adsorbed on the top of the sensing material. This results in a band bending and the formation of a depletion region known as the space charge region. The space charge field is a region which is void of charge carriers, and it is caused by the buildup of charges due to electron transfer reactions during the adsorption of oxygen on the metal oxide surface. When target gas particles arrive at the surface of the MOS sensor material, they interact with the oxygen anions and alter their concentration level, causing a change in the electrical properties of the MOS and the charge at the surface. This change in

electrical properties can be measured and used to detect the presence of the target gas [67]. The chemical reaction between the oxygen ions and the target gas molecule is represented in equation 5 [66].



where X and X' are the target gas and the gas post-reaction, respectively, and b is the number of electrons [66].

Sensing Mechanism of n-Type Semiconductor Metal Oxide

The sensing response of different types of MOS sensing materials varies depending on the type of gas analyte they are exposed to. Specifically, n-type MOS materials exhibit opposite sensing response polarities to reducing and oxidizing gases. When reducing gas molecules such as H_2S , H_2 , NH_3 , acetone, and ethanol react with oxygen ions on the surface of the sensing material, electrons are released back to the conduction band of the material. This leads to a reduction in the thickness of the electron depletion region and an overall decrease in the resistance of the sensing material. In other words, the material becomes more conductive in the presence of reducing gases. Conversely, oxidizing gases such as NO , NO_2 , N_2O , O_3 , and others capture electrons from oxygen species, which increases the resistance of the n-type sensing material. In this case, the material becomes less conductive in the presence of oxidizing gases.

Sensing Mechanism of p-Type Semiconductor Metal Oxide

In the case of p-type MOS, with holes as majority carriers, the sensing material acts as an electron acceptor, which creates a hole accumulation region upon surface adsorption of oxygen

anions. When the p-type MOS interacts with reducing analytes, electrons are released, and the hole accumulation layer becomes thinner. This is because the electrons and holes in the layer recombine, reducing the number of holes in the p-type MOS. As a result, the overall device resistance increases. On the other hand, when p-type MOS interacts with oxidizing gas species, the resistance is reduced. This is because the oxidizing species capture the holes from the p-type MOS, leading to an increase in the number of electrons in the whole accumulation layer. This increase in the number of minority carrier electrons in the layer reduces the overall device resistance. Figure 1.3 shows the sensing mechanism of n-type and p-type MOS nanostructures [64].

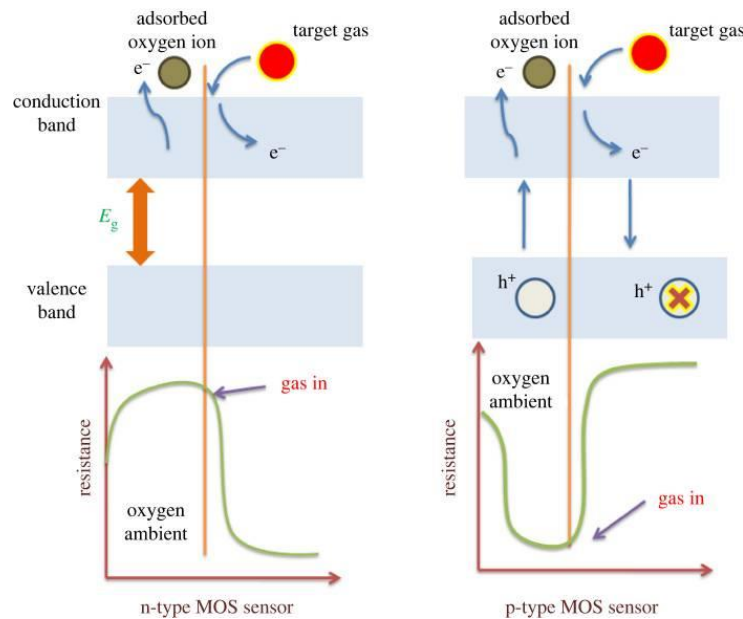


Figure 0.3. Schematic diagram illustrating the sensing mechanism of n-type and p-type MOS [67].

The gas sensing mechanism can also essentially be explained by the energy-band bending theory. When oxygen molecules are adsorbed on the surface of MOS, they extract electrons from

the conduction band by trapping charges at the sensor material surface in the form of ions. The delocalization of electrons from the bulk to the surface creates an excess of negative charge on the surface. This leads to the formation of an electron-depleted region, called a space-charge layer, which then results in an upward energy-band bending (a shift in the energy levels of electrons at the surface).

Between the grains of the polycrystalline sensor material, the merging of the two depletion regions leads to an energetic interface known as a Schottky barrier whose magnitude depends on the conductivity of the material. Essentially, this barrier prevents electrons from moving freely across the surface and can have significant effects on both the electronic and optical properties of the material. The reaction of adsorbed oxygen species with adsorbed gas can modify the intensity of the Schottky barrier, resulting in a variation of conductivity (as shown in Figure 4). Because the magnitude of the energy level is directly related to the number of molecules reacting with the metal oxide surface, the variation of the electrical parameter of the sensor (i.e. resistance, current) could be used as a variable to monitor the concentration of the target gas [2]. From Figure 1.4, E_F , E_C , and E_V are important parameters in solid-state physics that describe the energy levels of electrons in a material. The Fermi level (E_F) represents the highest occupied energy level at absolute zero temperature, and it determines the electrical conductivity of the material. The conduction band (E_C) is the lowest unoccupied energy level in a solid, and electrons in this band are free to move and carry current. The valence band (E_V) is the highest filled energy level in a solid and is separated from the conduction band by an energy gap [68].

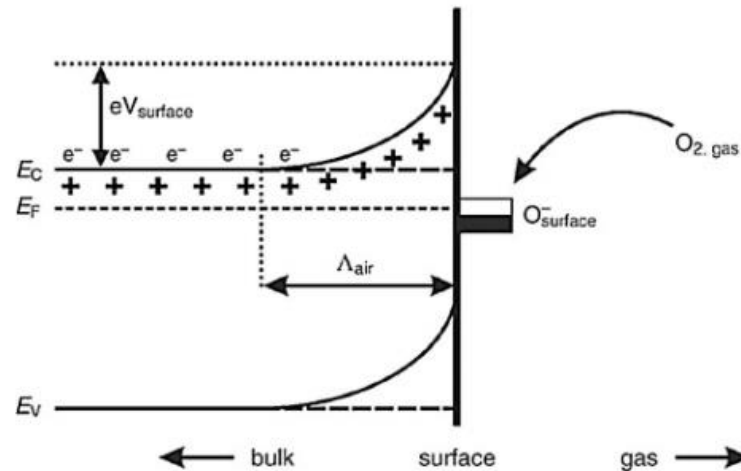


Figure 0.4. A schematic diagram of the reaction mechanism of a MOS sensor showing the band bending at the surfaced the material when exposed to a gas [69].

There are several effects to consider: the surface junction at the oxidized sensor material and the effect of the grain boundaries and the grain size. The size of the grains in the polycrystalline sensor material significantly impacts the change in energy barrier when the MOS interact with the analyte species. Sensitivity is greatly increased when the MOS structure is in the nanoscale range. Viewing the polycrystalline sensor material as aggregate particles in contact with each other can help to comprehend this effect. When oxygen adsorbs on the grain surface, it forms a space-charge layer of an appropriate width. Three different scenarios arise from the contrast between the case of double the width of the space-charge layer (L) and the grain size (d) (Figure 1.5):

- When the grain sizes are large enough ($d \gg 2L$), the conductivity of the material is mainly influenced by the mobility of carriers within the grains. In this scenario, slight changes in potential barrier caused by surface effects due to interaction with gas molecules do not significantly impact the overall conductivity of the material, resulting in reduced sensitivity.

- When the dimensions of the grains approach or exceed the width of the depletion region ($d \geq 2L$), it starts to influence the material's conductivity. As a result, even minor fluctuations in the space-charge layer's width due to reactions on the grain surface can cause substantial alterations in conductivity.

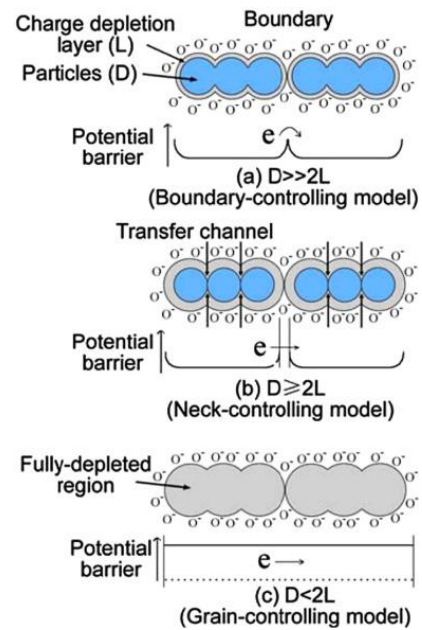


Figure 0.5. Schematic representation of how the sensitivity of metal-oxide gas sensors is influenced by the size of crystallites [2].

- Finally, if the grain sizes are smaller than the width of the depletion region ($d < 2L$), it is possible to consider that the grains are fully integrated into the space-charge layer where the entire grain is influenced by electron depletion. Under these circumstances, the material's conductivity relies entirely on charges captured on the surface of grains from adsorbed oxygen species. As a result, minor releases of electrons into bulk due to surface reactions will lead to significant variations in conductivity and high sensitivity [2].

The band bending, which is related to the built-in-potential, creates the electron-depleted layer that is more resistive than the bulk [70].

The relationship between the majority carrier concentration and the built-in potential V_{bi} is based on Poisson's one-dimensional equation, as shown in Equation 6.

$$\frac{d^2\phi}{dx^2} = \frac{qN_i}{\epsilon} \epsilon_0 \quad (6)$$

where, ϕ represents the potential, N_i represents the net density of ions in the depletion region, ϵ represents the dielectric constant of the semiconductor, and ϵ_0 represents the permittivity of free space. The built-in potential can therefore be calculated as follows.

$$V(x) = \phi_b - \phi(x) \quad (7)$$

where ϕ_b represents the potential within the semiconductor bulk. The initial integration of Poisson's equation yields:

$$\frac{dV}{dx} = \frac{qN_i(x-x_0)}{\epsilon\epsilon_0} \quad (8)$$

where the width of the depletion layer is represented by x_0 . Equation 8 can be integrated to yield the following result:

$$V = \frac{qN_ix_0^2}{2\epsilon\epsilon_0} \quad (9)$$

Equation 10 shows the value of the built-in potential, V_s , when $x = x_0$, and V is zero.

$$V_s = \frac{qN_ix_0^2}{2\epsilon\epsilon_0} \quad (10)$$

For n-type MOS material, the quantity of electrons per unit thickness is $N_Dx_0 = N_ix_0$ (where N_i represents the intrinsic carrier concentration) and equals to N_s (the number of

electrons that have moved to the surface). As a result, Equation 10 is modified to accommodate this relationship.

$$V_s = \frac{qN_s^2}{2\epsilon\epsilon_0N_i} \quad (11)$$

The energy acquired by electrons in moving towards the surface is represented by qV_s . This energy can be understood as the difference between the energy levels at the surface and in the bulk. The term N_s represents the number of electrons that migrate to the surface. It can also be used to indicate the number of electrons that return to or depart from the conduction band during oxidation or reduction processes. The association between N_s and electron concentration, which is the majority carrier in n-type, implies that N_s is linked to electron concentration [70].

During oxidation, electrons are transferred from the conduction band to the surface. This leads to an increase in N_s and a decrease in the semiconductor's bulk electron concentration. According to Equation 11, an increase in electron migration to the sensor's surface, as indicated by N_s , will result in an increase in built-in potential, V_s . The conductivity or resistivity of the semiconductor can be evaluated using V_{bi} and the majority carrier concentration.

It is important to note that the transfer of electrons during oxidation and reduction processes has significant implications for the semiconductor's behavior. As the concentration of electrons decreases, the semiconductor's conductivity or resistivity may change. Therefore, understanding the relationship between N_s and electron concentration is critical for accurately evaluating the properties of a semiconductor [70].

The conductive properties of an MOS gas sensor are ultimately determined by the total width of the depletion region at the MOS surface junction, which correlates with the V_{bi} as depicted in Equation 12.

$$W = \sqrt{\frac{2\epsilon_s}{q} \left(\frac{N_A + N_D}{N_A N_D} \right) V_{bi}} \quad (12)$$

Figure 1.6 provides a detailed schematic of the structural and band models of a MOS gas sensor before and after it has been exposed to a reducing gas, such as carbon monoxide (CO). When the MOS gas sensor is exposed to oxygen, the oxygen molecules present in the environment attract electrons from the conduction band of the semiconductor. This phenomenon results in the formation of a layer of negative oxygen ions on the surface of the MOS gas sensor. The negative oxygen ions create an electric field that opposes the flow of electrons from the conduction band to the valence band of the semiconductor. This causes an increase in the width of the depletion region and the V_{bi} between the conduction and valence bands. The increase in the potential barrier height and width reduces the concentration of free charge carriers, which in turn results in an increase in the overall resistance of the MOS gas sensor. Moreover, the reduction in the concentration of free charge carriers also reduces the sensitivity of the MOS gas sensor to the reducing gases such as CO. Thus, the schematic in Figure 1.6 is a crucial representation of the mechanism of structural and band models of a MOS gas sensor, which aids in understanding the changes in the sensor's behavior when exposed to different gases [68].

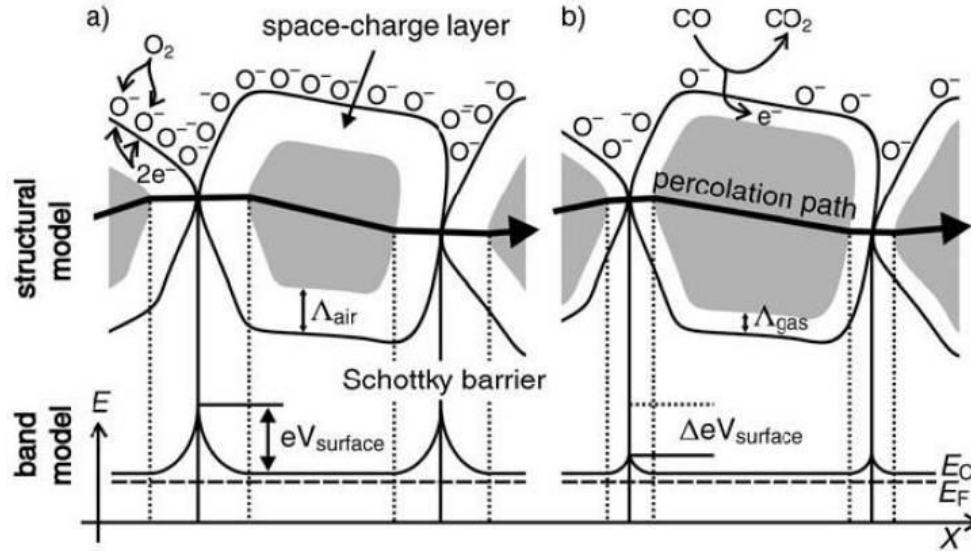


Figure 0.6. Structural and band models of conductive mechanism upon exposure to reference gas. (a) with or (b) without CO [68].

1.4.3 MOS sensor performance characteristics

The evaluation of sensor performance is based on various parameters, including the limit of detection, sensitivity, response and recovery times, selectivity, stability, and operating temperature. These parameters are critical in determining the most suitable sensor solution for a given application. Sensitivity and limit of detection are particularly important in assessing the reliability, capacity, and variability of sensor techniques and devices [71, 72]. Sensitivity and selectivity are crucial for accurately detecting and distinguishing target gases, while stability and a long-life cycle ensure the sensor's durability and reliability over time [73, 74]. Additionally, low operating temperature is essential for energy efficiency and safety, and fast response and recovery time are vital for real-time monitoring and rapid detection of gas concentrations [71].

Sensitivity

The sensitivity of a gas sensor is a crucial parameter that determines how well it can detect gases. It represents the change in electrical signal (i.e., change in the resistance of the MOS device) that occurs as a result of a change in the concentration of a particular gas. This sensitivity (S) is defined as the ratio between the response signal generated by the sensing material when exposed to the target gas analyte (R_g), and the response signal produced in the presence of air (R_a) [71]. For an n-type MOS sensor, the sensitivity can be defined by the following equation:

$$S^n = \frac{R_g}{R_a} \text{ (for a reducing gas),} \quad (13)$$

and for a p-type MOS sensor:

$$S^p = \frac{R_g}{R_a} \text{ (for an oxidizing gas),} \quad (14)$$

Where, R_g is the resistance of the sensor under exposure to a gas and R_a is the resistance of the sensor in air [67, 75]. Table 1.3 summarizes the difference between the type of MOS, the type of gas, the resistance changes, and the corresponding response equation.

TABLE 0.3

The type of resistance for n-type and p-type MOS-based sensors changes depending on the presence or absence of oxidizing and reducing gases [67].

Type of sensitive material	Type of target gas	Resistance change	Response/Sensitivity
n-type	oxidizing	resistance increase	$S = \frac{R_g}{R_a}$
n-type	reducing	resistance decrease	$S = \frac{R_a}{R_g}$
p-type	oxidizing	resistance decrease	$S = \frac{R_a}{R_g}$
p-type	reducing	resistance increase	$S = \frac{R_g}{R_a}$

Selectivity

The selectivity is the sensor's ability to distinguish between different gases when they are present in a mixture. Specifically, selectivity measures the accuracy of the sensor in detecting and identifying one specific gas among other gases that are present at the same concentration level [67]. A highly selective gas sensor is able to provide accurate and reliable readings, even when multiple gases are present in the same environment [76].

Limit of detection

The limit of detection (LOD) refers to the minimum concentration of the target analyte gas that a sensor can detect under a specific set of conditions, such as temperature, humidity, and pressure. Typically, the LOD is determined by measuring the smallest change in the sensor's output signal that can be reliably detected above the noise level [67]. High-performance sensors are

specifically designed to detect even the smallest concentrations of substances, with LODs as low as parts per million (ppm) or even lower [77].

Response and recovery times

The dynamic behavior of gas sensors can be expressed by their response and recovery times. The response time is the duration that the sensor takes to attain a stable signal when exposed to a specific concentration of the test gas. In the literature, it is often described as the duration in which the resistance of the sensing material takes to attain 90% of the saturation value after being exposed to the target gas as depicted in Figure 1.7 [71]. It is an essential parameter for gas sensors because it determines how quickly the sensor can detect a gas.

The recovery time of a gas sensor refers to the duration needed for the sensor's resistance to return to the value it had before the presence of the target gas analyte [71]. In other words, it's the time taken by the sensor to reach 90% of its initial value once the gas has been eliminated from the sensing environment [76]. A fast recovery time is crucial because it enables the sensor to be ready for the next test measurement quickly. The recovery time can vary based on the type of sensing material used, the composition of the gas analyte, added dopants, and the operating temperature of the sensor, among other factors [78].

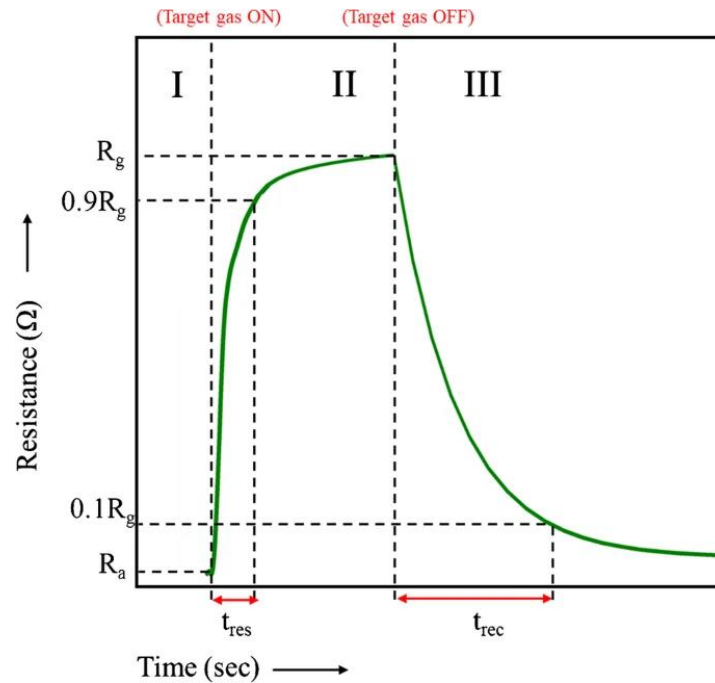


Figure 0.7. An illustration that shows the response time and recovery time of a specific MOS gas sensor. The graph displays how fast the sensor reacts to changes in gas concentration and how long it takes to return to its initial state after the gas concentration has changed [71].

Stability

The stability, or reproducibility, of a sensor determines its consistency over a certain period of time. Typically, MOS sensors have low stability which can result in undesired output or false alarms. However, in some cases, it is possible to improve their stability by lowering the operating temperature [76].

Operating temperature

The sensitivity of a gas sensor is highly dependent on the operating temperature or working temperature as shown in Figure 1.8. This is the temperature at which a gas sensor

exhibits the highest response for a particular concentration of the target gas. The sensitive materials used in the sensor require a specific temperature range to fully stimulate the chemical activity necessary to produce the maximum response. If the temperature is too low, the chemical reaction will be slow, leading to a less sensitive sensor. On the other hand, if the temperature is too high, it can cause damage to the sensor's components, leading to inaccurate readings. Therefore, it is crucial to maintain the sensor at its optimum temperature (typically in the range of 25–500 °C) to ensure accurate and reliable gas detection. [67, 77].

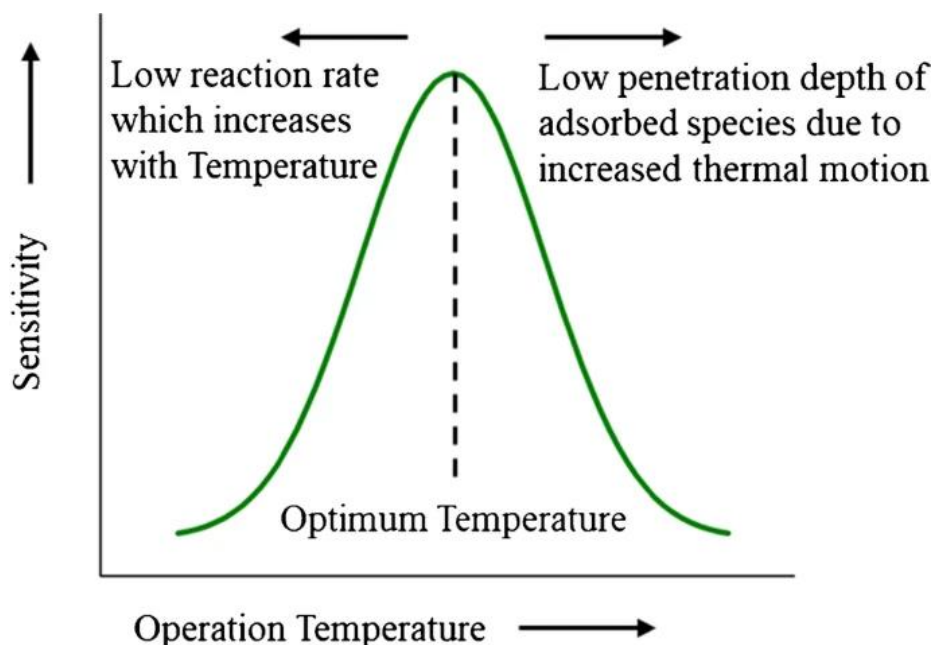


Figure 0.8. Dependence of the sensitivity of MOS gas sensors on the sensor operating temperature. Initially, an increase in temperature leads to an increase in the adsorption of gas species (both chemisorption and physisorption). However, this effect only persists up to a certain threshold, which varies depending on the specific MOS and the target gas molecule. Once this threshold is reached, the high thermal motion of the adsorbed species promotes desorption, leading to a decrease in sensor sensitivity [71].

1.4.4 Strategies for enhancing sensor performance.

In recent years, there has been notable advancement in the sensing capabilities of MOS sensors. This progress is mainly due to advancements in three key areas: controlling the structure at a microscopic level, introducing foreign atoms (doping) into the material's structure, and creating interfaces between different semiconductor materials [79].

Morphological Design

The physical and chemical properties of MOS materials determine their structure, which includes shape, size, and arrangement. The amount of adsorbed gas is directly related to the gas-sensing response. The morphology and surface condition of the sensing material are key factors in determining the quantity of adsorbed gas and thus have a significant impact on the response value. Over time, research on sensitive materials has progressed from irregular powder materials to micro-nano materials. Different shapes of materials can be designed to increase overall surface area and facilitate gas-sensitive properties by promoting the activation of reaction sites. These include 0-dimensional nanoparticles and quantum dots, 1-dimensional nanowires and nanofibers, 2-dimensional nanosheets, as well as 3-dimensional nanostructured materials such as flower-like structures and spherical shapes. Nanomaterials have an advantage in Gas Sensing Technology due to their unique properties at a nanometer scale [79].

This has emerged as an effective method for enhancing sensing capabilities. Different material shapes can be crafted to enhance the overall surface area and promote the activation of reaction sites, thus facilitating gas-sensitive properties. These varied shapes include nanoparticles, nanoflowers, nanofibers, and nanosheets [79, 80].

Doping

Doping refers to the introduction of an element into a carrier material, which results in changes to its crystal structure, size, and electrical conductivity [81]. Doping is the most direct and effective way to improve the gas-sensing abilities of sensitive materials and allows for the creation of defects which changes the electronic properties of MOS materials. By introducing metal atoms into the host material, vacancies in the structure are occupied, resulting in thicker electron withdrawal layers on the surface. This increases surface-active sites, enhancing sensing performance. Metals like Rh and Ru can serve as active sites for oxygen activation, improving atom utilization and producing a high amount of adsorbed oxygen. Noble metals like Au exhibit sensitization mechanisms related to the spillover effect. In this mechanism, the Au catalyst breaks down oxygen molecules, causing an influx of oxygen ions onto the host material's surface. This alters the electronic state on the gas-sensitive material's surface by creating a thicker electron withdrawal layer which affects its electrical conductivity and significantly reduces operational temperature [79, 82].

Formation of heterojunctions

As previously discussed, MOS materials can be categorized into n-type and p-type. Combining two or more MOS materials with similar or different band gaps to form heterojunctions enhances the sensing capability. When p-type and n-type MOS materials are combined, electrons transfer from n to p and holes from p to n, leading to electron-hole recombination and interactions at Fermi energy levels. This process increases the electron depletion layer, enhancing sensor sensitivity. Similarly, combining n-type MOS materials results in a narrower Fermi barrier within

composites comprising the n-n heterojunction which promotes rapid change in resistance for improved gas sensing performance. Introducing an energy barrier at the p-p heterojunction interface creates an additional electron depletion layer promoting enhanced gas sensing performance through increased electron transfer rate [79].

1.5 Dissertation Objectives

Traditional gas sensing techniques suffer from various drawbacks, making them less practical for certain applications as pointed out in the literature review. Many existing methods are plagued by issues such as high cost, bulkiness, and the necessity for time-consuming pretreatment steps, all of which contribute to their limited usability. Moreover, a significant concern lies in their elevated power consumption, hindering their applicability in energy-conscious environments. Additionally, these methods often lack the capability to provide real-time information, a crucial aspect in scenarios requiring immediate response.

In contrast, Metal Oxide Semiconductor (MOS) gas sensors have emerged as a preferred choice due to several advantageous features. Their adoption is primarily attributed to their low cost, straightforward design, and ease of production, making them economically viable and accessible for various applications. MOS sensors exhibit a short response time, allowing for rapid detection of changes in the surrounding gas environment. This characteristic is particularly valuable in applications where timely data acquisition is paramount [83].

Furthermore, the wide detection range of MOS gas sensors enhances their versatility, enabling them to identify and measure a broad spectrum of gases. This attribute is advantageous in diverse settings where the composition of the gas mixture may vary. Additionally, MOS sensors

showcase resilience in harsh working environments, making them suitable for applications where exposure to extreme conditions is inevitable.

However, it is essential to acknowledge a notable challenge associated with MOS devices. The process of establishing electrical contacts to the sensing material, while necessary for functionality, introduces a potential source of contact resistance errors into the measurand. These errors can impact the accuracy and reliability of the measured data, posing a challenge that needs to be addressed in the design and calibration of MOS gas sensors. Despite this limitation, ongoing research and advancements in sensor technology aim to mitigate these issues, ensuring that the benefits of MOS gas sensors continue to outweigh their challenges in a wide array of practical applications.

In the realm of material measurement, particularly when dealing with sensitive materials that could be altered or influenced by physical contact, the need for noncontact metrology becomes imperative. Traditional measurement methods that involve physical contact can introduce contamination, alter the material's surface, or interfere with its properties. To address these challenges, noncontact metrology techniques have become pivotal, offering a means to obtain accurate measurements without direct interaction with the material under examination [84].

An alternative approach to gas sensing is provided by microwave sensors. Microwaves interact differently with different materials according to their dielectric properties, causing frequency-dependent reorientation of molecular dipoles and motion of mobile charges [85, 86]. One such advanced microwave-based technique is Broadband Dielectric Spectroscopy (BDS). BDS plays a crucial role in overcoming the limitations associated with conventional measurement methods. Unlike techniques that necessitate physical contact, BDS operates on the principle of analyzing the response of materials to varying frequencies of electromagnetic fields without direct

touch. This enables researchers and scientists to acquire precise data on the dielectric properties of materials, including their electrical conductivity, permittivity, and impedance, without causing any physical alterations [84].

The versatility of BDS lies in its capability to cover a broad spectrum of frequencies, ranging from radio frequencies to microwave frequencies. This extensive frequency range allows for a comprehensive analysis of material behavior across different energy levels. As a result, BDS becomes particularly valuable when dealing with complex or multi-phase materials that may exhibit varying dielectric properties under different conditions.

Moreover, BDS is suitable for studying a diverse range of materials, including polymers, liquids, biological samples, and more. Its nonintrusive nature makes it an ideal choice for applications where the preservation of the material's integrity is paramount, such as in pharmaceutical research, biomaterial characterization, or the analysis of delicate electronic components [85, 87].

In summary, Broadband Dielectric Spectroscopy has emerged as a pivotal tool in noncontact metrology, facilitating accurate and reliable measurements of sensitive materials without the need for physical contact. Its ability to provide comprehensive insights into the dielectric properties of diverse substances positions BDS as a versatile and invaluable technique in various scientific and industrial domains.

This study has the following objectives:

Objective 1: ZnO as the detection element

Develop a comprehensive understanding of the initial oxidization mechanism of ZnO gas sensing material in air at temperatures below 100 °C, while also exploring the detection of ethanol

using the BDS technique. This aims to reveal unique mechanistic insights inaccessible through conventional resistance-based measurements, contributing to the advancement of gas sensing technology.

Objective 2: Metal doped ZnO as the detection element

Investigate the impact of doping on ZnO gas sensing material in air at temperatures below 100 °C for ethanol detection using the BDS technique, aiming to unveil novel mechanistic insights beyond conventional resistance-based measurements. This study aims to develop a deeper understanding of doping effects, contributing to advancements in gas sensing technology.

Objective 3: Metal-Organic Framework MOF films as detection element

Utilize broadband dielectric spectroscopy (BDS) in conjunction with TCNQ-doped HKUST-1 SURMOF films (SURMOF - Surface Anchored Metal-Organic Frameworks) to detect aliphatic alcohol and acetone vapors, thereby advancing understanding and application of this sensing methodology for volatile organic compounds.

Objective 4: Side by Side comparison of ZnO vs MOF sensor material

Utilize BDS metrology to conduct a comparative analysis of ethanol vapor sensing performance between ZnO nanorods and surface-anchored metal–organic-framework thin films (HKUST-1 SURMOF) as sensing materials, focusing on temperatures below 100 °C. This

investigation aims to uncover the differences in sensing capabilities and performance between the two materials, contributing to the advancement of ethanol sensing technology.

References

- [1] E. S. Ioannis Manisalidis, Agathangelos Stavropoulos, and Eugenia Bezirtzoglou, "Environmental and Health Impacts of Air Pollution: A Review," *Front Public Health*, vol. 8, no. 14, 2020, doi: 10.3389/fpubh.2020.00014.
- [2] S. G. L. A. Mirzaei, G. Neri "Detection of hazardous volatile organic compounds (VOCs) by metal oxide nanostructures-based gas sensors: A review," *Ceramics International*, vol. 42, no. 14, pp. 15119-15141, 2016, doi: 10.1016/j.ceramint.2016.06.145.
- [3] S. V. Bhaskar Kura, Elena Ajdari, Amrita Iyer, "Growing Public Health Concerns from Poor Urban Air Quality: Strategies for Sustainable Urban Living," *Computational Water, Energy, and Environmental Engineering*, vol. 2, no. 2, pp. 1-9, 2013, doi: 10.4236/cweee.2013.22B001.
- [4] B. K. P. S.S. Anand, H.M. Mehendale, P. Wexler, Ed. *Volatile Organic Compounds*, 3 ed. (Encyclopedia of Toxicology (Third Edition)). Academic Press, 2014.
- [5] S. A. R. Muhammad Shahzad Kamal, Mohammad M. Hossain, "Catalytic oxidation of volatile organic compounds (VOCs) e A review," *Atmospheric Environment*, vol. 140, pp. 117-134, 2016, doi: 10.1016/j.atmosenv.2016.05.031.
- [6] "Volatility of a Liquid." <https://sites.duke.edu/aep/module-4-alcohol-and-the-breathalyzer-test/biology-and-chemistry-connections/volatility-of-a-liquid/> (accessed.
- [7] H. M. M. S. Satheesh Anand, *Volatile Organic Compounds (VOC)*, 2 ed. (Encyclopedia of Toxicology). Elsevier, 2005.
- [8] Ö. Ö. Arslan, Bülent, "Influence of Fuel Types and Combustion Environment on Emission of VOCs from Combustion Sources: A Review," *Muş Alparslan Üniversitesi Fen Bilimleri Dergisi*, vol. 8, no. 1, pp. 747-756, 2020.
- [9] "Ground-level Ozone Basics." [https://www.epa.gov/ground-level-ozone-pollution/ground-level-ozone-basics#:~:text=Tropospheric%2C%20or%20ground%20level%20ozone,volatile%20organic%20compounds%20\(VOC\).](https://www.epa.gov/ground-level-ozone-pollution/ground-level-ozone-basics#:~:text=Tropospheric%2C%20or%20ground%20level%20ozone,volatile%20organic%20compounds%20(VOC).) (accessed January 23, 2024).
- [10] C. Pénard-Morand, and I. Annesi-Maesano, "Air pollution: from sources of emissions to health effects," *Breathe*, vol. 1, no. 2, pp. 108-119, 2004, doi: 10.1183/18106838.0102.108.
- [11] L. A. Oltmans SJ, Harris JM, Galbally I, Scheel HE, Bodeker G, Brunke E, Claude H, Tarasick D, Johnson BJ, Simmonds P, "Long-term changes in tropospheric ozone," *Atmospheric Environment*, vol. 40, no. 17, pp. 3156-3173, 2006, doi: 10.1016/j.atmosenv.2006.01.029.
- [12] S. Rossabi, "Characterization of Volatile Organic Compound Emissions from Anthropogenic and Emerging Biogenic Sources," Doctor of Philosophy, Department of Chemistry, University of North Carolina Asheville, 2014.

- [13] R. A. a. J. Arey, "Atmospheric Degradation of Volatile Organic Compounds," *Chemical Reviews*, vol. 103 no. 12, pp. 4605-4638, 2003 doi: 10.1021/cr0206420.
- [14] A. Kansal, "Sources and reactivity of NMHCs and VOCs in the atmosphere: A review," *Journal of Hazardous Materials*, vol. 166, no. 1, pp. 17-26, 2009, doi: 10.1016/j.jhazmat.2008.11.048.
- [15] M. Wang, "Study of Volatile Organic Compounds (VOC) in the cloudy atmosphere : air/droplet partitioning of VOC," Doctor of Philosophy, Université Clermont Auvergne, 2019.
- [16] Y. Y. B. Meggie Hakim, Orna Barash, Nir Peled, Michael Phillips, Anton Amann, and Hossam Haick, "Volatile Organic Compounds of Lung Cancer and Possible Biochemical Pathways," *Chemical Reviews*, vol. 112 no. 11, pp. 5949-5966, 2012, doi: 10.1021/cr300174a.
- [17] D. R. B. B. J. Novak, S. Meinardi, F. S. Rowland , A. Pontello, D. M. Cooper, and P. R. Galassetti "Exhaled methyl nitrate as a noninvasive marker of hyperglycemia in type 1 diabetes," vol. 104, no. 40, pp. 15613-15618, 2007, doi: 10.1073/pnas.0706533104.
- [18] L. Z. H. H. Yoav Y. Broza, "Combined Volatolomics for Monitoring of Human Body Chemistry," *Scientific Reports*, vol. 4611 2014, doi: 10.1038/srep04611.
- [19] P. T. Pritam Sukul, Jochen K Schubert and Wolfram Miekisch, "Immediate effects of breath holding maneuvers onto composition of exhaled breath," *Journal of Breath Research*, vol. 8, no. 3, p. 037102, 2014 doi: 10.1088/1752-7155/8/3/037102.
- [20] J. K. S. Pritam Sukul, Peter Oertel, Svend Kamyssek, Khushman Taunk, Phillip Trefz & Wolfram Miekisch "FEV manoeuvre induced changes in breath VOC compositions: an unconventional view on lung function tests," *Scientific Reports*, vol. 6, no. 1, p. 28029, 2016, doi: 10.1038/srep28029.
- [21] M. K. a. H. Haick, "Sensors for Volatile Organic Compounds," *ACS Nano*, vol. 16 no. 5, pp. 7080-7115, 2022, doi: 10.1021/acsnano.1c10827.
- [22] S. F. Ronil J. Rath, Farshad Oveissi, Fariba Dehghani, Sina Naficy, "Chemiresistive Sensor Arrays for Gas/Volatile Organic Compounds Monitoring: A Review," *Advanced Engineering Materials*, vol. 25, no. 3, p. 2200830, 2022, doi: 10.1002/adem.202200830.
- [23] A. G. Shan Gu, and Celia Faiola, "Effects of Anthropogenic and Biogenic Volatile Organic Compounds on Los Angeles Air Quality," *Environmental Science & Technology*, vol. 55, no. 18, pp. 12191-12201, 2021, doi: 10.1021/acs.est.1c01481.
- [24] Z.-G. Chen, Wei-Ping Wu, Jing Li, and Yu-Heng Zeng, "Dynamic Supervision and Control of VOCs Emission From China's Furniture Manufacturing Based on Big Data and IoT," *Front. Environ. Sci.*, vol. 10, p. 807216, 2022, doi: 10.3389/fenvs.2022.807216.
- [25] J. Picazo-Aragonés, Anass Terrab, and Francisco Balao., "Plant Volatile Organic Compounds Evolution: Transcriptional Regulation, Epigenetics and Polyploidy," *21*, vol. 23 p. 8956, 2020, doi: 10.3390/ijms21238956.
- [26] J. A. Nazemi H, Park J, Emadi A, "Advanced Micro- and Nano-Gas Sensor Technology: A Review," *Sensors*, vol. 19, no. 6, p. 1285, 2019, doi: 10.3390/s19061285.
- [27] F.-L. J. Ollé EP, Casals-Terré J, "Advancements in Microfabricated Gas Sensors and Microanalytical Tools for the Sensitive and Selective Detection of Odors," *Sensors*, vol. 20, no. 19, p. 5478, 2020, doi: 10.3390/s20195478.
- [28] J. A. d. G. Carsten Warneke, William C. Kuster, Paul D. Goldan, and Ray Fall, "Validation of Atmospheric VOC Measurements by Proton-Transfer- Reaction Mass

- Spectrometry Using a Gas-Chromatographic Preseparation Method," *Environmental Science & Technology*, vol. 37, no. 11, pp. 2494-2501, 2003 doi: 10.1021/es026266i.
- [29] M. N. H. Zainab Yunusa, Ahsanul Kaiser, Zaiki Awang, "Gas Sensors: A Review," *Sensors & Transducers*, vol. 168, no. 14, pp. 61-75, 2014.
- [30] Y. L. Yong Zhao, Bo Han, Mingyue Wang, Qi Wang, Ya-nan Zhang, "Fiber optic volatile organic compound gas sensors: A review," *Coordination Chemistry Reviews*, vol. 493, p. 215297, 2023, doi: 10.1016/j.ccr.2023.215297.
- [31] M. I. A. Asri, Hasan, M.N., Fuaad, M.R.A., Yunus, Y.M. and Ali, M.S.M, "MEMS Gas Sensors: A Review," *IEEE Sensors Journal*, vol. 21, no. 17, pp. 18381-18397, 2021, doi: 10.1109/JSEN.2021.3091854.
- [32] L. H. Sun L, Kohlstedt KL, Schatz GC, Mirkin CA, "Design principles for photonic crystals based on plasmonic nanoparticle superlattices," *Proceedings of the National Academy of Sciences*, vol. 115, no. 28 pp. 7242-7247, 2018, doi: 10.1073/pnas.1800106115.
- [33] a. T. F. K. Giampaolo Pitruzzello, "Photonic crystal resonances for sensing and imaging," *Journal of Optics*, vol. 20, no. 7, p. 073004, 2018 doi: 10.1088/2040-8986/aac75b.
- [34] Y. L. a. H. W. M. Salemink, "Photonic crystal-based all-optical on-chip sensor," *Optics Express*, vol. 20, no. 18, pp. 19912-19920, 2012, doi: 10.1364/OE.20.019912.
- [35] Z. Z. Xiaomei Shi, Zhanghua Han, "Highly sensitive and selective gas sensing using the defect mode of a compact terahertz photonic crystal cavity," *Sensors and Actuators B: Chemical*, vol. 274, pp. 188-193, 2018, doi: 10.1016/j.snb.2018.07.156.
- [36] S. S. Saronika Jindal, Mukesh Kumar, Siddharth Sharma, and Manoj Kumar Pal, "Nanocavity-Coupled Photonic Crystal Waveguide as Highly Sensitive Platform for Cancer Detection," *IEEE SENSORS JOURNAL*, vol. 16, no. 10, pp. 3705-3710, 2016, doi: 10.1109/JSEN.2016.2536105.
- [37] Y. Z. Ya-nan Zhang, Ri-qing Lv, "A review for optical sensors based on photonic crystal cavities," *Sensors and Actuators A: Physical*, vol. 233, 2015, doi: 10.1016/j.sna.2015.07.025.
- [38] D. Dash, Saini, J. and Goyal, A.K., "Photonic Crystal Cavity Optimization Using AI," *In 2021 7th International Conference on Signal Processing and Communication (ICSC)*, pp. 111-113, 2021, doi: 10.1109/ICSC53193.2021.9673247.
- [39] A. B. e. al, "A tiny gas-sensor system based on 1D photonic crystal," *Journal of Physics D: Applied Physics*, vol. 48, p. 495102, 2015, doi: 10.1088/0022-3727/48/49/495102.
- [40] L. P. Cui S, Zhu H, Keener HM, "Plant Pest Detection Using an Artificial Nose System: A Review," *Sensors* vol. 18, no. 2, p. 378, 2018, doi: 10.3390/s18020378.
- [41] N. L. Hongye Yuan, Weidong Fan, Hong Cai, and Dan Zhao, "Metal-Organic Framework Based Gas Sensors," *Advanced Science*, vol. 9, no. 6, p. 2104374, 2022, doi: 10.1002/advs.202104374.
- [42] a. F. L. D. Adnan Mujahid, "Surface AcousticWave (SAW) for Chemical Sensing Applications of Recognition Layers," *Sensors*, vol. 17, p. 2716, 2017, doi: 10.3390/s17122716.
- [43] K. V. Ming Fang, Michael Rothery, Jacqueline Hines, Gregory C Frye, "Detection of organic chemicals by SAW sensor array," *Sensors and Actuators B: Chemical*, vol. 56, no. 1-2, pp. 155-157, 1999, doi: 10.1016/S0925-4005(99)00176-8.

- [44] X. Z. Junyu Zhang, Xinwei Wei, Yingying Xue, Hao Wan, Ping Wang, "Recent advances in acoustic wave biosensors for the detection of disease-related biomarkers: A review," *Analytica Chimica Acta*, vol. 1164, 2021, doi: 10.1016/j.aca.2021.338321.
- [45] O. P. Devkota J, Greve DW, "SAW sensors for chemical vapors and gases," *Sensors*, vol. 17, no. 4, p. 801, 2017, doi: 10.3390/s17040801.
- [46] C. Z. Kewei Liu, "Volatile organic compounds gas sensor based on quartz crystal microbalance for fruit freshness detection: A review," *Food Chemistry*, vol. 334, p. 127615, 2021, doi: 10.1016/j.foodchem.2020.127615.
- [47] Y. M. Lim, Swamy, V., Ramakrishnan, N., Chan, E.S. and Kesuma, H.P, "Volatile organic compounds (VOCs) in wastewater: Recent advances in detection and quantification," *Microchemical Journal*, vol. 195, p. 109537, 2023, doi: 10.1016/j.microc.2023.109537.
- [48] D. A. Nicola Luigi Bragazzi, Donatella Panatto, Daniela Tramalloni, Ivana Valle, Roberto Gasparini, "Chapter Six - Quartz-Crystal Microbalance (QCM) for Public Health: An Overview of Its Applications," *Advances in Protein Chemistry and Structural Biology*, vol. 101, pp. 149-211, 2015, doi: 10.1016/bs.apcsb.2015.08.002.
- [49] I. Burda, "Quartz Crystal Microbalance with Impedance Analysis Based on Virtual Instruments: Experimental Study," *Sensors*, vol. 22, no. 4, p. 1506, 2022, doi: 10.3390/s22041506.
- [50] A. I. K. Siti Zulaikha Ngah Demon, Norli Abdullah, Siti Aminah Mohd Noor, Ong Keat Khim, Noor Azilah Mohd Kasim, Muhd Zu Azhan Yahya, Nor Azlian Abdul Manaf, Ahmad Farid Mohd Azmi, and Norhana Abdul Halim, "Graphene-based Materials in Gas Sensor Applications: A Review," *S&M2135 Review Paper*, vol. 2, no. 3, pp. 759-777, 2020, doi: 10.18494/SAM.2020.2492.
- [51] P. S. a. P. Shukla, "A review on recent developments and advances in environmental gas sensors to monitor toxic gas pollutants," *Environmental Progress & Sustainable Energy*, vol. 42, no. 5, 2023, doi: 10.1002/ep.14126.
- [52] M. P. M. Denoual, D. Robbes, O. Sagazan, J. Grand, H. Awalaet al, "Microfabricated test structures for thermal gas sensor," *2016 International Conference on Microelectronic Test Structures (ICMTS)*, pp. 16-19, 2016, doi: 10.1109/ICMTS.2016.7476165.
- [53] X. Liu, Cheng, S., Liu, H., Hu, S., Zhang, D. and Ning, H, "A Survey on Gas Sensing Technology," *Sensors*, vol. 12, no. 7, pp. 9635-9665, 2012, doi: 10.3390/s120709635.
- [54] M. P. P. P. Richard Warburton, Robert Hoover, Michael Logman, and Kurtis Crytzer, "Amperometric Gas Sensor Response Times," *Analytical Chemistry*, vol. 70, no. 5, pp. 998-1006, 1998, doi: 10.1021/ac970644y.
- [55] J. R. S. a. J. Li, "Amperometric Gas SensorsA Review," *Chemical Reviews*, vol. 108 no. 2, pp. 352-366, 2008 doi: 10.1021/cr0681039.
- [56] P. J. Alexia W.E. Hodgson, Larry R. Jordan, and Peter C. Hauser, "Amperometric Gas Sensors of High Sensitivity," *Electroanalysis*, vol. 11, no. 10-11, pp. 782-787, 1999, doi: 10.1002/(SICI)1521-4109(199907)11:10/11<782::AID-ELAN782>3.3.CO;2-J
- [57] R. Y. Sari Lakkis, Yasser Alayli, Mohamad Sawan, "Review of recent trends in gas sensing technologies and their miniaturization potential," *Sensor Review*, vol. 34, no. 1, pp. 24-35, 2014 doi: 10.1108/SR-11-2012-724.
- [58] T. F. Gorbova E, Molochas C, Chloros D, Demin A, Tsiakaras P., "Fundamentals and Principles of Solid-State Electrochemical Sensors for High Temperature Gas Detection," *Catalysts*, vol. 12, no. 1, p. 1, 2022, doi: 10.3390/catal12010001.

- [59] M. N. H. Zainab Yunusa, Ahsanul Kaiser, Zaiki Awang, "Gas Sensors: A Review," *Sensors & Transducers*, vol. 168, no. 4, pp. 61-75, 2014, doi: 10.13074/jent.2015.12.153163.
- [60] G. Tidei, "Metal Oxide gas sensors for Volatile Organic Compounds detection," Doctoral Politecnico di Torino, 2019.
- [61] G. Heiland, "Surface Conductivity Of Semiconductors And Its Variation By Adsorption, Transverse Electric Fields And Irradiation," *Discussions of the Faraday Society*, vol. 28, pp. 168-182, 1959.
- [62] A. T. Seiyama, Fujiishi, K. and Nagatani, M, "A new detector for gaseous components using semiconductive thin films," *Analytical Chemistry*, vol. 34, no. 11, pp. 1502-1503, 1962.
- [63] M. V. Nikolic MV, Vasiljevic ZZ, Stamenkovic Z, "Semiconductor Gas Sensors: Materials, Technology, Design, and Application," *Sensors (Basel)*, vol. 20, no. 22, p. 6694, 2020, doi: 10.3390/s20226694.
- [64] B. Yang, Myung, N.V. and Tran, T.T., "1D metal oxide semiconductor materials for chemiresistive gas sensors: a review," *Advanced Electronic Materials*, vol. 7, 9, p. 2100271, 2021, doi: 10.1002/aelm.202100271.
- [65] S. M. S. H.R. Shwetha, B. Guruprasad, S.B. Rudraswamy, "MEMS based metal oxide semiconductor carbon dioxide gas sensor," *Micro and Nano Engineering*, vol. 16, p. 100156, 2022, doi: 10.1016/j.mne.2022.100156.
- [66] N. H. a. E. W. Supab Choopun, "Metal-oxide nanowires for gas sensors," *Nanowires - Recent Advances*, pp. 3-24, 2012, doi: 10.5772/54385.
- [67] S. K. Gautam YK, Tyagi S, Ambedkar AK, Chaudhary M, Pal Singh B, "Nanostructured metal oxide semiconductor-based sensors for greenhouse gas detection: progress and challenges," *R Soc Open Sci*, vol. 8, no. 3, p. 201324, 2021, doi: 10.1098/rsos.201324.
- [68] A. Dey, "Semiconductor metal oxide gas sensors: A review," *Materials Science and Engineering: B*, vol. 229, pp. 206-217, 2018, doi: 10.1016/j.mseb.2017.12.036.
- [69] Y. L. Wang C, Zhang L, Xiang D, Gao R, "Metal oxide gas sensors: sensitivity and influencing factors," *Sensors (Basel)*, vol. 10, no. 3, pp. 2088–2106, 2010, doi: 10.3390/s100302088.
- [70] P. Lin, "Enhanced Sensing Performance Of Novel Nanostructured ZnO Gas Sensors In Ethanol Vapor Concentration Detection Applications," Doctor Of Philosophy, Department Of Electrical And Computer Engineering, Old Dominion University, 2019.
- [71] N. A. Isaac, Pikaar, I. & Biskos, G., "Metal oxide semiconducting nanomaterials for air quality gas sensors: operating principles, performance, and synthesis techniques," *Microchim Acta*, vol. 196 2022, doi: 10.1007/s00604-022-05254-0.
- [72] T. A. P. R.-S. Celine I.L. Justino, Susana Cardoso, Armando C. Duarte, "Strategies for enhancing the analytical performance of nanomaterial-based sensors," *TrAC Trends in Analytical Chemistry*, vol. 47, pp. 27-36, 2013, doi: 10.1016/j.trac.2013.02.004.
- [73] X. L. Dandan Liu, You Li, Shu Yin, Jiajia Liu, and Jiatao Zhang, "Fe-Functionalized α -Fe₂O₃/ZnO Nanocages for ppb-Level Acetone Gas Sensing," *ACS Applied Nano Materials* vol. 5 no. 4, pp. 5745-5755, 2022 doi: 10.1021/acsanm.2c00769.
- [74] K. a. Y. Eu, K, "Overcoming long recovery time of metal-oxide gas sensor with certainty factor sensing algorithm," *International Journal on Smart Sensing and Intelligent Systems*, vol. 7, no. 5, pp. 1-6, 2014, doi: 10.21307/ijssis-2019-077.

- [75] P. Patial, Deshwal, M, "Selectivity and Sensitivity Property of Metal Oxide Semiconductor Based Gas Sensor with Dopants Variation: A Review," *Trans. Electr. Electron. Mater.*, vol. 23, pp. 6–18, 2022, doi: 10.1007/s42341-021-00367-4.
- [76] N. Goel, Kunal, K., Kushwaha, A. and Kumar, M, "Metal Oxide nanostructures-based Gas Sensors," *Authorea Preprints*, 2022.
- [77] Y. G. Zhang Hua, and Fanli Meng, "Metal Oxide Semiconductor Sensors for Triethylamine Detection: Sensing Performance and Improvements," *Chemosensors*, vol. 10, no. 6, p. 231, 2022, doi: 10.3390/chemosensors10060231.
- [78] L. F. R. Saruhan Bilge, Nahirniak Svitlana, "Review: Influences of Semiconductor Metal Oxide Properties on Gas Sensing Characteristics," *Frontiers in Sensors* vol. 2, 2021, doi: 10.3389/fsens.2021.657931.
- [79] K. L. Qiang Fu, Ning Li, Zhanhua Dong, "Advances in the development of MOS-based sensors for detection of ethanol: A review," *Materials Research Bulletin*, vol. 168, p. 112457, 2023, doi: 10.1016/j.materresbull.2023.112457.
- [80] Z. C. Yuan, Yang, "Strategies for Improving the Sensing Performance of Semiconductor Gas Sensors for High-Performance Formaldehyde Detection: A Review," *Chemosensors*, vol. 9, no. 7, p. 179, 2021, doi: 10.3390/chemosensors9070179.
- [81] P. Niroula, "Optimization of Nanocrystalline Metal Oxides-based Gas Sensors for Hydrogen Detection," Master of Science Degree, The University of Toledo, 2022.
- [82] W. X. Zhang F, Liu H, Liu C, Wan Y, Long Y, Cai Z, "Recent Advances and Applications of Semiconductor Photocatalytic Technology," *Applied Sciences*, vol. 9, no. 12, p. 2489, 2019, doi: 10.3390/app9122489.
- [83] J. L. G. Sun, S. Choi, W. Lee, H. Kim, & C. Lee, "Selective oxidizing gas sensing and dominant sensing mechanism of n-cao-decorated n-zno nanorod sensors," *Acs Applied Materials & Interfaces*, vol. 9, no. 11, pp. 9975-9985, 2017, doi: 10.1021/acsami.6b15995.
- [84] P. L. Papa K Amoah, Helmut Baumgart, Rhonda R Franklin, Yaw S Obeng, "Broadband dielectric spectroscopic detection of volatile organic compounds with ZnO nanorod gas sensors," *Journal of physics D: Applied physics*, vol. 54, no. 13, p. 135104, 2021, doi: 10.1088/1361-6463/abd3ce.
- [85] G. R. P. Yang Wu, Gianluca Verderame, Daniele Annicchiarico, Thanuja Galhena, Stephen Hodge, Hannah Joyce, Patrizia Livreri, Antonio Lombardo, "Microwave gas sensor based on graphene aerogels," *IEEE SENSORS JOURNAL*, vol. 23, no. 17, pp. 19282-19289, 2023, doi: 10.1109/JSEN.2023.3295176.
- [86] W. H. H. Woodward, *Broadband Dielectric Spectroscopy: A Modern Analytical Technique*. 2021.
- [87] G. G. N. S. K. Kumar, U. Sailaja, "Dielectric relaxation and crystallization behaviour of amorphous nilutamide," *Soft Condensed Matter*, 2016, doi: 10.48550/arxiv.1606.06049.

CHAPTER 2

MATERIALS AND EXPERIMENTAL TECHNIQUES

The focus of this chapter is on the description of the synthesis and characterization of the two sensing materials used in this study, viz (ZnO and Metal-Organic Frameworks MOFs). An in-depth description of the measurement mechanism of broadband dielectric spectroscopy (BDS) and the details of the measurement setup for sensing are also presented in Chapters 4 through 7.

2.1 Sensing Material: ZnO

Zinc oxide (ZnO) is a versatile n-type MOS material with a wide range of unique properties and characteristics. It exhibits a large direct band gap of 3.4 eV, excellent chemical and thermal stability, a high electron mobility $200 \text{ cm}^2/\text{V}\cdot\text{s}$, and possesses the electrical properties of a II–VI semiconductor with a large exciton binding energy of 60 meV. ZnO also demonstrates piezoelectric properties and self-carrier generation when subjected to tensile strain force or bending [1]. These properties, among others, make ZnO suitable for various applications, such as in antibacterial surface coatings, optoelectronics, photocatalysis, and photovoltaic devices. The excellent chemical and thermal stability and photoelectric response, make ZnO a promising choice for gas sensor [1-3].

2.1.1 Structural Properties of ZnO

Under moderate temperature and pressure conditions, the thermodynamically stable form of ZnO is the wurtzite structure [4]. The wurtzite ZnO has lattice parameters a and c measuring 3.2495 Å and 5.2062 Å, respectively. From a chemical perspective, the lattice can be described as two interwoven hexagonal close-packed Zn and O lattices. In this arrangement, each Zn^{2+} ion is tetrahedrally coordinated by four O^{2-} ions, and reciprocally, each O^{2-} ion is coordinated by four Zn^{2+} ions in a similar manner (refer to Figure 2.1). Table 2.1 displays fundamental physical characteristics of the ZnO structure [5]. Other crystalline morphologies of ZnO exists under special conditions: the cubic structure of zinc blende can be partially stabilized through the epitaxial growth of ZnO on seed crystal with cubic substrates, whereas the rock salt structure is only stable when subjected to high pressures [6].

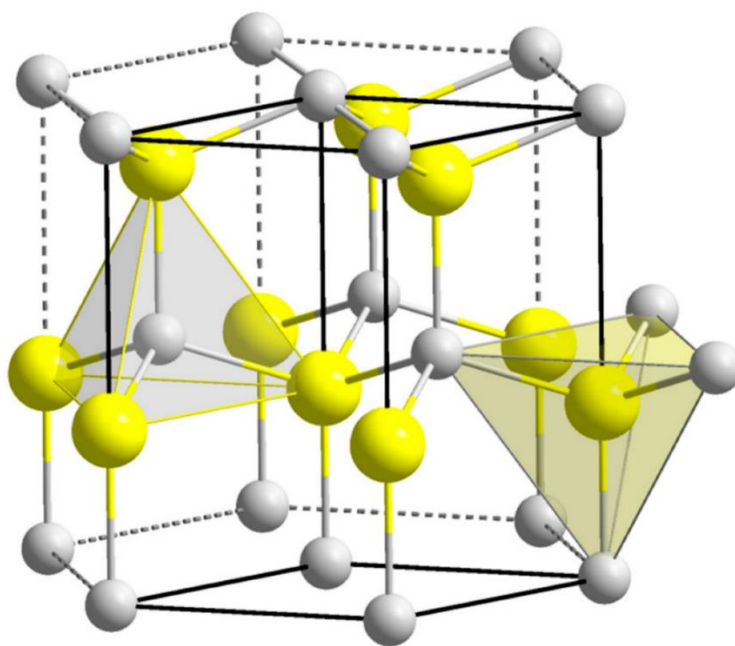


Figure 2.1. The wurtzite unit cell of ZnO is illustrated, with Zn represented in yellow and O in grey [5].

TABLE 2.1

Basic physical parameters of ZnO structure.

Physical Parameters	Values
Stable phase at 300 K	Wurtzite
Lattice Constants	$a = b = 0.32495 \text{ nm}$ and $c = 0.52069 \text{ nm}$
Melting Point	$1975 \text{ }^{\circ}\text{C}$
Density	5.66 g/cm^3
Refractive Index	2.01
Band Gap	3.4 eV, Direct
Electron effective mass	0.24
Hole effective mass	0.59
Exciton binding energy	60 meV
Static dielectric constant	8.656

2.1.2 Native defects

Defects in ZnO are typically point defects, such as oxygen vacancies (V_O), interstitial zinc (I_{Zn}), interstitial oxygen (I_O), as well as interstitial hydrogen (I_H). In n-type ZnO under thermal equilibrium, V_O , I_{Zn} , and I_H are considered as potential donors, but they exist in small quantities. This suggests that any conductivity in ZnO is due to residual impurities. Interestingly, while zinc vacancies (V_{Zn}), interstitial oxygen (I_O), and antisite oxygen (O_{Zn}), are possible acceptors, the energy required to form defects indicates a preference for contributor defects over acceptors, regardless of whether the ZnO material is type-n or type-p. Thus, point defects will lead to surface imperfections within nanostructured ZnO which can influence its final properties [3].

The clearly depicted crystal structures show various types of structural imperfections, which can impact properties such as grain boundaries, mechanical characteristics, electrical conductivity in semiconductors, and atomic diffusion. These defects within crystalline structures are categorized into four fundamental types: point defects (zero-dimensional), line defects (one-dimensional), surface defects (two-dimensional), and volumetric defects (three-dimensional). These classifications correspond to the morphologies of nanostructures. Defects can arise during the synthesis process as a result of fluctuations in temperature, pressure, solvent composition, concentration and duration of synthesis. These factors can impact the morphology of the nanostructure and consequently alter the crystal lattice of the material [3].

2.1.3 Electronic Properties

The band structure of a semiconductor refers to the distribution of energy levels of the electrons in the material. It is an essential characteristic that determines the semiconductor's properties and potential applications in electronic devices. The band structure consists of two crucial components: the valence band and the conduction band. The valence band is the highest energy level occupied by electrons at absolute zero. On the other hand, the conduction band is the lowest energy level where electrons can move freely. The band structure of ZnO (Figure 2.2), a widely used semiconductor material, is a critical factor in determining its suitability for various device applications. By understanding the energy levels of the electrons in the material, scientists and engineers can tailor the properties of the semiconductor to optimize its performance in these devices. To accurately determine the band structure of ZnO, various theoretical approaches have been employed, ranging from simple models to more complex calculations based on quantum mechanics. These methods take into account various factors such as the crystal structure,

composition, and temperature to obtain a precise understanding of the electronic properties of the material [7].

X-ray or ultraviolet (UV) reflection, absorption, or emission techniques have long been used as effective tools for measuring electronic core levels in solids. These techniques are based on inducing transitions between electronic levels or exciting collective modes. For example, one can measure the energy difference between the upper valence-band states and the upper conduction-band states, the lower valence-band states, or excitations of plasmons. Another method that is widely used for investigating the energy region is photoelectron spectroscopy (PES). This technique is based on the photoelectric effect and is extended to the X-ray region. PES measures the kinetic energy of photoelectrons that are emitted from a sample when it is irradiated with X-rays. The emitted electrons carry information about the electronic structure of the sample, which can be used to determine core-level binding energies and other important properties of the material [7].

The band gap is a region in the energy levels of a material where there are no available electronic states. The calculated energy band structure of ZnO shows a direct-type band gap of about 3.4 eV. This gap is located either at the center of the Γ k-point grid or at the Brillouin zone path G-G [8]. The band structure of ZnO is primarily determined by the valence band, mainly composed of O 2p states, and the conduction band, dominated by Zn 3d states [9]. Experimental investigations of the electronic structure of zinc oxide have yielded detailed insights. The density of states analysis has shown two primary bands located between 0 and -10 eV measured from the valence band maximum. The upper band is primarily derived from the orbitals of O 2p and Zn 4s, while the lower band arises almost solely from Zn 3d electrons with a maximum located between -7 and -8 eV [10].

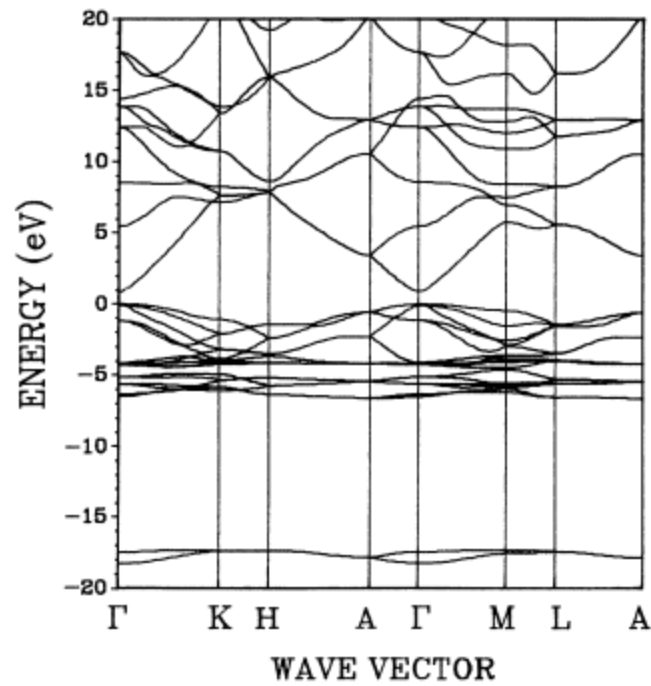


Figure 2.2. Band structure of wurtzite ZnO [11].

2.1.4 Overview of doping in ZnO

In an intrinsic semiconductor, native electrons are thermally promoted into the conduction band from the valence band to enhance the electrical conductivity the material; thus, these intrinsic semiconductors behave as insulators at 0 K. It is relatively easy to introduce “foreign” atoms into semiconductors to create impurities that that alter the properties of the host materials, such as enhanced electrical conductivity. The doped semiconductor is then described as an ‘extrinsic semiconductor’ because its behavior is controlled by the introduced dopants.

When free atoms bond into a crystalline monolith their electronic orbitals interact to create new ones with energy levels that are different from those in the constituent atoms. In a semiconductor crystal, when the constituent atoms are located at a distance from the inter-atomic

distance apart, the highest occupied orbitals interact to create new symmetry formed orbitals, and with a large number of orbitals interacting, new energy bands. In semiconductors the energy levels split and form two continuous bands known as the conduction band (CB) and the valence band (VB). The band arrangement is made up of a sequence of symmetry driven closely spaced energy levels. The lower energy levels, i.e., valence band, are populated by the electrons of from the highest occupied atomic orbitals in the constituent atoms that participated in the bonding that created the crystal. On the other hand, the conduction band is made up of a series of symmetry informed energy levels. The energy difference between the valence and lowest of the conduction bands is known as the band gap energy (E_g) (Figure 2.3), and it significantly influences the electronic properties of the material. E_g is also described as the minimum energy necessary to promote an electron from the valence energy band in its ground state to the otherwise empty conduction energy band. The width of an energy band is determined by the interaction between neighboring particles, and the number of levels within the band is influenced by the total number of interacting particles (which correlates to the quantity of atoms in a crystal). Different materials have different E_g values. For example, ZnO has a E_g of around 3.37 electron volt (eV) while that of pure silicon is around 1.12 eV.

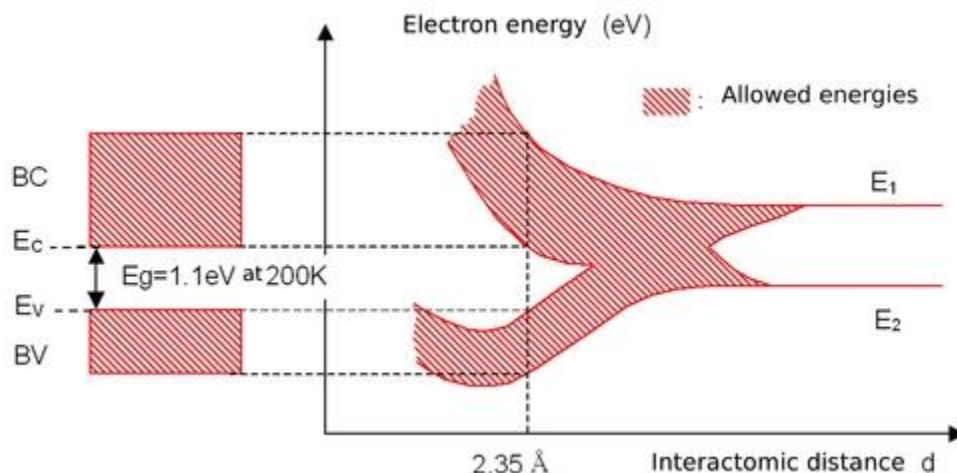


Figure 2.3. The creation of energy bands for electrons in a silicon crystal possessing a lattice structure similar to that of diamond [12].

The Fermi energy or Fermi level, E_F , refers to the highest energy state occupied by electrons at absolute zero temperature in a system. It represents the energy level at which the probability of finding an electron is $\frac{1}{2}$ [13].

When a semiconductor is doped, it results in the creation of impurity states within or outside the E_g . If impurity states are generated within the range of the E_g , they will likely decrease the size of the gap and potentially move the E_F into these impurity bands. They also increase surface defects which ultimately increases the surface area (a mandatory aspect if there is to be a significant increase in photocatalytic activity), and/or alter the electrical properties of the semiconductor metal oxide (such as ZnO and TiO₂) [14]. Conversely, when impurity states form outside of the gap, they are not anticipated to significantly impact on the value of E_g . Essentially, doping with different elements can lead to either an increase or decrease of the E_g value, depending on the specific type and amounts of dopants used.

Doped semiconductors can be classified into two types: n-type and p-type. An n-type doped semiconductor refers to a semiconductor where a foreign atom with more valence electrons (electron rich) than the original host atom is added, making electrons the majority carriers. Conversely, adding an atom with fewer valence electrons creates a p-type doped semiconductor with the majority carriers being holes [15-19]. The addition of impurities in the form of substitutional and interstitial doping (Figure 2.4) can significantly impact electronic and transport properties, lattice parameters, phase transitions, and various physicochemical properties and can reach up to pure metallic phases. For example, the modification of ZnO properties through doping plays a vital role in improving their intrinsic characteristics via alteration of their electronic structure and energy levels.

Doping can be classified into two types: substitutional doping and interstitial doping. Substitutional doping involves replacing atoms of the host metal with foreign atoms, while interstitial doping involves foreign atoms occupying the interstitial sites. Substitutional doping features foreign elements with atomic sizes and electronic properties that closely match those of the native atoms in the host crystal. While interstitial doping changes the electronic configuration, maintaining the stability of these alloys poses a challenge due to the dopant atom's tendency to lack a strong preference for location and have low mobility barriers, leading to diffusion and instability at higher temperatures. This could result in segregation or even loss of dopant, ultimately resulting in a blend of pure constituents. In metals, interstitial alloys form when foreign atoms are small enough to diffuse into the interstitial sites. Traditional examples of these alloys include metal hydrides, carbides, borides, and nitrides. These elements typically have small atomic radii and occupy the largest available interstitial site due to their dominant s-p orbitals [20].

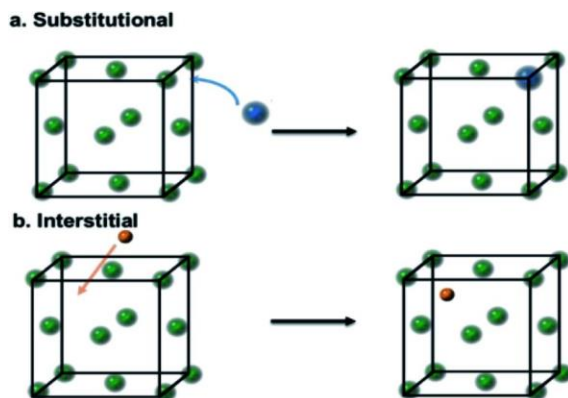


Figure 2.4. A diagram illustrating the changes made to a face-centered-cubic host metal lattice by substitutional and interstitial atomic modifications using light elements. In (a), foreign light atoms are shown displacing the original atoms in a substitutional manner. In (b), the foreign light atoms are depicted as being inserted into vacant spaces within the lattice structure [20].

It is currently unclear how certain doping elements affect the texture (i.e., grain and grain boundaries) of ZnO [21]. This lack of clarity is probably due to the effects in diverse systems, under varying experimental conditions, where individual dopants may also be influenced by other multi-component dopants present in ZnO. Hence, additional research is required to gain a comprehensive understanding of how doping impacts the electronic structure and energy levels of ZnO across different doping configurations [21, 22].

Common dopants in ZnO

ZnO exhibits relatively straightforward n-type conductivity through surplus Zn or via substitution for Zn with doping group III A elements, such as Al, B, Ga, or In. Incorporating Al, In, or Ga into ZnO improves the material's optical transmittance and reduces electrical resistivity at lower dopant levels [23, 24]. Similar to other optically transparent metal oxides, doping ZnO with p-type materials is challenging, due to the presence of native defects. Various group-V

dopants elements, such as, N, P, As, and Sb have been employed to generate p-type ZnO on the O-sites. Group IA elements, e.g., Li, Na, and K, as well as group 1B elements such as Cu, Ag, and Au, can also be used to achieve p-type ZnO via substitution on the Zn site [25, 26]. Nevertheless, achieving high-quality p-type ZnO with low resistivity and superior mobility is yet to be realized and precludes the successful fabrication of P-N junctions in ZnO. This challenge is also frequently observed in wide-bandgap semiconductors, where attaining both n- and p-type bipolar doping poses difficulties. Unlike ZnTe, which is challenging to dope n-type but easily achieves p-type doping, materials like ZnSe and GaN can be readily doped with the former facing hurdles in achieving p-type dopants [27, 28].

2.1.4.1 Roadblocks to achieving p-type ZnO

Typically, there are three main challenges in achieving p-type conductivity in wide gap semiconductors like ZnO: (i), the occurrence of defects that counteract p-type impurities; secondly, (ii) acceptors have low solid solubility and may form precipitates; and (iii) acceptor levels with considerable depth that do not ionize effectively at operational temperatures. Of these three difficulties, compensation is the most formidable challenge in widegap semiconductors.

When donors or acceptors are added to semiconductors, the position of Fermi level (E_F) is altered, causing the spontaneous creation of compensating charge defects. For example, when a semiconductor is doped with an acceptor impurity, E_F moves closer to the valence band maximum. This decrease in formation energy promotes the formation of charged donor-type defects. Since the valence band minimum is energetically more distant from the vacuum level, there can be a significant reduction in formation energy for donor defects [29]. As a result, this enhances their

formation and offsets the presence of acceptor impurities that were initially introduced into the semiconductor material. The doping defects, which inhibit the formation of p-type ZnO, are O vacancies and Zn anti-sites. These are deep donors and exhibit low energies of formation in p-type ZnO.

Beyond the inherent challenge of acceptor compensation caused by defects, the presence of contaminants which may act as donor elements can also hinder achieving p-type material. These contaminants may diffuse out from the substrate or become incorporated into the growing ZnO film due to various factors such as sample holders, process gases, chamber walls, and impurities present in raw materials. Several donors can create this effect, including hydrogen and elements from Group III B (such as aluminum, gallium, and indium); they can substitutionally occupy the zinc sites, while Group I to V (for example fluorine, chlorine, and bromine) elements can occupy the oxygen sites in the ZnO crystal [29-31]. Similarly, the challenge of obtaining high hole concentrations in p-type ZnO using traditional carrier doping methods remains a significant hurdle. This difficulty arises from the substitution of host O anion in ZnO by acceptors like N, which have high formation energy and therefore low solubility as dopants. In addition, the instability of N dopants due to weak chemical bonding with Zn compared to that of Zn-O leads to reversion from p-ZnO back into n-type over time. Thus, the key to achieving high-hole-density p-type ZnO: N lies in increasing the solubility and stability of acceptors like N dopants [32]. Finally, the high electronegativity of oxygen leads to metal oxides like ZnO having significantly high ionization energies leading to a lower valence band maximum. This results in deep acceptor levels and presents a significant challenge for achieving p-type doping and fully harnessing the potential of ZnO as an optoelectronic material [33].

2.1.4.2 Methods of Doping ZnO

Numerous physical and chemical techniques have been employed to introduce dopants into the lattices of different metal oxides, such as ZnO. Among these are methods such as atomic layer depositions (ALD), chemical vapor deposition (CVD), spray pyrolysis, ion implantation, hydrothermal methods, evaporation techniques, vacuum arc deposition, Pulsed laser deposition (PLD), and sputtering [34, 35]. Each of these approaches offers its own set of benefits and drawbacks. For instance, in CVD and ALD, evaporation processes, or spray techniques, the elements responsible for film growth operate with thermal energies that typically range around 0.1 eV and do not damage the developing film. Conversely, plasma-assisted methods, like PLD or magnetron sputtering, involve species with much higher energies (around 1 eV) impinging onto the growing film from the plasma, resulting in sputtering off, as well as introducing plasma generated defects in the growing. The benefit of higher energies is a heightened surface diffusivity and enhanced chemical reactivity [36]. Hence, it can be said that the energy level of the film-forming species exerts an influence on the doping efficiency. Figure 2.5 illustrates the lowest resistivity values reported for ZnO films doped using different deposition methods. Films with low resistivities ($\rho < 10^{-3} \Omega \text{ cm}$) can be produced using various methods. Ion-assisted deposition techniques allow for resistivities within the range of $1^{-3} \cdot 10^{-4} \Omega \text{ cm}$, while thermally stimulated methods are restricted to higher values in the range of $4^{-7} \cdot 10^{-4} \Omega \text{ cm}$. [14, 36].

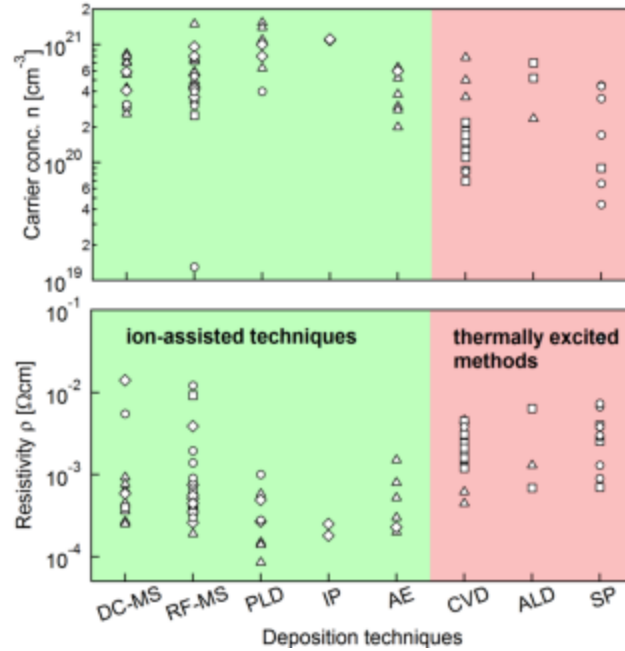


Figure 2.5. Lowest resistivities and highest free carrier concentrations achieved using various ion-assisted or thermal deposition methods [36].

The hydrothermal deposition process is significantly influenced by the experimental conditions, including temperature, concentration, and substance/substrate preparation. It can be utilized for introducing metals like Co, Al, Fe and Na into ZnO. This method of growth is more convenient as it operates at low temperatures and involves lower costs. The doping process during hydrothermal synthesis is straightforward and usually consists of mixing the precursors in a suitable ratio. However, despite its advantages, the performance of transition metal doped TiO_2 has been constrained by thermal stability issues along with an increase in charge carrier recombination centers and high costs [14, 37].

2.1.4.3 Effects of Doping on ZnO's Electronic Structure

Band gap engineering involves modifying the energy needed for electrons to transition from the valence band to the conduction band in a semiconductor material. Introducing dopants, also known as impurities, can alter electronic properties. Recently, researchers have been particularly interested in adjusting the band gap of ZnO semiconductor materials due to enhancements in their characteristics and advancements in device performance. This progress allows for precise modification of its band gap through doping with various metals such as main group metal elements, transition metals, rare earth elements, and noble elements [38].

2.1.4.3.1 Bandgap modification

Narrow bandgap semiconductors are desirable for effective operation under light irradiation. Achieving narrow bandgap engineering is challenging, as most semiconductors exhibit enlarged bandgaps with reduced dimensions due to surface defects [39]. The process of doping in ZnO has been found to play a crucial role in narrowing the bandgap, resulting in improved performance in various applications. Various elements such as non-metals, transition metals, rare-earth metals, and metal oxides have been studied for their ability to create new energy levels within the bandgap, thereby promoting the separation of photogenerated electron-hole pairs [40]. This narrowing of the bandgap is influenced by the type and quantity of dopant, resulting in localized states within the ZnO band structure and corresponding structural modifications [41]. Various mechanisms, such as band tailing, Mott critical density, the Burstein-Moss effect, and band-gap renormalization effects induced by doping different elements in the ZnO system have been attributed to this phenomenon by different research groups.

The introduction of dopants and defects in semiconductors disrupts the perfect band structure, resulting in the formation of tails within the energy gap and impacting the physical properties of the system. This phenomenon, known as band tailing, is caused by factors such as the creation of impurity bands, point defects, structural disorder, excitonic transitions, or variations in strain homogeneity. It has been observed in various semiconductor systems. When induced by doping, the decrease in the bandgap can be attributed to the introduction of dopant ions that create localized levels within the bandgap. At higher densities, these levels can overlap and form an impurity band, which may eventually merge with either the valence or conduction band as doping concentrations increase. Essentially, the interactions between electrons, holes, and impurities can lead to a downward shift of the conduction band and an upward shift of the valence band, resulting in bandgap narrowing [39].

In p-type conduction, where holes are the majority carriers, and in n-type conduction, where electrons dominate, exceeding a critical carrier concentration (Mott critical density) causes the overlap of donor wave functions. This overlap merges the impurity band into the conduction band, leading to a downward shift of the conduction band as the Fermi energy level enters it [39]. On the other hand, in highly doped n-type semiconductors, where donor electrons occupy states near the bottom of the conduction band, there are optical transitions that occur at higher photon energies in accordance with the Fermi exclusion principle [42]. This results in a widening of the band gap known as the Burstein-Moss effect. When the concentration of electrons surpasses a critical value called the Mott critical value, changes occur in crystal structure due to interactions and scattering between charge carriers and ionized impurities. These many-body interactions (to electron-electron and electron-ion interactions) cause a renormalization of the bandgap, in turn leading to narrowing of the band gap. Both effects, the Burstein-Moss shift and narrowing,

compete in determining the optical properties and performance characteristics of doped semiconductors devices [39, 42]. In summary, the mechanisms for the narrowing of the bandgap in semiconductors involve various factors such as the creation of new energy levels within the bandgap, Mott critical density, the Burstein-Moss effect, and electron-impurity interactions. These findings collectively emphasize the importance of incorporating dopants to reduce the bandgap of ZnO, consequently improving its optical and photocatalytic characteristics.

2.1.4.3.2 Energy Levels

Individual energy levels are typically formed in the band gap when the dopant concentrations are low or moderate. This occurrence is attributed to the fact that the values of donor and acceptor concentrations (N_D and N_A) are significantly smaller than the effective density of states at the band edges, namely N_C and N_V . This is referred to as non-degenerate doping. In this case, the presence of free carriers has minimal impact on the overall properties of the bulk semiconductor.

As N_D and N_A concentrations increase and approaches or exceeds N_C and N_V , the energy levels of individual particles begin to overlap, resulting in the formation of energy bands instead of discrete energy levels. This phenomenon occurs at typical dopant concentrations of 10^{19} and 10^{20} cm^{-3} , which are comparable to the concentrations of N_C and N_V (both at 10^{20} cm^{-3}). This is referred to as degenerate doping, and their energy band diagram is depicted in Figure 2.6 [43].

Further, the energy levels of the dopants can hybridize (combine) with either the conduction or valence band, resulting in the Fermi energy being situated within the band. Consequently, semiconductors that are degenerate in nature exhibit characteristics more like

metals rather than typical semiconductors. These degenerate-doped semiconductors find application in certain opto-electronic devices such as lasers, owing to their high carrier concentration [44].

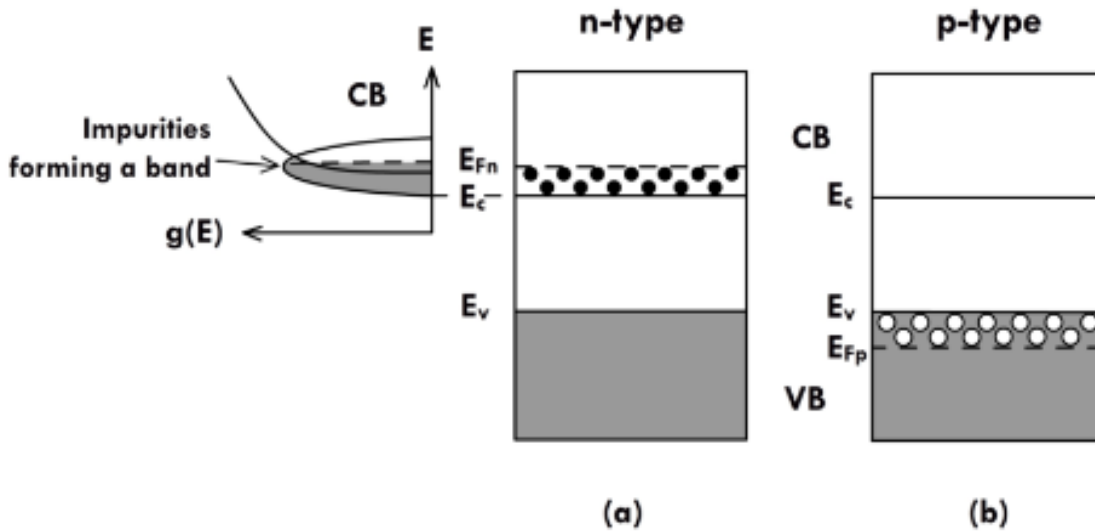


Figure 2.6. In (a) n-type and (b) p-type semiconductors, impurities can create an energy band that can merge with the valence or conduction band. Unlike regular semiconductors, the Fermi level in degenerate semiconductors is within this energy band, not the band gap. As a result, degenerate semiconductors behave more like metals [43].

By adding specific impurities to a pure semiconductor material, dopants create new energy levels in the bandgap as stated above. This alters the number and type of charge carriers and thus affecting the material's conductivity; For example, the band gap of ZnO decreases from 3.25 eV to 2.75 eV as the doping concentration increases from 5 atoms % to 20 atoms %, probably due to the interaction between Mn^{+2} dopant ions and ZnO host material through the s-p-d orbital electrons exchange mechanism. Incorporation of Mn^{+2} into the ZnO lattice introduces impurity levels which result in orbital overlap between Mn d orbital, oxygen p-orbital, and Zn s-orbital. Consequently,

this leads to an exchange interaction that elevates the valence band maximum while reducing the conduction band minimum. Thus, highlighting how adjusting dopant concentration allows for tuning of the band gap property [45].

2.1.4.3.3 Carrier Concentration

The addition of dopants in ZnO has a significant impact on the concentration of carriers, resulting in modifications to its electrical and optical properties. Various types of dopants can influence the carrier concentration, leading to changes in resistivity, mobility, and the presence of free charge carriers [46]. For example, boron dopants have been found to effectively enhance the free-carrier concentration in ZnO films[47]. Additionally, computational first-principles calculations have been utilized to assess the n-type/p-type characteristics of each dopant in ZnO by identifying primary dopant configurations and calculating carrier concentrations at specific doping [48]. Furthermore, studies on hexagonal nanocrystals doped with Ga show that higher concentrations of Ga lead to a narrower bandgap, suggesting that dopant concentration plays a role in determining carrier concentration and the structure of energy bands [49].

In certain instances, the introduction of multiple elements into ZnO can result in high carrier concentration. This phenomenon is commonly referred to as dual or co-doping. By employing dual doping, it becomes possible to precisely adjust the carrier concentration, thereby enhancing the material's suitability for applications that necessitate an equilibrium between electrons and holes. This can be observed in a study on co-doped ZnO nano powders, where the introduction of dopants resulted in an increase in carrier concentration up to a specific ratio [50]. Furthermore, the addition of Al and Ga as dopants has been found to affect the carrier concentration

in ZnO thin films. The presence of Ga atoms diffusing into the ZnO from the GaN substrate leads to a high carrier concentration [51]. However, it is important to note that there is an optimal doping concentration where the positive effect on conductivity reaches its maximum. Beyond this critical doping level, the dopants can act as impurity scattering centers and degrade carrier mobility [52].

This increase in the number of charge carriers due to doping also improves the electrical conductivity and their mobility within the crystal lattices. Moreover, higher dopant concentrations usually result in decreased resistivity, thereby promoting electrical conductivity within the material [53].

In summary, doping ZnO with different elements has a substantial effect on carrier concentration, thus altering the electrical and optical properties of the material. The concentrations and types of dopants used, as well as any resulting structural and electronic modifications in the ZnO matrix, can influence the carrier concentration.

2.1.4.3.4 Impact on Optical properties

Multiple studies have extensively examined the effects of doping on the optical properties and photoluminescence characteristics of ZnO semiconductors. Researchers have investigated different dopants and techniques to observe various optical behaviors in ZnO materials. By carefully choosing appropriate dopants and controlling their amounts, it is possible to modify the bandgap of ZnO, thus customizing its optoelectronic properties for applications like solar cells, LEDs, and sensors.

These studies reveal that doping significantly influences the way ZnO emits light, altering its photoluminescence properties. For instance, Yuan et al. investigated how adding gallium (Ga)

to ZnO nanowires affects their n-type conductivity and transport properties, influencing the material's photoluminescence behavior. [54]. Similarly, Li et al. investigated the influence of Lu doping on the PL spectrum and photovoltaic performance of ZnO, demonstrating how Lu doping influences the PL properties of the material. These investigations emphasize that dopant introduction can effectively modify and tailor the emission characteristics of ZnO for various optoelectronic applications [55].

Moreover, doping ZnO has also been proven to improve its light absorption capability and suppress the recombination of electron-hole pairs. For example, Li et al. showed that the photocatalytic performance of ZnO nanowires can be enhanced through doping with metal ions, which improves light absorption and inhibits electron-hole pair recombination [56]. Likewise, Rissi et al. found that doped ZnO nanoparticles exhibited improved optoelectronic properties, including near-infrared absorption [57].

2.1.4.4 Experimental Techniques for Studying Doping Effects

2.1.5 Characterization methods

The following are some examples of the various experimental techniques have been employed to investigate the changes in the structural, electronic, and optical characteristics of doped semiconductors:

- *Hall effect measurements:* The Hall effect is a commonly employed method for determining the carrier concentration, mobility, and conductivity, which are essential parameters for understanding the behavior of the doped material. It entails applying a magnetic field

perpendicular to the current in the semiconductor to reveal the type (i.e., electrons or holes) and amount of charge carriers [58, 59].

- *Photoluminescence Spectroscopy*: The emission of light from semiconductors upon photon excitation can be analyzed using photoluminescence spectroscopy. This technique is used to study the emission spectra and obtain insights into the bandgap, defect states, and optical characteristics of the material. It allows for the investigation of factors, such as intensity, peak position, and width of the emission bands [60].
- *Raman Spectroscopy*: Raman spectroscopy is a very powerful tool that can be used to examine the vibrational and lattice characteristics of semiconductors. This technique can offer insights into the structural changes induced by doping and identify any vibration modes associated with the dopants [61].

2.1.5.1.1 Simulation and theoretical modeling (e.g., DFT) approaches

It is a well-known that the electronic structure of materials plays a critical role in determining their properties. However, it is only thanks to recent advancements in electronic structure theory, better software, and continually increasing computing power that we can now confidently and routinely perform precise material simulations. These simulations have become an indispensable tool in studying materials, enabling us to accurately interpret experimental data and even guiding the design of new experiments [62].

In particular, calculations like Density Functional Theory (DFT) are essential and have demonstrated their unparalleled accuracy in predicting the electronic and structural properties of solids [63]. The success in uncovering the phenomena behind certain materials has opened the

door to the concept of "materials by design." This idea proposes that by using DFT calculations, it is possible to predict new materials with superior properties as compared to the existing ones. DFT can predict not only the thermodynamically stable crystal structures under standard conditions but also extend these predictions to extreme pressures. This capability represents a significant advancement in material science, enabling the exploration and comprehension of materials across a vast range of conditions [62].

2.1.5.2 Electronic Structure Calculations

An accurate prediction of energy levels, band structures, and the density of states of electrons within the material is necessary to effectively calculate the electronic structure of doped ZnO. Simulating the addition of dopants to the ZnO lattice allows for the observation of resultant changes in electronic structure and associated properties such as electrical conductivity and optical absorption [64]. There are several DFT software packages available for the calculations, each with its strengths and limitations. Some may require more computational resources (money, expertise, time), accessibility, or specialized features to execute the desired calculations [65]. The most commonly used packages include Quantum Espresso and Siesta, which are free, and the Vienna Ab initio Simulation Package (VASP) or CASTEP, which are some of the best commercially available options [66].

Xue et al. conducted a comprehensive investigation utilizing density functional theory (DFT) to explore the electronic configurations and magnetic properties of Ni-doped zincblende ZnO. Their study exemplifies the application of DFT in the analysis of Doped-ZnO systems. By substituting Ni atoms for neighboring Zn atoms, they assessed the stability of magnetic interactions

and developed a model to further understand the behavior of these systems. To study Ni-doped zincblende ZnO, the researchers performed first-principles calculations using the VASP software package. They utilized specific parameter configurations, such as projector-augmented wave potentials to address the pseudopotential and the Perdew-Burke-Ernzerhof formulation of Generalized Gradient Approximation to determine the electron exchange-correlation potential. The calculated results reveal that the anti-ferromagnetic state exhibits metallic characteristics, while the ferromagnetic state displays half-metallic magnetic properties. This indicates that Ni-doped zincblende ZnO is an excellent material with half-metallic magnetic properties. The magnetic coupling is attributed to the 100% electron-spin polarization and the partially occupied t_{2g} orbital electron. These significant findings provide valuable insights for utilizing ZnO as a Diluted Magnetic Semiconductor [67].

2.1.5.3 Applications of Doped ZnO

The intentional introduction of dopants into the ZnO allows for precise tuning of its electrical, optical, and magnetic characteristics. In the field of electronics, doped ZnO is utilized in the creation and enhancement of efficient transistors, sensors, memory devices, light-emitting diodes, solar cells, and various other optoelectronic devices. This is due to its enhanced conductivity and improved light absorption properties. The versatility of doped ZnO makes it a promising material with a broad spectrum of functionalities spanning multiple technological areas. It is highly sought after for applications ranging from optoelectronic devices to sensors and catalysis in different industrial processes [27, 68].

2.1.5.3.1 Use in optoelectronic Devices.

Doped ZnO materials offer a range of unique electrical, optical, and structural properties that make them ideal for optoelectronic devices. Dopants have been found to greatly enhance the optical and electrical characteristics of ZnO, making it a promising material for various optoelectronic applications including light-emitting diodes (LEDs), photodetectors, photocatalysis, touchscreens, displays, and solar cells.

2.1.5.3.2 Light-emitting diodes (LEDs)

LEDs are semiconductors which generate light when an electric current passes through them. This is achieved through a process called radiative recombination, where electrons flowing in one direction combine with holes flowing in the opposite direction. When these two currents meet, they recombine and neutralize each other and restore electrical balance. However, due to the higher energy level of the electrons compared to the holes, as the electron descends it emits light with a specific wavelength. The color emitted by an LED can be controlled by controlling how far the electron falls into its corresponding hole. Different voltage potentials between these two currents result in different wavelengths and thus different colors of light being produced. Ultimately, the chemical composition of the semiconductor determines both color and intensity of light output from LEDs [69].

Using doped ZnO in LEDs involves controlling the levels of doping to create p-type and n-type regions, forming a p-n junction. This enables efficient generation and recombination of electron-hole pairs, resulting in light emission. The distinctive optical and electrical properties of

doped ZnO make it an attractive material for LED applications, providing possibilities for developing efficient and high-performance light-emitting devices [70].

ZnO-based LEDs have promising applications, but there are challenges that need to be addressed for their commercialization. One challenge is the difficulty in fabricating reliable p-type ZnO, which is crucial for device development. Achieving high-quality p-n junctions in ZnO and obtaining desired threshold and breakdown voltages also pose obstacles for LED functionality. While diode-like behavior and light emission have been observed, more research is needed to fully understand these properties and improve ZnO-based LEDs [71].

2.1.5.3.3 Photodetectors

The concept of photodetection has garnered significant attention due to its wide-ranging applications in optical signal devices, industrial settings, and everyday use. Photodetectors, which convert light into electrical signals, are crucial for important tasks like ozone monitoring, space communications, and water purification. Incorporating wide bandgap semiconductors such as ZnS, GaN, and ZnO has been key in producing high-performance photodetectors [72]. The UV photo response in ZnO films was initially identified by Mollow in the 1940s, but it wasn't until the 1980s that research on ZnO-based photodetectors began to thrive. Initially, these devices had a simple structure, and their properties were not very impressive. However, as advancements in fabrication techniques for ZnO-based films emerged, more sophisticated photodetectors such as p-n junction, p-i-n junction and Schottky junction with high performance characteristics were developed [73, 74].

The addition of dopants has been demonstrated to have a substantial impact on the optical and electrical characteristics of ZnO. This allows for the creation of self-powered visible-light photodetectors with improved generation of photocurrent even without applying any bias [75]. Furthermore, modifying the shape and composition of colloidal nanocrystals with dopants has been shown to help create solution-processable UV photodetectors that have shorter cutoff wavelengths. This enhancement leads to improved device performance [76]. Additionally, advances in doped ZnO one-dimensional nanostructures have opened up new possibilities for creating high-performance photodetectors, especially when it comes to the contact technologies employed in their fabrication. These advancements highlight the potential of doped ZnO to transform photodetection technology by offering enhanced optoelectronic properties and broader applications in this field [77, 78].

2.1.5.3.4 Photocatalysis

The study of the interaction between photons and valence electrons of semiconductors was explored by Steinbach in 1972. In 1955, Markham discussed the various photochemical changes that metal oxides can undergo when exposed to UV light, including photoconductivity, fluorescence, phototropy, and photolysis. These findings have contributed greatly to the understanding of the behavior of materials under varying light conditions [79].

Photocatalysis is a widely applicable chemical process with significant industrial, research, and everyday life implications. In this process, which is inspired by natural photosynthesis, light energy can be harnessed to initiate or accelerate chemical reactions with high efficiency and precision. At the core of this process lies the photocatalyst material, which functions by absorbing

photons from light and utilizing them to propel the chemical reactions forward. Semiconductors are the most utilized photocatalysts, generating electron-hole pairs that drive the chemical reactions [80, 81].

The process has proven to be an invaluable tool in the fields of environmental purification and energy conversion. For instance, by using photocatalysts, it is possible to effectively remove organic pollutants from both air and water by using the reaction of electron-hole pairs generated, which serve to break them down into harmless byproducts during the process. Furthermore, photocatalysis plays a crucial role in various solar energy conversion processes. One such example is the splitting of water into hydrogen and oxygen.

ZnO is a widely used photocatalyst, and other metal oxides such as TiO₂ also exhibit photocatalytic properties. Of these, ZnO stands out as one of the few oxide semiconductor materials that display a quantum size effect. Additionally, it possesses excellent UV absorption and piezoelectric properties. Research has revealed a correlation between the surface composition and structure of ZnO nanoparticles and their photocatalytic properties. Oxygen vacancies on the ZnO surface have been observed to capture photogenerated electrons, indicating a strong interaction between oxygen vacancies and adsorbed oxygen, which benefits oxidation reactions. Consequently, a higher concentration of oxygen vacancies or defects results in enhanced photocatalytic activity [81, 82]. Chen et al. conducted research on N,S,C–ZnO using the precipitation method and found that non-metal dopants interfered with ZnO crystallization, leading to improved photoactivity through increased light absorption and more efficient electron-hole transportation [83].

The recombination of photoinduced holes and electrons poses a significant challenge in semiconductor-assisted photocatalysis, leading to reduced quantum efficiency and energy loss. To

enhance the effectiveness of photocatalysts, it is crucial to minimize the recombination rate and prolong the lifespan of charge carriers. The introduction of metal or non-metal elements can address this issue by improving the separation of charges between electrons and holes. Furthermore, dopants can also capture electrons, reducing the likelihood of electron-hole recombination and accelerating the photocatalytic process. Notably, incorporating non-metal elements into ZnO is highly beneficial in enhancing its characteristics for optoelectronic applications and environmental purification by narrowing bandgaps and shifting towards absorbing visible light. Using co-dopants can prevent the quick recombination of electron-hole pairs. Co-doped ZnO has been effective in eliminating dyes such as Methylene Blue, Naphthol Blue Black, Methyl Orange, Reactive Red 120, and Acid Black 1. The photodegradation effectiveness of co-dopant-ZnO surpasses that of pure ZnO and single-dopant ZnO frameworks because the co-dopants capture photo-induced electrons from ZnO's conduction band while also decreasing the recombination rate of electron-hole pairs. This sustained generation of electron-hole pairs through light exposure leads to a significant production of highly potent superoxide radical anions and hydroxyl radicals ($\bullet\text{OH}$), thereby boosting dye photo-decomposition efficiency[82, 84].

2.1.5.3.5 Solar cells

Photovoltaic cells, also known as solar cells, are devices that convert light, typically from the sun, into electrical energy through the photovoltaic effect. This process creates an electric current when certain materials are exposed to light. Solar panels make use of photovoltaic cells to capture solar energy and utilize it for a wide range of applications [85]. They are typically made from semiconductor materials, such as silicon, and designed to efficiently capture and convert

sunlight into electricity. Extensive research has been dedicated to improving the efficiency and performance of solar panels by exploring various types of solar cells like crystalline silicon, thin-film, multi-junction, and perovskite cells with efforts focused on enhancing their efficiency, stability, and cost-effectiveness [86].

Zinc oxide is widely used as an n-type semiconductor material in modern solar cells due to its abundance, high stability, simple composition, and suitability for low-temperature processing. One of the main challenges is controlling its properties to optimize performance for photovoltaic applications. Doping ZnO offers a cost-effective way to modify the built-in potential and electron-driving force in various types of solar cells. For example, doping can be used to adjust the conduction band and Fermi level positions to improve device performance. A common method involves tuning the ZnO conduction band through magnesium doping, which raises the energy level of the Zn 4s orbitals at the minimum point within the ZnO conduction band, thereby increasing its band gap [87].

More than two decades after O'Regan and Grätzel's initial study on dye-sensitized solar cells, these devices continue to generate growing interest due to their appealing characteristics and their potential in providing an answer to many environmental and energy problems [88, 89]. These include transparency, various color options, seamless integration into architectural design, a rapid energy payback period, and the potential for cost-effective production. Recent progress has led to significant improvements with a power conversion efficiency of 12.3% achieved under simulated air mass 1.5 global sunlight conditions. The principle behind DSSC relies on using light to stimulate a dye, which then causes an electron to move into the conduction band of a structured metal oxide with a wide energy gap. The oxidized form of the dye is later restored to its original state by receiving an electron from a redox couple found in an electrolyte that surrounds the

sensitized structured metal oxide film. By effectively combining three materials - metal oxide, dye, and electrolyte - the process separates light absorption (i.e., charge generation) and transport of charge carriers [89].

TiO₂ has historically been the preferred metal oxide material due to its wide band gap, physical properties, and high electronic mobility that enhances electron transportation. However, ZnO is now considered the primary alternative for DSSCs. Both substances have similar electron affinities and nearly identical band gap energies at around 3.2 eV and 3.3 eV respectively. ZnO has notably greater electron diffusivity compared to TiO₂, with an impressive electron mobility of 115–155 cm² V⁻¹ s⁻¹. This makes it particularly advantageous for facilitating good electron transport within the semiconductor and minimizing recombination rates in dye-sensitized solar cells when compared with TiO₂. Furthermore, owing to the various morphologies of ZnO, several designs of photoanodes can be realized for DSSCs using nanorods, nanowires, or nanosheets. As opposed to the crystalline structure of TiO₂, the crystalline structure of ZnO's allows for anisotropic growth making it a prime candidate for use in DSSCs with varied photoanode configurations.

Generally, the cell's effectiveness is restricted by the recombination of injected electrons and holes within it. To address this significant challenge, a range of successful strategies have been implemented. These include altering the semiconductor film in DSSC with a metal oxide or mixing the semiconductor material with another substance to enhance electron transport in the resulting film. Several materials have been doped into ZnO to enhance electron transport in the photoanode and suppress recombination reactions between injected electrons of the conduction band of ZnO and tri-iodide ions in the electrolyte. For instance, Zhao et al. reported on hierarchically structured iodine-doped ZnO-based dye-sensitized solar cells using indoline D205 and N719 as sensitizers. These findings indicated that I-ZnO cells showed longer electron lifetimes, lower charge-transfer

resistances, stronger peak currents, and extended visible light harvest—all contributing to improved cell performance. It was observed that iodine doping increased the efficiencies of both D205-I-ZnO-based DSSC and N719-I-ZnO-based DSSC by 20.3 % and 17.9 %, respectively compared to cells without iodine enhancements [88].

2.1.5.4 Conclusion

Doped ZnO, with its tunable electrical, optical, and magnetic properties, plays a pivotal role in diverse electronic applications. In the realm of optoelectronic devices, it serves as a versatile material for creating efficient transistors, sensors, memory devices, LEDs, and solar cells. The enhanced conductivity and light absorption properties of doped ZnO make it highly desirable in emerging technological areas, for applications such as in LEDs with precise doping to create p-n junctions, enabling efficient generation and recombination of electron-hole pairs for light emission. Despite the promising potential of ZnO-based LEDs, challenges in fabricating reliable p-type ZnO and achieving optimal junction characteristics require further research for successful commercialization. Additionally, doped ZnO finds application in high-performance photodetectors, where advancements in fabrication techniques and the use of dopants contribute to the development of sophisticated devices, showcasing enhanced optoelectronic properties.

Moreover, doped ZnO exhibits significant contributions to photocatalysis and solar cell technologies. In photocatalysis, ZnO serves as a widely utilized material for environmental purification and energy conversion processes. The quantum size effect, excellent UV absorption, and piezoelectric properties of ZnO, coupled with doping strategies, contribute to improved photocatalytic activity. Non-metal dopants, introduced to ZnO, enhance photoactivity and

electron-hole transportation. In the domain of solar cells, ZnO's role as an n-type semiconductor material facilitates its use in various cell types, including dye-sensitized solar cells (DSSCs). Doping ZnO offers a cost-effective means to modify its properties, optimizing performance for photovoltaic applications. Compared to traditional choices like TiO₂, ZnO demonstrates superior electron diffusivity and varied morphologies, presenting opportunities for tailored photoanode configurations in DSSCs. Research highlights the effectiveness of co-doping ZnO in enhancing electron transport, reducing recombination rates, and ultimately improving the efficiency of DSSCs. Ongoing advancements showcase the potential of doped ZnO in addressing key challenges and expanding its applications in cutting-edge electronic and optoelectronic technologies.

2.1.6 Synthesis Methods for ZnO nanorods

Current thin-film ZnO gas sensors are considered to be state-of-the-art technology, but they have been found to suffer from some limitations. These limitations include insufficient sensitivity, long response times, and long recovery times [90]. To address these shortcomings, a lot of research has gone into the development and synthesis of one-dimensional ZnO nanostructures, such as nanorods, nanotubes, nanowires, and nanofibers, due to their unique properties such as high surface-to-volume ratio, crystalline structure, and charge confinement ability. The benefits of this approach include improved sensitivity, faster response times, and shorter recovery times. These improvements will make the sensors more efficient, reliable, and effective [91]. The synthesis of ZnO nanomaterials can be broadly classified into two categories, namely wet and dry processing routes. Wet processing routes include hydrothermal methods, sonochemical growths, chemical bath depositions, and so on. In contrast, dry processing routes include vapor phase transport, sputtering, and thermal evaporation. These methods can be used to produce a variety of

morphologies which have unique properties that can be exploited for specific applications. For instance, ZnO nanowires exhibit excellent electrical and optical properties, making them suitable for use in field-effect transistors, solar cells, and optoelectronic devices. On the other hand, ZnO nanorods, nanotubes and nanobelts have high surface areas, which make them ideal for gas sensing applications [91]. Nanorods possess distinctive shape anisotropy, making them a compelling subject for research and well-suited for various applications. The enhanced capabilities of nanorods compared to spherical particles are attributed to their increased aspect ratio, which leads to heightened excitation of surface plasmons in the nanoparticles. This greater aspect ratio results in a more pronounced dipole moment within a nanoparticle, leading to stronger electrical fields in nanorods as opposed to spherical particles [92]. In this work, we used atomic layer deposition ALD for the growth of the ZnO seed layer on top of a native oxide covered p-type silicon substrate. Subsequently, a hydrothermal growth method was used to promote the growth of the ZnO nanorods from the seed layer.

2.1.6.1 Atomic Layer Deposition

Currently, the primary techniques for producing flat ZnO films consist of magnetron sputtering, atomic layer deposition (ALD), pulsed laser deposition, molecular beam epitaxy, the sol-gel process, chemical vapor deposition, and others. Of these fabrication methods, ALD is the only technology which is capable of precise control of deposition thickness and composition at the Angstrom level [93]. This study will take advantage of ALD's ability to deposit the ZnO Seed layer on a Si wafer one atomic layer per growth cycle with the two precursors Diethylzinc and water vapor at a growth rate of 1.6 Å/cycle at 200 °C where water vapor serves as the oxidizing agent (as shown in Figure 2.7).

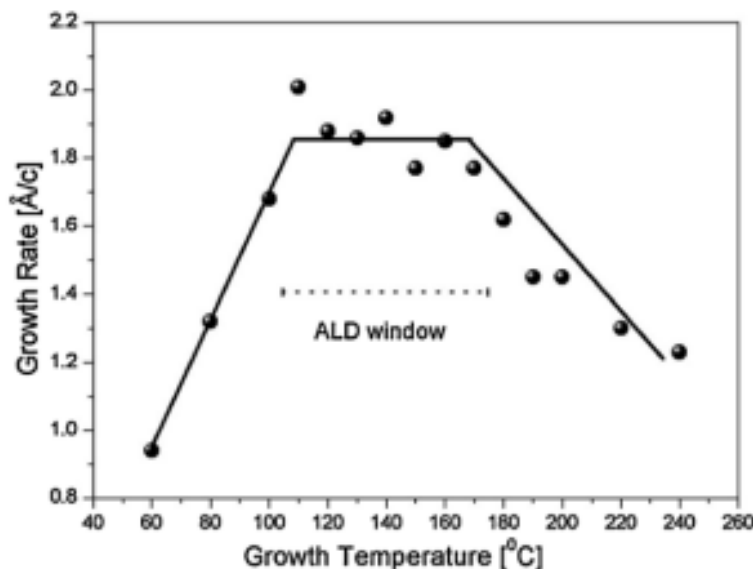


Figure 2.7. The relationship between the growth rate of ZnO and the temperature at which it is grown when diethylzinc (DEZ) and water are utilized as precursors in the ALD process [94].

ALD is used for the deposition of thin films for nanotechnology (<100 nm) in the gas phase. It involves exposing the substrate to a sequence of alternating vapor phase reactants. The ensuing self-saturating surface reactions enable precise control of film thickness at the atomic level. In the ALD process, the two reactants, called precursors, are introduced into the reaction chamber one at a time, and each precursor dose is followed by a purge step, during which the chamber is evacuated and filled with an inert gas such as nitrogen or argon. This purging step removes any excess precursor molecules and reaction by-products from the chamber, ensuring that only the desired reaction products are deposited on the substrate surface. By repeating this cycle of precursor introduction and purging, a uniform, conformal thin film can be deposited on the substrate surface with precise control over its thickness and composition.

A typical ALD process involves multiple ALD cycles, and each cycle comprises four characteristic steps:

- The first step involves the introduction of the first precursor into the reaction chamber, followed by its adsorption onto the substrate surface in a self-terminating reaction.
- In the second step, any unreacted precursor is purged from the chamber as well as the by-products.
- The second precursor is introduced. The second precursor reacts with the adsorbed first precursor to form a monolayer of the desired material.
- In the third step, any excess second precursor is purged from the chamber.
- The process is repeated for subsequent cycles until the desired thickness is achieved [95].

This process is illustrated in figure 2.8.

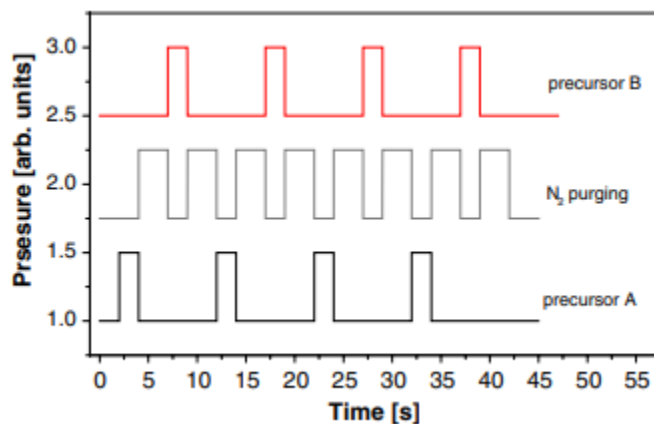


Figure 2.8. The following is a schematic representation depicting the sequential procedure involved in the ALD process [94].

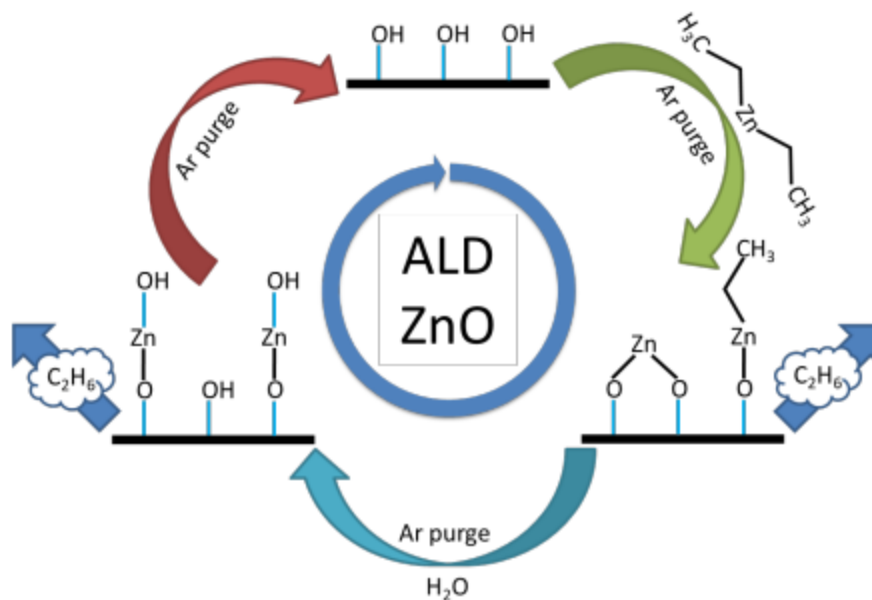
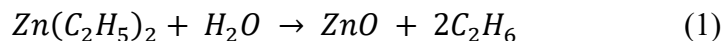


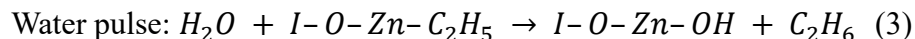
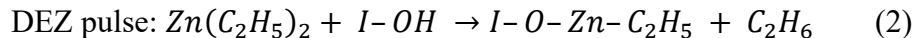
Figure 2.9. Schematic representation of the suggested surface reaction of ALD ZnO using DEZ and water as the precursors [96].

ZnO, or zinc oxide, was one of the earliest compounds to be deposited using atomic layer deposition (ALD). The first study on ALD deposition of ZnO was reported in 1985, which used zinc acetate (ZnAc) and water as precursor materials. Since then, a variety of ALD processes have been developed for ZnO growth, using different precursor combinations. These include Zn/water, ZnCl_2 /water, diethylzinc (DEZ)/water, dimethylzinc (DMZ)/water, DEZ/ O_2 , and methylzinc isopropoxide/water. Currently, the DEZ/water precursor pair is the most popular for ZnO deposition. This is due to the high vapor pressures and strong reactivity of DEZ and water, as well as the wide range of deposition temperatures (23 – 350 °C) that can be achieved with this precursor pair. Additionally, DEZ and water are readily available and cost-effective, making them an ideal choice for large-scale ZnO deposition [96]. The ALD ZnO growth cycle is depicted in Figure 2.9.

The formation of ZnO from diethylzinc and water precursors can be represented by the following overall reaction [97]:



The anticipated elementary sequences of reactions are the following:



where “I–” denotes the surface [97].

2.1.6.1.1 ALD reactors

An ALD reactor must meet certain key requirements. To begin, the reactor is responsible for heating the samples to reach the desired deposition temperature. It also involves injecting pulses of precursors and co-reactants into the reactor volume, while an inert gas often purges the reactor volume between these steps. Typically, continuous pumping of the reactor volume is necessary to maintain specific low pressure levels ranging from 0.1 to 10 Torr; however, pressures at mTorr levels and atmospheric pressure are also feasible. The design of the reactor is determined by the specified requirements. Many ALD reactor designs are based on CVD reactors. Unlike CVD, however, ALD is not a continuous process, so it's essential to efficiently fill and purge the reactor volume to achieve reasonable cycle times. Additionally, precise automation of precursor and co-reactant pulsing with accurate timing is necessary. It should be noted that growth occurs on all surfaces in the reactor exposed to both precursor and co-reactant. Figure 2.10 illustrates a summary of the reactor varieties that have been addressed [98].

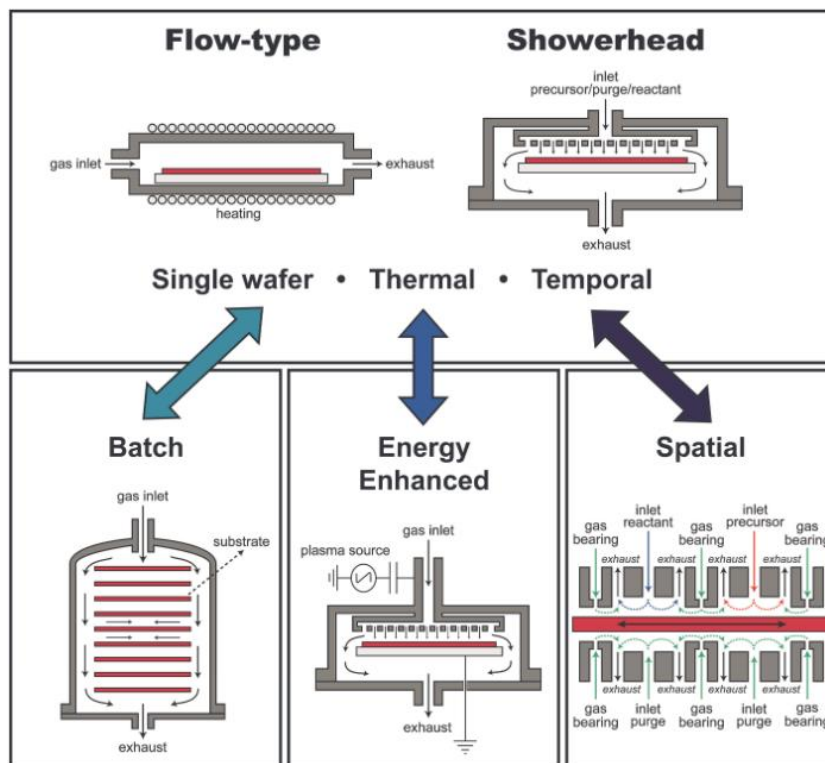


Figure 2.10. A diagram displaying the different types of ALD reactor systems. [98]

Flow-type ALD reactor

A flow-type reactor operates like a furnace with gases passing through (Figure 2.11). The substrate is positioned at the bottom of the reactor and heated by the elevated temperatures of the walls. An inert carrier gas is used to transport the precursor and co-reactant. Each precursor pulse is isolated from the next by adequate flow or inert gas, along with a sufficiently long purging time. By choosing an inlet gas flow and pumping speed, it's possible to achieve an optimal flow (e.g., laminar or streamline) and pressure, for example 1 Torr [98].

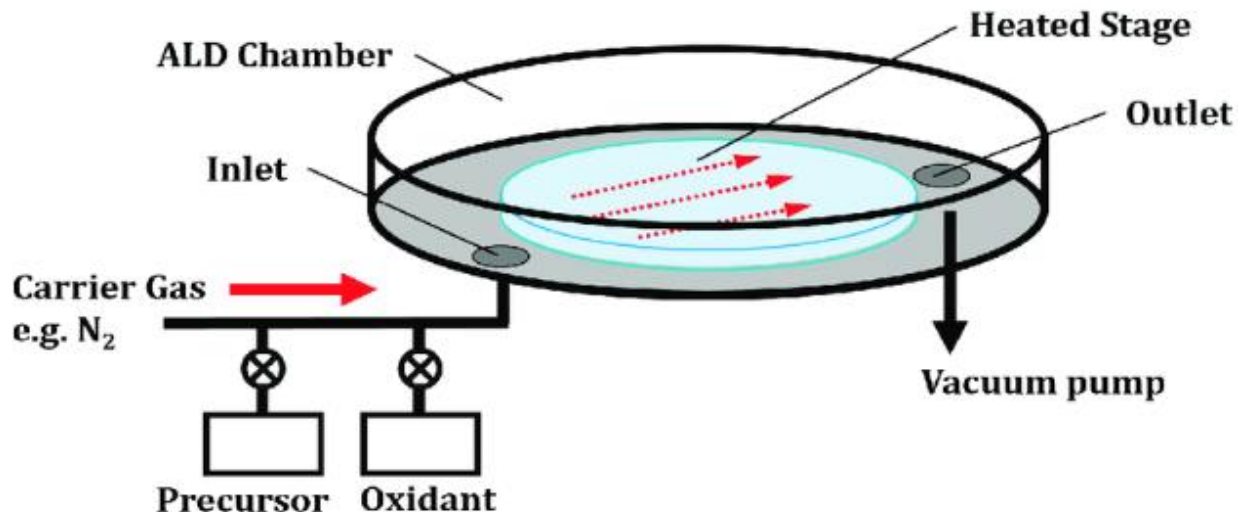


Figure 2.11. ALD flow type reactor [99].

For the deposition of the ZnO seed layers for the work in this thesis, a flow type reactor was used as shown in figure 2.11.

Showerhead ALD reactor

Upon entry into the reactor, a showerhead evenly disperses precursor and co-reactant flux for incoming gases. This design is advantageous for very large samples like industrial sized 300mm Si wafers and for processes that may have a limited CVD component or experience chemical side effects such as decomposition, etching, surface poisoning, and process interaction. When elevated substrate temperatures are required, a heated substrate platform can be utilized with the wall temperature adjusted lower for practical purposes (e.g., to avoid using costly high-temperature-resistant components). These types of reactors are referred to as "warm wall" or even "cold wall" reactors.

Batch ALD reactor

To enhance the efficiency of ALD reactors in industrial settings, batch reactors can be utilized. This type of reactor, illustrated in figure 2.10, typically consists of a furnace capable of accommodating multiple substrates (usually 50-500) for simultaneous coating. Due to the larger volume and slower gas diffusion within the reactor, extended exposure and purging times are necessary to maintain ALD behavior. However, the benefit of processing numerous wafers simultaneously generally outweighs the drawback of longer processing times. The extended cycle times may result in smaller CVD components or chemical side-effects having a more significant impact on uniformity compared to single-wafer tools.

Others

Some other types of ALD reactors include the plasma energy-enhanced ALD reactor, which is used for processes that require more than just thermal energy to obtain a high-quality film. There's also the spatial ALD reactor, where the exposure of the precursors occurs at different positions using various reaction zones separated by purging areas.

ALD methods can be carried out in reactors that operate under different pressure regimes, ranging from atmospheric to ultra-high vacuum. There are two main categories of reactors used for ALD: inert gas flow reactors and high- or ultra-high-vacuum reactors. Inert gas flow reactors operate under viscous or transition flow conditions at pressures above approximately 1 Torr. These reactors utilize an inert carrier gas, such as nitrogen or argon, to transport precursor gases to the substrate surface. The reactive gas is then introduced to the substrate surface, which reacts with the precursor gas to form a thin film. High- or ultra-high-vacuum reactors, on the other hand,

operate under molecular flow conditions. These reactors are characterized by extremely low pressures, typically in the range of 10^{-6} to 10^{-9} Torr. In these reactors, precursor and reactive gases are introduced to the substrate surface using a molecular beam [100].

2.1.6.1.2 ALD precursors

ALD methods heavily rely on precursors, whose characteristics such as reactivity, thermal stability, and volatility significantly impact the success of the ALD process. Ideally, these precursors should exhibit high reactivity, thermal stability, and volatility and surface saturating properties while maintaining a high level of purity to prevent contamination of the thin film. Moreover, they need to react on the surface at suitable temperatures without decomposing in order to avoid undesirable side products [101]. The most frequently utilized chemical precursors include metal halides, metal alkyls, metal alkoxides, metal alkylamides, metal nitrides, metallic B-diketonates, and metal cyclopentadienyls [102].

2.1.6.1.3 Advantages of ALD

ALD stands out in comparison to other thin film deposition techniques such as CVD and physical vapor deposition (PVD) due to the self-limiting chemisorption of precursors in each half-cycle. CVD and PVD are continuous methods that do not rely on stepwise growth, leading to variable growth rates determined by the rate and time of precursor exposure. Moreover, heterogenous nucleation, which often results in film discontinuities, is common with CVD and PVD [103, 104]. This sets ALD apart in its ability to control both sub-nanometer film thickness and conformality, with consistent growth-per-cycle values using the same precursors across

different equipment. ALD can produce high-quality films with excellent conformality at low temperatures. It is particularly adept at coating surfaces with ultra-high aspect ratios and creating multilayer films with high-quality interfaces [104].

ALD is different from other deposition techniques because it does not rely on a line-of-sight process, allowing it to uniformly coat surfaces with varying compositions, porosity, roughness, and high aspect ratios. The self-limiting nature of the half-reactions in ALD ensures precise control of film thickness by depositing the same number of atoms or molecules in each cycle. Through adjusting the number of precursor pulses, ultrathin films with thicknesses less than 10 nm can be created with Angstrom level precision.

One of the main advantages of ALD is its chemical selectivity. This is because adsorption to a surface is based on a chemical reaction at the surface. Depending on the location of reactive sites on the substrate surface, the technique can be area-selective, which means that it can deposit material only on specific areas of the surface.

Additionally, surface reactions in ALD can be carried out at very low temperatures which is beneficial for working with temperature-sensitive materials. Furthermore, ALD occurs through chemisorption, which means that the molecular self-assembly of layer formation reduces nucleation. As a result, the film has fewer discontinuities in the growth grain that would cause increased compressive stress in the final product [103].

2.1.6.1.4 Challenges in ALD

ALD is still a relatively small research and technology field. Currently, the challenges in depositing materials as thin films by ALD can be divided into different categories, such as:

- Some materials (like halides other than fluorides, borides, sulfates) have never been deposited using ALD.
- Certain materials (like electropositive metals, boron nitride) have been difficult to deposit.
- Improvement is needed in the ALD processes for many metals and nitrides, ternary compounds.
- Process development (fine-tuning) for specific applications is required.
- There is also a need to develop novel precursors and find suitable precursor combinations [105].

2.1.6.2 Hydrothermal synthesis

Nanorods are typically formed by controlling the growth of nuclei instead of their transverse expansion. Several techniques have been proposed for creating nanorods, such as thermal hydrolysis, hydrothermal synthesis, sol-gel method, vapor condensation, spray pyrolysis, pulse laser decomposition, laser ablation, thermal evaporation, and low energy beam deposition.

The hydrothermal technique has attracted significant interest due to its distinct benefits. It is a simple process that operates at low temperatures (60–100°C), yielding high quantities at minimal cost while producing well-defined structures and controllable processing, alongside excellent morphology [92].

Hydrothermal synthesis involves a solution-based reaction method that allows for the formation of nanomaterials. By employing either low-pressure or high-pressure conditions based on the vapor pressure of the primary composition in the reaction, one can control the morphology of the materials being prepared. A variety of nanomaterials have been effectively produced using

this technique. The hydrothermal synthesis method offers significant advantages over other methods. It can produce nanomaterials that are not stable at high temperatures and create nanomaterials with high vapor pressures while minimizing material loss. Furthermore, the composition of synthesized nanomaterials can be carefully controlled in hydrothermal synthesis through liquid phase or multiphase chemical reactions [106].

The detailed fabrication parameters for the hydrothermal synthesis of the ZnO nanorods in this research are as follows:

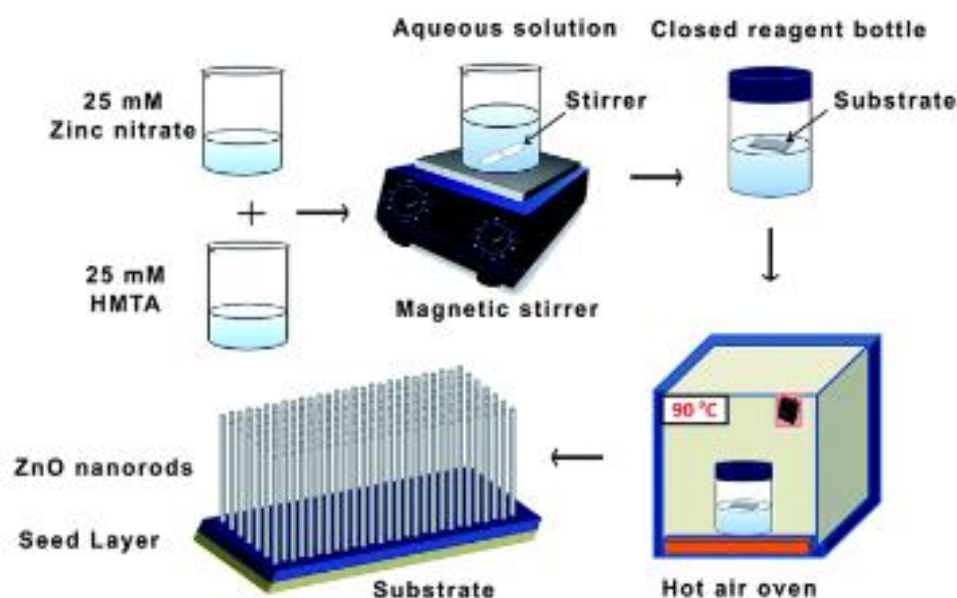


Figure 2.12 Schematic diagram of the process steps for the hydrothermal solution growth of ZnO nanorods [133].

Figure 2.12 illustrates the detailed process steps essential for synthesizing ZnO nanorods via hydrothermal growth. To initiate the synthesis:

1. Zinc nitrate hexahydrate and Hexamethylenetetramine (HMTA) serve as the precursor materials, meticulously dissolved in deionized (DI) water at an equimolar concentration of 25 mM.
2. Employing a magnetic stirrer, the solutes undergo complete dissolution within the solvent to ensure the preparation of a homogeneous reaction solution.
3. The substrate, Si coated with a finely grained polycrystalline ALD ZnO seed layer, is securely enclosed within an autoclave housing the prepared reaction solution.
4. Subsequently, the reaction autoclave undergoes heating up to 90°C within a laboratory oven for a duration of 16 hours. Throughout this incubation period, the nucleation of single crystal ZnO nanorods occurs atop the seed layer, constituting a crucial phase of the synthesis process.

2.2 Sensing Material: Metal Organic Frameworks (MOFs)

2.2.1 Introduction

Metal-organic frameworks (MOFs) are a relatively new class of porous solids which have garnered significant interest due to their distinct crystalline characteristics. MOFs are designed scaffold-like compounds that consist of metal ions connected by organic ligands, resulting in ordered high porosity structures that can accommodate up to 90% free volume and a substantial internal surface area exceeding 6,000 m²/g (Figure 2.13). The late 1990s marked the rapid growth of research on metal-organic frameworks, spearheaded by Omar Yaghi at UC Berkeley. With over 90,000 reported MOF structures and continuous expansion in number, their versatility and

potential applications continue to drive ongoing research and development. Their high porosity and internal surface area make them appealing for various clean energy applications including as storage media for gases like hydrogen and methane due to their ability to store significant amounts of gas. Additionally, they can function as high-capacity adsorbents for meeting diverse separation needs such as separating carbon dioxide from other gases in industrial processes. Furthermore, researchers have begun exploring the potential of MOFs as chemical sensors because of their unique structure's selective adsorption capabilities which make them useful for detecting specific chemicals.[107].

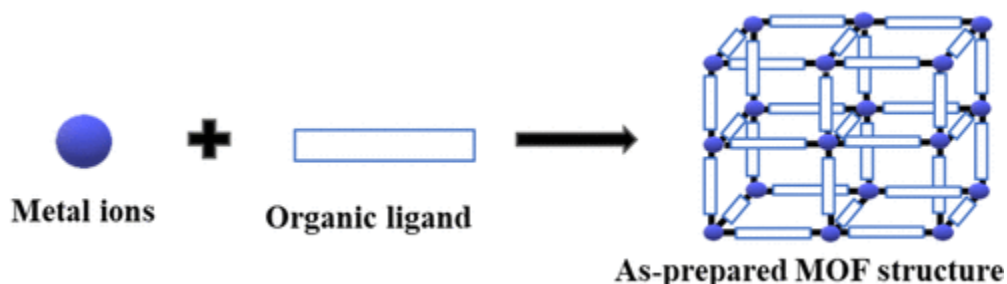


Figure 2.13. The MOF structure is formed through the creation of chemical bonds between metal ions as nodes and organic molecules as linkers [108].

The MOFs used in this research are called HKUST-1, derived from the abbreviation of Hong Kong University of Science and Technology-1, composed of Cu^{2+} dimers connected by benzenetricarboxylate (BTC) units represented by the chemical formula $[\text{Cu}_3(\text{BTC})_2(\text{H}_2\text{O})_3]_n$, possess open metal sites within their structure and exhibit a rigid porous open-framework. These open metal sites exhibit a strong affinity for coordination with polarizable molecules or guest molecules, including water and ethanol (Figure 2.14) [109].

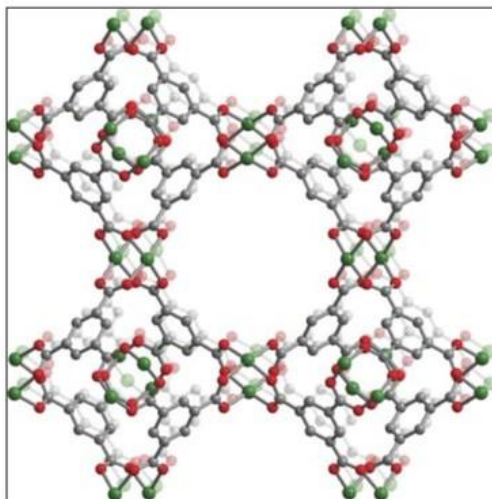


Figure 2.14. Model depicting a portion of the crystal structure of the Metal-Organic Framework MOF Film (HKUST-1) showing an open pore structure without any loading. Green, gray, and red spheres represent Cu, C, and O atoms, respectively; H atoms are omitted for clarity [109].

2.2.2 MOF Synthesis and Structures

2.2.2.1 Synthesis methods

MOFs consist of metal ions and organic ligands or bridging linkers. They are created by mixing these components to produce porous and crystalline materials. Various preparation methods have been developed over the past few decades, including conventional solvothermal methods, unconventional methods, and alternative methods.

2.2.2.1.1 Solvothermal synthesis

The solvothermal approach is commonly used to synthesize MOFs due to its simplicity, high crystallinity, and favorable yield. This method involves stirring metal salts and organic ligands in protic (such as methanol, ethanol, or mixed solvents) or aprotic (like acetonitrile and toluene)

organic solvents containing the formamide group. When water is used as a solvent in MOF synthesis, it's known as the hydrothermal method. The mixture is then placed into a closed vessel at elevated pressure and temperature for several hours or even a day. Glass vials are suitable for low temperatures while high-temperature reactions require Teflon-lined stainless-steel autoclaves. One crucial parameter of this reaction mixture is the temperature - determining whether it's classified as either a solvothermal or non-solvothermal reaction. High-pressure conditions help heat the solvent above its boiling point and melt the salt to facilitate the reaction process. Slow crystallization from a solution is essential for obtaining large crystals with high internal surface areas [108].

2.2.2.1.2 Microwave-assisted synthesis

Microwave-assisted approaches are widely used for rapid MOF synthesis under hydrothermal conditions, resulting in the production of small metal and oxide particles. This method efficiently heats the solution through electromagnetic waves interacting with solvent charges, leading to rapid crystallization and formation of nanoscale products. The process involves placing a substrate mixture in a Teflon vessel and subjecting it to microwave radiation for an appropriate duration to elevate the temperature. By choosing the right frequency, this approach enables uniform size nanocrystals to be produced due to direct interaction between radiation and reactants. Frequencies between 300 and 300 000 MHz are typically utilized for this purpose [110].

2.2.2.1.3 Electrochemical synthesis

The electrochemical method is used for the rational construction of a vast number of MOFs. HKUST-1 was first synthesized in 2005 through the electrochemical method, aiming to isolate anions like chloride, perchlorate or nitrate throughout the synthesis procedure and avoiding corrosive anions (nitrate and chloride). This approach is considered green chemistry for MOFs preparation due to its avoidance of corrosive anions like nitrate and by-products while being environment friendly with metal ions added through an electrochemical procedure rather than metal salts or acid reactions. The electrode placed in a solution containing the primary building unit (PBU) and electrolyte allows controlled deposition near the surface using electrons as a source of metal ions passed through a reaction mixture containing organic linker molecules. This methodology ensures consistent higher solid content compared to ordinary batch reaction processes [110].

2.2.2.1.4 Mechanochemical synthesis

Mechanochemistry focuses on solid reactions initiated using mechanical energy. A metal salt and an organic ligand are ground in a ball mill or with a mortar and pestle without solvent, followed by mild heating to remove volatile compounds and H₂O formed during the reaction. This approach simplifies the preparation of MOFs compared to other methods since it involves chemical transformation through mechanical breaking of intramolecular bonds at room temperature without the use of organic solvents. The first MOF synthesis through this method was reported in 2006, and it is now widely used for preparing various types of MOFs [108].

2.2.2.1.5 Sonochemical synthesis

The sonochemical method is used for rapid synthesis of MOFs as it decreases the time for crystallization through ultra radiation. A cyclic mechanical vibration (from 20 kHz to 10 MHz) is applied in a horn-shaped Pyrex reactor with a sonicator bar and variable power output, where a mixture of the metal salt and organic linker is added without external cooling. The main factor impacting liquid cavitation during sonication is ultrasonic waves, which lead to the development and collapse of bubbles in the solution. This process produces very fine crystallites at high temperatures around 4000 K and pressures up to 1000 bar. Sonication was first used for MOF synthesis in 2008 [108].

2.2.2.1.6 Layer-by-Layer Synthesis

Traditional hydro/solvothermal synthesis poses challenges in controlling film thickness and formation, as well as high costs from reactant consumption and waste production. The LBL deposition strategy provides precise control over film thickness and roughness by keeping metal and organic precursors separate. This concept is rooted in surface chemistry and is closely connected to the solid-phase creation of complex (bio-)organic polymers, such as peptides, DNA, etc., using a suitably functionalized organic surface as a starting point for nucleation. This method involves depositing alternating layers of oppositely charged precursor species to produce well-defined MOF thin films, particularly for surface-mounted metal-organic frameworks (SURMOFs) [110, 111].

2.2.3 Classes of MOF films

MOF films can be classified into two categories: polycrystalline powder films and highly oriented Surface-anchored Metal-Organic Frameworks (SURMOFs).

2.2.3.1 SURMOFs

MOF's can be affixed to a surface leading to a desired orientation known as SURMOFs (figure 2.15). Initially, the process involves anchoring the MOF onto the glass substrate by first functionalizing the gold covered substrate surface with MHDA (16-mercaptohexadecanoic acid) a self-assembled monolayer SAM to achieve highly oriented SURMOF films. Subsequently, the framework's cage structure is constructed atop the initially anchored MOF in a layer-by-layer spray process. Following this, the MOF is loaded, after which it becomes viable for use as a sensor [112]. SURMOF films are composed of extremely thin layers of MOF in the nanometer scale. They offer advantages such as precise control over film thickness, crystallographic orientations, low processing temperatures, compatibility with automatic deposition instrumentation, and the ability to fabricate a wide variety of structures on different substrates. Often, they are grown quasi-epitaxially on the substrate, allowing for precise control over film thickness and crystallite domain size interdependency. The optimal SURMOF would also possess sizable single-crystal domains within its plane [113].

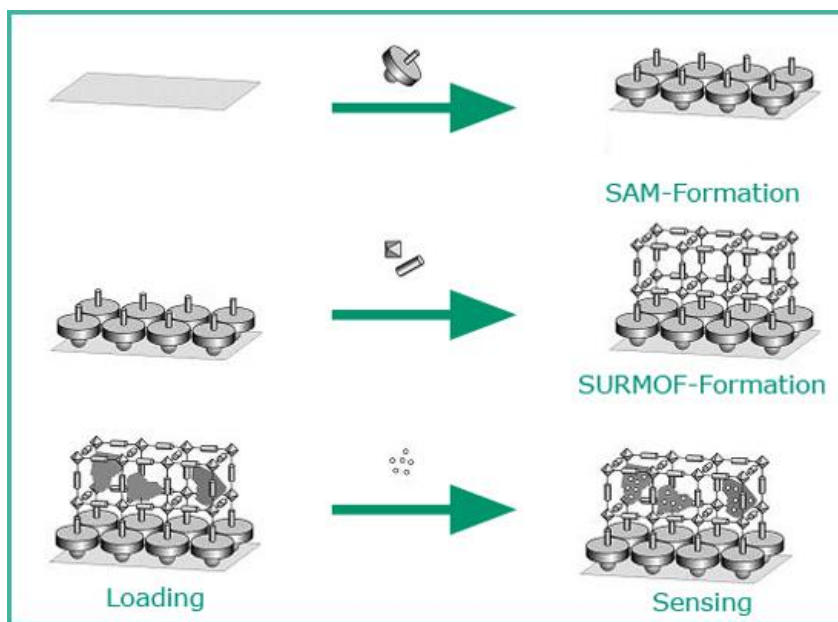


Figure 2.15. Illustration of the SURMOF assembly process via Layer-by-Layer spray deposition where the substrate was pre-treated with MHDA (16-mercaptohexadecanoic acid) a Self-Assembled Monolayer (SAM) for surface functionalization [112].

2.2.3.2 Polycrystalline

Polycrystalline films or powders are composed of MOF crystals or particles that are arranged on a surface. These crystals can be oriented randomly and form a disordered structure, or they can be well-integrated and cover the surface completely, or they can be scattered with holes and gaps. The attachment of crystals in one direction can occur due to the interaction with the surface, which leads to preferential orientation. This preferential orientation can be useful in creating functional films with specific properties. The thickness of these films is determined by the size of the MOF particles or crystallites and is usually in the micrometer range. The properties of these films are expected to be like those of the bulk powder material, which means that their performance can be evaluated and modeled based on the properties of the bulk material [113].

2.2.3.3 Applications of MOFs

MOF films possess numerous advantageous characteristics, including high porosity and a substantial specific surface area. Consequently, they have found diverse applications in various chemical fields like gas sensing, gas storage and separation, catalysis, and drug delivery.

2.2.3.3.1 Gas Storage and Separation

MOFs have been identified as potential adsorbents for gas storage since their permanent porosities were first discovered. In contrast to traditional porous materials like activated carbons and zeolites, MOFs possess advantageous structural characteristics including high porosity, large surface area, adjustable pore size and shape, and modifiable pore surfaces. Therefore, the development of MOFs holds significant promise for the storage of important gases such as hydrogen (H_2), methane, and acetylene (C_2H_2). Hydrogen storage plays a vital role in the application of hydrogen energy. It relies primarily on weak van der Waals forces. Thus, pure MOF configurations may not offer sufficient effectiveness for achieving targeted limits of hydrogen storage. This issue can be addressed by introducing active metal sites or incorporating benzene rings into the MOF structure. By employing these derivatives of MOFs, one can attain the desired storage capacities at low temperatures. [114].

MOFs can serve not only for the storage of pure gases but also for the selective separation of gases within a mixture. Gas separation processes are crucial for manufacturing fuels, polymers, and plastics. Membrane separations dominate the gas separation market due to their cost-effectiveness and easy large-scale production. MOFs have emerged as ideal adsorbents for gas separation because of their high surface area, porosity, modularity, and thermal stability. MOF

membranes for gas separation can be categorized into pure MOF membranes and mixed matrix membranes [115].

2.2.3.3.2 Catalysis

As industries continue to evolve and grow, there is a constant demand for finding ways to make procedures more cost-effective and efficient. This pursuit of more economical and streamlined processes has become a driving force in diverse sectors such as manufacturing, energy production, and chemical engineering. One area that has received significant attention in this quest for improved efficiency is the exploration of catalysts. Catalysts are substances that facilitate chemical reactions by lowering the activation energy required for the reaction to occur. They are used in various industrial processes to increase the rate of reaction, reduce energy consumption, and enhance product yield. MOFs can function as catalysts in chemical reactions, offering high substrate selectivity and ease of separation from reaction media for reuse. In the literature, researchers have reported the catalysis of diverse chemical reactions at both small and large scales using MOFs, including conventional catalysis, biocatalysis, and electrocatalysis. The development and application of these materials on an industrial scale are highly valuable due to their exceptional catalytic properties. Nonetheless, addressing the stability of MOFs under different reaction conditions such as pH levels, temperature variations, and organic solvents remains a significant challenge for researchers [116].

2.2.3.3.3 Drug Delivery

The limitations of traditional orally administered drugs in providing controlled release of medication have sparked significant interest and research into new approaches for drug delivery. Innovative delivery systems that have been developed include those based on polymers, liposomes, microporous zeolites, mesoporous silicon, and other mesoporous materials. These diverse delivery methods can be broadly categorized as organic or inorganic systems. Organic systems offer a wide range of biocompatibility and the ability to accommodate various drugs but lack a mechanism for controlled release. In contrast, inorganic delivery materials are capable of delivering adsorbed drugs at a controlled rate due to their ordered porous structure; however, they have reduced loading capacity compared to organic systems. As hybrid compounds combining organic and inorganic elements, MOFs offer potential as effective drug-delivery materials due to the ability to customize the functional groups of the framework and adjust pore sizes. The use of MOFs allows for leveraging the advantages of both organic materials (biocompatibility and high drug absorption capacity) and inorganic materials (controlled release). Nevertheless, a notable disadvantage is that their small pore size, typically falling within the microporous range, restricts the amount of drugs that can be absorbed or stored within the framework. Addressing this issue requires synthesizing MOFs with pores in the mesoporous range [117].

2.2.3.3.4 Sensing

Detection of substances in the gaseous state poses significant challenges across various fields, including environmental monitoring, security, public health, food safety, and industrial processes. The use of MOFs can be expanded to include detecting small molecules, solvents, and explosives. MOFs are characterized by their extensive surface areas and functional groups that create strong interactions with guest molecules. These interactions can alter the properties of MOFs

through changes in optical, electrical, and mechanical signals. Main approaches for gas sensing include optical methods (e.g., vapochromism, luminescence, and interferometry), mechanical techniques (such as quartz crystal microbalance, surface acoustic wave devices, microcantilevers), magnetism-based sensing, and electrical methods (including impedance measurements and chemiresistive techniques) [118]. The effectiveness of MOF-based detection heavily relies on the method used for signal transduction. Incorporating an analyte effectively into the sensing material helps achieve lower detection limits.[119].

2.2.3.4 Challenges and Limitations

Despite the advancements in numerous MOF-related research fields, several challenges persist:

- Firstly, the precise mechanism of MOF growth remains unclear and understanding the self-assembly process is limited, making it difficult to control target structures for pristine MOFs. A deeper comprehension of this mechanism is essential for designing suitable MOFs with specific pore structures, composition adjustability, and high surface area.
- Secondly, the exact process of MOF growth is not fully understood, and there are limited insights into the self-assembly process. This hinders our ability to effectively control the formation of desired structures in pristine MOFs. A more thorough understanding of this mechanism is crucial for creating tailored MOFs with precise pore structures, adjustable composition, and high surface area.

- Thirdly Controlling the production of various materials derived from MOFs is difficult because it's challenging to precisely shape and size the pores, despite their high surface area and porosity.
- Lastly, Finally, concerns surrounding expenses, durability, electrical conductance, and other factors need to be resolved in order to make practical advancements on an industrial level. There is still work to be done in developing cost-effective methods for producing MOFs on a large scale [120].

2.3 Characterization Techniques

To perform the characterization of the ZnO nanorod sensing material, several techniques were employed. Scanning Electron Microscope (SEM) was used to analyze the morphology of the material, Energy Dispersive X-ray Spectroscopy (EDS) was used for the elemental analysis or chemical characterization, and Raman spectroscopy is used to provide finger-print spectra.

2.3.1 Scanning Electron Microscope (SEM)

The scanning electron microscope (SEM) is a powerful and versatile tool for optical characterization of nanostructured materials. Since its inception in 1965, it has significantly contributed to the advancement of nanotechnology and has found applications in medical, forensic, life sciences, biology, and other disciplines. The SEM generates images through the interaction between the specimen's surface and a high-energy electron beam. This interaction can induce elastic or inelastic scattering leading to various types of emitted electrons collected by detectors attached to the SEM. Despite its usefulness and diverse applications, the SEM is expensive and

sensitive with associated disadvantages. Overcoming these challenges has led to several developments in the instrument over time [121].

2.3.1.1 Resolution

The limit of resolution defines the minimum distance for two structures to be distinguished as separate objects, which is dependent on the wavelength of the illumination source. This can result in blurry magnified images when the resolution exceeds the limit due to diffraction and interference, creating an Airy disk where the image appears larger than the source. As shown in figure 2.16, two wavefront peaks can only be distinguished when separated by a distance equivalent to the radius of an Airy disk [122].

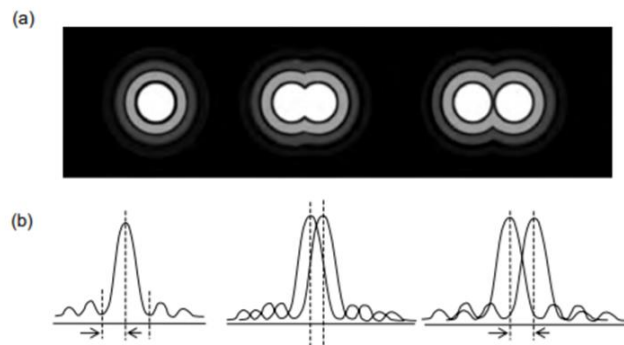


Figure 2.16. Depiction of resolution through (a) Airy disk patterns and (b) wavefront peaks [123].

In a perfect optical system, resolution is mathematically described by Abbe's equation:

$$d = 0.612 \lambda / n \sin \alpha \quad (4)$$

where d is the distance of resolution, λ denotes the wavelength of the imaging radiation, n is the medium refractive index between the light source and the lens, α is the half-angle aperture of the light source. The term in the denominator of equation 4 ($n\sin\alpha$) is referred to as the numerical aperture (NA) [124].

De Broglie combined quantum theory with some principles of classical physics and proposed his equation:

$$\lambda = h/mv \quad (5)$$

where λ is the wavelength of the electrons, h is Planck's constant, m is mass of the particle, and v is the velocity of the electron. Therefore, if electron beams were to be used as a source, rather than light, which has a longer wavelength, the following equation can be used to calculate the wavelength of the electron beam:

$$\lambda = \frac{1.22 \times 10^{-9}}{\sqrt{v}} \quad (6)$$

Equations 5 and 6 demonstrate the importance that electron beams hold as a source of illumination for high resolution in electron microscopy [125].

2.3.1.2 Fundamental Principles

The SEM forms images by scanning a high-energy electron beam across the specimen. The interaction of the beam with the sample surface produces different types of information for SEM detectors to interpret, classified into elastic and inelastic interactions. The elastic interaction results from the deflection of the incident electron beam by the electric field of the atom on the sample

surface, leading to a new trajectory with minimal energy loss. The probability of elastic scattering is described mathematically as follows:

$$Q = 1.62 \times 10^{-20} \left(\frac{Z^2}{E^2} \right) \cot^2 (\phi_0/2) \quad (7)$$

where Q represents the elastic scattering cross-section, Z stands for the atomic number, E denotes the energy of the electron (in keV), and ϕ_0 is referred to as the threshold elastic scattering angle. This electron scattering cross-section Q also allows us to estimate the mean free path of an electron, which is essentially the average distance that an electron beam needs to travel for an elastic scattering event to occur. When primary electrons undergo elastic scattering with an angle greater than 90° , they are termed as backscattered electrons.

Inelastic scattering involves the incident primary electron losing energy to the atom it encounters at the sample surface [123]. The amount of energy lost is related to properties such as binding energy, which can result in secondary electrons, characteristic X-rays, continuum X-rays due to deceleration of the electron beam by the electric field of the atom, heating of specimen, and permeation of conducting metallic solids [122].

Secondary Electrons

Secondary electrons are produced when the specimen atoms receive enough kinetic energy from the inelastic scattering of the electron beam (Figure 2.17). The generated secondary electrons can propagate inside the solid, but only a small amount is able to breach the surface energy barrier and escape through the surface due to their low energy levels. More than 90% of them are emitted

with energies lower than 10 eV, allowing them to only escape from a distance of a few nanometers from the material's surface.

There are two types of secondary electrons: SE1 and SE2. SE1 electrons, formed closer to the surface due to beam-atom interaction, provide high-resolution signals for topographic contrast in SEM. On the other hand, SE2 electrons result from interactions between backscattered electrons and specimen electrons, possessing higher kinetic energy that allows them to escape from greater depths in the sample. While they offer lower image resolution than SE1, they provide different lateral and depth characteristics. An increase in SE2 results in better image contrast, making the observed region appear brighter. Additional types of secondary electrons (SE3 and SE4) generated from BSE interaction with SEM chamber walls contribute only noise to images [123, 126].

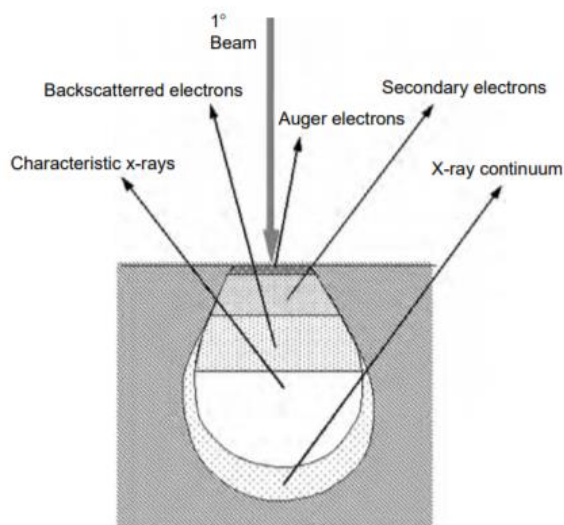


Figure 2.17. Illustration of the various kinds of signals generated upon impact of the primary beam with the surface specimen [123].

The collector of SE in SEMs is the Everhart–Thornley detector. It determines the strength of the signal based on the number of collected SEs, resulting in better contrast for surface features

oriented towards it. Low-energy SEs are attracted to the ET detector under positive bias (200-300 V). The electrons pass through a Faraday cage and make contact with the scintillator surface coated with thin metal, generating light upon impact that is converted into an electrical signal for image formation displayed on a monitor [122, 123].

The total secondary electron coefficient (δ) is given by the following expression:

$$\delta = \frac{N_{SE}}{N_B} = \frac{i_{SE}}{i_B} \quad (8)$$

where N_{SE} is the number of secondary electrons emitted from the sample, N_B is the number of incident primary electrons, and i denotes their corresponding currents. When the beam energy is lowered, δ rises consequentially [122].

The secondary electron coefficient is greatly affected by the tilt angle θ of the specimen with respect to the electron beam, as given by the following equation:

$$\delta(\theta) = \delta_0 \sec\theta \quad (9)$$

where δ_0 represents the SE coefficient when the e-beam is perpendicular to the surface of the specimen (zero tilt). As the tilt angle increases, δ also increases due to a longer primary electron path [122]. In contrast to BSE, SE emission is typically not significantly affected by the atomic number of the specimen elements [126].

Backscattered Electrons

Backscattered electrons are created by elastically scattered beam electrons with deflection angles greater than 90° , escaping the material's surface. They offer a spatial resolution of around

50-100 nm for beams at 10-20 eV, but their resolution is significantly worse than secondary electron images due to a larger volume of beam energies within the sample. However, BSE images are valuable in distinguishing between different chemical phases and can reveal subsurface defects as well as details about catalysts, multiphase materials, and contaminants. Notably, they are useful for observing biological specimens despite their low yield from these samples; heavy elements such as gold or lead attached to molecular groups make them appear brighter in BSE images [122, 126].

The total backscattering electron coefficient (η) is given by the following expression:

$$\eta = \frac{N_{BSE}}{N_B} = \frac{i_{BSE}}{i_B} \quad (10)$$

where, N_{BSE} is the number of backscattered electrons emitted from the sample, N_B is the number of incident primary electrons, and i is their corresponding currents [122, 126].

The backscattering electron coefficient is greatly affected by the tilt angle θ of the specimen with respect to the electron beam. As the angle increases, a larger amount of BSE can escape from the surface, leading to an increased BSE signal when the incident beam angle is small. The stable increase in η with θ is given by the following equation:

$$\eta(\theta)(1 + \cos\theta)^{-\frac{9}{\sqrt{2}}} \quad (11)$$

The direction of the emitted BSE influences the η value, as they follow the direction with which they escaped the surface. Therefore, η will have its largest value along that direction [126].

X-rays

The interaction of the electron beam with the specimen produces various signals such as SEs, BSEs, and characteristic X-rays. When inner-shell electrons are ejected from their orbit, they leave behind a vacancy in the orbital which leads to ionization and excited state. This is then followed by energy release when an outer shell electron moves to fill the vacancy. The excess energy can be released through Auger electron emission or emitted as characteristic x-rays. Atoms with larger sizes and more electrons result in a larger number of x-ray photons, leading to the production of an x-ray spectrum. The x-ray photon energy is given by the following equation:

$$E_{X-ray} = h\nu = E_K - E_L \quad (12)$$

where h is Planck's constant, ν is the frequency, E_K is the K shell binding energy, and E_L is the L shell binding energy. $E_K - E_L$ is the difference in the binding energies of the two shells.

Every shell around an atom holds a specific amount of energy, known as the atomic energy level. This characteristic energy release occurs when x-ray photons are emitted, representing a specific element, and creating characteristic X-ray lines used to detect and quantify elements present in the interaction. Additionally, deceleration and kinetic energy loss due to repulsion from atomic electrons result in the generation of continuous spectrum X-rays known as the X-ray continuum or Bremsstrahlung with energies ranging from zero up to that supplied by the beam electron. These continuum X-rays do not have a relationship with a unique element and appear as background noise in the X-ray spectrum, affecting measurements of characteristic X-rays [126].

In addition to the primary electron beam, other signal types are generated by the interaction with the specimen. These include auger electron emission, cathodoluminescence, and transmitted

electrons. These signals provide chemical information and can be used for imaging at high resolution. Specimen current is also a significant factor in surface analysis [122, 123, 126].

Instrumentation

The SEM consists of the electron column, specimen chamber, and a computer system for control. These components, along with various types of detectors, are crucial for microscopy and microchemical analysis. The electron column contains several devices such as the electron gun, electron lenses, scan coils, condenser, and objective aperture. To prevent scattering by air, electrons within the column must travel in a high-vacuum environment at all times [123].

Applications of SEM

SEM results are useful in various scientific disciplines like biology, forensic science, life science, gemology, and medical science. Using different detectors, a variety of information can be extracted from the specimen under observation. Some applications of the instrument include looking at film thicknesses and coatings, observing particle dispersion and shape in composites, detecting surface contaminants, analyzing microstructures, and identifying crystal structures [125, 127].

Advantages and Disadvantages

Using an SEM instrument has several benefits such as the ability to study large surface areas, high resolution and depth of field, convenient sample orientation change, and simple sample

preparation. However, SEMs are expensive and require a lot of space due to their size. Operating in a vacuum presents challenge when working with liquids. Special training is necessary for operation and sample preparation under observation. There are also safety risks associated with radiation exposure from electron scattering beneath the sample surface [127].

2.3.2 Energy Dispersive X-ray Spectroscopy (EDS)

Elemental analysis using EDS microanalysis involves the generation of characteristic X-rays in atoms of the specimen by incident beam electrons. After interacting with the atoms, two primary physical phenomena take place: elastic scattering and inelastic scattering. Upon ionization, the atoms emit characteristic X-rays as they return to their ground state. The energy of the emitted X-ray photon is a result of the potential energy difference between the two orbitals involved in this transition, which is unique to each element [128].

Characteristic X-rays serve as the analytical signals utilized in electron microscopy to conduct chemical analysis. The X-ray spectrum emitted by the specimen offers both qualitative and quantitative data, enabling the determination of which elements are present in the sample and their respective quantities. Aside from the emitted X-rays, a small amount of secondary X-rays may also be generated during the passage of primary X-rays through the specimen, interacting with its atoms [129].

2.3.3 Raman spectroscopy

When electromagnetic waves (e.g., with light) interacts with matter, the incident radiation is scattered. In elastic scattering, there is no change in photon frequency, wavelength, or energy.

In contrast, inelastic scattering involves a shift in photon frequency due to excitation or deactivation of molecular vibrations which can result in either gaining or losing energy. Three types of phenomena can occur:

- 1 When light strikes a molecule, it may interact with the molecule without any net exchange of energy ($E = E_0$), resulting in scattered light with the same frequency as the incident light. This phenomenon is referred to as Rayleigh scattering.
- 2 Alternatively, if the interaction results in an exchange of energy equal to one molecular vibration, the scattered light's frequency will be higher than that of the incident light ($E = E_0 + E_v$). This type of interaction is known as anti-Stokes Raman scattering.
- 3 On the other hand, if the molecule gains energy from the photon during this interaction, then the frequency of the scattered light will be lower than that of the incident light ($E = E_0 - E_v$). This process is termed Stokes Raman scattering.

In Raman spectroscopy, the shift in wavelength of scattered radiation by molecules to frequencies different from those of the incident beam and is to study molecular vibrations and gather information about molecule structure, symmetry, electronic environment, and bonding. It allows for both quantitative and qualitative analysis of individual compounds.

In its essence, Raman spectroscopy measures the frequency shift of inelastically scattered light from a sample, producing Stokes Raman scattering with lower frequency photons or anti-Stokes Raman scattering with higher frequency photons. The shift in wavelength depends on the chemical composition, structure, chemical environment, of the analyte species responsible for scattering and can be used as a fingerprint tool for different compounds, allowing qualitative analysis for unknown samples or mixtures [130, 131].

A Raman spectrometer consists of a light source, monochromator, sample holder and detector. Factors affecting the analysis include high signal-to-noise ratio, instrument stability and sufficient resolution. Several types of lasers are available for use as the excitation source, such as argon ion (488.0 and 514.5 nm), krypton ion (530.9 and 647.1 nm), He:Ne (632.8 nm), Nd:YAG (1064 nm and 532 nm) and diode laser (630 and 780 nm).

Raman spectroscopy has been employed coupled with various analytical techniques such as high-performance liquid chromatography, micro chromatography, scanning tunneling microscopy, and atomic force microscopy. This allows for useful analysis at trace level studies. Revolutionary developments in Raman instrumentation now make it possible to acquire spectra more quickly on more affordable and user-friendly equipment compared to the past [132]. This technique has been used in real-time monitoring systems to detect illegal drugs, toxic materials, and chemical and biological warfare agents [130].

The detailed characterization data are listed in chapter 5.

References

- [1] D. W. Rodwihok Chatchai, Yen Linh Thi Ngo, Mahima Khandelwal, Seung Hyun Hur, and Jin Suk Chung, "Effect of GO Additive in ZnO/rGO Nanocomposites with Enhanced Photosensitivity and Photocatalytic Activity," *Nanomaterials*, vol. 9, no. 10, p. 1441, 2019, doi: 10.3390/nano9101441.
- [2] V. K. Quanchang Li, Yan Li, Haitao Zhang, Tobin J. Marks, and Robert P. H. Chang, "Fabrication of ZnO Nanorods and Nanotubes in Aqueous Solutions," *Chemistry of Materials*, vol. 17, 5, pp. 1001-1006, 2005 doi: 10.1021/cm048144q.
- [3] P. P. C. Mariane A. Franco, Rafaela S. Andre, Daniel S. Correa, "A review on chemiresistive ZnO gas sensors," *Sensors and Actuators Reports*, vol. 4, p. 100100, 2022, doi: 10.1016/j.snr.2022.100100.
- [4] S. S. Dharendra Kumar Sharma, Kapil Kumar Sharma, Vipin Kumar, "A review on ZnO: Fundamental properties and applications," *Materials Today: Proceedings*, vol. 49, no. 8, pp. 3028-3035, 2022, doi: 10.1016/j.matpr.2020.10.238.
- [5] M. A. Borysiewicz, "ZnO as a Functional Material, a Review," *Crystals*, vol. 9, no. 10, p. 505, 2019, doi: 10.3390/cryst9100505.

- [6] C. Klingshirn, "ZnO: Material, Physics and Applications," *ChemPhysChem*, vol. 8, no. 6, pp. 782 – 803, 2007, doi: 10.1002/cphc.200700002.
- [7] Y. I. A. Ü. Özgür, C. Liu, A. Teke, M. A. Reshchikov, S. Doğan, V. Avrutin, S.-J. Cho, H. Morkoç, "A comprehensive review of ZnO materials and devices," *J. Appl. Phys*, vol. 98, p. 041301 2005, doi: 10.1063/1.1992666.
- [8] N. A. S. Kausar Harun, Bahri Deghfel, Muhamad Kamil Yaakob, Ahmad Azmin Mohamad, "DFT + U calculations for electronic, structural, and optical properties of ZnO wurtzite structure: A review," *Results in Physics*, vol. 16, p. 102829, 2020, doi: 10.1016/j.rinp.2019.102829.
- [9] D. H. L. Yoo Dong Jun, Yong Kang, Chan Gi Lee, and Gyung Min Kang, "Optical Properties of Nano-Structured ZnO: Sn Powders Prepared in a Micro Drop Fluidized Reactor," *Journal of Chemical Engineering of Japan*, vol. 50, no. 1, pp. 21-25, 2017.
- [10] K. A. Paul Erhart, and Andreas Klein, "First-principles study of intrinsic point defects in ZnO: Role of band structure, volume relaxation, and finite-size effects," *PHYSICAL REVIEW B*, vol. 73, p. 205203, 2006, doi: 10.1103/PhysRevB.73.205203.
- [11] Y.-N. X. a. W. Y. Ching, "Electronic, optical, and structural properties of some wurtzite crystals," *PHYSICAL REVIEW B*, vol. 48, no. 7, 1993.
- [12] "Fundamentals of Semiconductor physics." http://www.optique-ingenieur.org/en/courses/OPI_ang_M05_C02/co/Contenu.html (accessed 02/20/2024).
- [13] a. S. B. Ben G Streetman, *Solid State Electronic Devices*. Pearson/Prentice Hall, 2006.
- [14] A. M. Arshid M. Ali, Amir Shafeeq, Hafiz M. A. Asghar, Syed N. Hussain, Hamid Satta, "Doped metal oxide (ZnO) and photocatalysis," *Journal of Pakistan Institute of Chemical Engineers*, vol. 40, no. 1, pp. 11-19, 2012.
- [15] Y. L. Zhong Ouyang, Yunpeng Chen, Zheng Zhang, Zicong Jiang, Jiaxin Hu & Yuanyuan Lin "Preparation and Specific Capacitance Properties of Sulfur, Nitrogen Co-Doped Graphene Quantum Dots," *Nano Express*, 2019.
- [16] "Semiconductors and Doping." <https://openstax.org/books/university-physics-volume-3/pages/9-6-semiconductors-and-doping> (accessed).
- [17] I. M.-R. r. Aracely Hernandez-Ramirez, "Photocatalytic Semiconductors: Synthesis, Characterization, and Environmental Applications," doi: 10.1007/978-3-319-10999-2.
- [18] A. N. A. M. Menon, "Band gap engineering via doping: A predictive approach " vol. 117, no. 12, 2015, doi: 10.1063/1.4916252.
- [19] A. M. S. A. S. NIE, "Semiconductor Nanocrystals: Structure, Properties, and Band Gap Engineering," *ACCOUNTS OF CHEMICAL RESEARCH*, vol. 43, no. 2, pp. 190-200, 2010.
- [20] C. F. T. Chen, and S. C. Edman Tsang, "Interstitial and substitutional light elements in transition metals for heterogeneous catalysis," *Chem Science*, vol. 12, no. 2, pp. 517–532, 2021, doi: 10.1039/d0sc06496c.
- [21] "Effects of dopants and hydrogen on the electrical conductivity of ZnO."
- [22] "Doped ZnO 1D Nanostructures: Synthesis, Properties, and Photodetector Application ".
- [23] "Comparative first principles study of ZnO doped with group III elements."
- [24] "ZnO as a Functional Material, a Review."
- [25] "Conversion of n-type to p-type conductivity in ZnO by incorporation of Ag and Ag-Li," vol. 33, 2022.
- [26] J.-W. K. Yong-Seok Choi, Dae-Kue Hwang, and Seong-Ju Park, "Recent Advances in ZnO-Based Light-Emitting Diodes," *IEEE TRANSACTIONS ON ELECTRON DEVICES*, vol. 57, no. 1, 2010.
- [27] Y. W. H. D.P. Norton, M.P. Ivill, K. Ip, S.J. Pearton, M.F. Chisholm, T. Steiner, "ZnO: growth, doping & processing," *Materials Today*, vol. 7, no. 6, pp. 34-40, 2004.

- [28] Y. Y. M. M. A.-J. S.-H. Wei, "Doping of ZnO by group-IB elements " vol. 89, no. 18, 2006, doi: 10.1063/1.2378404.
- [29] "Doping Asymmetry Problem in ZnO: Current Status and Outlook."
- [30] "Origin of p-type doping difficulty in ZnO: The impurity perspective."
- [31] H. H. Zhizhen Ye, Li Jiang, "Co-doping: an effective strategy for achieving stable p-type ZnO thin films," *Nano Energy*, vol. 52, 2018.
- [32] X. Z.-Y. Li Bing-Sheng, Ma Jian-Gang, Liu Yi-Chun, "The p-type ZnO thin films obtained by a reversed substitution doping method of thermal oxidation of Zn₃N₂ precursors," *Chinese Physics B*, 2017.
- [33] J. L. S.H. Wei, and Y. Yan, "Design of Shallow p-Type Dopants in ZnO," 2008.
- [34] F. U. Hamelmann, "Thin film zinc oxide deposited by CVD and PVD," *Journal of Physics: Conference Series*, vol. 764, p. 012001, 2016 doi: 10.1088/1742-6596/764/1/012001.
- [35] S. N. P. H.S. Tangade, S.S. Shirguppikar, "Synthesis and characterization of ZnO thin films deposited by chemical route," *Materials Today: Proceedings*, vol. 33, no. 8, pp. 5147-5149, 2020, doi: 10.1016/j.matpr.2020.02.861.
- [36] K. E. a. A. Bikowski, "Intrinsic and extrinsic doping of ZnO and ZnO alloys," *Journal of Physics D: Applied Physics*, vol. 49, 2016, doi: 10.1088/0022-3727/49/41/413002.
- [37] "Advances in Doped ZnO Nanostructures for Gas Sensor," doi: 10.1002/tcr.2020000.
- [38] "Optical Band Gap Tuning, DFT Understandings, and Photocatalysis Performance of ZnO Nanoparticle-Doped Fe Compounds," *Materials (Basel)*, vol. 16, no. 7, p. 2676, 2023, doi: 10.3390/ma16072676.
- [39] "Defects induced luminescence and tuning of bandgap energy narrowing in ZnO nanoparticles doped with Li ions," *Journal of Applied Physics*, vol. 116, no. 8, p. 083510 2014, doi: 10.1063/1.4894153.
- [40] "Tuning the Optical Properties of ZnO by Co and Gd Doping for Water Pollutant Elimination," *Water*, vol. 15, no. 8, p. 1470, 2023, doi: 10.3390/w15081470.
- [41] "Effect of tin on bandgap narrowing and optical properties of ZnO–Zn₂SnO₄ electrospun nanofibre composite," *Journal of Taibah University for Science*, vol. 14, no. 1, pp. 1251-1261, 2020, doi: 10.1080/16583655.2020.1816369.
- [42] "Carrier Concentration Dependence of Band Gap Shift in n-Type ZnO: Al Films," *Journal of Applied Physics*, vol. 101, no. 8, 2007, doi: 10.1063/1.2721374.
- [43] "Lecture 11: Degenerate and Non-Degenerate Semiconductors."
<https://gyansanchay.csjmu.ac.in/wp-content/uploads/2021/11/303-L11.pdf> (accessed).
- [44] J. L. F. D. S. Aron Walsh, and Su-Huai Wei, "Origins of band-gap renormalization in degenerately doped semiconductors," *Phys. Rev. B*, vol. 78, no. 7, p. 075211, 2008, doi: 10.1103/PhysRevB.78.075211.
- [45] "Tuning of the band gap and dielectric loss factor by Mn doping of Zn_{1-x}Mn_xO nanoparticles," *Scientific Reports* 2023.
- [46] A. P. Vipul Shukla, "Effect of doping concentration on optical and electrical properties of intrinsic n-type ZnO (i-ZnO) and (Cu, Na and K) doped p-type ZnO thin films grown by chemical bath deposition method," *Nanosystems Physics Chemistry Mathematics*, vol. 11, no. 4, pp. 391-400, 2020, doi: 10.17586/2220-8054-2020-11-4-391-400.
- [47] A. A. L. Fanni, M. Morales-Masis, M. Ledinský, S. Escrig, A. Vetushkaet al., "Direct imaging of dopant distribution in polycrystalline zno films," *ACS Applied Materials & Interfaces*, vol. 9, no. 8, pp. 7241-7248, 2017, doi: 10.1021/acsami.6b14350.
- [48] "Property database for single-element doping in zno obtained by automated first-principles calculations," *Scientific Reports*, vol. 7, no. 1, 2017, doi: 10.1038/srep40907.

- [49] "Carrier concentration dependent optical and electrical properties of ga doped zno hexagonal nanocrystals," *Physical Chemistry Chemical Physics*, vol. 17, no. 24, pp. 16067-16079, 2015, doi: 10.1039/c4cp05480f.
- [50] "Efficient up-conversion zno co-doped (er, yb) nanopowders synthesized via the sol-gel process for photovoltaic applications," *Materials*, vol. 15, no. 21, p. 7828, 2022, doi: 10.3390/ma15217828.
- [51] "Highly conductive epitaxial zno layers deposited by atomic layer deposition," *Thin Solid Films*, vol. 562, pp. 485-489, 2014, doi: 10.1016/j.tsf.2014.04.047.
- [52] "Effect of indium doping on low-voltage zno nanocrystal field-effect transistors with ion-gel gate dielectric," *Japanese Journal of Applied Physics*, vol. 53, no. 7, p. 071101, 2014, doi: 10.7567/jjap.53.071101.
- [53] "Transition between grain boundary and intragrain scattering transport mechanisms in boron-doped zinc oxide thin films," *Applied Physics Letters*, vol. 90, no. 14, 2007, doi: 10.1063/1.2719158.
- [54] "Tunable n-type conductivity and transport properties of ga-doped zno nanowire arrays," *Advanced Materials*, vol. 20, no. 1, pp. 168-173, 2008, doi: doi.org/10.1002/adma.200701377.
- [55] "Lutetium-doped zno to improve photovoltaic performance: a first-principles study," *ACS Applied Electronic Materials*, vol. 4, no. 12, pp. 6253-6260, doi: 10.1021/acsaelm.2c01365.
- [56] "Enhanced visible light photocatalytic activity of zno nanowires doped with mn²⁺ and co²⁺ ions," *Nanomaterials*, vol. 7, no. 1, p. 20, 2017, doi: 10.3390/nano7010020.
- [57] "Doped plasmonic zinc oxide nanoparticles with near-infrared absorption for antitumor activity," *Acs Applied Nano Materials*, vol. 4, no. 9, pp. 9779-9789, 2021, doi: 10.1021/acsanm.1c02197.
- [58] "Improved Charge Transfer Contribution by Cosputtering Ag and ZnO," 2020, doi: 10.3390/nano10081455.
- [59] "Supramolecular cocrystals built through redox-triggered ion intercalation in π -conjugated polymers," *Communications Materials*, vol. 2, no. 1, 2021.
- [60] S. S. Dharendra Kumar Sharma, Kapil Kumar Sharma, Vipin Kumar, "A review on ZnO: Fundamental properties and applications," *Materials Today: Proceedings*, vol. 49, no. 8, pp. 3028-3035, doi: 10.1016/j.matpr.2020.10.238.
- [61] M. T. Frank Lee, Roque Sanchez Salas, Roque Sanchez Salas, Aline Amorim Graf, Izabela Jurewicz, Alan B. Dalton, "Localised strain and doping of 2D materials," *Nanoscale*, vol. 15, pp. 7227-7248, 2023, doi: 10.1039/D2NR07252A.
- [62] K. R. Philip J. Hasnip, Matt I. J. Probert, Jonathan R. Yates, Stewart J. Clark and Chris J. Pickard, "Density functional theory in the solid state," *Philosophical Transactions A*, vol. 372, no. 2011, 2014, doi: 10.1098/rsta.2013.0270.
- [63] M. X. Zhaoyang Li, Xinli Li, Jiwen Li, Nannan Wang, Shengkang Zhang,, "First principle study of electronic structure and optical properties of Mo doped ZnO with different concentrations," *Optik*, vol. 228, p. 166136, 2021, doi: 10.1016/j.ijleo.2020.166136.
- [64] K. S. Harun, Nor Azmira ; Deghfel, Bahri ; Yaakob, Muhamad Kamil ; Mohamad, Ahmad Azmin, "DFT + U calculations for electronic, structural, and optical properties of ZnO wurtzite structure: A review," *Results in Physics*, vol. 16, 2020, doi: 10.1016/j.rinp.2019.102829.
- [65] J. R. S. William F. Polik, "WebMO: Web-based computational chemistry calculations in education and research," *WIREs Computational Molecular Science*, vol. 12, no. 1, 2021, doi: 10.1002/wcms.1554.
- [66] H. Jappor, "Which is best software for Density Functional theory calculation?," ed, 2019.

- [67] Z. F. Suqin Xue, Shuili Zhang, Xiaoyang Wang, Tingting Shao, "Electronic and Magnetic Properties of Ni-Doped Zinc-Blende ZnO: A First-Principles Study," *Nanomaterials*, vol. 8, no. 5, 2018, doi: 10.3390/nano8050281b.
- [68] M. G. E. G. K. K. G. Ł. M. I. Ł. T. K. B. S. W. S. Gierałtowska, "Zinc oxide for electronic, photovoltaic and optoelectronic applications " *Low Temp. Phys*, vol. 37, pp. 235–240, 2011, doi: 10.1063/1.3570930.
- [69] C. CHEN. "LEDs." <https://sites.tufts.edu/eeseniordesignhandbook/2015/leds-technology/> (accessed).
- [70] A. Myllynen, "Laterally doped III-V diodes for large-area optoelectronics," Materials Science and Engineering, Aalto University School of Chemical Technology, 2018.
- [71] S. L. C. a. Z. X. J.C. Fan, "ZnO-Based Light-Emitting Diodes," *ptoelectronics - Advanced Materials and Devices. InTech*, 2013, doi: 10.5772/51181.
- [72] B. A. H. A. Kishwar Mohammed Wasman, "Review of Optoelectronic Properties of ZnO Photodetector," *Journal of Physical Chemistry and Functional Materials*, vol. 5, no. 1, pp. 9-21, 2022, doi: 10.54565/jphcfum.1026868.
- [73] M. S. Kewei Liu, and Masakazu Aono, "ZnO-Based Ultraviolet Photodetectors," *Sensors* vol. 10, no. 9, pp. 8604-8634, 2010, doi: 10.3390/s100908604.
- [74] M. S. Liu Kewei, and Masakazu Aono, "ZnO-Based Ultraviolet Photodetectors," *Sensors*, vol. 10, no. 9, pp. 8604-8634, 2010, doi: 10.3390/s100908604.
- [75] L. Z. Zhaoyao Zhan, Yongzheng Pan, Gengzhi Suna and Lin Lia, "Self-powered, visible-light photodetector based on thermally reduced graphene oxide–ZnO (rGO–ZnO) hybrid nanostructure," *J. Mater. Chem.*, vol. 22, no. 6, pp. 2589-2595, 2012, doi: 10.1039/c1jm13920g.
- [76] Y. J. Yefeng Yang†, Haiping He†, Qingling Wang†, Yao Tu†, Huanming Lu‡, and Zhizhen Ye†*, "Dopant-Induced Shape Evolution of Colloidal Nanocrystals: The Case of Zinc Oxide," *Journal of the American Chemical Society*, vol. 132, no. 38, pp. 13381-13394, 2010, doi: 10.1021/ja103956p.
- [77] S.-J. C. Cheng-Liang Hsu, "Doped zno 1d nanostructures: synthesis, properties, and photodetector application," *Small*, vol. 10, no. 22, pp. 4562-4585, 2014, doi: 10.1002/smll.201401580.
- [78] C.-L. H. a. S.-J. Chang, "Doped ZnO 1D Nanostructures: Synthesis, Properties, and Photodetector Application," *small*, vol. 10, no. 22, pp. 4562–4585, 2014, doi: 10.1002/smll.201401580.
- [79] N. S. a. A. V. Emeline, "Semiconductor Photocatalysis — Past, Present, and Future Outlook," *The Journal of Physical Chemistry Letters*, vol. 3, no. 5, pp. 673–677, 2012, doi: 10.1021/jz300071j.
- [80] X. Y. a. D. Wang, "Photocatalysis: From Fundamental Principles to Materials and Applications," *ACS Applied Energy Materials*, vol. 1, no. 12, pp. 6657-6693, 2018 doi: 10.1021/acsaem.8b01345.
- [81] W. X. Zhang F, Liu H, Liu C, Wan Y, Long Y, Cai Z, "Recent Advances and Applications of Semiconductor Photocatalytic Technology," *Applied Sciences*, vol. 9, no. 12, p. 2489, 2019, doi: 10.3390/app9122489.
- [82] C. W. L. Kian Mun Lee, Koh Sing Ngai, Joon Ching Juan, "Recent developments of zinc oxide based photocatalyst in water treatment technology: A review," *Water Research*, vol. 88, pp. 428-448, 2016,, doi: 10.1016/j.watres.2015.09.045.
- [83] Y.-J. T. Lung-Chuan Chen, Yu-Sheng Wang, Ruei-Sian Kan, Chao-Ming Huang, "Characterization and photoreactivity of N-, S-, and C-doped ZnO under UV and visible light illumination," *Journal of Photochemistry and Photobiology A: Chemistry*, vol. 199, no. 2-3, pp. 170-178, 2008, doi: 10.1016/j.jphotochem.2008.05.022.

- [84] A. M. Vijaya Kumari, Jitender Jindal, Suprabha Yadav & Naveen Kumar, "S-, N- and C-doped ZnO as semiconductor photocatalysts: A review," *Frontiers of Materials Science*, vol. 13, no. 1, pp. 1–22, 2019, doi: 10.1007/s11706-019-0453-4.
- [85] C. S. D. Qifeng Zhang, Xiaoyuan Zhou, and Guozhong Cao, "ZnO Nanostructures for Dye-Sensitized Solar Cells," *Adv. Mater.*, vol. 21, pp. 4087–4108, 2009, doi: 10.1002/adma.200803827.
- [86] A. F. M. a. V. Lugh, "Frontiers of photovoltaic technology: A review," *2015 International Conference on Clean Electrical Power (ICCEP)*, pp. 115-121, 2015, doi: 10.1109/ICCEP.2015.7177610.
- [87] R. L. Z. H. K. P. M. J. L. MacManus-Driscoll, "Research Update: Doping ZnO and TiO₂ for solar cells" *APL Materials* 1, vol. 060701 2013, doi: 10.1063/1.4833475.
- [88] R. Vittal, "Zinc oxide based dye-sensitized solar cells: A review," *Renewable & Sustainable Energy Reviews*, vol. 70, no. C, pp. 920-935, 2017, doi: 10.1016/j.rser.2016.11.273.
- [89] E. G. Juan A. Anta, and Ramón Tena-Zaera, "ZnO-Based Dye-Sensitized Solar Cells," *The Journal of Physical Chemistry C*, vol. 116 no. 21, pp. 11413-11425, 2012 doi: 10.1021/jp3010025.
- [90] P. L. Papa K Amoah, Helmut Baumgart, Rhonda R Franklin, Yaw S Obeng, "Broadband dielectric spectroscopic detection of volatile organic compounds with ZnO nanorod gas sensors," *Journal of physics D: Applied physics*, vol. 54, no. 13, p. 135104, 2021, doi: 10.1088/1361-6463/abd3ce.
- [91] A.-D. O. Kumar R, Kumar G, Umar A, "Zinc Oxide Nanostructures for NO₂ Gas-Sensor Applications: A Review," *Nanomicro Lett*, vol. 7, no. 2, pp. 97-120, 2015, doi: 10.1007/s40820-014-0023-3.
- [92] N.-A. M. a. Y. H. T.-Y. Alsultan Abdulkareem Ghassan, "Nanomaterials: An Overview of Nanorods Synthesis and Optimization," *Nanorods and Nanocomposites*, 2020, doi: 10.5772/intechopen.84550.
- [93] C. Y. Mo G, Yin J, Gao P, "Influence of ZnO Film Deposition Parameters on Piezoelectric Properties and Film-to-Substrate Adhesion on a GH4169 Superalloy Steel Substrate," *Micromachines (Basel)*, vol. 13, no. 4, p. 639, 2022, doi: 10.3390/mi13040639.
- [94] M. G. E Guziewicz, L Wachnicki, T A Krajewski, G Luka, S Gieraltowska, R Jakiela, A Stonert, W Lisowski, M Krawczyk, J W Sobczak and A Jablonski, "ALD grown zinc oxide with controllable electrical properties," *Semicond. Sci. Technol*, vol. 27, p. 074011, 2012, doi: 10.1088/0268-1242/27/7/074011.
- [95] R. L. P. Véronique Cremers, Jolien Dendooven "Conformality in atomic layer deposition: Current status overview of analysis and modelling featured," *Appl. Phys. Rev*, vol. 6, no. 2, p. 021302, 2019, doi: 10.1063/1.5060967.
- [96] Z. M. Jiyu Cai, Uche Wejinya, Min Zou, Yuzi Liu, Hua Zhou, and Xiangbo Meng, "A Revisit to Atomic Layer Deposition of Zinc Oxide Using Diethylzinc and Water as Precursors," *Journal of Materials Science*, vol. 54, no. 7, pp. 5236–5248, 2019, doi: 10.1007/s10853-018-03260-3.
- [97] N. V. Nguyen Tai, Jérôme Guillot, Jérôme Bour, Noureddine Adjeroud, Yves Fleming, Mael Guennou et al., "Elucidating the growth mechanism of ZnO films by atomic layer deposition with oxygen gas via isotopic tracking[†]," *J. Mater. Chem. C*, vol. 9, no. 12, pp. 4307-4315, 2021, doi: 10.1039/D0TC05439A.
- [98] S. E. P. H.C.M. Knoops, A.A. Bol, and W.M.M. Kessels, "Atomic Layer Deposition," *Handbook of Crystal Growth*, vol. 3, pp. 1101-1134, 2015, doi: 10.1016/B978-0-444-63304-0.00027-5.
- [99] R. K. Tzia Ming Onn, Paolo Fornasiero, Kevin Huang, Kevin Huang and R. J. Gorte, "Atomic Layer Deposition on Porous Materials: Problems with Conventional Approaches to Catalyst and Fuel

- Cell Electrode Preparation," *Inorganics*, vol. 6, no. 1, p. 34, 2018, doi: 10.3390/inorganics6010034.
- [100] S. M. George, "Atomic Layer Deposition: An Overview," *Chemical Reviews*, vol. 110, pp. 111-131, 2010, doi: 10.1021/cr900056b.
- [101] L. K. T. Thokozani Justin Kunene, Kingsley Ukoba, Tien-Chien Jen, "Review of atomic layer deposition process, application and modeling tools," *Materials Today: Proceedings*, vol. 62, 1, pp. S95-S109, 2022, doi: 10.1016/j.matpr.2022.02.094.
- [102] K. N. Tapily, "Synthesis of ALD zinc oxide and thin film materials optimization for UV photodetector applications," DOCTOR OF PHILOSOPHY, Electrical & Computer Engineering, Old Dominion University, 2011.
- [103] N. R. Altvater, "The Design and F The Design and Fabrication of an A abrication of an Atomic La omic Layer Deposition er Deposition Reactor for Coating Powders ", The University of Maine, 2017.
- [104] R. A. Peter Ozaveshe Oviroh, Dongqing Pan, Dongqing Pan, Tien-Chien Jen, "New development of atomic layer deposition: processes, methods and applications," *Sci Technol Adv Mater*, vol. 20, no. 1, pp. 465-496, 2019, doi: 10.1080/14686996.2019.1599694.
- [105] D. M. K. Dr. Nicola Pinna, *Atomic Layer Deposition of Nanostructured Materials*. John Wiley & Sons, 2011.
- [106] A. H. J. Yong X. Gan, Zhen Yu, Xi Chen, Mingheng L, "Hydrothermal Synthesis of Nanomaterials," *Journal of Nanomaterials*, vol. 2020, 2020, doi: 10.1155/2020/8917013.
- [107] J. R. L. Hong-Cai Zhou, and Omar M. Yaghi, "Introduction to Metal–Organic Frameworks," *Chemical Reviews*, vol. 112, no. 2, pp. 673-674, 2012, doi: 10.1021/cr300014x.
- [108] N. I. M. Vadia Foziya Yusuf, and Suresh Kumar Kailasa, "Review on Metal–Organic Framework Classification, Synthetic Approaches, and Influencing Factors: Applications in Energy, Drug Delivery, and Wastewater Treatment," *ACS Omega*, vol. 7, no. 49, pp. 44507-44531, 2022, doi: 10.1021/acsomega.2c05310.
- [109] D. L. R. Kenji Sumida, Jarad A. Mason, Thomas M. McDonald, Eric D. Bloch, Zoey R. Herm, Tae-Hyun Bae, and Jeffrey R. Long, "Carbon Dioxide Capture in Metal–Organic Frameworks," *Chemical Reviews* vol. 112 no. 2, pp. 724-781, 2012, doi: 10.1021/cr2003272.
- [110] a. C.-H. C. Yujing Zhang, "Metal–Organic Framework Thin Films: Fabrication, Modification, and Patterning," *Processes*, vol. 8, no. 3, p. 377, 2020, doi: 10.3390/pr8030377.
- [111] O. Shekhah, "Layer-by-Layer Method for the Synthesis and Growth of Surface Mounted Metal–Organic Frameworks (SURMOFs)," *Materials (Basel)*, vol. 3, no. 2, pp. 1302–1315, 2010, doi: 10.3390/ma3021302.
- [112] P. D. C. Wöll. "Anchoring of metal-organic frameworks, MOFs, to surfaces." <https://www.ifg.kit.edu/english/2872.php> (accessed 3/21/2024).
- [113] A. B. a. R. A. Fischer, "Metal–Organic Framework Thin Films: From Fundamentals to Applications.," *Chemical Reviews*, vol. 112, no. 2, pp. 1055-1083, 2012, doi: 10.1021/cr200167v.
- [114] L. L. Hao Li, Rui-Biao Lin, Wei Zhou, Zhangjing Zhang, Shengchang Xiang, and and B. Chen, "Porous metal-organic frameworks for gas storage and separation: Status and challenges," *EnergyChem*, vol. 1, no. 1, p. 100006, 2019, doi: 10.1016/j.enchem.2019.100006.
- [115] Y. S. Wenkui Chai, Jiahe Wang, Geling Zhang, "Applications of Metal–Organic Framework Materials," *Journal of Physics: Conference Series*, vol. 2194, p. 012014, 2022, doi: 10.1088/1742-6596/2194/1/012014.
- [116] J. Y. N. H. A. Allison R. M. Silva, José E. S. Souza, José G. Lima Neto, Paulo G. de Sousa Júnior, Maria V. P. Rocha, and José C. S. dos Santos, "The Chemistry and Applications of Metal–Organic

- Frameworks (MOFs) as Industrial Enzyme Immobilization Systems," *Molecules*, vol. 27, no. 14, p. 4529, 2022, doi: 10.3390/molecules27144529.
- [117] D. J. T. Ryan J. Kuppler, Qian-Rong Fang, Jian-Rong Li, Trevor A. Makal, Mark D. Young, Daqiang Yuan, Dan Zhao, Wenjuan Zhuang, Hong-Cai Zhou, "Potential applications of metal-organic frameworks," *Coordination Chemistry Reviews*, vol. 253, no. 23–24, pp. 3042–3066, 2009, doi: 10.1016/j.ccr.2009.05.019.
- [118] S.-N. Z. Hai-Yang Li, Shuang-Quan Zang and Jing Li, "Functional metal–organic frameworks as effective sensors of gases and volatile compounds," *Chem. Soc. Rev.*, vol. 49, pp. 6364–6401, 2020, doi: 10.1039/c9cs00778d.
- [119] A. D. Pawan Kumar, Ki-Hyun Kim, "Metal organic frameworks for sensing applications," *TrAC Trends in Analytical Chemistry*, vol. 73, pp. 39–53, 2015, doi: 10.1016/j.trac.2015.04.009.
- [120] J. Y. R. S. Long Jiao, William Scott Skinner, Zhiyong U. Wang, Hai-Long Jiang, "Metal–organic frameworks: Structures and functional applications," *Materials Today*, vol. 27, pp. 43–68, 2019, doi: 10.1016/j.mattod.2018.10.038.
- [121] a. Z. L. Zhou Weili, *Scanning Microscopy for Nanotechnology: Techniques and Applications*. Springer, 2007.
- [122] D. E. N. Joseph I. Goldstein , Patrick Echlin , David C. Joy , Charles E. Lyman , Eric Lifshin , Linda Sawyer , Joseph R. Michael, *Scanning Electron Microscopy and X-Ray Microanalysis*. Springer US, 2003.
- [123] Z. L. W. Weilie Zhou, *Scanning Microscopy for Nanotechnology: Techniques and Applications*. Springer, 2007.
- [124] "Limits to Resolution in the Transmission Electron Microscope." The University of Oklahoma. www.ou.edu/research/electron/bmz5364/resolutn.html (accessed 02/26/2024).
- [125] S. A. K. Kalsoom Akhtar, Sher Bahadar Khan & Abdullah M. Asiri *Scanning Electron Microscopy: Principle and Applications in Nanomaterials Characterization* (Handbook of Materials Characterization). Springer, 2018, pp. 113–145.
- [126] A. Ul-Hamid, *A Beginners' Guide to Scanning Electron Microscopy*. Springer, 2018.
- [127] O. P. Choudhary, and Priyanka Ka, "Scanning Electron Microscope: Advantages and Disadvantages in Imaging Components," *International Journal of Current Microbiology and Applied Sciences*, vol. 6, no. 5, pp. 1877–1882, 2017, doi: 10.20546/ijcmas.2017.605.207.
- [128] B. S. Scimeca M, Lamsira HK, Bonfiglio R, Bonanno E, "Energy Dispersive X-ray (EDX) microanalysis: A powerful tool in biomedical research and diagnosis," *Eur J Histochem*, vol. 62, no. 1, p. 2841, 2018, doi: 10.4081/ejh.2018.2841.
- [129] G. C. Ana Violeta Girão, Marta C. Ferro, "Application of Scanning Electron Microscopy-Energy Dispersive X-ray Spectroscopy (SEM-EDS)," *Comprehensive Analytical Chemistry*, vol. 75, pp. 153–168, 2017, doi: 10.1016/bs.coac.2016.10.002.
- [130] S. G. Paul Rostron, Dina Gaber, "Raman Spectroscopy, Review," *International Journal of Engineering and Technical Research (IJETR)*, vol. 6, no. 1, pp. 2454–4698, 2016.
- [131] N. Z. Mingjin Wang, Defeng Zhao, Jing Shang, and Tong Zhu, "Using Micro-Raman Spectroscopy to Investigate Chemical Composition, Mixing States, and Heterogeneous Reactions of Individual Atmospheric Particles," *Environmental Science & Technology*, vol. 55, no. 15, pp. 10243–10254, 2021, doi: 10.1021/acs.est.1c01242.
- [132] Y. K. A. Ruchita S. Das, "Raman spectroscopy: Recent advancements, techniques and applications," *Vibrational Spectroscopy*, vol. 57, no. 2, pp. 163–176, 2011, doi: 10.1016/j.vibspec.2011.08.003.
- [133] Lin, Pengtao. "Enhanced Sensing Performance of Novel Nanostructured ZnO Gas Sensors in Ethanol Vapor Concentration Detection Applications" (2019). Doctor of Philosophy (PhD),

Dissertation, Electrical/Computer Engineering, Old Dominion University, DOI: 10.25777/j9r7-vs61

CHAPTER 3

BROADBAND DIELECTRIC SPECTROSCOPY (BDS)

The electromagnetic spectrum encompasses a wide range of frequencies, from 0 to 10^{23} Hz, featuring diverse phenomena such as direct current (DC), radio waves, microwaves, terahertz radiation, infrared light, visible light, ultraviolet radiation, X-rays, and gamma rays. Materials exhibit unique behaviors across this spectrum, influencing their sensing capabilities. Understanding the interplay of electromagnetic waves with materials involves exploring amplitude, frequency, wavelength, and energy [1]. This chapter delves into the theory of electromagnetic radiation, scattering parameters, dielectric theory, dielectric properties, and microwave spectroscopy.

3.1 Electromagnetic Theory

3.1.1 Basic Concepts

The electromagnetic spectrum's behavior is determined by the interaction of waves with materials, resulting in varied transmission, reflection, and absorption characteristics. Metals, for example, transmit low radio frequencies while reflecting and absorbing visible light and X-rays. In contrast, glass acts as an insulator against low radio frequencies, prioritizing the transmission of visible light and X-rays. Electromagnetic properties are interconnected through time, power,

and wavelength considerations, where an oscillating field at a specific frequency corresponds to a specific wavelength and energy level [1].

3.1.2 Amplitude and Frequency

Amplitude, representing the wave's magnitude, is crucial, measured as the maximum amplitude multiplied by the sine of the associated angle. Frequency, expressed in Hertz, quantifies the number of complete waveforms occurring in one second. The speed of light (c) in a vacuum is related to frequency (f) and wavelength (λ) by equation 1.

$$c = f\lambda \quad (1)$$

highlighting the interdependence of these fundamental parameters.

3.1.3 Energy and Planck's Constant

Energy is determined by the interplay of frequency and Planck's constant (h). The relationship is expressed by equation 2:

$$E = h \times f \quad (2)$$

where E represents photon energy. Beyond 3 PHz (3×10^{15}) electromagnetic energy becomes ionizing radiation, capable of dislodging electrons from atoms. Below this threshold, non-ionizing radiation interacts with ions, inducing molecular rotation and elevating electrons to higher energy states.jjj

Figure 3.1 illustrates the electromagnetic spectrum, depicting associated frequencies and applications within the radio frequency and microwave frequency ranges [1].

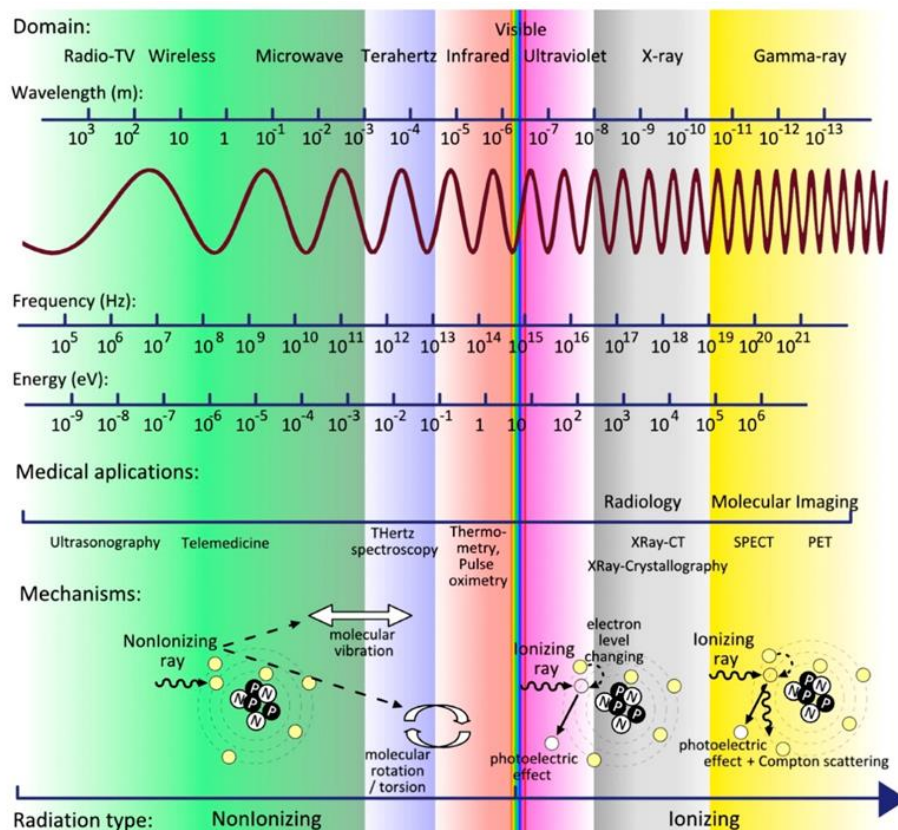


Figure 0.1. The electromagnetic spectrum featuring wavelength, frequency, and energy [2].

3.2 Electromagnetic Radiation

3.2.1 Electric and Magnetic Components

Electromagnetism comprises distinct electric and magnetic components, each exhibiting separate yet interconnected phenomena. Electric fields arise from charge magnitude, while the motion of charge generates magnetic fields.

3.2.2 EM Wave Propagation

Radiation involves the emission of energy in wave form and is linked to the presence of oscillating electrical and magnetic fields that mutually sustain and facilitate propagation. The movement of electrical currents generates electric (E) and magnetic (H) fields that oscillate perpendicularly to the direction of wave propagation (transverse) and at right angles to each other (orthogonal) (See figure 3.2). Electromagnetic radiation contributes to increased resistance in the transmission line, where energy is transformed into electromagnetic radiation rather than heat, as observed in ohmic resistance. Radiation from an AC source distributes energy in two distinct spatial regimes: near-field and far-field. The near field, also known as the reactive field and storage field, operates in close proximity to the source. In this zone, absorption of radiation may provide feedback, influencing the impedance of the sensor. This contrasts with far-field radiation, which does not offer feedback and affect the sensor's impedance. The measurement of near-field radiation proves inherently challenging, as any instrument introduced into the field interacts with the source, altering the resultant field. The near-field radius can be calculated using equation 3:

$$R = \frac{A}{2\lambda} \quad (3)$$

where R denotes the field's radius, and A represents the area of the antenna. This understanding of radiation characteristics and spatial regimes is pivotal for evaluating and optimizing sensor performance [1].

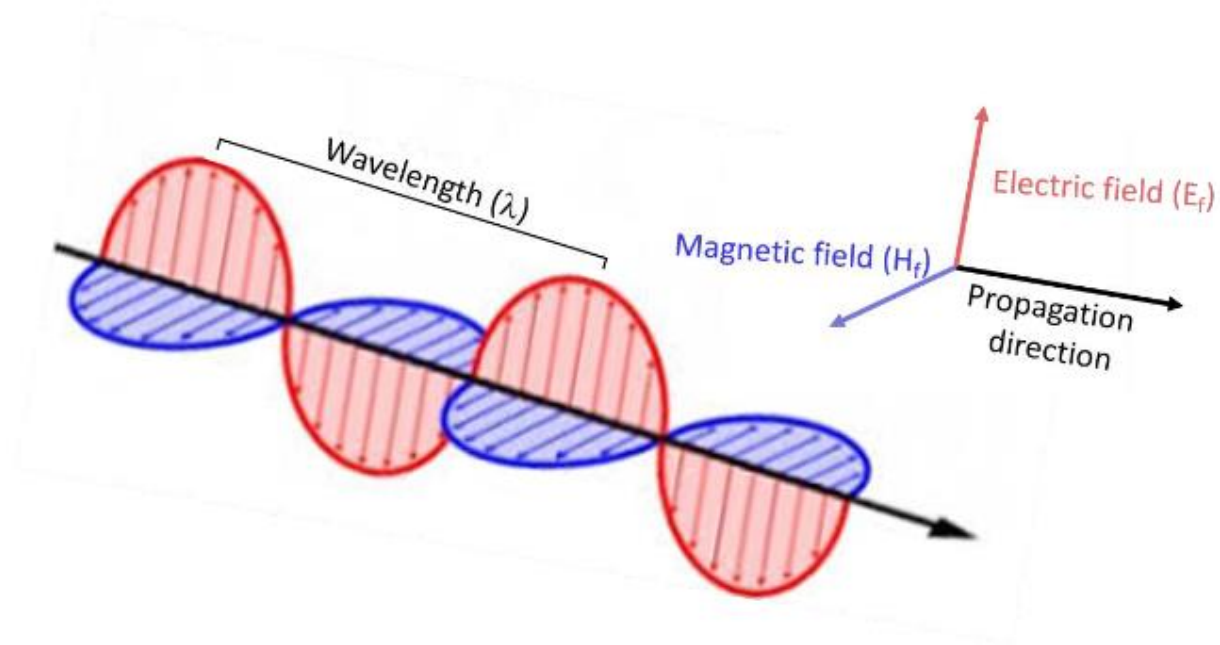


Figure 0.2. EM wave propagation showing electric (E) and magnetic field (B) [3].

3.3 Dielectric Theory

Dielectrics, materials with low electrical conductivity, support electrostatic fields. These substances exhibit polarization when subjected to an external electric field [4]. The introduction of an external electric field to a material prompts the storage of electrical energy through interactions with the material's molecular and structural properties. This electric field exerts a net force on charged particles, displacing them from their average random orientation. The removal of the external electric field allows these charged particles to revert to their initial random arrangement, leading to the release of a charge. The material's capacity to store energy in this manner is quantified by its permittivity (ϵ), typically expressed as a product of the permittivity of free space (ϵ_0) [1]. Dielectric materials are particularly valuable in capacitors, especially at radio frequencies and in the construction of radio-frequency transmission lines. Most dielectric materials

are solid, such as ceramics, mica, glass, plastics, and various metal oxides. Additionally, some liquids and gases can be good dielectrics; for instance, dry air functions as an excellent dielectric used in variable capacitors and specific types of transmission lines. Distilled water serves as a decent dielectric while vacuum stands out as an exceptionally efficient one. Furthermore, materials have specific electrical characteristics based on their dielectric properties, allowing for accurate measurements to aid in material integration and manufacturing quality control [4].

3.3.1 Dielectric Polarization

Dielectric materials, characterized by their nonmetallic nature, permanent or induced dipoles, negative temperature coefficient of resistance, absence of free charge, and high specific resistance, impose limitations on electron movement due to strong bonds with the parent molecule. These substances possess a substantial energy band gap exceeding 3 eV, preventing electron transition between the valence and conduction bands under normal thermal energy and voltage conditions. Dielectrics fall into two broad categories: active and passive. Active dielectrics actively accept electric charges in an electric field for energy storage applications, whereas passive dielectrics like rubber, mica, and glass function as insulators, hindering the flow of electricity.

Polarization is the rearrangement of charges within a dielectric material in response to an external electric field. This phenomenon occurs through two distinct mechanisms: stretching and rotation. In the presence of an external electric field, a neutral atom, consisting of a positively charged nucleus and a negatively charged electron cloud, experiences forces that align the positive part with the field direction and the negative part in the opposite direction. Equilibrium is reached when these forces balance out, resulting in no atom movement. Various mechanisms contribute to polarization generation, and most molecules exhibit polarization under a strong external electric

field. The categorization of polarization types is based on the mechanisms governing the process. Four well-known polarization mechanisms include ionic, orientation, atomic, and electronic polarization. Figure 3.3 illustrates the frequency-dependent variation of these polarization mechanisms.

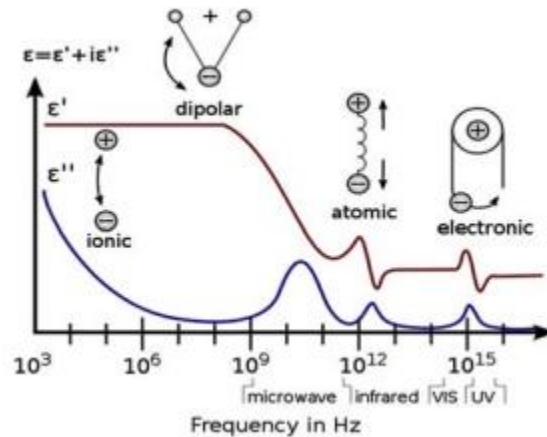


Figure 0.3. Polarization mechanisms versus frequency range [5].

Electronic or Atomic polarization

Electric and atomic polarization can take place in neutral atoms when an electric field causes displacement of the nucleus in relation to the surrounding electrons, as well as when neighboring positive and negative ions undergo stretching due to an applied electric field. These processes are particularly significant at microwave frequencies, with resonance occurring at a higher frequency [4]. At lower frequencies, there is a reconfiguration in the positioning of atomic nuclei within a molecule or lattice, which is known as atomic polarization. When subjected to an external electric field, dielectric materials cause all atoms in the material to produce a temporary dipole moment and assume an asymmetric shape. Atomic polarization, also referred to as vibrational polarization, is closely associated with electronic polarization. Due to its greater mass

involvement, atomic polarization shows lower resonant frequencies. Electronic polarization primarily occurs in the optical band while atomic polarization prevails in the infrared band. Electronic polarization is recognized as an induced effect and remains independent of temperature; it makes a significant contribution to overall dielectric constant of materials [5].

Ionic Polarization

Ionic polarization is the separation of positive and negative charges observed in materials with ions, such as salts or ionic compounds, when subjected to an external electric field [4]. This polarization type arises from the asymmetric sharing of electrons among different atoms within a molecule. Consequently, the electron cloud shifts toward the atom with stronger binding, causing the atoms to acquire charges of opposite polarity. When subjected to an electric field, ionic species typically shift, resulting in a remarkably high dielectric constant. Not influenced by thermal energy, ionic polarization is commonly identified in ceramics, inorganic crystals, and glasses [5].

Orientation or Dipolar Polarization

When atoms bond and share one or more electrons, they create a molecule. This electron rearrangement can result in an uneven distribution of charge, leading to a permanent dipole moment [4]. Orientation polarization manifests in dipolar materials which have a permanent dipole moment, generated by the transfer of valence electrons forming ionic bonds between molecules. This permanent dipole moment is determined by the product of the charges of transferred valence electrons and the interatomic distance. Initially, in dipolar materials, all dipoles are randomly oriented in space. However, when subjected to an electric field, they undergo a torque that leads it

to align in the same direction as the applied field, resulting in a net polarization in that direction. The rate of dipolar orientation is significantly influenced by intra- and intermolecular interactions, allowing molecular dipoles to orient over a broad range of frequencies, dictated by the ease with which dipoles rotate. In microwave or high-frequency fields, dipoles strive to follow the rapidly changing field, leading to orientation polarization, characterized by the alignment of dipoles in the direction of the electric field. The temperature impacts this polarization since thermal energy randomizes the molecular alignment. Furthermore, the movement of dipoles leads to changes in both ϵ'_r and ϵ''_r at frequencies related to relaxation often observed in the microwave region [5].

3.4 Dielectric Properties

Capacitance

Capacitance is the ability of a material to hold an electrical charge, measured as the amount of electric charge stored for a given electric potential. The capacitance can be calculated based on the geometry of conductors and dielectric properties between them. For example, for a parallel-plate capacitor with plates of area (A) separated by distance (d), the capacitance (C) is approximately given by:

$$C = \epsilon_r \epsilon_0 \left(\frac{A}{d} \right) \quad (4)$$

where ϵ_r represents relative dielectric permittivity and ϵ_0 signifies vacuum permittivity. Dielectric spectroscopy extensively involves evaluating the system's permittivity in different conditions using capacitance measurements.

Permittivity

Permittivity is a measure of how an electric field affects, and is affected by, a dielectric medium. It relates to the material's ability to transmit an electric field [4]. The permittivity of a material is intricately linked to its chemical composition, structural arrangement, molecular makeup, and atomic valence. Serving as a metric for diverse polarization phenomena, permittivity manifests across various frequency ranges of oscillating electric fields. One such manifestation is dipolar polarization, induced in molecules possessing an inherent dipole moment, often referred to as orientation polarization. When subjected to an external electric field, molecules with dipole moments undergo rotation over a duration proportional to the dipole moment and the local viscosity of the material. The dipole moment signifies the separation of positive and negative charges within a molecule, determining its overall polarity.

Due to a time delay in dipolar polarization aligning with the applied oscillating field, dispersions occur, preventing molecules from fully aligning with the higher frequency oscillating electric field. This phenomenon, known as dielectric relaxation, is notably observed in the microwave region of the electromagnetic spectrum. Beyond this frequency range, oscillating electric fields cease to induce molecular polarity in the material [1].

Dielectric Constant

A material is considered a dielectric if it has the capability to retain energy when an external electric field is applied. When a DC voltage source is connected across a parallel plate capacitor, the presence of a dielectric material between the plates allows for more charge storage compared

to having no material (a vacuum) between the plates. The dielectric material enhances the capacitor's storage capacity by counteracting charges at the electrodes that would normally contribute to the external field. The capacitance with the dielectric material is determined by its dielectric constant, often denoted as ϵ_r or sometimes K or κ , which is defined as:

$$\epsilon_r = \frac{\epsilon}{\epsilon_0} \quad (5)$$

where ϵ is the static permittivity of the material.

Resistivity

Electrical resistivity, also known as specific electrical resistance or volume resistivity, is a measure of how strongly a material opposes the flow of electric current. A low resistivity indicates that the material readily allows the movement of electrical charge. The term "electrical resistivity" (ρ) can be defined in two ways: first by $\rho = E/J$ where ρ is the static resistivity (measured in volt-meters per ampere, V m/A), E is the magnitude of the electric field (measured in volts per meter, V/m), and J is the magnitude of the current density; secondly by $\rho = R * \ell/A$ where ρ represents static resistivity, R denotes electrical resistance, A stands for cross-sectional area and ℓ represents length [4].

3.5 Dielectric Relaxation

The reduction of polarization to zero is not an immediate occurrence; instead, it unfolds over a finite duration when a prolonged direct voltage is exerted on a dielectric material. Correspondingly, when the electric field is eliminated, the same duration is necessary for the

dipoles to revert to a random distribution, influenced by the temperature of the medium. In situations where an abrupt direct voltage is applied, molecules need a finite amount of time to orient themselves, giving rise to the observed polarization effect. This phenomenon is referred to as dielectric relaxation [6]. Mathematical models, including Debye, Cole-Cole, and Cole-Davidson equations, describe dielectric relaxation behaviors in materials.

One of these models which was developed by Dutch born physicist Peter Debye gives an equation which puts dielectric relaxation in its simplest form.

$$\varepsilon' = \varepsilon + \frac{\Delta\varepsilon}{1+j\omega\tau} \quad (6)$$

Where j signifies the imaginary unit ($j = \sqrt{-1}$), occasionally denoted as κ , ω is the angular frequency ($\omega = 2\pi f$), τ is the orientational relaxation time of the dipole. Debye relaxation characterizes the dielectric response of an ideal and non-interacting assembly of dipoles when subjected to an alternating external electric field.

Debye relaxation is insufficient in describing all relaxation phenomena, leading to modifications to accommodate diverse materials in varying states. An enhancement to Debye's original equation was introduced by K.S. Cole and R.H. Cole, incorporating an empirical parameter denoted as $0 < \alpha < 1$ (Equation 7). Notably, when α equals 0, the equation reverts to the Debye equation.

$$\varepsilon' = \varepsilon + \frac{\Delta\varepsilon}{(1+j\omega\tau)^{1-\alpha}} \quad (7)$$

The Cole-Cole equation, as presented above, holds applicability for materials demonstrating a consistent and symmetrical distribution of relaxation times. Nevertheless, various relaxation phenomena, particularly evident in synthetic polymers, do not adhere to this

symmetrical pattern. Recognizing this non-uniform distribution, Cole and Davidson introduced an asymmetry parameter denoted as $0 < \beta < 1$ (Equation 8). It's noteworthy that when β equals 1, the equation aligns with the Debye equation. This augmentation addresses the intricacies of non-symmetrical relaxation distributions, providing a more comprehensive framework to capture the diverse relaxation behaviors observed in certain materials, such as synthetic polymers.

$$\varepsilon' = \varepsilon + \frac{\Delta\varepsilon}{(1+j\omega\tau)^\beta} \quad (8)$$

The equation evolved further with input from Havriliak and Negami. Their proposal involved merging the Cole-Cole and Cole-Davidson equations (Equation 9). In this formulation, when α equals 0, the equation transforms into the Cole-Davidson equation. Similarly, if β equals 1, the equation reverts to the Cole-Cole equation. This combination offers a versatile approach, allowing the equation to align with either the Cole-Davidson or Cole-Cole model based on the values assigned to α and β [1, 7].

$$\varepsilon' = \varepsilon + \frac{\Delta\varepsilon}{(1+j\omega\tau)^{(1-\alpha)\beta}} \quad (9)$$

Dielectric spectroscopy serves as a powerful tool for precisely measuring the material's permittivity in its complex form. The complex permittivity is intricately defined by the real and imaginary components, elegantly expressed through equation 10.

$$\varepsilon^*(\omega) = \varepsilon_r + \frac{\sigma^*}{j\omega} \quad (10)$$

Here, ε^* symbolizes the complex permittivity, and σ^* represents conductivity. The real and imaginary facets of the complex permittivity intricately capture the energy stored and lost by the

material. In an ideal relaxation scenario, the descent of ε' harmonizes with the ascent of ε'' to its pinnacle.

The quantification of a material's permittivity commonly adopts the approach of relative permittivity, where the material's permittivity is computed in relation to the permittivity of free space. This calculation is expressed in equation 11.

$$\varepsilon_r^* = \frac{\varepsilon^*}{\varepsilon_0} = \frac{\varepsilon'(\omega) - j\varepsilon''(\omega)}{\varepsilon_0} = \varepsilon_r' - j\varepsilon_r'' \quad (11)$$

Here, ε_r^* is the relative permittivity, ε_0 is the permittivity of free space, and ε_r' and ε_r'' denote the real and imaginary components of the relative permittivity, respectively.

3.6 Dielectric Spectroscopy

3.6.1 Introduction

Dielectric spectroscopy analyzes electrical properties of a material under test (MUT) across frequencies. This non-destructive, non-ionizing method relies on the interaction between an externally applied electric field and the electric dipole relaxation moment of the MUT, expressed in terms of real and imaginary permittivity. Various approaches have been developed, involving the measurement of capacitance and conductance of the MUT at different frequencies. The resulting dielectric spectra are then analyzed to differentiate between different MUTs.

A typical microwave sensor system includes three main components: a sensor, a vector network analyzer (VNA), and a graphical user interface (GUI) (See figure 3.4). The VNA, commonly used in Radio Frequency (RF) design, helps characterize RF and microwave devices by measuring network scattering parameters (S-parameters). It provides precise readings with a high number of sweep points, and the data can be presented in terms of magnitude, phase, and complex data. The GUI controls the entire system, initializing the VNA, configuring parameters, collecting information from a sensor via the VNA, analyzing data, and displaying relevant information on a computer screen [8].

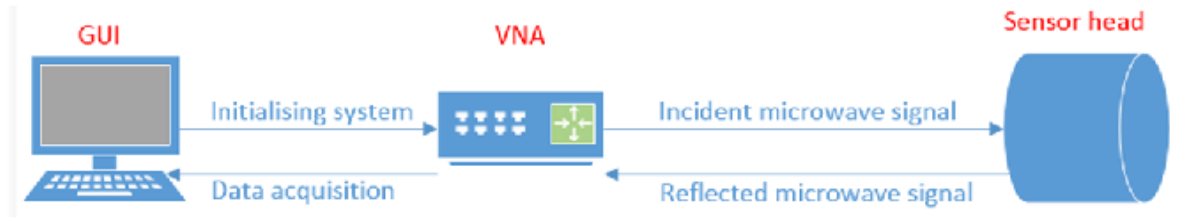


Figure 0.4. Diagram of a microwave sensor system (adapted from [8]).

The VNA displays the reflected signal as S_{11} parameters and the transmitted signal as S_{21} parameters, which can then be interpreted to calculate the permittivity of the material under test. The dielectric constant, dielectric loss, and loss tangent of the MUT can be determined using specific equations. This comprehensive method provides valuable insights into the electrical behavior of materials across different frequency ranges [1].

$$\epsilon' = \frac{V_c(f_c - f_s)}{2V_s f_s} + 1 \quad (12)$$

$$\varepsilon'' = \left(\frac{V_C}{4V_S}\right) \left(\frac{1}{Q_S} - \frac{1}{Q_C}\right) \quad (13)$$

$$\tan \delta = \frac{\varepsilon''}{\varepsilon'} \quad (14)$$

=energy lost per cycle/ energy stored per cycle.

In the equations (12-14), ε' represents the dielectric constant, while ε'' signifies the dielectric loss. $\tan \delta$ is also referred to as the loss tangent [4]. The variables f_c and f_s denote the resonant frequencies of the empty and loaded cavity, respectively, whereas V_S and V_C represent the volumes of the sample and cavity. Q_C and Q_S are the quality factors of the empty and loaded cavity, respectively. This method, although relatively straightforward, comes with certain limitations. When dealing with materials characterized by high losses, accurately determining the cutoff frequency of the waveguide can be challenging due to significant signal attenuation. Additionally, the assessment of permittivity is constrained by the physical dimensions of the waveguide, limiting its application to a specific range of frequencies [1].

This technique is appealing because it is non-invasive and non-destructive, and it is cost-effective with immediate results. The results can be presented in different ways, such as magnitude, phase angle, Smith chart, or polar format (see Figure 3.5). The output comprises both amplitude and phase, making it a vector quantity. For example, the amplitude, represented as the reflection coefficient magnitude ($|S_{11}|$), is displayed as a spectral response in dB on the y-axis against frequencies on the x-axis. This representation indicates the amount of energy absorbed at a specific frequency. To summarize, these outputs illustrate how the response varies at specific frequencies due to the permittivity of the MUT. For low frequencies, impedance (Z) measurements are used, including both resistance (R) and reactance (X) as described by Equation 13.

$$|Z| = \sqrt{R^2 + X^2} \quad (15)$$

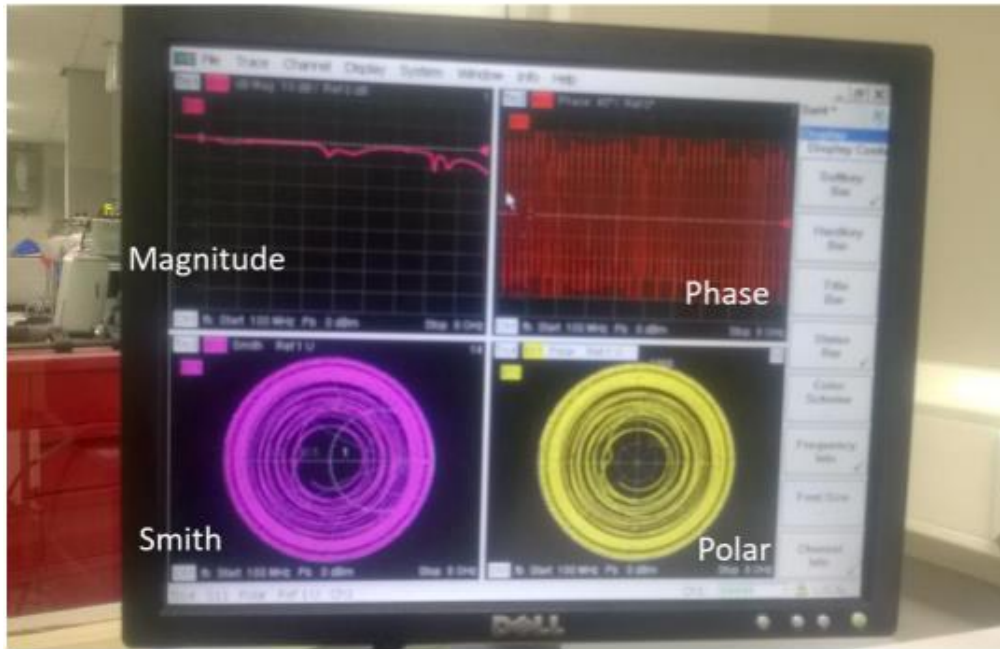


Figure 0.5. Example of raw output data as a reflection coefficient from a VNA [3].

By examining the electromagnetic spectral response, it becomes feasible to recognize changes associated with the MUT. However, it's crucial to note that the response can also be influenced by variations in other factors like temperature, density, and pressure. Overcoming potential interferences in the output signal requires a comprehensive understanding of these contributing factors [3].

3.6.2 Measuring methods

Numerous techniques exist to measure complex permittivity, each constrained by specific frequencies, materials, and applications. Examples include transmission/reflection line, open-

ended coaxial probe, free space, and resonant methods. Table 3.1 provides instances of materials, S-parameters, and dielectric properties measured using these methods [9].

TABLE 0.1
Comparison between measurement methods (adapted from [9]).

Measurement techniques	Materials	S-parameters
Transmission/Reflection Line	Coaxial line, waveguides	S_{11} , S_{22} , S_{12} , S_{21}
Open-ended coaxial probe	Liquids, biological specimen, semi-solids	S_{11} , S_{22}
Free space	High temperature material, large flat solid, gas, hot liquids	S_{11} , S_{22} , S_{12} , S_{21}
Resonant Method (Cavity)	Rod shaped solid materials, waveguides, liquids	Frequencies, Q-factors

Transmission/Reflection line method

In the Transmission/Reflection line method, a sample is placed in a segment of waveguide or coaxial line, and a VNA is used to measure the complex scattering parameters at two ports (See figure 3.6). Calibration precedes the measurement, and parameters like reflected (S_{11} , S_{22}) and transmitted signal (S_{21} , S_{12}) are assessed. These scattering parameters are closely tied to the material's complex permittivity and permeability through specific equations. Converting S-parameters to complex permittivity and permeability involves utilizing specialized software for

solving these equations. In many cases, preparing the sample includes machining to ensure a precise fit in the waveguide or coaxial line. Calibration techniques in transmission line measurements yield various resonant behaviors using different terminations. For accurate dielectric measurement, an open-circuited or other capacitive termination is employed to maximize the electric field. When conducting coaxial line measurements, calibration may include using short-circuited, open-circuited, or matched load terminations. This approach enables the determination of a material's permittivity effectively.

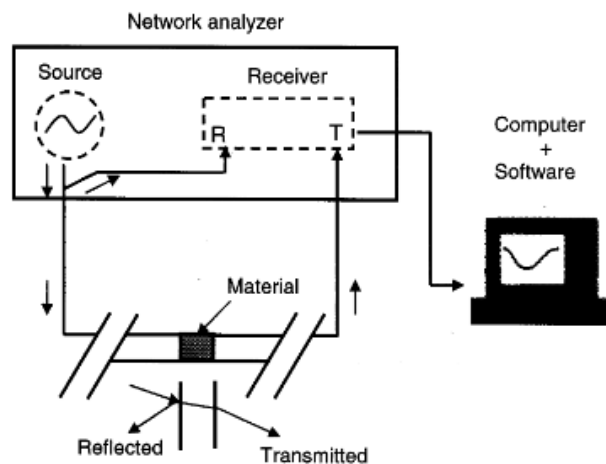


Figure 0.6. Schematic of a transmission line utilizing the waveguide technique (R = power reflected, T = power transmitted) [10]

In the transmission/reflection line method, the VNA undergoes initial calibration at the connector calibration plane, with the material under test (MUT) securely placed in a holder to minimize air gap-induced measurement uncertainty. Two methods extend the calibration plane to the sample surface. The first method manually incorporates the phase factor, adjusting the calibration plane from connector to MUT surface. The second method employs the VNA's de-

embedding function, canceling out the holder's influence on material measurement. Both approaches yield identical results. Post-processing the measured s-parameters with dedicated software determines complex dielectric properties. This method is advantageous for samples with medium to high loss, allowing determination of both permittivity and permeability. However, accuracy is limited by air-gap effects, and precision diminishes when the sample length is a multiple of one-half wavelength in the material.

Open-ended coaxial probe

The open-ended coaxial probe method is a well-established non-destructive testing technique. It involves pressing the probe against a specimen or immersing it in liquids (Figure 3.7). The measured reflection coefficient helps determine permittivity. Notably, for certain measurements, especially with biological specimens where material characteristics may change, cutting out a sample might not be feasible. This method allows placing the sample in close contact with the probe without altering its characteristics. A VNA calibrates the probe system, referencing reflection coefficient measurements to the probe aperture plane. Calibration is achieved through two methods. The first method involves direct calibration at the open-end using reference liquids, though uncertainties arise from characterizing these liquids. Water, saline, and methanol are common choices. Standard one-port full calibration is then applied to measurements on the MUT, with post-processing using a program to derive dielectric parameters [9].

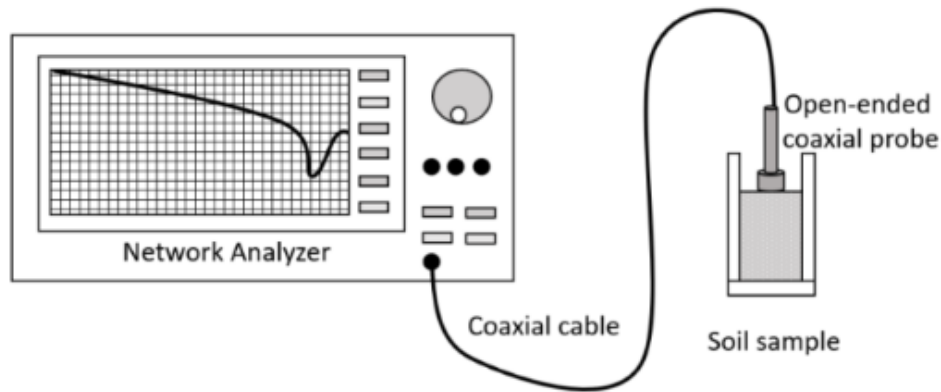


Figure 0.7. Network analyzer and dielectric probe measuring the permittivity of contaminated soil [6].

In the calibration process, the VNA is calibrated at the connector plane using standards (open, short, and match), and the probe is then connected at the connector plane. To minimize reflections from the connector, the VNA's time domain feature with a gating function is employed. Complex coefficient data (K_C) referenced to the connector plane are recorded and processed in two steps. The first step involves a de-embedding model that compensates for probe propagation characteristics, translating the measurement reference from the connector plane to the probe aperture plane. The second step applies a rational function model to calculate the sample's permittivity using the embedded reflection coefficient (K_a). The method has advantages such as no sample machining, easy preparation, and rapid measurement of dielectric properties for numerous samples after calibration. It allows measurements in a controlled temperature environment. However, it is limited to reflection measurements and can be affected by air gaps in specimen measurements [9].

Free space method

Free space measurement enables testing materials under high temperatures or hostile environments, operating across wide band frequencies. This method requires the MUT to be large and flat. Two antennas, connected to a network analyzer, are positioned facing each other for measurements. Calibration is crucial, with through-reflect-line (TRL), through-reflect-match (TRM), and line-reflect-line (LRL) being common methods. LRL calibration typically yields the highest quality. The line standard is achieved by separating antenna focal planes to about a quarter of a wavelength, while the reflect standard involves placing a metal plate on the sample holder between the antennas. Once calibrated, s-parameters of an empty sample holder are measured, and using the de-embedding function, the influence of the sample holder is canceled when determining the MUT's s-parameters. Time domain gating prevents multiple reflections in the sample and eliminates energy diffraction from antenna edges. Post-processing measured coefficients with dedicated software determines dielectric properties.

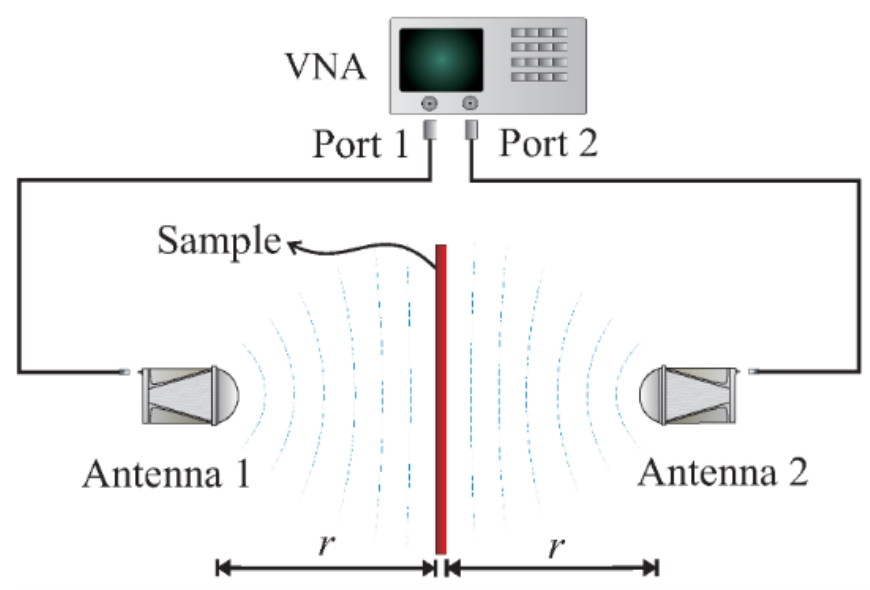


Figure 0.8. Measurement of sample using free space method [11].

Figure 3.8 illustrates the idea of transmission and reflection free space method. The antennas and the space between them form a two-port network, characterized by four S-parameters [11].

Advantages of the free space method include its applicability for high-frequency measurements, non-destructive nature, suitability for measurements in hostile environments, and the ability to evaluate both magnetic and electric properties. However, it has limitations, requiring a large and flat MUT, potential for multiple reflections between antennas and the sample surface, and susceptibility to diffraction effects at the sample's edge [9].

Resonant method

Resonant measurements, while highly accurate for obtaining permittivity, have limitations related to material frequencies and loss characteristics. Various resonant methods exist, including reentrant cavities, split cylinder resonators, and cavity resonators. Two commonly used resonant measurements are perturbation methods, suitable for all permittivity and magnetic material measurements, and low-loss methods, applicable to larger samples with low loss. The perturbation method, particularly with a transverse magnetic cavity geometry, is popular. By monitoring the resonance characteristics of the material under test (MUT) in the cavity, including quality factor and resonance frequency, dielectric parameters can be determined. This involves measuring the resonant frequency and quality factor of an empty cavity, repeating the measurement with the MUT, and calculating permittivity or permeability using frequency, volume, and q-factor.

Calibration of the network analyzer is unnecessary for this type of measurement. An example of a cavity resonator is shown in figure 3.9.

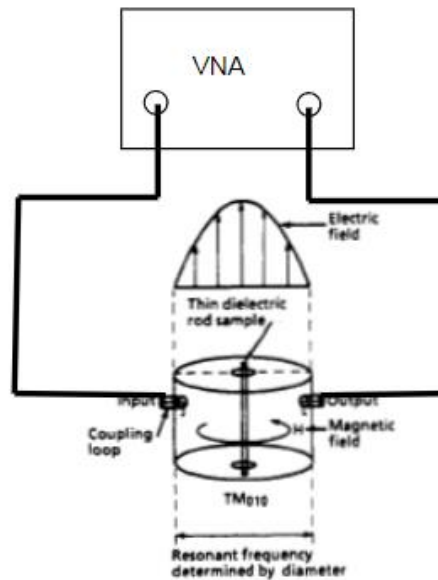


Figure 0.9. Measurement of thin film using cavity resonator [9].

Advantages of the resonant method include the ability to measure very small MUT and the use of approximate field expressions in the sample and cavity. However, it has limitations, requiring a high-frequency resolution VNA and being limited to a narrow band of frequencies [9].

3.7 Scattering Parameters

The detection instrument used in this study is specifically designed for operation within the microwave region, encompassing wavelengths ranging from 1 mm to 1 m, corresponding to frequencies between 300 MHz and 300 GHz. At these frequencies, the application of high-

frequency theory supplements traditional circuit theory. Instead of utilizing lumped impedance and reactance to characterize circuits, the focus shifts towards the relevance of reflected and transmitted power, given the distributed nature of the elements.

3.7.1 S-Parameter Matrices

At high frequencies, measuring total voltage or current becomes challenging. Hence, S-parameters, also known as "scattering parameters," are commonly utilized. These parameters, encompassing measurements like gain, loss, reflection/transmission coefficient, and impedance/admittance, offer simplicity and avoid the need for connecting undesirable loads to the MUT. The number of S-parameters for a device equals the square of its port number; for instance, a two-port device has four S-parameters. The numbering convention designates the first number after "S" as the port where energy emerges, and the second number as the port where energy enters. Thus, S_{21} measures the power emerging from port 2 due to a high-frequency stimulus at port 1, while identical numbers (e.g., S_{11}) indicate a reflection measurement [12, 13].

The scattering parameters are represented by the following equations:

$$b_1 = S_{11}a_1 + S_{12}a_2 \quad (15)$$

$$b_2 = S_{21}a_1 + S_{22}a_2 \quad (16)$$

In these equations, the traveling wave variables a_1 , b_1 at port 1 and a_2 , b_2 at port 2 in the two-port network. These variables are defined in terms of total voltage and current phasors (U_1 , I_1 at port 1 and U_2 , I_2) and the reference impedance Z_0 according to the following equations:

$$a_1 = \frac{U_1 + I_1 Z_0}{2\sqrt{Z_0}} \quad a_2 = \frac{U_2 + I_2 Z_0}{2\sqrt{Z_0}} \quad (17)$$

$$b_1 = \frac{U_1 - I_1 Z_0}{2\sqrt{Z_0}} \quad b_2 = \frac{U_2 - I_2 Z_0}{2\sqrt{Z_0}} \quad (18)$$

The wave variables' magnitudes ($|a_1|^2$, $|a_2|^2$, $|b_1|^2$, $|b_2|^2$) represent incident and reflected power in a two-port network. $|a_1|^2$ is the power incident on port 1, $|a_2|^2$ is the power incident on port 2,

S-parameters are measured by connecting the network to a transmission line with a network analyzer. The reference impedance is often set to be $Z_0 = 50 \Omega$.

The S-parameters are measured by connecting to a matched load ($Z_L = Z_0$), eliminating reflected waves from the load ($a_2=0$). The S-parameter equations 15 & 16 above then simplify to 19a and 19b.

$$S_{11} = \left. \frac{b_1}{a_1} \right|_{a_2=0} \quad S_{21} = \left. \frac{b_2}{a_1} \right|_{a_2=0} \quad (19a \text{ \& } 19b)$$

By reversing the roles of the generator and load, similar measurements can be made for S_{12} and S_{22} :

$$S_{12} = \left. \frac{b_1}{a_2} \right|_{a_1=0} \quad S_{22} = \left. \frac{b_2}{a_2} \right|_{a_1=0} \quad (20a \text{ \& } 20b)$$

Parameter S_{11} (S_{22}) corresponds to the input (output) reflection coefficient, while S_{21} (S_{12}) corresponds to the forward (reverse) transmission coefficient as depicted in figure 3.10. Each scattering parameter is generally complex, denoted as $S_{ij} = |S_{ij}| e^{j\theta_{ij}}$, where $|S_{ij}|$ is the amplitude ratio, and θ_{ij} is the phase difference of traveling waves (a_1 , b_1 , and a_2 , b_2) [12, 13].

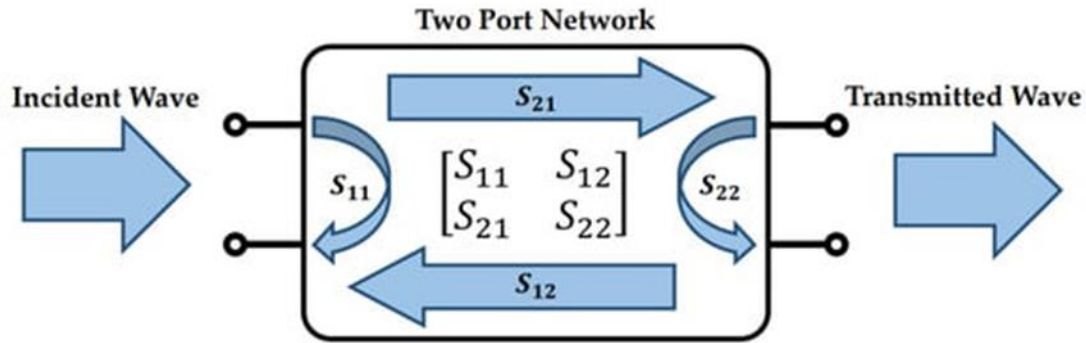


Figure 0.10. The S-parameter matrix of a two port system [14].

3.7.2 Advantages of using S-parameters

Advantages of using S-parameters include gaining valuable insights into the performance of linear electrical networks like amplifiers, filters, and RF components. They capture details on signal reflection, attenuation, signal magnitude, and phase. Furthermore, S-parameters enable the extraction of various transmission line parameters using specific mathematical models and equations such as R , L , C , G , TD , and Z_0 . They facilitate circuit optimization by identifying locations of signal loss and impedance mismatches. Additionally, the S-parameters of an S-matrix can be easily transformed into other parameters, including Z-parameters, Y-parameters, H-parameters, T-parameters, and ABCD-parameters, offering flexibility and convenience in analyzing and designing electronic circuits.

Return Loss serves as an indicator of signal degradation caused by reflection or disturbances in a transmission line, measured in decibels (dB) as a scalar (amplitude-only) parameter. A well-matched MUT contributes to substantial power dissipation in the reflected signal, yielding a heightened return loss. Conversely, a poorly matched MUT characterized by

heightened reflections results in diminished loss, hence a reduced return loss. The logarithmic expression for return loss is given by the formula [15]:

$$\text{Return loss (dB)} = -10 * \log \left(\frac{\text{Incident Power(W)}}{\text{Reflected Power(W)}} \right) \quad (21)$$

Insertion loss represents the energy attenuation experienced by a signal during its journey along a cable link. This phenomenon, known as attenuation, is an inherent aspect of any transmission, be it electrical or data. The extent of signal reduction, influenced by the cable's length, directly correlates with insertion loss—the longer the cable, the more pronounced the insertion loss. Additionally, any connection points within the cable link, such as connectors and splices, contribute to insertion loss. The equation for insertion loss is given by equation[5].

$$\text{Insertion loss (dB)} = 10 * \text{Log} \left(\frac{\text{Incident Power(W)}}{\text{Transmitted Power(W)}} \right) \quad (22)$$

3.7.3 Relationship between S-parameters and Impedance

VNA's are useful test instruments for characterizing rf circuits and amplifiers. But what about the measurement of simple passive components? How can a chip impedance be calculated from the measured S-parameters? The following equations show how this is done for the reflection and transmission [16-18].

For Reflection (Z_r):

$$Z_r = \frac{Z_0(1+S_{11})}{1-S_{11}} \quad (23)$$

For Transmission (Low-level Impedance):

$$Z_t = \frac{Z_0 S_{21}}{2(1-S_{21})} \quad (24)$$

For Transmission (Average and high-level Impedance):

$$Z_t = \frac{2Z_0(1-S_{21})}{S_{21}} \quad (25)$$

3.8 Practical Considerations for BDS

3.8.1 Instrumentation - Network Analyzers

Network analysis involves creating a data model for transfer and/or impedance characteristics of linear networks, achieved through stimulus response testing across the frequency range of interest. Network analyzers perform this through point-to-point frequency testing or sweeping the entire frequency band at once. While network analysis is typically limited to defining linear networks, sine wave testing is ideal for characterizing magnitude and phase response with frequency variation. These analyzers measure transfer and impedance functions by separating signals from the device under test, requiring detection of appropriate signal ratios and displaying the results. In microwave frequencies with potential standing waves, analyzers must handle signal separation from travelling waves. Automatic Vector Network Analyzers (AVNA) are commonly used for precise measurements, available in both scalar (magnitude only) and vector (both magnitude and phase) types. Two detection methods are employed: broadband detection covers the full frequency spectrum of the input signal, while narrow-band detection uses tuned receivers converting continuous wave (CW) or swept RF signals to a constant intermediate frequency (IF) signal. Each detection scheme offers its advantages [10].

Scalar analyzers typically utilize broadband detection techniques, which reduce instrument costs by eliminating the need for the IF section found in narrowband analyzers. However, this sacrifice results in lower noise and harmonic rejection. Broadband systems are advantageous for making measurements when input and output frequencies differ, such as in assessing the insertion loss of mixers and frequency doublers—an ability not present in narrowband systems.

On the other hand, VNAs typically employ narrowband detection techniques, leading to more sensitive and low-noise detection of a constant IF. This enhances accuracy and dynamic range for frequency-selective measurements compared to broadband systems. Analyzer systems offer adaptability and flexibility, showcasing impedances on a Smith chart overlay for a polar display. S-parameter measurements can be performed by attaching a suitable test set. Computer-controlled network analyzers can be programmed for automated setup and measurements, accelerating the process. Additionally, the computer's capability to store, transform, summarize, and output data in various formats to multiple peripherals further expedites the measurement process. Furthermore, functions initially displayed in the frequency domain can be converted to the time domain for additional analysis [10].

3.8.2 Microwave Measurements with VNA's

When using a network analyzer system for microwave measurements, inherent errors fall into two categories: instrument errors and test set/connection errors. Instrument errors involve variations due to noise, imperfect conversions, crosstalk, logarithmic conversion inaccuracies, non-linear displays, and system drift, with modern analyzers exhibiting minimal instrument errors. Test set/connection errors at ultra-high frequency and microwave frequencies contribute to measurement uncertainty in a probe network analyzer system, quantified as directivity, source

match, and frequency tracking errors. Hewlett Packard has developed an analytical model to correct reflectivity measurements, especially for in-vivo measurement probes, incorporating equations that account for open-circuit fringing capacitance. For accurate microwave frequency measurements, power rather than voltage or current is preferred due to variations along the transmission line.

Noise, categorized into internal and external, influences signal-to-noise ratios (SNR), which is vital for electronic system evaluation. SNR is expressed in decibels and considers the ratio of signal to noise power.

Frequency measurements at microwave frequencies can be made directly with a frequency counter or through down-conversion techniques like prescaling, transfer oscillator, and harmonic heterodyne. Prescaling involves dividing the frequency of the input signal to make it countable. However, its frequency limitations must be considered. Also, when the amplitude of the microwave signal is low, the detector operates in its quadratic or square-law region, while in its linear region, it rectifies the applied signal when the microwave signal power exceeds -15 dBm [10]. Table 3.2 compares a wide range of microwave dielectric measurement systems.

TABLE 0.2

A Broad Comparison Of Microwave Dielectric Measurement Systems [10].

	Slotted line reflection system	Guided wave transmission system	Free space transmission system	Filled cavity resonance system	Partially filled cavity resonance system	Probe reflection system
Frequency	broad band	banded	banded	single	single	broad band
Sample size	moderate	moderate	large	large	very small	small
Temperature monitoring/control	difficult	difficult	very easy	very easy	very easy	easy
Accuracy for:	very low	Moderate	Moderate	very high	high	low
Low-loss material	low	moderate	moderate	does not	low	high
High-loss material				work		
Sample preparation	easy	difficult	easy	very difficult	very difficult	easy
Most suitable test material	solids, semi- solids	solids	large flat sheets	solids, semi- solids, liquids	solids	solids, semi- solids, liquids
To test material	destructive	destructive	non- destructive	destructive	destructive	non- destructive
Commercial vendors	no	yes	yes	no	no	yes

3.8.3 Lecroy SPARQ

The VNA employed in this study is the SPARQ-4004E manufactured by Teledyne LeCroy (See figure 3.11). SPARQ stands out as an excellent tool for analyzing multi-port devices often encountered in signal integrity applications, all while being more affordable compared to conventional methods. Its versatility makes it suitable for various tasks, including the development of measurement-based simulation models, design validation, compliance testing, high-performance time-domain reflectometry (TDR), PCB testing, and fulfilling portable measurement needs [19].



Figure 0.11. A Lecroy SPARQ analyzer connected to a pc with a USB cable [20].

3.8.4 Microstrips and Waveguides

A microstrip is a printed circuit version of a wire placed over a ground plane. As the distance between the ground plane and the strip increases, it tends to emit radiation. To minimize radiation while avoiding narrow strip widths, a substrate thickness of a few percent of a wavelength is ideal. The Microstrip line exhibits dispersion, meaning that as frequency increases, the effective dielectric constant gradually approaches that of the substrate, resulting in a decrease in phase

velocity. This holds true even with non-dispersive substrate materials, where the dielectric constant typically decreases with frequency.

A coplanar waveguide (CPW) comprises a conductor separated from two ground planes, all etched on one side of a dielectric on the same plane. The dielectric should be sufficiently thick to attenuate electromagnetic fields within the substrate. Another type of CPW, known as grounded coplanar waveguide (GCPW), features a ground plane on the opposite side of the dielectric. GCPW is preferred over microstrip for thick substrates [21, 22]. GCPWs, used as an alternative to microstrip lines on printed circuit boards, typically have a gap between the strip and ground larger than the substrate thickness. This concentrates the GCPW field between the strip and the substrate ground plane, behaving similarly to microstrip. By connecting ground planes with vias, GCPW is less prone to radiation and offers higher isolation than microstrip [22].

The advantages of CPWs include simple fabrication, straightforward surface mounting and assembly, absence of via holes, and reduced radiation loss. Additionally, CPWs' ground planes isolate adjacent signals, effectively minimizing crosstalk commonly encountered in close-proximity conductive lines. The design of a coplanar waveguide transmission line consists of a center conductor acting as the signal line, surrounded by two ground planes [21].

In this study, a ground–signal–ground (GSG) CPW fabricated from gold-covered alumina (1 mm thick polished alumina with a dielectric constant of 9.5) is utilized. End launch connectors hold it together, connecting it to the VNA for measurement (see figures 3.12 and 3.13). Details and dimensions of the waveguide and end launch connectors are shown in APPEN Figure 13 shows the dimension of the GSG CPW. Most of the samples I used were deposited on highly resistive Si substrates. Despite the high resistivity, they are still conductive. As such the sensing

substrate is isolated from the gold signal traces by a Corning glass cover slide cover to prevent shortening of the ground and signal traces.

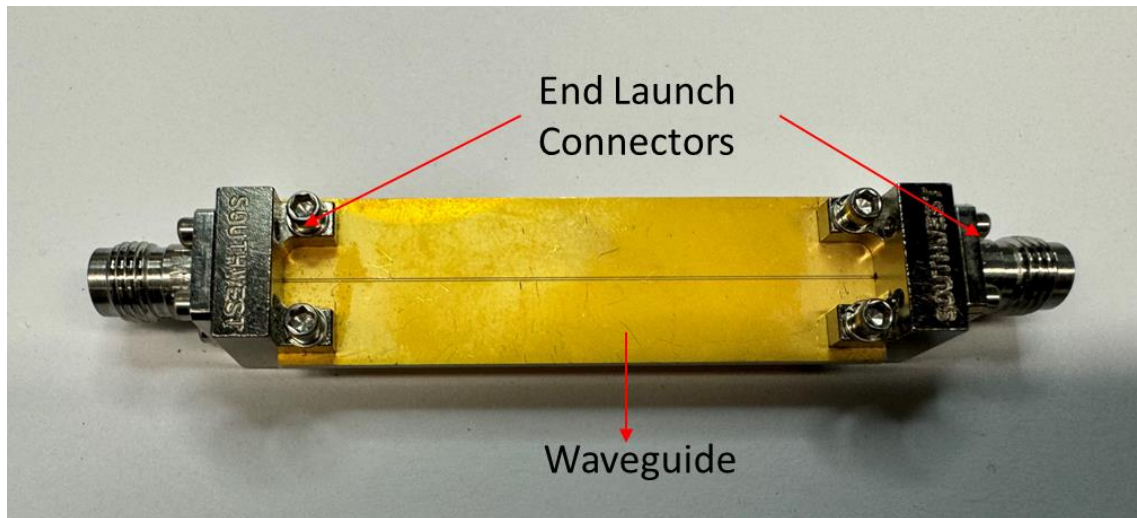


Figure 0.12. Image of the top-down view of the grounded coplanar waveguide with end launchers.

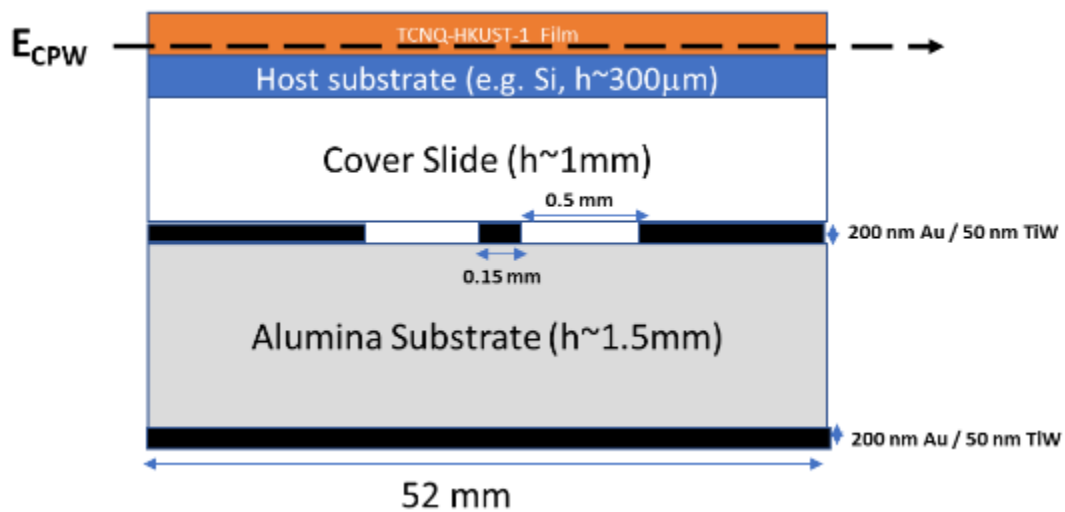


Figure 0.13. A schematic cross section of a GSG coplanar waveguide with its dimensions shown [23].

3.9 Some examples of BDS use in other studies

This section highlights the diverse applications of Broadband Dielectric Spectroscopy (BDS) in the investigation of dielectric responses in different systems. The examples presented demonstrate the versatility of BDS in studying water structure, alkali metal chlorides, and biomolecules.

3.9.1 Water Structure

In a study conducted by Shiraga et al., they explore how saccharides affect freezing and dehydration by examining their hydration properties and impact on water's hydrogen bond network. Researchers measured dielectric constants of glucose solutions at different frequencies and analyzed the data to understand underlying mechanisms. The results show that water around glucose has slower relaxation times and disrupted hydrogen-bonded structures, indicating that saccharides break down hydrogen bonds in water [24].

3.9.2 Alkali Metal Chlorides

Alkali metal chlorides, like table salt, dissolve in water, forming strong electrolyte solutions. In Chen et al.'s study, dielectric relaxation of KCl and CsCl solutions was examined at 25°C using various measurement methods. The findings, similar to those for NaCl, were well-matched by a Cole-Cole equation. The spectra from their results revealed that the impact of the solute on the water structure was evident in the reduction of bulk-water relaxation time with increasing electrolyte concentration and follows this sequence: NaCl>KCl>CsCl. This effect was proportional to the surface-charge density of the cation [25].

3.9.3 Biomolecules

Understanding the electromagnetic properties of biomolecules is crucial for advancing interactions between electric fields and biosystems, aiding the development of innovative biomedical diagnostic and therapeutic approaches. A study conducted by Havelka et al., introduces a method for designing radiofrequency and microwave chips to quantitatively sense the dielectric properties of biomolecule solutions. The approach involves determining the primary frequency band of interest based on the targeted molecule's relaxation time through the Stokes–Einstein–Debye equation. A microwave sensing chip is then proposed, its performance evaluated through analytical modeling and numerical electromagnetic simulations. The fabricated chip is experimentally shown to extract the complex permittivity (0.5–40 GHz) of water solutions of alanine, a common amino acid, without requiring calibration liquid and with a significantly smaller volume than commercial methods. Molecular dynamics simulations help interpret the observed dependence of complex permittivity on alanine concentration. This method can be broadly applied for developing dielectric sensing of various polar biomolecule solutions [26].

3.10 How BDS was used for this Research Work

Conventional methods for gas sensing, such as resistance-based direct current (DC) methods, require establishing electrical connections with the sensing materials. However, these connections are prone to imperfections, leading to inaccuracies in measurements. The present study introduces an alternative approach by exploring the viability of utilizing contactless BDS

as a metrology technique for gas monitoring. By employing BDS, the aim is to circumvent the issues associated with inaccuracies in resistivity values caused by the use of probes and unintended interactions between measurement tools and the material being measured [27, 28].

This study demonstrates that BDS-based metrology offers a promising solution to these challenges. By eliminating the need for physical contact with the sensing material, BDS minimizes distortions in the reported resistivity values and reduces parasitic errors resulting from interactions between the measurement tools and the material under observation. Furthermore, the analysis of BDS data at specific frequencies enabled the extraction of valuable electrical insights that can be linked to fundamental processes occurring within the sensing material. For instance, these electrical signals can be correlated to phenomena such as charge-transfer reactions involving point defects in materials like ZnO and the adsorption of molecules from the surrounding gaseous environment [29]. The exact experimental details and parameters concerning the application of BDS to measure the performance of the sensors are provided in Chapters 4, 5, 6 and 7.

References

- [1] R. T. Blakey, "Development of Dielectric Spectroscopic Resonant Sensors for Biomedical and Industrial Applications," Doctor of Philosophy, Liverpool John Moores University, 2014.
- [2] T. A.-S. Danciu Mihai, Cipriana Stefanescu, Gianina Dodi, Bogdan Ionel Tamba, Cosmin Teodor Mihai, Gabriela Dumitrita Stanciu, Andrei Luca, Irene Alexandra Spiridon, Loredana Beatrice Ungureanu, et al. , "Terahertz Spectroscopy and Imaging: A Cutting-Edge Method for Diagnosing Digestive Cancers," *Materials*, vol. 9, p. 1519, 2019, doi: 10.3390/ma12091519.
- [3] I. Frau, "Microwave and functional materials: a novel strategy for detecting toxic metals in polluted freshwater," Doctor of Philosophy, Liverpool John Moores University, 2020.
- [4] M. S. Sukhdeep Kaur, Jaipreet Kaur, "Dielectric Theory and Its Properties," *International Journal of Emerging Technologies in Engineering Research (IJETER)*, vol. 4, no. 3, pp. 145-150, 2016.

- [5] G. W. Shaohua Qu, Jianwu Fang, Duyang Zang, et al., "Dielectric and Magnetic Loss Behavior of Nanooxides," in *Spectroscopic Methods for Nanomaterials Characterization*, 2017, ch. 301-319.
- [6] A. G. Andrea Vergnano, Carla Maria Raffa, Fulvia Chiampo, Jorge A. Tobon Vasquez, and Francesca Vipiana, "Open-Ended Coaxial Probe Measurements of Complex Dielectric Permittivity in Diesel Contaminated Soil during Bioremediation," *Sensors*, vol. 20, no. 22, p. 6677, 2020, doi: 10.3390/s20226677.
- [7] W. H. H. Woodward, "Broadband Dielectric Spectroscopy—A Practical Guide," in *Broadband Dielectric Spectroscopy: A Modern Analytical Technique*, (ACS Symposium Series, no. 1375), 2021, ch. 1, pp. 3-59.
- [8] M. Muradov, "Prediction of Water Activity in Cured Meat using Microwave Spectroscopy," Doctor of Philosophy, Liverpool John Moores University, 2017.
- [9] R. Schwarz, "Measurement of Dielectric Material Properties," ed, 2012.
- [10] a. G. S. V. R. M.S. Venkatesh, "An overview of dielectric properties measuring techniques," *Canadian biosystems engineering*, vol. 47, no. 7, pp. 15-30, 2005.
- [11] A. G. M. P. Fábio Júlio F Gonçalves, Renato C. Mesquita, Elson J. Silva, and Adriana Brancaccio, "Free-Space Materials Characterization by Reflection and Transmission Measurements using Frequency-by-Frequency and Multi-Frequency Algorithms," *Electronics*, vol. 7, no. 10, p. 260, 2018, doi: 10.3390/electronics7100260.
- [12] R. Dosoudil, "Determination Of Permeability From Impedance Measurement Using Vector Network Analyzer," *Journal Of ELECTRICAL ENGINEERING*, vol. 63, no. 7, pp. 97-101, 2012.
- [13] H. Packard, "S-parameters.... circuit analysis and design," vol. 95, 1968.
- [14] A. M. Christos Sad, Thomas Noulis, and Kostas Siozios, "A Hybrid GA/ML-Based End-to-End Automated Methodology for Design Acceleration of Wireless Communications CMOS LNAs," *Electronics*, vol. 12, no. 11, p. 2428, 2023, doi: 10.3390/electronics12112428.
- [15] R. W. Beatty, "Insertion Loss Concepts," *Proceedings Of The Ieee*, pp. 663-671, 1964.
- [16] B. Walker, "Make Accurate Impedance Measurements Using a VNA," in "Microwaves & RF," 2019.
- [17] A. A. L. G. Guba, A.A. Savin, "Classificaion and Analysis of Vector Network Analyzer Calibration Methods," *Reports of the Tomsk State University of Control Systems and Radioelectronics*, vol. 2, no. 24, pp. 149-155, 2011.
- [18] V. G. G. A.A. Savin, O.N. Bykova,, "Measurement of Electronic Component Impedance Using a Vector Network Analyzer," *Copper Mountain Technologies*.
- [19] T. Lecroy, "SPARQ Signal Integrity Network Analyzer," 2012.
- [20] TestWorld. "Teledyne LeCroy – SPARQ-4004E Signal Integrity Network Analyzer." <https://testworld.com/product/teledyne-lecroy-sparq-4004e-signal-integrity-network-analyzer/> (accessed).
- [21] C. M. Tae-Ho Kang, B. Karaguzel, J. Wilson, P. Franzon, et al., "Sensors on Textile Substrates for Home-Based Healthcare Monitoring," *1st Transdisciplinary Conference on Distributed Diagnosis and Home Healthcare, 2006. D2H2*, pp. 5-7, 2006, doi: 10.1109/DDHH.2006.1624783.
- [22] I. Rosu, "Microstrip, Stripline, CPW, and SIW Design."
- [23] Z. M. H. Papa K. Amoah, Rhonda R. Franklin, Helmut Baumgart, Engelbert Redel, and Yaw S. Obeng, "Broadband Dielectric Spectroscopic Detection of Aliphatic Alcohol

- Vapors with Surface-Mounted HKUST-1 MOFs as Sensing Media," *Chemosensors*, vol. 10, no. 10, 2022, doi: 10.3390/chemosensors10100408.
- [24] T. S. Keiichiro Shiraga, Naoshi Kondo, Takuro Tajima, Masahito Nakamura, Hiroyoshi Togo, Akihiko Hirata, Katsuhiro Ajito, Yuichi Ogawa, "Broadband dielectric spectroscopy of glucose aqueous solution: Analysis of the hydration state and the hydrogen bond network," *The Journal of Chemical Physics*, vol. 142, no. 23, p. 234504, 2015, doi: 10.1063/1.4922482
- [25] G. H. Ting Chen, and Richard Buchner, "Dielectric Spectroscopy of Aqueous Solutions of KCl and CsCl," *J. Phys. Chem. A*, vol. 107, no. 20, pp. 4025–4031, 2003, doi: 10.1021/jp026429p.
- [26] O. K. Daniel Havelka, Jiří Průša, Michal Cifra, "Rational design of sensor for broadband dielectric spectroscopy of biomolecules," *Sensors and Actuators B: Chemical*, vol. 273, pp. 62-69, 2018, doi: 10.1016/j.snb.2018.05.124.
- [27] Y. S. O. e. al, "Low Frequency Radio Wave Detection of Electrically Active Defects in Dielectrics," *ECS Journal of Solid State Science and Technology*, vol. 5, p. P3025, 2016, doi: 10.1149/2.0051604jss.
- [28] M. B. N. G. Orji, B. M. Barnes, C. Beitia, B. D. Bunday, U. Celano, R. J. Kline, M. Neisser, Y. Obeng, and A. E. Vladar, "Metrology for the next generation of semiconductor devices," *Nat Electron*, vol. 1, 2018, doi: 10.1038/s41928-018-0150-9.
- [29] F. G. Christian Heine, Annette Trunschke, Robert Schlögl, Maik Eichelbaum, "The model oxidation catalyst α -V₂O₅: insights from contactless in situ microwave permittivity and conductivity measurements," *Appl. Phys. A*, vol. 112 pp. 289–296, 2013.

CHAPTER 4

THE USE OF ZnO AS SENSING MATERIAL

Part of this chapter is reprinted adaptation from Papa K. Amoah, Pengtao Lin, Helmut Baumgart, Rhonda R. Franklin, Yaw S. Obeng; “Broadband Dielectric Spectroscopic Detection of Volatile Organic Compounds with ZnO Nanorod Gas Sensors,” *Journal of physics D: Applied physics*, vol. 53, no. 13, p. 135104, 2021, doi: 10.1088/1361-6463/abd3ce with permission from IOP Publishing.

4.1 Introduction

Metal-oxide (MO) nanostructures are used in multiple fields, including optoelectronics, microelectronics and gas sensing. In gas sensing applications, most of the MO tend to be II-VI semiconducting metal oxide materials due to their low cost, simple design and ease of production, short response time, wide detection range, and resistance to harsh working environments [1-2]. We have developed and demonstrated the utility of ZnO and ZnO/Al₂O₃ MO nanorods for ethanol detection [3]. However, the intrinsic properties of these MO and their complex point defect physics are not well understood, partly due to tool-measurand interactions because of the electrical techniques used in the characterization. The electrical contacts to the metal oxide devices invariably introduce parasitic artifacts that distort the measurands. Thus, we need non-contact metrology that will enable an unbiased understanding of how these metal oxide devices work; broadband dielectric spectroscopy (BDS) has the potential for probing the intrinsic properties of material systems [4-5].

ZnO is a well-known in gas sensing due to its good inherent electrical properties, wide band gap of 3.37 eV, ≈ 60 meV exciton binding energy at room temperature, high electrochemical- and mechanical stabilities. In general, ZnO based gas sensors tend to work well for ethanol

detection with high sensitivity, short response time, and fast recovery time. However, the state-of-the-art thin film ZnO gas sensors suffer from insufficient sensitivity, long response times, and long recovery times. To address this shortcoming, we synthesized ZnO nanorods (see Fig. 4.1) to increase the surface-to-volume ratio offering significantly increased sensing surfaces. [3]

Mechanistically, when n-type MO semiconductor material, such as ZnO, are exposed to oxygen-rich ambient, oxygen molecules adsorb on the metal oxide moieties, and in a standard oxidation reaction withdraw electrons from the conduction band of ZnO, resulting in a layer of oxygen-negative ions being formed on the surface. This leads to a decrease in its majority carrier density, plus an increase in the width of the depletion region, and the built-in potential barrier on the MO-air interface. This causes the resistance of a MO gas sensor material to increase.

As a standard volatile organic compound (VOC) sensor activation step, the MO solid-state gas sensors need to be heated to their operating temperature. This MO sensor preparation step is typically conducted in ambient air, with oxygen ionic species adsorbing and oxidizing the n-type ZnO surface. In this chemical oxidation reaction, electrons transfer from the conduction band of the semiconducting ZnO nanorod surface into the adsorbed oxygen species, causing a negative charge build-up on the nanorod surface. This, in turn, causes an increase in the depletion width and results in the initial increase of resistance during the sensor preparation step. In the subsequent sensing step, upon exposure to a reducing target gas (in our case ethanol), electrons are injected back into the conduction band, thus restoring the depletion layer with increasing majority carrier density and decreasing the electrical resistance of the MO solid-state sensor device.

Microwave signals are absorbed when inserted into such materials due to the interactions with the intrinsic electrical and magnetic properties of the material, in addition to the changes in the polarizability of the MO-adsorbate interface. In general, the electromagnetic signal-material

interactions result in changes in the signal's characteristics such as attenuation constant and phase constant, used to define the propagation constant, which can be monitored with a 2-port vector network analyzer. Contactless broadband dielectric spectroscopy (BDS) is most advantageous for monitoring reactions involving some degree of charge transfer regardless of the nature of the charge carriers, i.e., electrons and holes [6]. This makes BDS an ideal method for monitoring gas-sensing reactions, especially volatile organic compounds (VOC) interactions with metal-oxides, since they involve reversible charge transfer reactions that result in measurable changes in the electrical properties of the sensing element such as the ac impedance [7-8]. In this work, we demonstrate the feasibility of the BDS, as an alternative technique, and use it to investigate the sensor activation step for VOC detection with our ZnO nanorod materials.

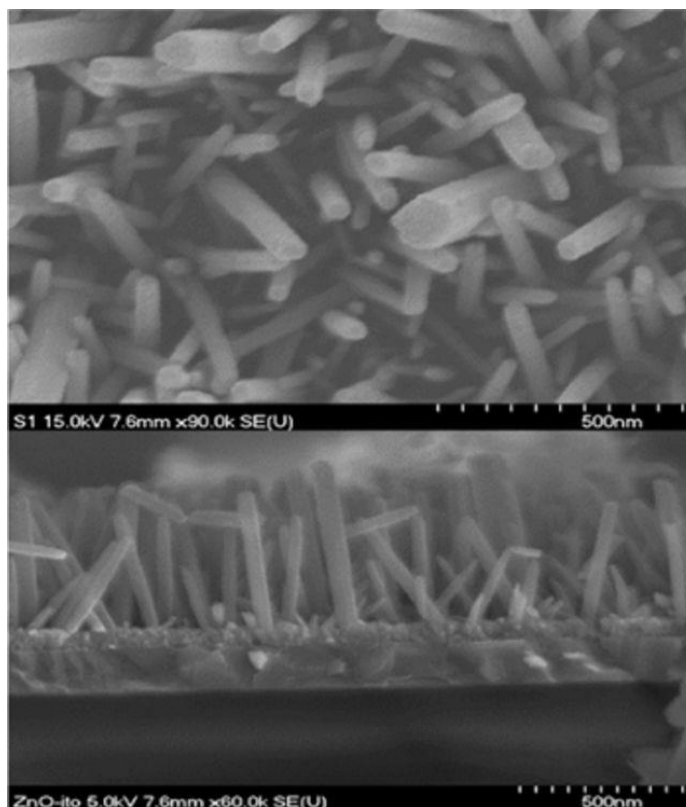


Figure 0.1. Planar view and Cross-sectional FE-SEM images of intrinsic ZnO nanorods highlighting the fine grain polycrystalline ALD ZnO seed layer underneath and the resulting morphology of a dense array of ZnO nanorods (adapted from Reference 3).

4.2 Experimental

For this study, the MOS solid-state gas sensor device consisted of hydrothermally synthesized ZnO nanorods grown on a fine grain ZnO seed layer fabricated by atomic layer deposition (ALD) on a highly doped p-type silicon substrate [3, 8]. We note that the resistivity of the substrate is not critical to the ZnO growth. The ZnO samples were used as-received, and 1 ml of target gas (analytical grade ethanol, C_2H_5OH , EtOH) was injected into the reactor via a long-needled hypodermic syringe as needed.

Because of the low resistivity of the silicon substrate, the sample chip (4.5 mm wide by 9 mm length) was insulated from the 50 Ohm ground-signal-ground coplanar waveguide (CPW) by a 0.2 mm thick precleaned glass microscope slide coverslip (24 mm by 24 mm) to prevent shorting the signal lines as shown in Figure 4.3. The sample-CPW assembly was situated in a thermally heated Pyrex tube, with porous endcaps, that allowed us to independently control the environment around the ZnO nanorods, as shown in Figure 4.2. The temperature of the assembly was manually controlled with a power supply from room temperature to approximately 120 °C; the heater was turned off after about 26 min. Both the S-parameters in the 0.1 GHz to 20 GHz range and the temperature were measured every 30 s.

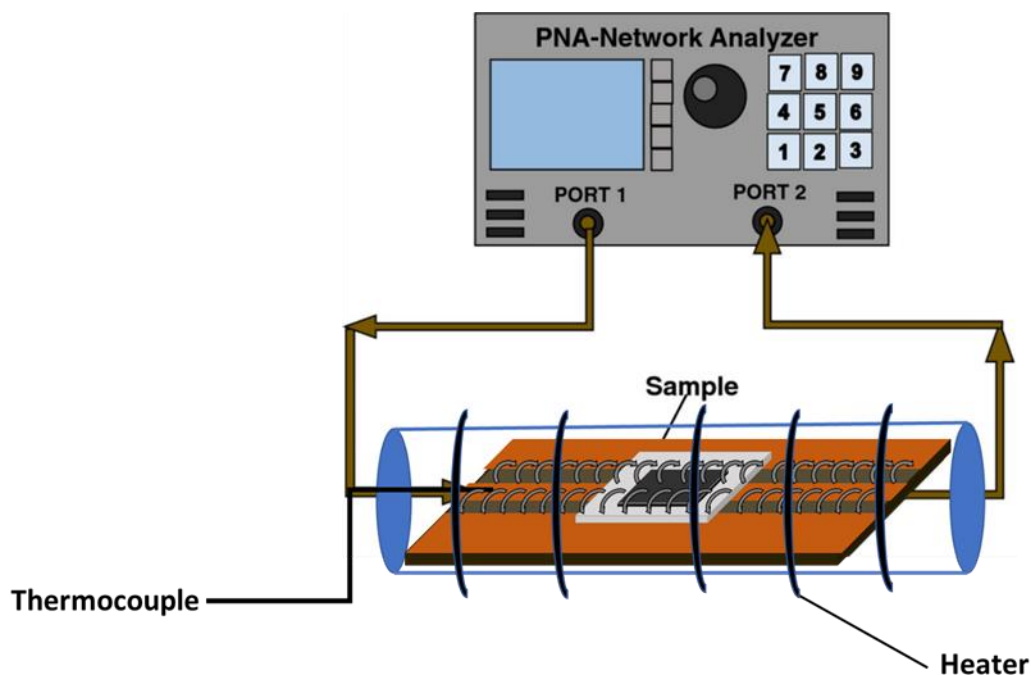


Figure 0.2. A schematic representation of experimental setup used in this study showing the ZnO sample on a ground-signal-ground (GSG) waveguide situated in a controlled environment (Pyrex tube).

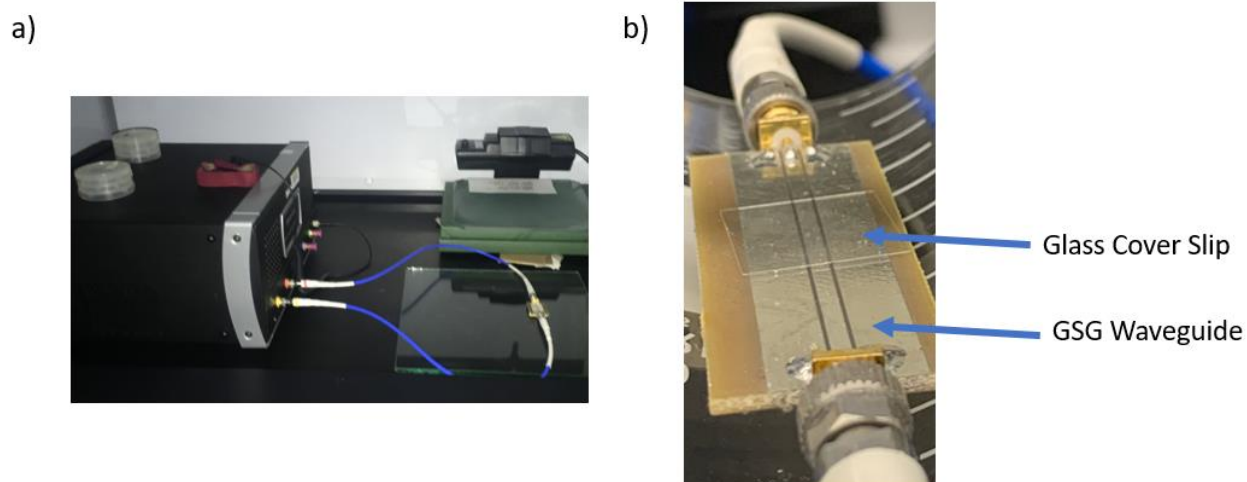


Figure 0.3. Images of a) BDS instrumental arrangement, and b) a zoomed-in view of the waveguide with the cover slip on top of it.

The CPW was fabricated from a tin-covered printed circuit board (RF4, 61 mm long, with 5 mm wide ground lines separated from the 1.5 mm wide signal line by 1.2 mm gaps). The cables to the VNA were connected to the CPW with edge mount connectors (Amphenol RF SMA). This configuration effectively converts the coaxial mode signal into microstrip mode propagating towards the device under test (DUT). The cables connecting the CPW were de-embedded, with a 2-port short-open-load-through (SOLT) calibration in which the calibration standards were attached to the end of the feed cables, i.e., the reference plane of the measurement was moved from the port faces of the VNA to the connector/cable interface. Thus, the launch connectors and CPW itself were part of the device under test (DUT), and the reported S-parameters are those resulting from experimental perturbations to the DUT. In this configuration, the ZnO gas sensing element perturbs the electric fields emanating from the signal and terminating on ground lines in the CPW. While the system response in a broadband (0.1 GHz to 20 GHz) range was monitored, a reporting

frequency of 6 GHz was chosen based on the sample dimensions and the fact that it provided data free of resonances and minimized signal reflections due to the experimental setup [9].

4.3 Results and Discussion

In the following discussion of the results, elapsed time and reactor temperature are the independent variables. Figure 4.4 shows the time evolution of the reactor temperature, measured with a thermocouple attached to the RF cable from the VNA port-1 and hovering over the GSG waveguide, as shown in Figure 4.2. Thus, the changes we observe in the S-parameters are both temperature and time-dependent. The data from the 10-24 minutes time window represent the steady temperature state, any observed changes in that time window is time dependent.

Figures 4.5 and 4.6 show a phenological and an electrical equivalent circuit model without the host silicon substrate, respectively, of the ZnO nanorods under microwave interrogation in a gaseous ambient during the oxidative sensor preparation step as used in this study. In Figure 4.5 we distinguish three electrically distinct zones: the residual core ZnO nanorod (ϕ_{bulk}), the depletion layer (ϕ_{d}) around the core ZnO due to the adsorption of polarizable electroactive gaseous species from the ambient onto nanorods, and the adsorption layer (ϕ_{ads}) comprised of a complex mix of negatively charged species confined to the surface of the nanorods. In Figure 4.5 the quantities R_{bulk} , C_{bulk} and the ϕ_{bulk} are the residual resistance, capacitance, and diameter, respectively, of the bulk ZnO nanorod after the depletion layer formation, while R_{d} , C_{d} , and ϕ_{d} are the resistance, capacitance and diameter (strictly, the arc length because of radial length of the electric fields associated with the GSG waveguide), respectively, of the depletion layer, while the R_{ads} , C_{ads} and ϕ_{ads} are the characteristics of the adsorption layer formed due to the adsorption of electroactive

gaseous species on the ZnO nanorods. The electrical elements in Figure 4.6 are related to features in Figure 4.5 by equations 1 and 2 below. C_{ads} , C_{bulk} , are to be determined experimentally.

$$R_{bulk} = K\phi_{bulk}, \text{ where } K \text{ is a constant} \quad (1)$$

Note that R_{bulk} is not constant; it is only a constant before the start of the oxidative sensor preparation step. As soon as negative charge accumulates on the surface, the ZnO nanorods surface become depleted. Instead, the growing depletion width is restricting the available conducting bulk cross-section and causing an increase in the dc resistance. As we modulate the depletion width, we automatically increase R_{bulk} by progressively reducing the bulk ZnO nanorod cross-section.

The negative oxide charge on the surface following the preparation step can be regarded as wrap-around gate charge surrounding the semiconducting ZnO nanorod cylinder. Thus, the depletion capacitance in a semiconductor cylinder is given. Using the standard formula for capacitance of coaxial cylinders gives:

$$C_d = 2\pi \epsilon \epsilon_o / \ln(r_2/r_1) \quad (4.2)$$

where ϵ is the silicon dielectric constant, ϵ_o is the vacuum permittivity and r_1 , r_2 are the inner and outer radii of the depletion region, respectively [10].

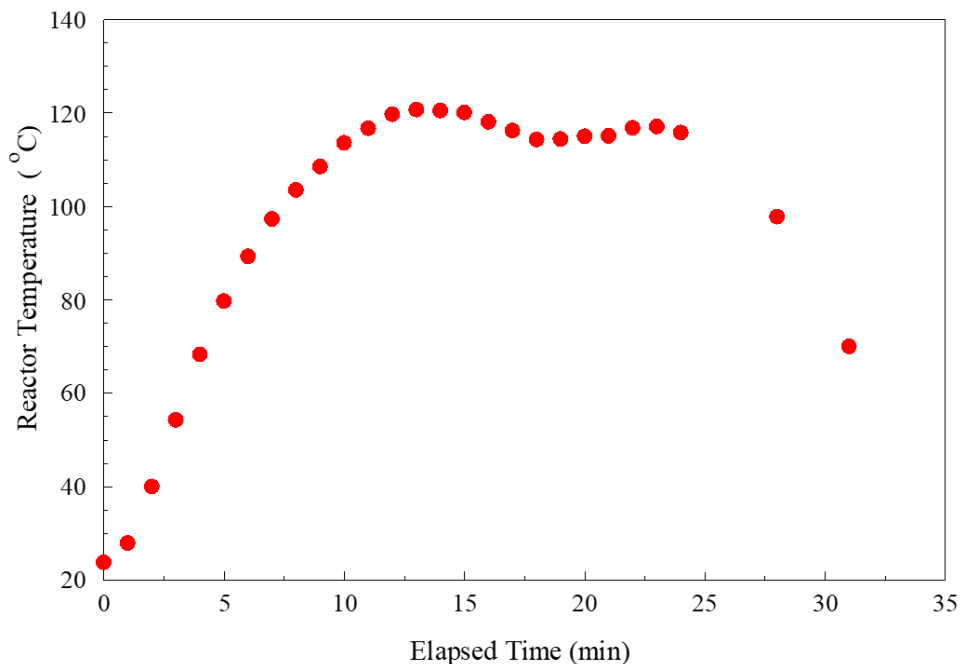


Figure 0.4 The time evolution of the reactor temperature during the experiments described in this work.

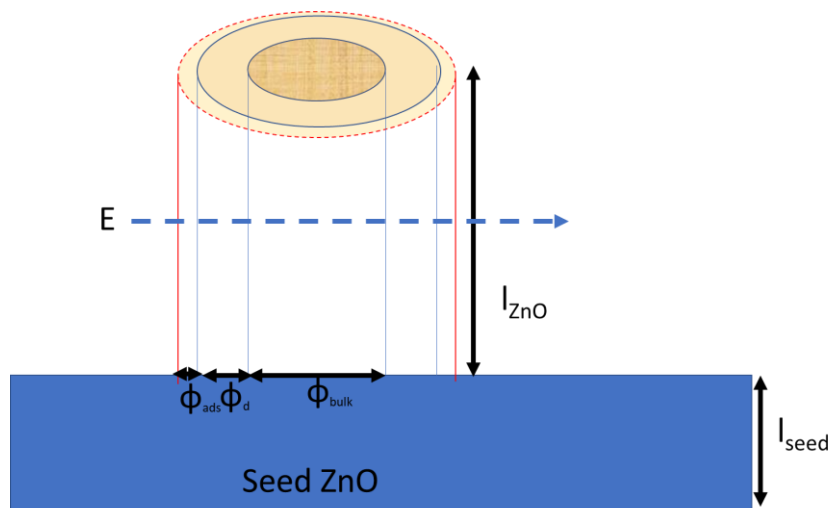


Figure 0.5. A phenomenological model of a ZnO nanorod under microwave interrogation in a gaseous ambient during sensor preparation step, where adsorbed oxygen species cause a negative charge build-up on the nanorod surface as used in this study. E is an electric field fringe from the microwave emanating from the signal line and terminating on the ground line of the GSG coplanar waveguide, l_{ZnO} is the mechanical length of the nanorod, while ϕ_{bulk} , is the diameter of the bulk, and ϕ_d is the depletion layer thickness of the ZnO nanorod, respectively. It is important to note that the seed ZnO layer thickness is exaggerated for illustrative purposes in Figure 4.5; it is very small compared to the length of the ZnO nanorods as seen in the cross-sectional SEM micrograph of Fig.1.1.

In the experimental configuration we used, the ZnO nanorods were interrogated by the interaction of the electric fields emanating from the signal line and terminating on the ground lines of the coplanar waveguide. Given the thicknesses of the glass cover slip, silicon substrate and the ZnO seed layer, the electric fields reaching the nanorods can be approximated as a planar field (although in reality it is actually an arc length / segment). With this approximation, the microwave insertion loss (i.e., S21) measures the fraction of energy that is transmitted from the source to the detector through the device under test (DUT, i.e., ZnO sample). With proper calibration, the S21 amplitude can be correlated to the total impedance of the GSG waveguide, the glass cover slip and ZnO/Si device. Thus, we can use the S21 magnitude as an index to the changes in the DUT in response to external perturbation.

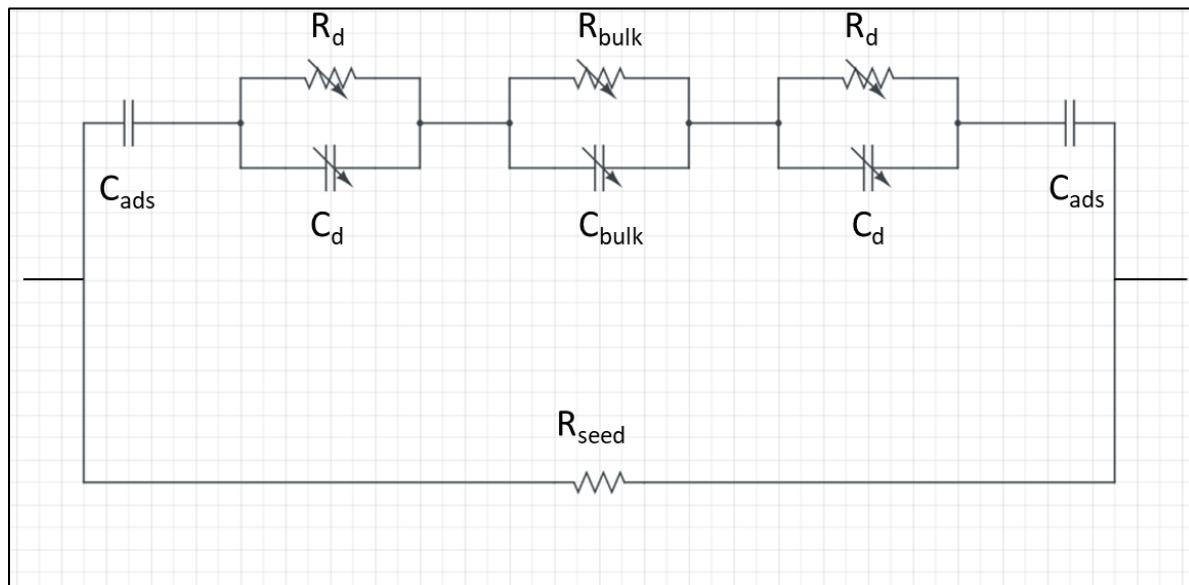


Figure 0.6. An electrical equivalent circuit model of the ZnO nanorod configuration in Figure 4.5 as used in this study. Note that inductance has been excluded from the seed layer representation.

With reference to Figure 4.6, the total impedance is the sum of the bulk ZnO resistance and reactance of the interfaces. The latter is mostly due to the variable capacitances of all the interfaces, as identified in Figure 4.5, and as described by Equation 3. Analysis of the BDS data (at specific frequencies) provides electrical information that can be correlated to elementary processes, such as charge-transfer reactions involving the point defects in the ZnO material, and adsorbed molecules from the gaseous environment [11].

$$X = \frac{1}{2}\pi f C_s \quad \sim \quad \frac{L}{A} \left[\frac{1}{2} f \epsilon_0 \epsilon' \rho^2 \right] \quad (3)$$

X is the reactance, where C_s is the total series capacitance of the interfaces between the bulk-ZnO and the depletion layer, the interface between the depleted area and the adsorbed ambient species interface, and the interfaces between the overlayers of ambient species within the adsorbed layer, ρ is the resistivity of the interfacial layer (assuming the layer is mechanically very thin), f is the frequency, L is the length, ϵ' is the effective permittivity of all the interfacial layers, as shown in Figures 4.5 and 4.6, and ϵ is the permittivity of free space.

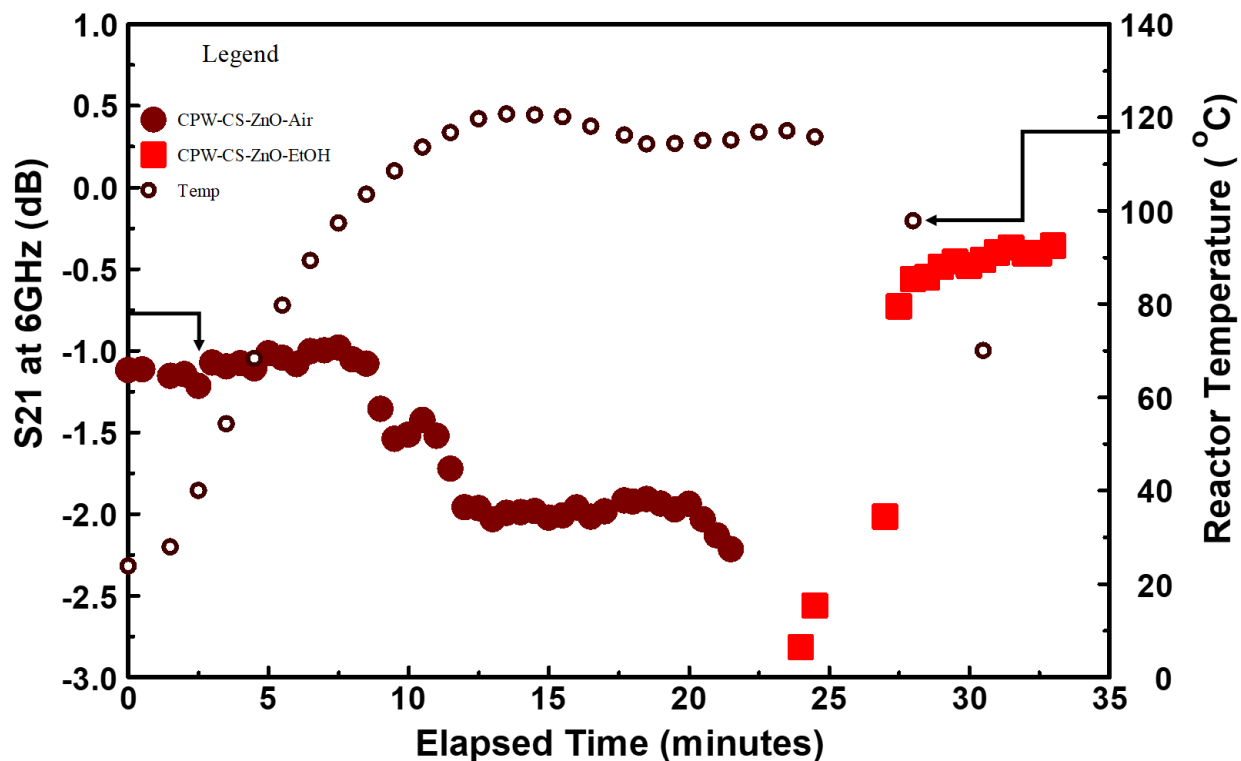


Figure 0.7. Temperature dependence of microwave insertion loss (S21 amplitude) of ZnO on Si in air and in alcohol gaseous environments, monitored at 6 GHz as a function of elapsed time.

Figure 4.7 shows the time evolution of temperature at 6 GHz in our experimental setup. The S21 amplitude was stable below 100 °C, while the system became less resistive at above that temperature. This suggests that, in air, the impedance was relatively high at temperatures below 100 °C and decreased with temperature in a series of discrete steps within the temperature range of 100 °C to 140 °C, as shown in Figure 4.7. These changes could be attributed to the temperature dependence of the intrinsic semiconductor resistivity of the ZnO-silicon substrate combination, at temperatures above 100 °C. Indeed, the observed reduction of system impedance with increasing temperature is consistent with the well-characterized ZnO resistance decrease with increasing temperature at temperatures below 200 °C due to the temperature dependence of the resistive

metal-oxide semiconductor such as ZnO in the 100 °C to 200 °C temperature regime [12-14]. However, the discrete nature of the impedance transitions indicates contributions from other phenomena besides resistivity changes due to the mobility of carriers in the ZnO nanorods. The stepped impedance change with increasing temperature could be due to differences in the temperature dependence of resistivity in the ZnO seed layer and the nanorods, due to the differences in crystallography and defect densities in the two ZnO allotropes [15]. The interface capacitances, as shown in Figure 4.5, could also contribute to the observed impedance changes. This is supported by the impact of ethanol vapor on the impedance change in Figure 4.7. The ethanol molecules could adsorb on, and react through a redox reaction with, the pre-existing oxygen adsorbed layer on the ZnO nanorod surface to alter the electronic structure of the adsorbed layer in Figure 4.5. We suggest that the stepped impedance changes with increasing temperature have contributions from events at the interfaces, possibly involving the adsorption / desorption and speciation of molecules from the ambient on the ZnO rods. The system became more resistive when ethanol was injected into the reactor at the 24-minute time stamp, i.e., the impedance of the ZnO was relatively higher in the ethanol environment than in air. In our experiment, the introduction of ethanol resulted in a reactor temperature drop, due to energy consumed in the analyte's evaporation that could not be compensated for due equipment constraints. The changes in the insertion loss may not be due to ethanol's interaction with the ZnO, as the reactor temperature may be too low.

Alternatively, the steps in the microwave insertion loss (S_{21} amplitude) response may be simply due to the thermal characteristics of the GSG waveguide as shown in Figure 4.8. The RF4 substrate used for GSG waveguide fabrication has a glass transition temperature (T_g) of 115 °C to 200 °C and may undergo structural deformation at the temperatures used in this work. The

alternative explanations for the observed impedance changes with temperature and ambience will be fully resolved in future work.

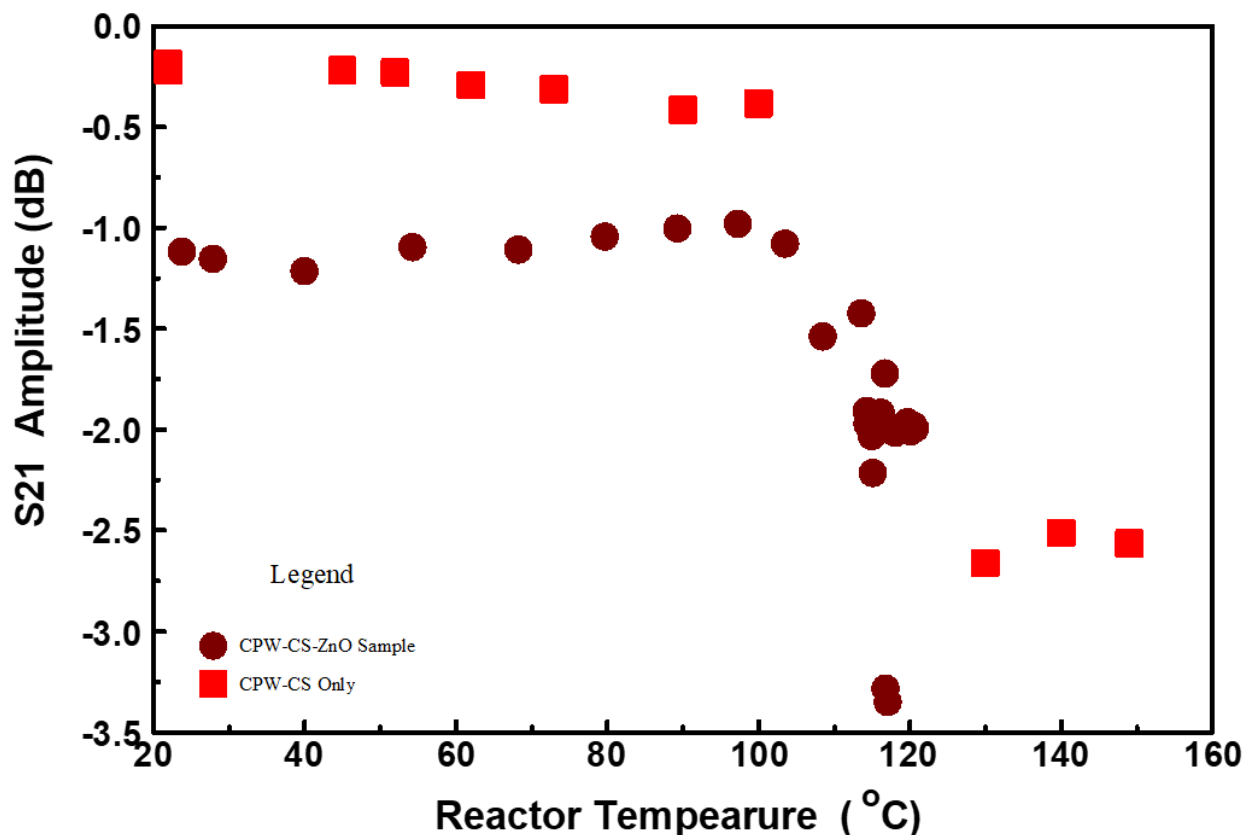


Figure 0.8. Comparison of the temperature dependence of microwave insertion loss (S_{21} amplitude) of the waveguide-cover glass stack with / without the ZnO/Si sample in air monitored at 6 GHz.

We quantified energy dissipation into the ZnO material by calculating the microwave attenuation constant (i.e., the real part of the microwave propagation constant) by numerical RLCG modeling using a custom MATLAB (MathWorks, Natick, MA) code to process the raw S-

parameter data [16]. Figure 4.9 presents a flow diagram delineating the process by which raw data undergoes conversion into RLGC values and subsequent exportation for visualization.

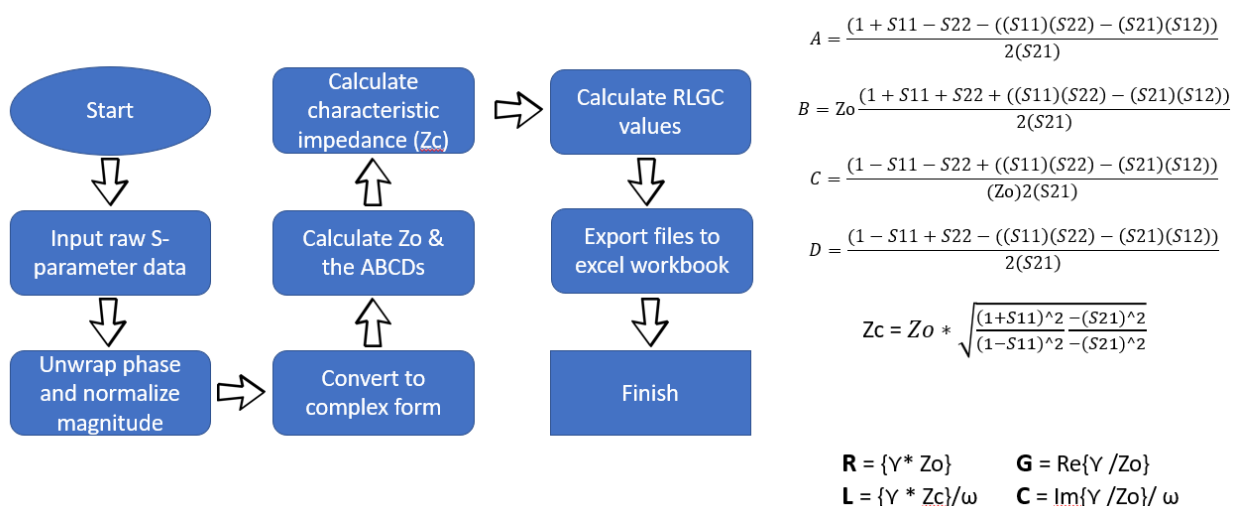


Figure 0.9. Flow diagram illustrating the conversion process of raw data into RLGC values.

The attenuation represents the total microwave signal losses probably due to the reorientation of electric dipoles of the charge transfer adducts on the MO surface. The changes in attenuation constant give us indications of changes in the chemical and electrical properties of the MO material matrix, especially when polar defects are generated during the experiments. As shown in Figure 4.10, the attenuation constant depends on the reactor temperature and the gaseous environment; the attenuation constant was higher in the ethanol environment but converged to that of the air at temperatures below 100 °C. In any event, the attenuation data clearly indicates that the impedance changes on the ZnO samples are reversible within the temperature range of our current experiments, and that the impedance modulates in response to interfacial events, including possible redox reactions occurring on the ZnO nanorod surfaces [11]. It is remarkable, that we observe

these impedance changes in the 100 °C to 120 °C temperature range, associated with the sample activation step, well below the optimum direct current resistance sensing temperature of around 320 °C [3, 8].

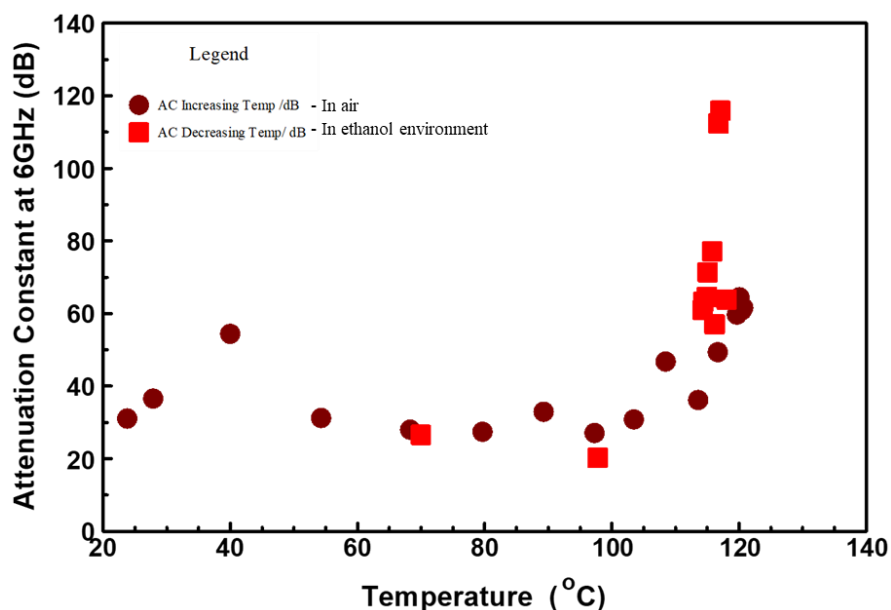


Figure 0.10. A comparison of the temperature dependence of microwave attenuation constant of ZnO on Si in air only and with air-ethanol vapor mixture present in the reactor environments, monitored at 6 GHz. The data suggest that the attenuation constant is independent of the gaseous environment in the temperature regime used in this work.

In air at least two competing processes impact the resistance of the ZnO sample. Atmospheric water chemisorbs and dissociates on the ZnO surface to form hydroxyl (OH^-) ions on the surface, and directly introduce electrons into the conduction band to increase the conductivity of the n-type sensor. Ambient oxygen also adsorbs on the MO surface initially as O^- and slowly transforms into O^{2-} , at temperatures around 100 °C, through the acquisition of electrons from the ZnO surface, thereby removing electrons from the conduction band of the n-type semi-

conductor [17]. There is ample evidence in the literature to suggest that the homolytic dissociation of water and the subsequent electron transfer reactions on the surface dominate in air ambient leading to net reduction of the ZnO resistance [18]. Such changes in surface polarization are readily detected by BDS. The ZnO nanorod samples used in this work have very large surface areas relative to their volume and can adsorb large quantities of gaseous species to form polarons on the surface [15-16]. When exposed to microwaves, at temperatures above 100 °C, the polarons appear to fluctuate, thus dissipating the microwave energy through dipolar relaxation [20]. In the temperature regime of this work, the resistance increase from the depletion of the carriers from the ZnO surface can be neglected, so the energy dissipation from the polarons on the ZnO surfaces dominates the observed impedance change. Thus, the impedance we measured by BDS on the ZnO nanorods is probably predominantly due to dielectric relaxation, with a small contribution from the conductivity due to carrier concentration. The observed impedance changes are attributable to the discrete charge transfer events occurring in the ZnO sensing surface in response to various environmental conditions at temperatures above 100 °C.

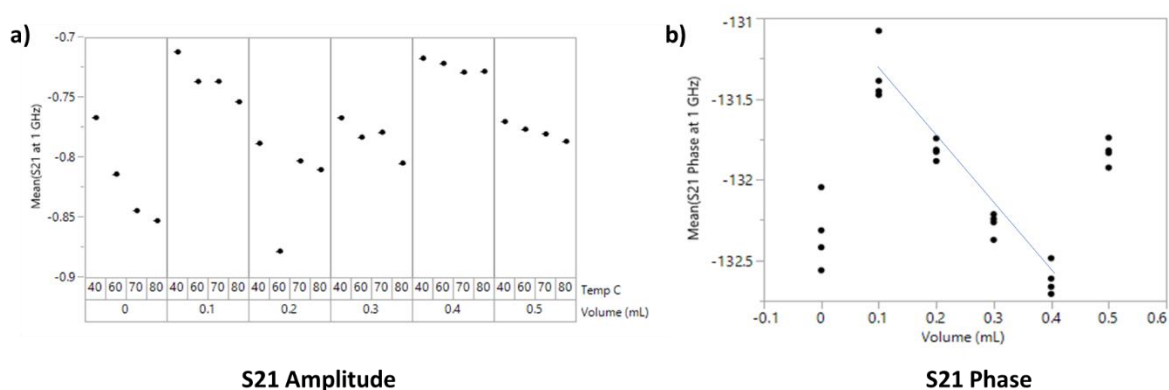


Figure 0.11. The real part of the S_{21} data, denoted as the S_{21} amplitude, positioned on the left, and the imaginary part, known as the S_{21} phase, located on the right where the four data points at volume indicate measurements at the four temperatures (40, 60, 70, 80 °C in ascending order).

Upon closer examination of the S_{21} data and its variations under different conditions, the data was segregated into two distinct components (Figure 4.11): the real part, denoted as the S_{21} amplitude, and the imaginary part, known as the phase. Figure 4.11a shows a three-dimensional plot illustrating the correlation between the S_{21} amplitude, temperature, and the volume of injected ethanol. Starting from the initial data point at 0 (prior to ethanol addition), the S_{21} value diminishes with increasing temperature, indicating heightened resistivity within the system and a subsequent reduction in stored energy, a phenomenon associated with the formation of the depletion layer. Upon ethanol introduction, the system initially exhibits reduced resistivity, with the S_{21} decreasing uniformly across all temperatures. Subsequently, the S_{21} value diminishes proportionally with ethanol concentration until reaching approximately 0.4 ml, beyond which the system's responsiveness plateaus, indicative of non-linearity. This behavior suggests the occurrence of chemical redox reactions driving electrons into the conduction band, concurrent with ethanol adsorption at the surface, thereby increasing the adsorbed layer. Two reactions ensue: an increase in the adsorbed layer with temperature and a chemical reaction facilitating electron transfer to the conduction band, thereby reducing resistance/impedance with rising temperature.

A noteworthy observation is seen in the phase behavior (Figure 4.11b), which irrespective of temperature, exhibits a linear decrease as ethanol concentration increases. Above 0.4 ml, just like the amplitude, the phase enters a distinct regime. Initially, at 0 volume, the phase reflects the adsorbed oxygen layer on the nanorod's surface. Upon ethanol introduction, which adsorbs onto the existing oxygen layer, a reduction in phase occurs relative to volume, until saturation around 0.5 ml, leaving the system unresponsive to further changes in ethanol concentration.

The variation in phase data with temperature underscores its sensitivity to the underlying chemistry. Alterations in ethanol concentration on the surface affect the ZnO's conductivity, thereby influencing the phase. In contrast, the amplitude, being related to material permittivity, offers insight into the system's dielectric properties.

Moreover, the phase's strictly linear dependence on ethanol volume presents calibration opportunities for accurate ethanol concentration detection, with potential applications in device development. Consequently, we have filed a patent disclosure for this technology (Appendix D).

4.4 Conclusions

Using microwave signal attenuation, we have demonstrated physics consistent with increasing conductivity of the semiconductor ZnO with increasing temperature during the sensor activation step in the 100 °C to 120 °C range. However, the semiconductor behavior is perturbed by depletion layer thickness modulation and charge transfer to the gaseous species adsorbed on the ZnO nanorod sensing element. The charge transfer reactions create polarized species on the ZnO nanorod, and fluctuations of the polarons dominate the impedance of the ZnO. Further, the S_{21} data was analyzed, and separated into two components: the S_{21} amplitude and phase. Changes in S_{21} amplitude with temperature and ethanol volume indicated alterations in system resistivity, while phase exhibited a linear decrease with ethanol concentration, suggesting potential for calibrated ethanol detection, highlighting its sensitivity to underlying chemistry and conductivity variations. Thus, the BDS technique affords new mechanistic insights into the elementary events that occur on the ZnO surface during the initial activation step for ethanol detection.

References

- [1] A. Mirzaei, S.G. Leonardi, G. Neri, Detection of hazardous volatile organic compounds (VOCs) by metal oxide nanostructures-based gas sensors: A review, *Ceramics International*, 42, 14, 15119- 15141, 2016 <https://doi.org/10.1016/j.ceramint.2016.06.145>.
- [2] A. Umar and Y. B. Hahn (Eds.). *Metal Oxide Nanostructures and their Applications*. American Scientific Publishers, CA, USA, (2010)
- [3] Lin, Pengtao. "Enhanced Sensing Performance of Novel Nanostructured ZnO Gas Sensors in Ethanol Vapor Concentration Detection Applications" (2019). Doctor of Philosophy (PhD), Dissertation, Electrical/Computer Engineering, Old Dominion University, DOI: 10.25777/j9r7-vs61
- [4] Orji, N.G., Badaroglu, M., Barnes, B.M. et al. Metrology for the next generation of semiconductor devices. *Nat Electron* 1, 532–547 (2018). <https://doi.org/10.1038/s41928-018-0150-9>
- [5] Y. S. Obeng et al, Low Frequency Radio Wave Detection of Electrically Active Defects in Dielectrics, *ECS J. Solid State Sci. Technol.* 5 P3025, 2016 <https://doi.org/10.1149/2.0051604jss>
- [6] A. M. Wernbacher et al, Operando Electrical Conductivity and Complex Permittivity Study on Vanadia Oxidation Catalysts, *J. Phys. Chem. C* 2019, 123, 8005–8017, DOI: 10.1021/acs.jpcc.8b07417
- [7] H.-J. Kim, and J.-H. Lee, “Highly sensitive and selective gas sensors using p-type oxide semiconductors: Overview”, *Sensors and Actuators B* 192 (2014) 607– 627
- [8] P. Lin, X. Chen, K. Zhang, and H. Baumgart “Improved Gas Sensing Performance of ALD AZO 3-D Coated ZnO Nanorods”, *ECS Journal of Solid-State Science and Technology*, 7 (12) Q246-Q252 (2018)
- [9] Papa K. Amoah, et al., “Microwave Monitoring of Atmospheric Corrosion of Interconnects”, *ECS J Solid State Sci Technol.*, 2018; 7: 10.1149/2.0181812jss., doi: 10.1149/2.0181812jss
- [10] Garnett, E., Tseng, Y., Khanal, D. et al. “Dopant profiling and surface analysis of silicon nanowires using capacitance–voltage measurements.”, *Nature Nanotech*, vol. 4, pp. 311–314, 2009 <https://doi.org/10.1038/nnano.2009.43>
- [11] C. Heine, F. Girgsdies, A. Trunschke, R. Schlögl, and M. Eichelbaum, “The model oxidation catalyst α -V₂O₅: insights from contactless in situ microwave permittivity and

- conductivity measurements”, *Applied Physics A*, vol. 112, pp. 289–296, 2013 DOI 10.1007/s00339-013-7800-6
- [12] P. T. Mosely and B. C. Tofield, *Solid State Gas Sensor*, Adam Hilger, Bristol and Philadelphia, 1987
- [13] Yongki Min, “Properties and Sensor Performance of Zinc Oxide Thin Films”, Thesis submitted to the Department of Materials Science and Engineering in Partial Fulfillment of the Requirements for the Degree of Doctor of Philosophy in Electronic, Photonic, and Magnetic Materials at the Massachusetts Institute of Technology, September 2003,
- [14] S. Zhang, H. Byun, J. Lim, J. Huh and W. Lee, "Controlled Synthesis of ZnO Nanostructures for Sub-ppm-Level VOC Detection”, *IEEE Sensors Journal*, 12, 11, pp. 3149-3155, 2012, doi: 10.1109/JSEN.2012.2208950.
- [15] Wisz, G., Virt, I., Sagan, P. et al. Structural, Optical and Electrical Properties of Zinc Oxide Layers Produced by Pulsed Laser Deposition Method. *Nanoscale Res Lett* 12, 253 (2017). <https://doi.org/10.1186/s11671-017-2033-9>
- [16] C. E. Sunday et al, “Broadband Dielectric Spectroscopic Characterization of Thermal Stability of Low-k Dielectric Thin Films for Micro- and Nanoelectronic Applications”, *ECS J Solid State Sci Technol.*, 2017; 6(9): N155–N162, doi:10.1149/2.0141709jss
- [17] T. I. Barry and F. S. Stone, “The Reactions of Oxygen at Dark and Irradiated Zinc Oxide Surface”, *Proceedings of the Royal Society of London, Series A, Mathematical and Physical Sciences*, 1960, 255, 1280, 124-144
- [18] Z. Bai, C. Xie, M. Hu, S. Zhang, D. Zeng, "Effect of humidity on the gas sensing property of the tetrapod-shaped ZnO nanopowder sensor", *Materials Science and Engineering: B*, 149, 1, 2008, pp 12-17, <https://doi.org/10.1016/j.mseb.2007.11.020>.
- [19] Mario Maglione, “Free charge localization and effective dielectric permittivity in oxides”, *Journal Of Advanced Dielectrics*, 6, 2, (2016) 1630006, DOI: 10.1142/S2010135X16300061
- [20] Mario Maglione. “Polarons, free charge localisation and effective dielectric permittivity in oxides”. V.S. Vikhnin and G. K. Liu. Springer Series of Topics in Solid-State Sciences, Springer Verlag, (2010), Topics in Solid-State Sciences. fhal-00493298f

CHAPTER 5

METAL-DOPED ZnO AS THE DETECTION ELEMENT

5.1 Introduction

Chapter 2 provided an overview of doping in ZnO and discussed the advantages provided in various applications. The purpose of this chapter is study transition-metal doped ZnO nanorods, specifically doping with Cobalt (Co), as well as the coinage metals silver (Ag) and gold (Au) in order to improve the gas response of the sensor. Introducing impurities into the ZnO structure is done to change its electronic characteristics by adjusting the bandgap and affecting the density of charge carriers, which in turn influences its conductivity [1].

Transition metals are commonly applied to the surface of MOS materials, serving as sites for adsorbates, catalysts, or promoters for surface reactions. They also contribute to enhancing the thermodynamic stability of nanostructured materials [2]. When transition metals are doped into ZnO, they adjust the energy levels and surface states, leading to changes in electrical, optical, and magnetic properties [3]. Co, as a transition metal, is frequently utilized as a surface modifier known to enhance gas sensing capabilities. Being a relatively cost-effective noble metal, Co^{2+} ions are promising candidates for successful doping and are compatible with Zn^{2+} ions. Co^{2+} ions also exhibit higher solubility within the ZnO matrix compared to other dopants. Moreover, Co doping introduces morphology regulation and active sites into ZnO. Hence, Co-doping offers several desirable properties at various levels [4]. Coinage metal nanostructures have remarkable

properties, including catalytic, electrical, optical, and chemical properties. These properties are influenced by the size and shape of the nanostructures, making them highly interesting for development and exploration of potential applications.

Doping ZnO with Ag and Au, affords some notable distinctions compared to doping with other transition metals; the Ag and Au dopant atoms tend to occupy both interstitial and substitutional sites within the lattice. In contrast, most other transition metal dopant atom typically only occupies interstitial sites which limits the dopant concentrations that are achieved within the lattice. The distinctive doping behavior of Ag and Au in ZnO can bring about significant modifications in the material's optical, electrical, and structural properties. For example, introducing Ag can enhance its optical absorption while Au doping can elevate the material's catalytic activity. Overall, the distinct characteristics of coinage metal nanostructures combined with their unique doping behavior in ZnO offer great potential for various applications [1].

Yousefi et al. [5] reported that the doping of ZnO with silver improved its sensitivity and selectivity towards ethanol detection, due to the catalytic effects of the silver dopant [1]. Meanwhile, Deshwal et al. [6] showed that ZnO thin films doped with 3% Au can act as an acetone sensor, with significantly higher sensitivity and faster response and recovery times at a lower optimal working temperature compared to undoped ZnO thin films. Further analysis showed that at a concentration of 500 ppm acetone vapors and a temperature of 280°C, the Au-doped ZnO thin films demonstrated notably superior response compared to undoped ZnO thin films. The addition of Au to ZnO significantly enhanced sensing responses, leading to shorter response and recovery durations[1].

The objective of this study was to produce ZnO nanorods by incorporating transition metals like Co and coinage metals such as Ag and Au. Efforts to dope our ZnO nanorods with other metals

like Cu and Pt were unsuccessful; the ZnO nanorods were damaged during the doping processes, rendering them unsuitable for sensing applications.

5.2 Experimental Details

5.2.1 Chemicals and materials

A thin ZnO seed layer with nano-sized crystals was uniformly deposited onto a highly doped p-type silicon substrate using atomic layer deposition (ALD). The ALD process involved the use of diethyl zinc (DEZ, $\text{Zn}(\text{C}_2\text{H}_5)_2$) with a .015 sec pulse time and water vapor (H_2O) with a .015 sec as chemical precursors, which were introduced alternately into the chamber by N_2 carrier gas flow (20 Sccm). The polycrystalline ZnO seed layer was grown at 200°C and controlled to a thickness of 30 nm. Subsequently, it underwent annealing at 350°C for 30 minutes in ambient atmosphere.

Subsequently, an in-situ hydrothermal process was utilized to produce Co-doped ZnO nanorods. A solution comprised of 0.07437 g of zinc nitrate hexahydrate ($\text{Zn}(\text{NO}_3)_2 \cdot 6\text{H}_2\text{O}$), 0.088 g of hexamethylenetetramine ($(\text{CH}_2)_6\text{N}_4$), and .0727g of Cobalt(II) nitrate hexahydrate ($(\text{NO}_3)_2 \cdot 6\text{H}_2\text{O}$) was dissolved in 100 ml deionized water. The prepared ZnO seed layers were sealed in an autoclave in the solution and incubated at 90°C for 16 hours.

For the doping of Ag and Au, a similar hydrothermal synthesis process was employed after the pristine ZnO nanorods were synthesized. The doping solution comprised of 0.07437 g of zinc nitrate hexahydrate ($\text{Zn}(\text{NO}_3)_2 \cdot 6\text{H}_2\text{O}$) and 0.088 g of hexamethylenetetramine ($(\text{CH}_2)_6\text{N}_4$) dissolved in 100 ml deionized water. Then the prepared ZnO seed layers were sealed in an

autoclave along with the reaction solution at 90 °C for 16 hours. The ZnO surface was subsequently doped with Au and Ag nanoparticles.

For the preparation of self-assembled gold nanoparticles, an HAuCl_4 solution (1 mL of 1% in 100 mL water) was boiled with vigorous stirring, followed by the rapid addition 4 mL of 1% sodium citrate solution. The solution was then boiled for another 20 min until it turned wine red, indicating the formation of citrate stabilized reduced gold nanoparticles [7]. Similarly, Silver nanoparticles were synthesized using silver nitrate to create a 1 mM aqueous precursor solution, which was then reduced using 250 μL of a fresh aqueous solution of 180 mM sodium borohydride (NaBH_4) in the presence of the capping agent beta-cyclodextrin. The resulting silver solution was stirred for two hours to facilitate nanoparticle formation [8]. These nanoparticles were deposited uniformly on the surface of hydrothermally formed ZnO nanorods resulting in 2–3 nm nanoparticles on their surface [9].

5.2.2 Characterization

The morphological characterization of the as synthesized doped ZnO nanorods was performed by scanning electron microscopy (SEM, JEOL JSM-6060LV) with an acceleration voltage of 15 kV. The elemental analysis of the nanorods was performed by energy-dispersive X-ray spectroscopy (EDS) using a solid-state detector attached to the SEM. The Raman spectra were recorded at room temperature on a LabRAM HR Evolution confocal microscope (HORIBA JOBIN–YVON) using laser light excitation at 473 nm and equipped with a Synapse Plus detector. Gas sensing performance were done in a similar fashion as was explained in Chapter 4 with the undoped ZnO. The sensitivity studies were carried out over different concentrations of ethanol gas

from 0 ml to 0.3 ml of injected neat technical grade ethanol volume at temperatures well above the flash point of ethanol.

5.3 Results and Discussion

5.3.1 Morphological and elemental characterization (SEM/EDS)

Figure 5.1a shows the SEM micrograph, and Figure 5.1b, the EDS spectrum of the Ag-doped ZnO deposited on a p-type silicon substrate. Figure 5.2 shows the SEM image of the metal particles deposited on a p-type silicon substrate as well as the EDS spectra of Au nanoparticles doped ZnO revealing the Au peak. Figure 5.3 shows the SEM image of the metal particles deposited on a p-type silicon substrate as well as the EDS spectra of Co-nanoparticles doped ZnO showing the Co peak.

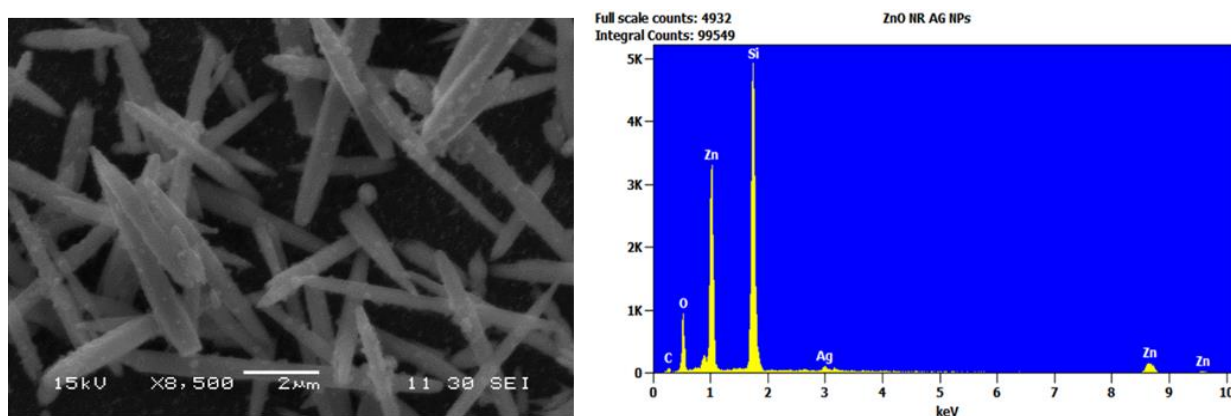


Figure 0.1. a) SEM images and b) EDS spectra of Ag nanoparticles doped ZnO nanorods

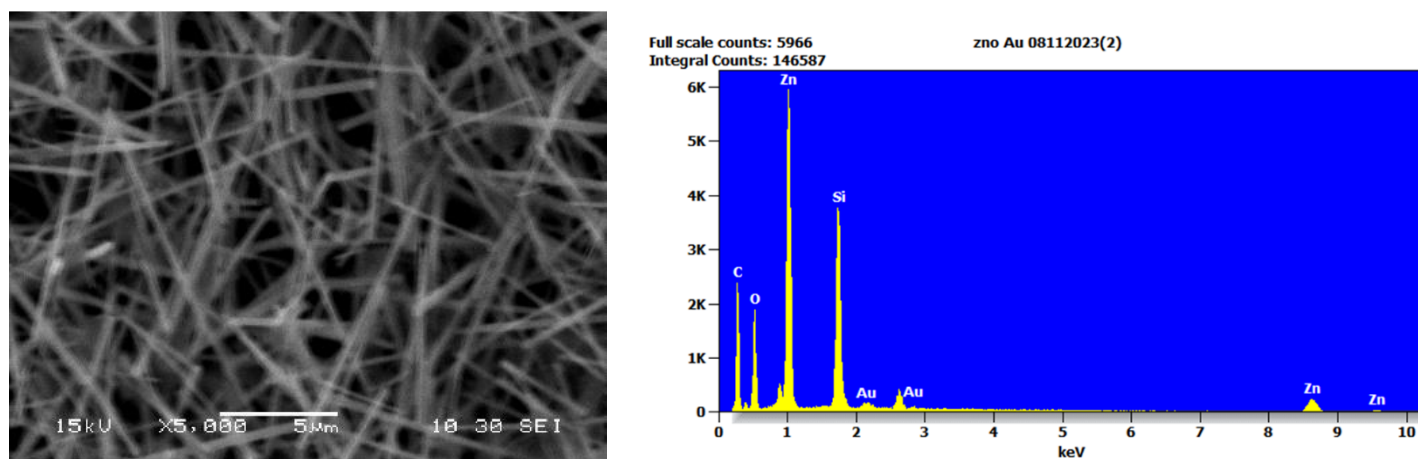


Figure 0.2. a) SEM images and b) EDS spectra of ZnO nanorods doped with Au nanoparticles.

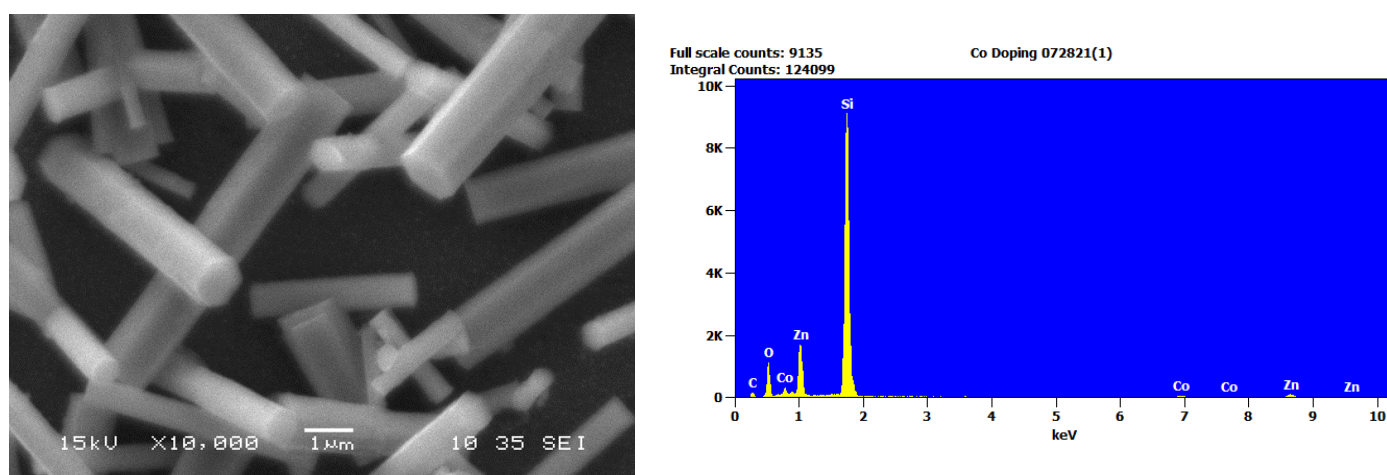


Figure 0.3. a) SEM images and b) EDS spectra of ZnO nanorods doped with Co nanoparticles.

These peaks are indicative of the silicon substrate and the ZnO nanorods grown on them. Additionally, the metal dopants can clearly be seen as shown by their peaks.

5.3.2 Structural Characterization (Raman spectroscopy)

The Raman spectra were measured at room temperature in the range between 100 and 600 cm^{-1} wavelength to probe the disorder induced to the lattice structure of the ZnO crystals by incorporating various metal dopants.

The Raman scattering technique measures the frequency shift ($\Delta\omega = \omega_{\text{phonon}}$), which represents the difference between the incident light frequency (ω_{inc}) and scattered light frequency (ω_{scat}). The process where ω_{phonon} represents the vibration of optical phonon modes is referred to as Raman scattering. In contrast, when ω_{phonon} corresponds to an acoustic phonon, this phenomenon is known as Brillouin scattering. In this case, $\omega_{\text{acous}} \ll \omega_{\text{opt}}$ represents the significant difference between their frequencies. In Raman scattering, incident light undergoes inelastic scattering, causing changes in the polarizability of bonds. The scattered light contains photons with an unchanged frequency (known as Rayleigh scattering) ($\Delta\omega=0$) and photons with higher or lower frequencies due to molecular vibration. This results in Raman spectra being symmetrical around the Rayleigh spectral line, with higher frequency lines corresponding to Stokes region and lower frequency lines belonging to anti-Stokes region. The scattering frequency is defined as $\omega_{\text{scat}} = \omega_{\text{inc}} \pm \omega_{\text{phonon}}$ [10, 11].

Crystal lattice vibrations (phonon modes) determine a wide range of material properties, such as thermal conductivity, heat capacities, the chemical reaction free energies, and the. There are 12 phonon modes in total in wurtzite ZnO crystals belonging to the $C_{6v}^4(P6_3mc)$ space group, with an irreducible representation given by:

$$\Gamma = 2A1 + 2B1 + 2E1 + 2E2 \quad (5.1)$$

where the A1, E1, and E2 modes, which originate from Brillouin's point, are Raman active. A1 and E1 are phonon modes that describe the vibrations of oxygen atoms along different axes. A1 vibrations occur along the c axis, while E1 vibrations happen perpendicular to it [10]. Figure 5.4 visually illustrates the movement of atoms within the ZnO structure corresponding to the active optical modes.

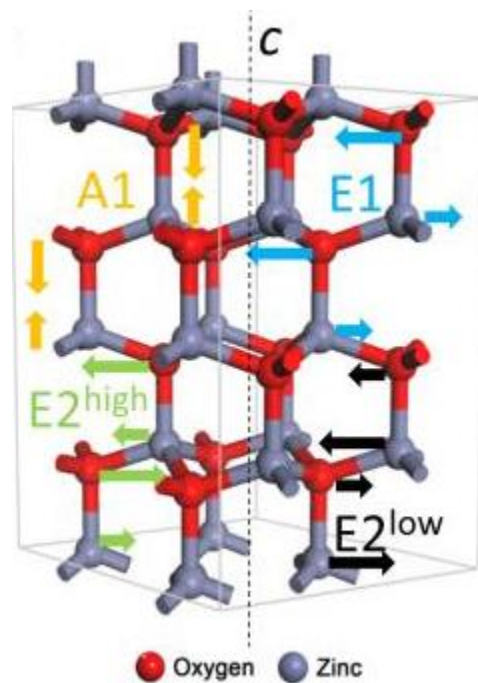


Figure 0.4. A visualization of the movement of atoms associated with the active optical modes in the wurtzite structure of ZnO [10].

These vibrations cause oscillating polarization, which splits the A1 and E1 modes into longitudinal (LO) and transversal (TO) optical modes, each with distinct frequencies that are intrinsically linked to the macroscopic electric fields of LO phonons. The E2 modes are nonpolar and do not undergo LO-TO splitting. Their presence is indicative of ZnO, and their width and

intensity determine the quality of ZnO crystals. There are six peaks in total with their overtone counterparts observed in Raman spectra of bulk ZnO samples, but their visibility depends on measurement arrangements used [10, 12, 13].

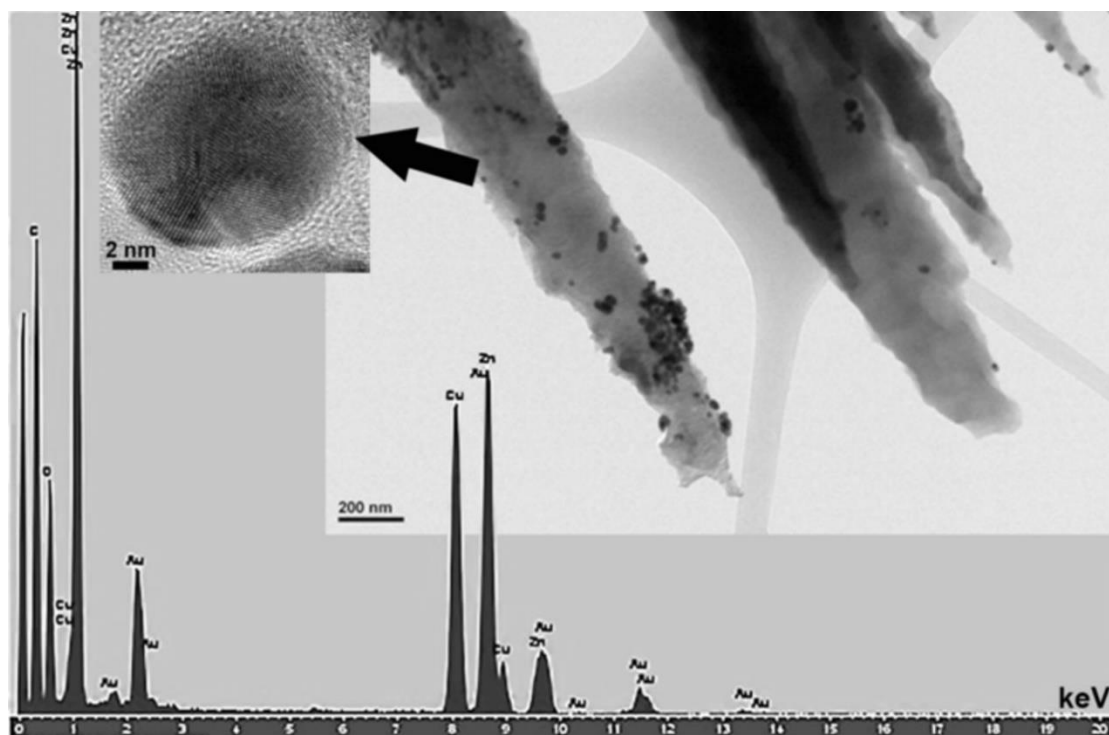


Figure 0.5. TEM image depicting Au nanoparticles decorating ZnO nanorods, with EDS spectra confirming the presence of Au [9].

The Raman spectra depicted in the figure 5.6 exhibit only the signals in the Stokes region, with the Rayleigh spectral line being excluded through filtering. Thus, Raman spectroscopy is an effective method for gathering data about the vibrational properties of crystal lattices. Further, phonon modes are important for describing physical phenomena such as superconductivity phase transitions and ferroelectricity, which are critical to the performance of emerging and established

functional materials. Additionally, they provide important spectral signatures (e.g., IR/Raman), which are frequently used for identification and characterization [14].

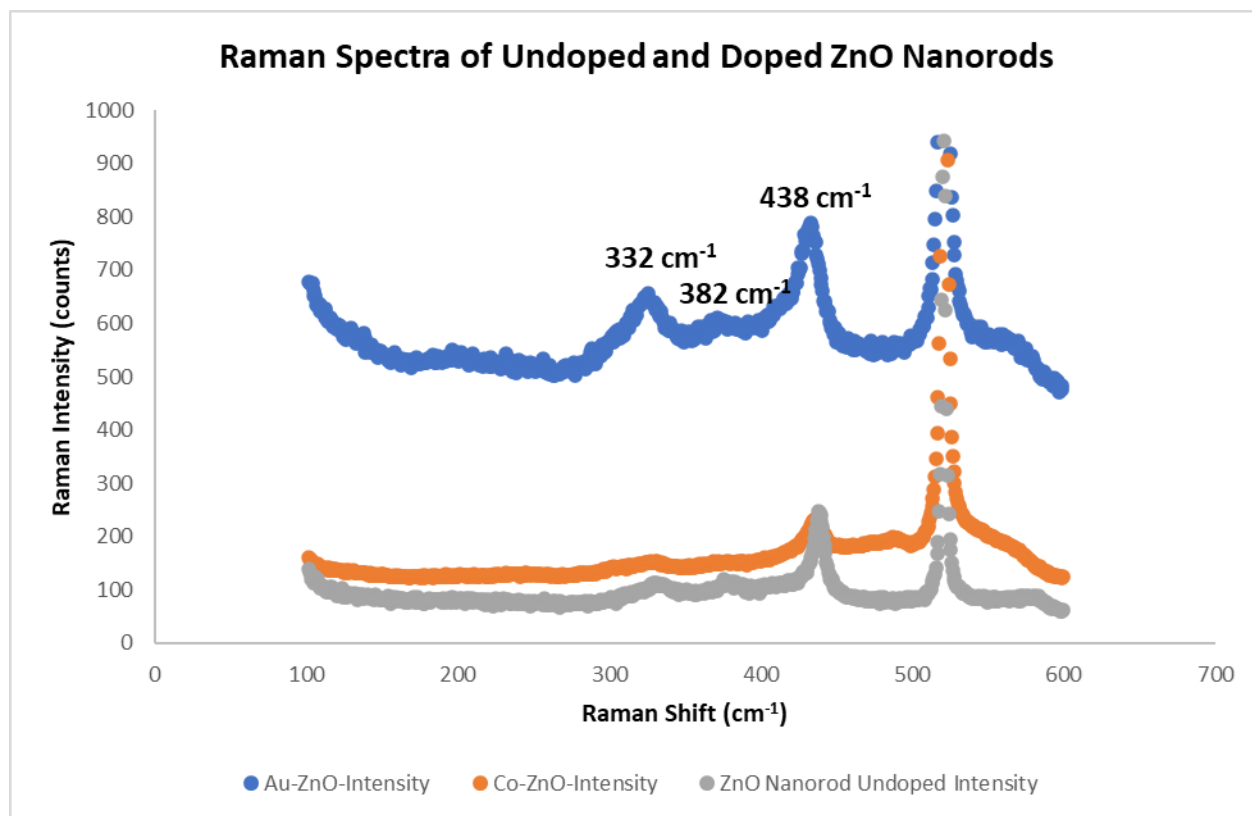


Figure 0.6. Raman spectra of pure and metal-doped ZnO samples taken at room temperature in the range of 100–600 cm^{-1} .

The introduction of Co doping leads to a reduction in the peak intensity, indicating a dopant induced disruption in the packing of the ZnO nanorods or the amorphization of the ZnO nanorods. Conversely, Au doping results in an increase and broadening of the peak intensity, suggesting an enhancement in the packing regularity of the ZnO nanorods [13, 15]. This suggestion is supported by the red-shift of the E2 mode frequency upon Au doping. Red-shifts are commonly associated with increased crystallinity in materials [16]. The Raman peaks at 332 cm^{-1} and 380 cm^{-1} are

attributed to the $E_{2H} - E_{2L}$ modes (the difference mode between the E_2 high and E_2 low frequencies) and A_1 modes, respectively. The intensities of both peaks are reduced in the Co-doped ZnO because of the dopant-induced disorder and are much increased in the case of the Au-doped ZnO which is an indication of Surface-Enhanced Raman Scattering (SERS) due to Au nanoparticles on the ZnO rod surface. Figure 5.5 from a study by Fattah et al., demonstrates that employing solution-based doping of Au, using an $HAuCl_4$ solution (1 mL of 1% in 100 mL water) with the rapid addition of 4 mL of 1% sodium citrate solution, invariably results in self-assembled Au nanoparticles on the surface of ZnO nanorods, giving rise to the observed SERS signal.

In our hands, we were unable to obtain the Raman spectra of the Ag-ZnO nanorod samples because the incident laser appears to damage the sample (vaporize). Consequently, further exploration of the phenomena pertaining to that sample was impeded. Conversely, other researchers, such as Zeferino et al. and Saravan et al., have reported successful acquisition of Raman spectra using lasers of different wavelengths, indicating feasibility in their studies [17, 18].

These findings suggest that different dopants have varying effects on the Raman scattering properties of ZnO nanorods, potentially altering their structural and vibrational characteristics [10, 12-14].

5.3.3 Gas Sensing

These metal doped ZnO films were evaluated as microwave VOC sensing agents, by variations in detection temperature and analyte concentrations. The experimental results were substantially different from those on undoped-ZnO nanorods. While undoped ZnO sensors yielded linear responses, the introduction of metal doping led to intriguing and unexpected findings. With

undoped ZnO (Figure 5.7a), observable changes in both amplitude and phase were gradual. However, upon introducing silver doping (Figure 5.7b), a notably reactive behavior was observed, particularly evident at low temperatures and concentrations. Contrary to anticipated linear responses, the system exhibited saturation beyond these thresholds, suggesting a potential decomposition phenomenon.

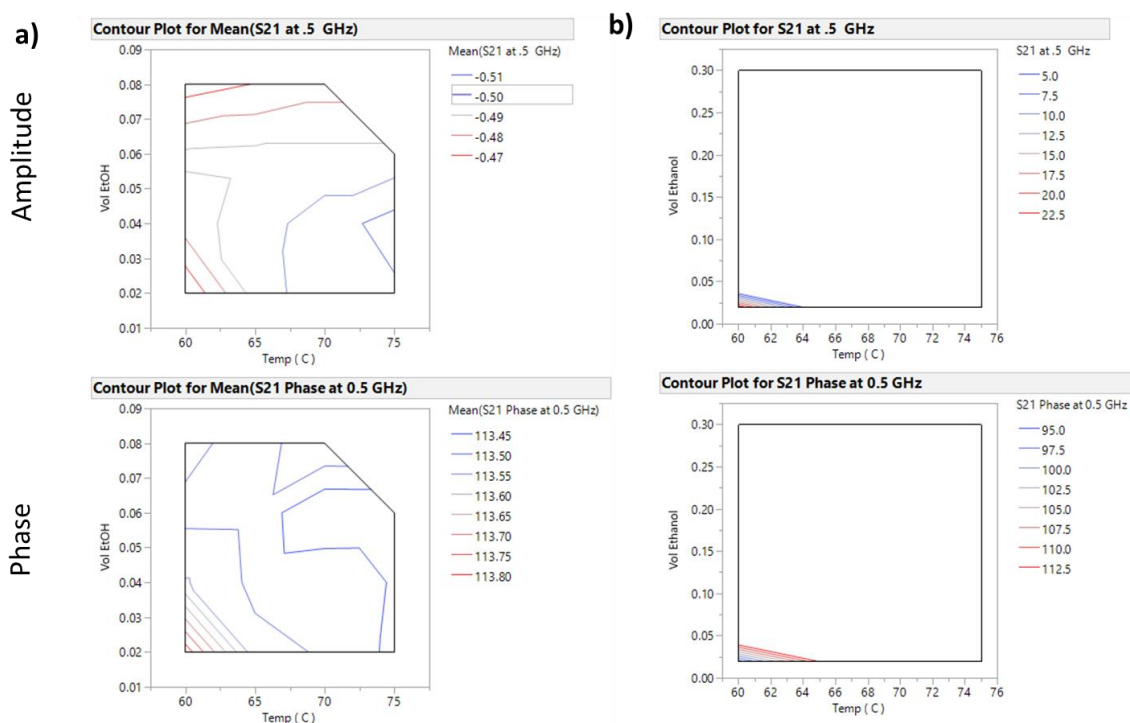


Figure 0.7. Contour plots of the amplitude and phase of Ethanol (EtOH) detection as a function of temperature with a) undoped ZnO nanorods and b) Ag doped ZnO nanorods. Each color on the legend to the right of each plot represents a mean S21 amplitude or phase value at .5 GHz.

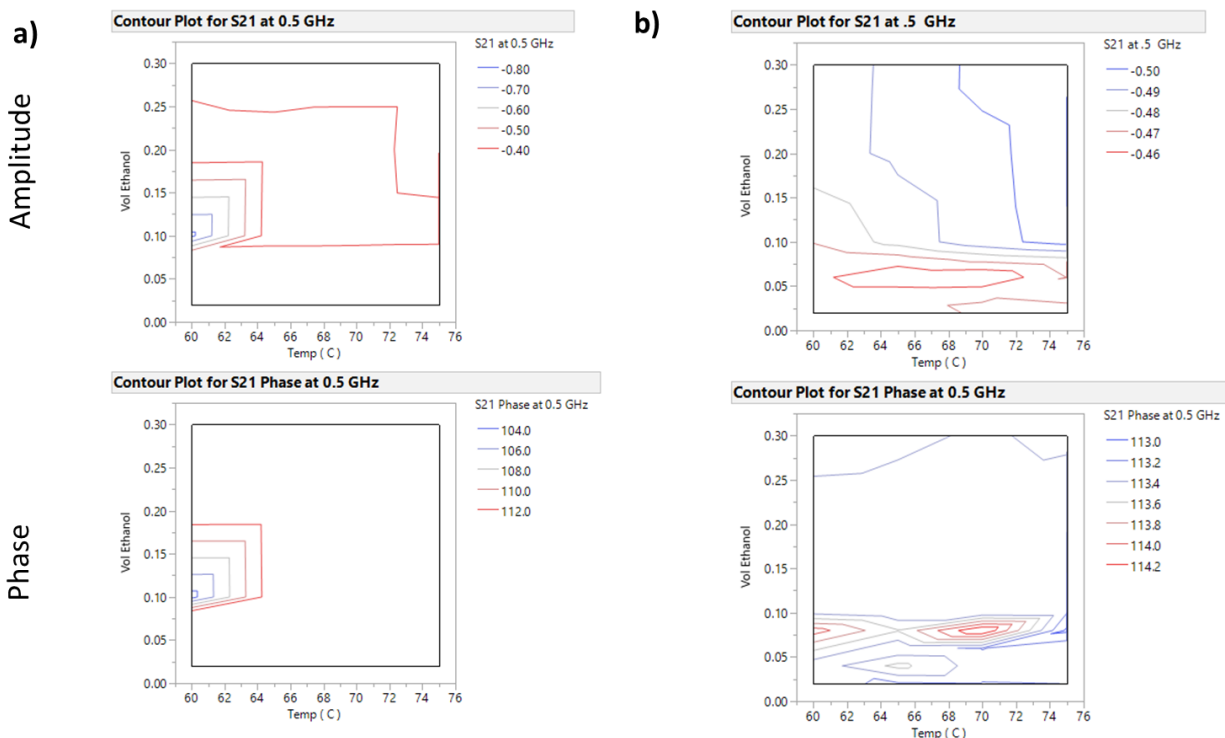


Figure 0.8. Contour plots of the amplitude and phase of EtOH detection with a) Co-ZnO nanorods and b) Au-doped ZnO nanorods.

The behavior of Au-doped ZnO nanorods presented even more peculiar characteristics (figure 5.8b). As concentrations increased, the system displayed heightened resistivity, counterintuitively hindering electron incorporation rather than facilitating it. This counteraction even suggested a possibility of electron withdrawal. Such anomalous behaviors deviated from conventional expectations, prompting a reassessment of the system's underlying dynamics.

Presently, our investigation primarily focuses on lower temperatures, allowing for a meticulous examination of phenomena. However, the impending concern lies in understanding the system's response at elevated temperatures, where decomposition processes may exert substantial influence, thereby raising questions regarding the true nature of observed phenomena in the literature.

Comparatively, Co-doped ZnO nanorods demonstrated behavior similar to the undoped ZnO nanorods than to the coinage metals (Figure 5.8a). Notably, an increase in cobalt concentration corresponded to a linear increase in the system's response. This divergence in behavior suggests a closer alignment of the Co-doped ZnO with undoped ZnO nanorods and implies that the drastic behaviors observed with Ag- and Au-doped ZnO films may be related to the catalytic decomposition of the ethanol analyte on those surfaces which in turn limits the measurability of the analyte.

5.3.4 Examples of Catalytic Decomposition of VOC

The notion of catalytic decomposition is not novel. Literature examples demonstrate that the application of isopropanol on ZnO leads to its decomposition into carbon dioxide and water, releasing electrons whose fate remains uncertain [19]. Similarly, experiments with metal doped NiO nanorods show how the composition of the doped material can influence the catalytic decomposition of ethanol, suggesting multiple potential pathways dependent on the structure and composition of the adsorbed ethanol layer [20, 21].

Hence, two plausible pathways for detecting ethanol on metal-oxide sensing elements emerge: one involving the reduction of impedance through redox reactions on undoped ZnO, and another where the analyte undergoes complete catalytic decomposition on coinage metal-doped ZnO nanorods, resulting in a fundamentally distinct mechanism. Further exploration is required to elucidate these pathways and their implications comprehensively.

5.4 Conclusions

This chapter focuses on doping ZnO nanorods with Co, as well as coinage metals Ag and Au, to enhance gas sensing capabilities. Coinage metal nanostructures offer unique properties influenced by size and shape, making them promising for various applications. Doping ZnO with transition metals like Co modifies its electronic characteristics, influencing conductivity. Experimental results, including morphological, elemental, and structural characterization, along with gas sensing performance, highlight the diverse effects of metal doping on ZnO nanorods. Furthermore, literature examples illustrate the catalytic decomposition of VOCs on ZnO, indicating the need for further exploration to understand these mechanisms thoroughly.

References

- [1] C. M. V. Cristina Maria Vlăduț, Cristina Maria Vlăduț, "Coinage Metals Doped ZnO Obtained by Sol-Gel Method—A Brief Review," *Gels*, vol. 9, no. 5, p. 424, 2023, doi: 10.3390/gels9050424.
- [2] H. S. Teboho P. Mokoena, David E. Motaung, "A review on recent progress of p-type nickel oxide based gas sensors: Future perspectives," *Journal of Alloys and Compounds*, vol. 805, pp. 267-294, 2019, doi: 10.1016/j.jallcom.2019.06.329.
- [3] V. D. M. Umadevi Godavarti, M.V. Ramana Reddy, P. Nagaraju, Y. Vijaya Kumar, Kalyana Tulasi Dasari, Madhava P. Dasari "Precipitated cobalt doped ZnO nanoparticles with enhanced low temperature xylene sensing properties," *Physica B: Condensed Matter*, vol. 553, pp. 151-160, 2019, doi: 10.1016/j.physb.2018.10.034.
- [4] S.-J. Y. Yen-Lin Chu, Liang-Wen Ji, Tung-Te Chu, Kin-Tak Lam, Yu-Jen Hsiao, I-Tseng Tang, and Tzu-Hao Kuo, "Characteristics of Gas Sensors Based on CoDoped ZnO Nanorod Arrays," *Journal of The Electrochemical Society*, vol. 167, no. 11, p. 117503, 2020, doi: 10.1149/1945-7111/aba00d.
- [5] B. H. Hamid Reza Yousefi, Ali Mirzaei, Hossein Roshan, Mohammad Hossein Sheikhi, "Effect of Ag on the ZnO nanoparticles properties as an ethanol vapor sensor," *Mater. Sci. Semicond. Process*, vol. 117, p. 105172, 2020, doi: 10.1016/j.mssp.2020.105172.
- [6] A. A. Manish Deshwal, "Enhanced acetone detection using Au doped ZnO thin film sensor," *J. Mater. Sci. Mater. Electron*, vol. 29, pp. 15315–15320, 2018.
- [7] D. G. Tarek M. Abdel-Fattah, and Helmut Baumgart, "Atomic Layer Deposition Grown Hafnia Nanotubes Functionalized with Gold Nanoparticle Composites," *ECS Solid State Letters*, vol. 2, no. 4, pp. P31-P34 P31-P34 doi: 10.1149/2.001303ssl.
- [8] J. M. L. Clay Huff, and Tarek M. Abdel-Fattah, "Beta-Cyclodextrin-Assisted Synthesis of Silver Nanoparticle Network and Its Application in a Hydrogen Generation Reaction," *Catalysts* vol. 10, no. 9, p. 1014, 2020, doi: 10.3390/catal10091014.

- [9] A. W. Tarek M. Abdel-Fattah, Kai Zhang, Wei Cao, and Helmut Baumgart, "Highly Uniform Self-Assembled Gold Nanoparticles over High Surface Area ZnO Nanorods as Catalysts," *ECS Journal of Solid State Science and Technology*, vol. 3, no. 10, 2014, doi: 10.1149/2.0211410jss.
- [10] K. J. Jakub Cajzl, Pavla Nekvindová, Alena Michalcová, Martin Veselý, Anna Macková, Petr Malinský, Adéla Jágerová, Romana Mikšová, and Shavkat Akhmadaliev, "Creation of Gold Nanoparticles in ZnO by Ion Implantation–DFT and Experimental Studies," *Nanomaterials (Basel)*, vol. 10, no. 12, p. 2392, 2020, doi: 10.3390/nano10122392.
- [11] P. K. J. Amit Kumar Bhunia, Dibyaranjan Rout and Satyajit Saha. , "Morphological Properties and Raman Spectroscopy of ZnO Nanorods," *Journal of Physical Sciences*, vol. 21, pp. 111-118, 2016.
- [12] G. Z. Jianbo Yin, Huan Liu, Jia Liang, "Hydrothermal Fabrication and Ferroelectric Behavior of Lithium-Doped Zinc Oxide Nanoflakes," *Science of Advanced Materials*, vol. 5, no. 9, pp. 1139-1149, 2013, doi: 10.1166/sam.2013.1639.
- [13] S. G. Anupama Chanda, Vasundhara Mutta, Shalik R. Joshi, Geeta Rani Mutta, Jai Singh, "Study of Structural, Optical and Magnetic Properties of Cobalt Doped ZnO Nanorods," *RSC Advances*, vol. 7, no. 80, 2017, doi: 10.1039/C7RA08458G.
- [14] P. K. Ioanna Pallikara, Jonathan M Skelton, and Lucy D Whalley, "The physical significance of imaginary phonon modes in crystals," *Electronic Structure*, vol. 4, no. 3, p. 033002, 2022, doi: 10.1088/2516-1075/ac78b3.
- [15] A. C. L. Ouarez, T. Touam, R. Mahiou, D. Djouadi, A. Potdevin, "Au-doped ZnO sol-gel thin films: An experimental investigation on physical and photoluminescence properties," *Journal of Luminescence*, vol. 203, pp. 222-229, 2018, doi: 10.1016/j.jlumin.2018.06.049.
- [16] K. R. S. s. Q. A. Thread:, "Red and Blue shift in Raman Spectra. What is the explanation," ed. ReseachGate, 2018.
- [17] M. S. a. T. S. Shanmugam Saravanan, "Structural, morphological and optical studies of Ag-doped ZnO nanoparticles synthesized by simple solution combustion method," *Japanese Journal of Applied Physics*, vol. 53, p. 11RF01, 2014, doi: 10.7567/JJAP.53.11RF01.
- [18] R. S. Z. M. B. F. U. Pal, "Photoluminescence and Raman Scattering in Ag-doped ZnO Nanoparticles," *J. Appl. Phys.*, vol. 109, no. 1, 2011, doi: 10.1063/1.3530631.
- [19] A. V. Vasile Postica, David Santos-Carballal, Torben Dankwort, Lorenz Kienle, Mathias Hoppe, Abdelaziz Cadi-Essadek, Nora H. de Leeuw, Maik-Ivo Terasa, Rainer Adelung, Franz Faupel, and Oleg Lupan, "Tuning ZnO Sensors Reactivity toward Volatile Organic Compounds via Ag Doping and Nanoparticle Functionalization," *ACS Applied Materials & Interfaces*, vol. 11 no. 34, pp. 31452-31466, 2019, doi: 10.1021/acsami.9b07275.
- [20] M. T. Javier Bartolomé, Ruth Martínez-Casado, David Maestre, and Ana Cremades, "Ethanol gas sensing mechanisms of p-type NiO at room temperature," *Applied Surface Science*, vol. 579, p. 152134, 2022, doi: 10.1016/j.apsusc.2021.152134.
- [21] P.-C. C. Yu-Yao Hsia, Lu-Hsin Lee, Yu-Ling Lai, Li-Chung Yu, Yao-Jane Hsu, Jeng-Han Wang and Meng-Fan Luo, "Dependence on co-adsorbed water in the reforming reaction of ethanol on a Rh(111) surface†," *RSC Advances*, vol. 10, no. 30, pp. 17787-17794, 2020, doi: 10.1039/D0RA02015J.

CHAPTER 6

METAL-ORGANIC FRAMEWORK MOF FILMS AS SENSING MEDIA

Part of this chapter is a reprinted adaptation from Papa K. Amoah, Zeinab M. Hassan, Rhonda R. Franklin, Helmut Baumgart, Engelbert Redel, and Yaw S. Obeng; “Broadband Dielectric Spectroscopic Detection of Aliphatic Alcohol Vapors with Surface-Mounted HKUST-1 MOFs as Sensing Media,” *Chemosensors*, vol. 53, no. 13, p. 135104, 2022, doi: 10.1088/1361-6463/abd3ce with permission from MDPI Publishing.

6.1 Introduction

Chemical sensors are based on reversible and proportional changes in physicochemical properties of the detector when exposed to the target analyte [1,2]. In addition, most gas sensors must be cost effective and usable in rather harsh conditions [3]. Emerging gas sensors based on metal-organic frameworks (MOFs) appear to meet these criteria [4]. These MOFs could potentially address the difficulties with selectivity [5] that limit other sensor materials [6]; in principle, the charge transfer processes in these MOF materials which result in altering band structures are similar to those in the metal-oxide semiconductor, and could be suitable as gas sensors [2,6].

Moreover, MOFs are highly porous materials which are able to form coordination complex clathrate-like structures with gas molecules, making them ideal for selective gas sensors [7–10]. The MOFs used in this research are called HKUST-1, derived from the abbreviation of Hong Kong University of Science and Technology-1, represented by the chemical formula $[\text{Cu}_3(\text{BTC})_2(\text{H}_2\text{O})_3]_n$ [11]. HKUST-1 surface-anchored MOF thin films (SURMOFs) doped with TCNQ [7,7,8,8-tetracyano-quinodimethane] is a well characterized platform for investigating selective gas detection [7,12,13]. Doping with TCNQ is done with the purpose of modulating the electrical conductivity of the HKUST-1 material (Figure 6.1) [14].

It has been shown elsewhere [15] that the thermal conductivities of SURMOF are commensurate with their single crystalline MOF analogues, and decrease in the presence of adsorbates, due to increased vibrational scattering and guest molecule-induced hybridization of low frequency modes [16]. When coupled with emerging transient electrical techniques, these MOF platforms enable highly selective and ultra-trace gas-phase sensing. For example, AC-impedance spectroscopy has been used in combination with optimized hydrophobic MOFs to selectively detect iodine with part-per-billion (ppb) level sensitivity [17]; the microwave resonant cavity technique has been used to detect and distinguish between methanol, ethanol, and acetone in the 0–200 ppm range at room temperature [18]; and HKUST-1-like Cu-BTC nanoparticles have been used in the capacitive sensing of VOCs [7].

We have also demonstrated elsewhere that in contrast to the traditional coulometric techniques, surface mounted ZnO nanotubes, and HKUST SURMOF, can sense ethanol at temperatures under 100 °C, using broadband microwave dielectric spectroscopy (BDS) [19,20]. While gas monitoring with such emerging metrology has been demonstrated, the performance metrics such as selectivity, sensitivity, reproducibility, and long-term stability are not yet well established. Furthermore, the impact of such environmental factors as temperature and humidity are currently not well understood [21]. Thus, there is a need to improve our fundamental knowledge of these metrology tools such as microwave gas sensors.

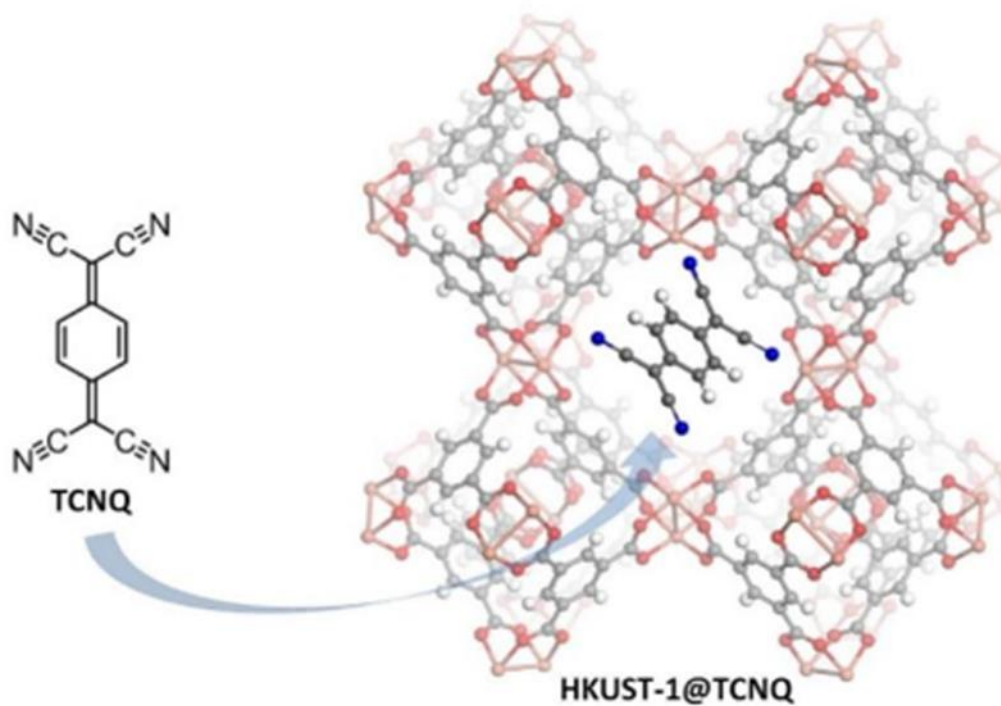


Figure 0.1. Schematic illustration depicting the structure of HKUST-1 SURMOF films, where the pores are loaded with TCNQ (TCNQ, tetracyanoquinodimethane) [14].

In this study, broadband dielectric spectroscopy (BDS) was investigated [22], in combination with TCNQ-doped HKUST-1 SURMOF, to sense aliphatic alcohol and acetone vapors. First, the alcohol vapor analyte access (i.e., size limited loading) to the reactive metal sites in the SURMOF for detection was investigated. Then, the thermodynamic- and kinetic-controlled analyte uptake by the SURMOF sensing medium from the responses of neat solvents and 1:1 v/v methanol - ethanol mixture was compared. Finally, the proposed cooperative electrocatalytic oxidation mechanism were investigated by comparing the responses of the aliphatic alcohols and acetone. It was expected that the acetone reacts differently from alcohols as the former cannot form the prerequisite alkoxide intermediate, under the experimental conditions [23].

6.1.1 Broadband Dielectric Spectroscopy (BDS) Background

Broadband dielectric spectroscopy (BDS) [22] rapidly interrogates a wide range of material physicochemical characteristics through the movement of dipoles in the presence of an external electric field such as microwaves (MW). It measures the material under test's (MUT's) complex relative permittivity (i.e., dispersive, and dissipative dielectric behavior) in response to the rapidly changing electrical and magnetic fields, which in simple one-component systems is mainly due to dielectric polarization [24]. Thus, BDS should lend itself well to the electronic detection of volatile organic compounds (VOCs) as they invariably involve changes in polarizability, including, but not limited to, changes in bond polarizability [20]. The microwave signal is scattered by the analyte (i.e., MUT) according to the material's permittivity. The signal reflecting from the electrical connections and transmitted between the two connectors is summarized as a matrix of scattering parameters (S-parameters). These parameters capture how RF energy travels through a multiport network, such as using a vector network analyzer (VNA), with the analyte between the source and receiver. Thus, the output of the S-parameters is convoluted with the transfer function of the sensor loaded with the MUT, i.e., $(h(f))$ [25]; thus, the S-parameters can be deconvoluted to produce the circuit elements characteristic of the analyte [26].

In this work, we used the S-parameters to evaluate the chemo-induced changes (CIC) that result from the volatile organic compounds (VOCs, e.g., aliphatic alcohols) adsorbed on the SURMOF sensing materials, by measuring the MW insertion loss characteristics of the transmitted signal (S_{21}) as a function of the experimental variables. In the experimental configuration used, the sensing material was interrogated by the interaction of the electric fields which are emitted from the signal line, located in the center of the electrode, and terminated on the two ground lines adjacent to the signal line of the coplanar waveguide (GSG CPW). The electric fields reaching the

sensing materials can be approximated as a planar field. With this approximation, the microwave insertion loss (i.e., S_{21}) measures the fraction of energy that is transmitted from the source (port 1) to the detector (port 2) through the device under test (DUT) with the gas sensing device on top. In this work, we used the S-parameters to evaluate the chemo-induced changes (CIC) that result from the volatile organic compounds (VOCs, e.g., aliphatic alcohols) adsorbed on the SURMOF sensing materials, by measuring the MW insertion loss characteristics of the transmitted signal (S_{21}) as a function of the experimental variables. In the experimental configuration used, the sensing material was interrogated by the interaction of the electric fields which are emitted from the signal line, located in the center of the electrode, and terminated on the two ground lines adjacent to the signal line of the coplanar waveguide (GSG CPW). The electric fields reaching the sensing materials can be approximated as a planar field. With this approximation, the microwave insertion loss (i.e., S_{21}) measures the fraction of energy that is transmitted from the source (port 1) to the detector (port 2) through the device under test (DUT) with the gas sensing device on top. In our experimental setup, the device under test (DUT, comprised of the waveguide, end-launchers, and the MUT) matched very well to the characteristic impedance (Z_0) of the VNA; it had very low reflections (S_{11}/S_{22}) [27]. Thus, with proper calibration, the S_{21} amplitude and phase can be correlated to the total impedance of the GSG CPW waveguide and gas sensing device.

6.2 Experimental

6.2.1 Preparation of the TCNQ Doped HKUST-1 MOF Sensing Material Preparation

HKUST-1 SURMOF films were made available through a research collaboration with Dr. Engelbert Redel from Karlsruhe Institute of Technology (KIT) in Germany. The compact polycrystalline SURMOF films were grown in a layer-by-layer (LbL) fashion on plasma-activated borosilicate SiO₂ glass substrates as illustrated in figure 6.2 [16,28]. Before MOF film deposition, the glass substrates were cleaned with ethanol and activated with O₂ plasma cleaning. Subsequently, the gold covered substrate surface was functionalized with MHDA (16-mercaptohexadecanoic acid), a self-assembled monolayer (SAM), to achieve highly oriented HKUST-1 SURMOF films. The MOF precursors, i.e., the copper acetate solution (1.0 mM) and the benzene-1,3,5-tricarboxylic acid (BTC) linker solution (0.2 mM), were subsequently sprayed on the substrate with spraying times of 15, and 25 s, respectively, followed by a rinsing step with pure EtOH for 5 s for each spray deposition cycle. By varying the number of spray cycles, the HKUST-1 film thickness could be easily tuned; in this work the thickness of SURMOF films was ≈ 35 nm, formed from 30 spray cycles [29].

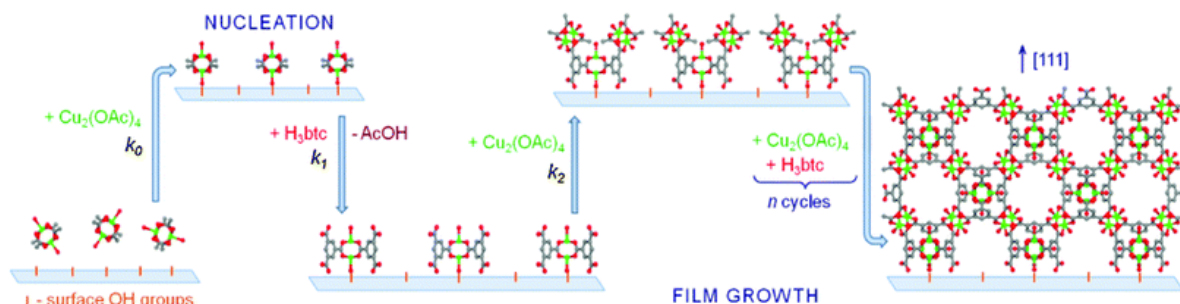


Figure 0.2 Schematic representation illustrating the HKUST-1 SURMOF film growth with MOF precursors Copper acetate inorganic solution (1.0 mM) and Benzene tricarboxylic acid BTC organic linker (0.2 mM). Copper atoms are depicted in green, oxygen atoms in red, and carbon atoms in gray [72].

The 7,7,8,8-tetracyano-quinodimethane (TCNQ) loading of fresh HKUST-1 SURMOF was accomplished as described in the open literature [30,31]. The greenish color of our films is indicative of mixed valent $\text{Cu}^{2+}/\text{Cu}^{+}$ defects [32] that form reactive adducts with dioxygen molecules and are probably responsible for the catalytic aerobic oxidative properties of the HKUST-1 SURMOF films [33]. The samples were diced into 1.5 cm by 2.5 cm pieces and stored in a pure nitrogen atmosphere prior to use.

Analytical grade solvents—methanol, ethanol, 2-propanol, and acetone—were obtained from Sigma-Aldrich (Milwaukee, St. Louis, MO, USA), and were used as received.

6.2.2 BDS Setup and Measurements

In this work, we used a ground–signal–ground (GSG) coplanar waveguide (CPW) fabricated from gold-covered alumina (1 mm thick polished alumina (dk 9.5)). The cables from the CPW to the vector network analyzer (VNA, SPARQ 4004E, Teledyne LeCroy, Chestnut Ridge, NY, USA) were connected through edge mount connectors (Model 1492-04A-6, Southwest Microwave, Tempe, AZ, USA). This configuration effectively converts the coaxial mode signal of the cable into a coplanar waveguide mode propagating towards the material under test (MUT). A two-port short-open-load-through (SOLT) calibration is used to shift the VNA reference plane to end of the connector/cable interface by attaching the calibration standards to the ends of the cables. The cables connecting to the CPW were de-embedded, moving the reference plane of the measurement from the port faces of the VNA to the connector/cable interface. Thus, the device under test (DUT) is defined as two launch connectors and the CPW itself with the MUT on top,

and the reported S-parameter data variations are those from experimental perturbations to the MUT. If the SURMOF film is deposited on a conductive substrate (e.g., silicon substrate) the sensing substrate is isolated from the gold signal traces by a Corning #1 glass coverslip (Product number CLS284518, Aldrich-Sigma, Milwaukee, WI, USA), as shown in Figure 6.3 below; otherwise, the glass cover slide is optional.

In this experimental configuration, the sensing material is interrogated by the interaction of the electric fields emanating from the signal line and terminating on the ground lines of the coplanar waveguide. The electric fields reaching the sensing material layer can be approximated as planar given the size of the gap compared to the signal line width in the CPW and distance from the given thicknesses of the silicon substrate and glass coverslip, as shown in Figure 6.3. With this approximation and proper calibration, the microwave insertion loss (i.e., S_{21}) measures the fraction of energy that is transmitted from the source to the detector through the MUT, and the S_{21} amplitude can be correlated to the total impedance of the GSG waveguide, the optional glass coverslip, and the SURMOF/Si sensor device.

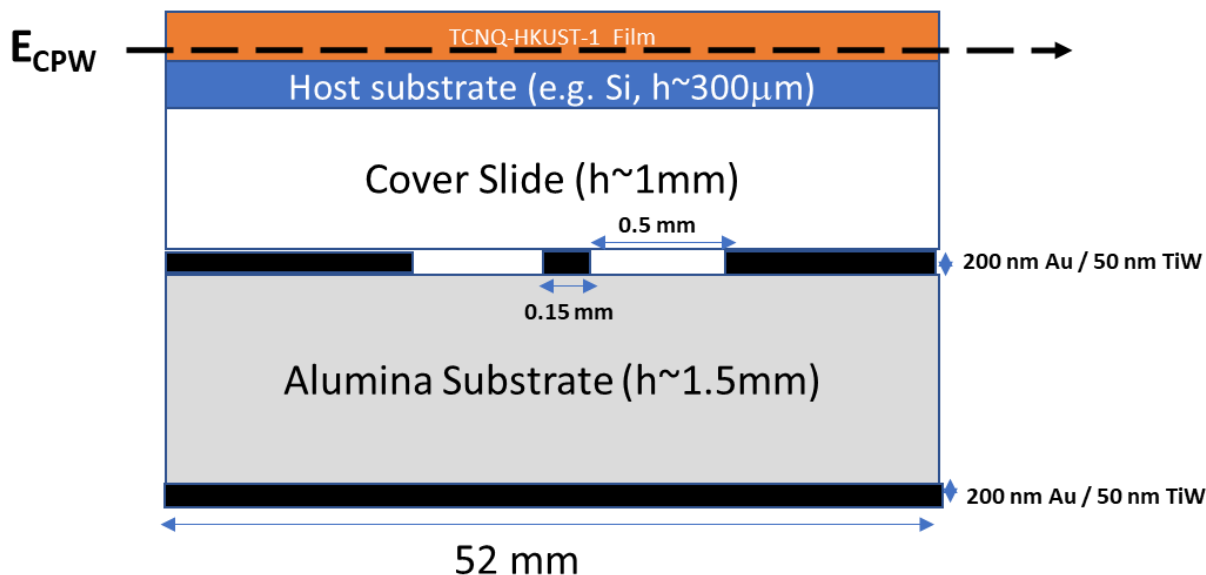


Figure 0.3. A phenomenological model of a doped HKUST-1 SURMOF under microwave interrogation in a gaseous ambient. E_{CPW} is an electric field fringe from the microwave emanating from the signal line and terminating on the ground line of the GSG CPW. Note that the figure is for illustration only, and not to scale. Some features important features have been deliberately exaggerated for illustrative purposes.

The sample CPW assembly was situated in a resistively heated Pyrex tube reactor, with porous endcaps, that allowed independent control of the environment around the sensing material. The temperature of the assembly can be manually controlled with a power supply from room temperature to approximately 120 °C. For this study, the temperature was maintained at 65 °C to extend the life of the edge mount connectors to the CPW. Both the S-parameters, in the 0.1 to 20 GHz range, and the reactor temperature, were measured every 30 seconds. The response of the BDS system to analyte concentration was investigated by flash vaporizing varying amounts (0.01 to 1.0 mL) of neat analytical grade analyte (i.e., methanol, ethanol, 2-propanol, acetone, and 1:1 volume-by-volume methanol–ethanol mixture) into the reactor using a long-needled hypodermic Hamilton syringe [20]. Saturation (over 1000 ppm) was observed in the test chamber for solvent

amounts of 0.01 ml of solvent in the temperature window used in this study. The system response was monitored for five minutes after each dosing followed by a five-minute ambient gas purge before the next aliquot of solvent was injected. Although a broad range of frequencies was monitored, selected reporting frequencies were chosen based on the experimental setup, the sample dimensions, and the molecular species of interest¹⁴. We quantified energy dissipation into the sensing material by calculating the microwave attenuation constant (α) (i.e., defined as the real part of the microwave propagation constant ($\gamma = \alpha + j\beta$)), by numerical RLCG modeling [34] using custom MATLAB (MathWorks, Natick, MA) code. Statistical data analysis to determine the impact of the guest molecule loading and gaseous environment on the measurand was performed with JMP software (JMP, SAS Institute, Cary, NC, USA).

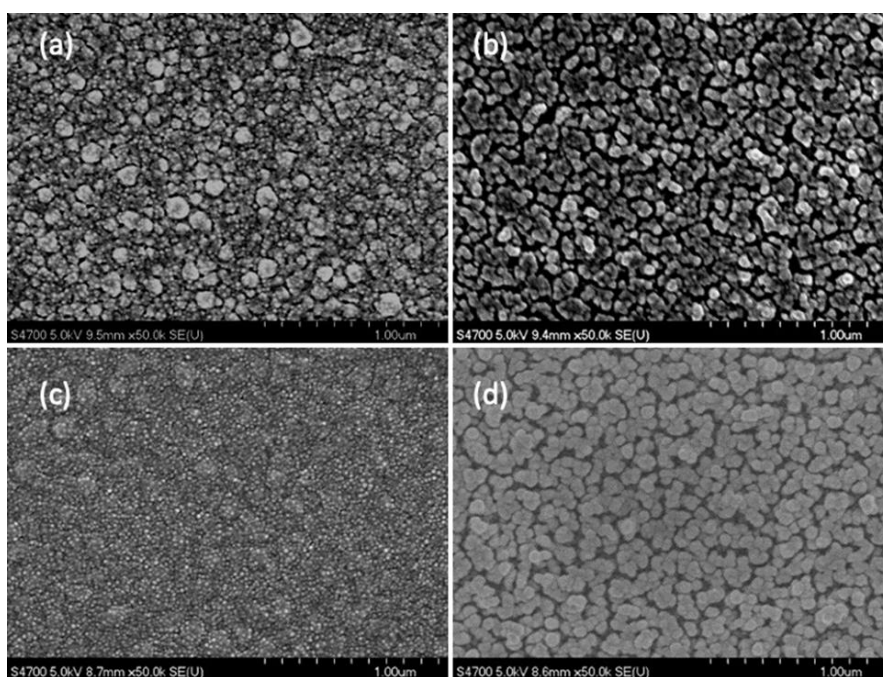


Figure 0.4. Planar view FE-SEM micrographs of HKUST-1 SURMOF thin films grown on borosilicate glass substrates displaying the differences in MOF morphology between undoped pristine MOFs versus TCNQ-doped MOFs of very loosely stacked MOF grains with very noticeable gaps between individual MOF grains, which are especially pronounced following

TCNQ loading of thicker 40 deposition cycles of MOF films: (a) 10 cycles pristine MOF; (b) 10 cycles TCNQ; (c) 40 cycles MOF pristine; and (d) 40 cycles MOF with TCNQ-loaded MOF [adapted from Reference #35].

Figure 6.4 compares the planar-view FE-SEM micrographs of HKUST-1 SURMOF thin films grown on borosilicate glass substrates. The main difference between pristine HKUST-1 SURMOF films and the TCNQ-infiltrated MOF films is that the pristine undoped case exhibits large crystalline domains interspersed by many much smaller grains, while the TCNQ-doped SURMOFs films show a uniformly distributed grain size comprised of primarily large grains separated by wide gaps between the MOF domains, which were presumably formed as a result of significant unit cell changes during the doping [28]. The full characterization of these films is described elsewhere [35]. The pre-existing TCNQ does not prevent the further uptake of other guest molecules by HKUST-1 crystals [36]; hence, we expect the uptake of N_2 or other small Lewis base molecules to be unimpeded by the TCNQ dopant already in the MOF [20,37].

6.3 Results and Discussion

6.3.1 Characterization of the HKUST-1 SURMOF Sensing Material

The electrical conductivity of the doped materials is higher than that of the undoped films due to dopant-induced electronic structural change [38]; Seebeck coefficient measurements show holes as the majority charge carriers in the doped films at room temperature [28,39]. Figure 6.5 compares the temperature dependence of microwave insertion loss (S_{21} amplitude) for pristine- and TCNQ-doped HKUST-1 SURMOF films on Si, at 1 GHz in a N_2 -rich air environments. The

doped MOF system becomes more lossy when electron-rich N_2 molecules (Lewis base) coordinate to the open Cu^{2+} centers [37], and reduce the concentration of the majority hole carriers [39]. Furthermore, the temperature sensitivity of the electrical conduction of the doped KHUST-1 material is consistent with guest-induced electronic and vibrational structures changes in the SURMOF [16,40]. Specifically, the temperature dependence of the S_{21} in the doped material suggests that either nitrogen adsorption at the open metal sites is limited by heat-induced conformational changes in the MOF cage to allow access to the open metal sites [41,42], or the device has temperature-dependent drifts below 50 °C [43]. By comparison, the poor temperature dependence of the S_{21} of the “pristine” material is more consistent with the electron hopping between localized orbitals of adjacent metal centers [44,45]. All subsequent experiments were conducted using the TCNQ-doped SURMOF films at 65 °C to avoid the S_{21} drift [20], and to preserve the performance of the end-launchers of the GSG CPW waveguide.

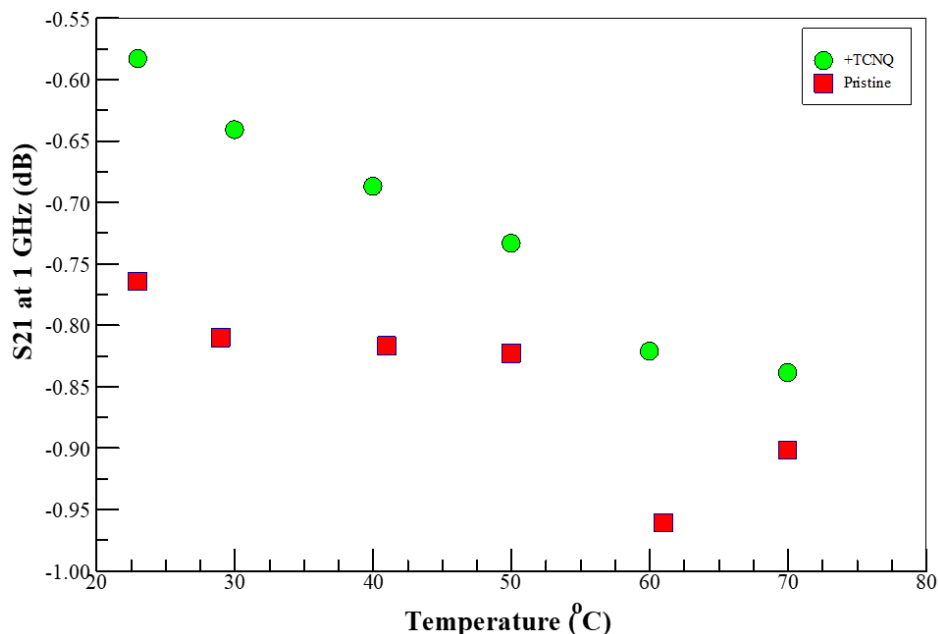


Figure 0.5. Temperature dependence of microwave insertion loss amplitude (S_{21}) of pristine and TCNQ-doped HKUST-1 SURMOF on Si in a N_2 -rich air environments, at 1 GHz. The error bars represent the standard deviation of at least three measurements on the same sample and are substantially smaller than the symbol sizes and are therefore not visible.

6.3.2 Aliphatic Alcohol Oxidation in TCNQ-loaded HKUST-1 MOF

Figure 6.6 shows the time-averaged methanol vapor concentration dependence of the insertion loss ($|S_{21}|$) of the TCNQ-doped HKUST-1 MOF in an air ambient at 65 °C. The $|S_{21}|$ depended only on the methanol vapor concentration, as summarized in Figure 5, which is the time-averaged $|S_{21}|$ monitored at 0.5 GHz of methanol vapor concentration dependence on TCNQ-loaded HKUST-1 at 65 °C, in air. The DUT becomes more resistive with increasing volume of solvent flash vaporized into the reactor, and then levels off at around 0.4 ml of neat methanol injected. As in the nitrogen environment, the system becomes more lossy as the electron-rich aliphatic alcohol (Lewis base) associates and donates electrons to the open Cu^{2+} centers [37], and color centers, which results in the reduced concentration of the majority hole carriers.

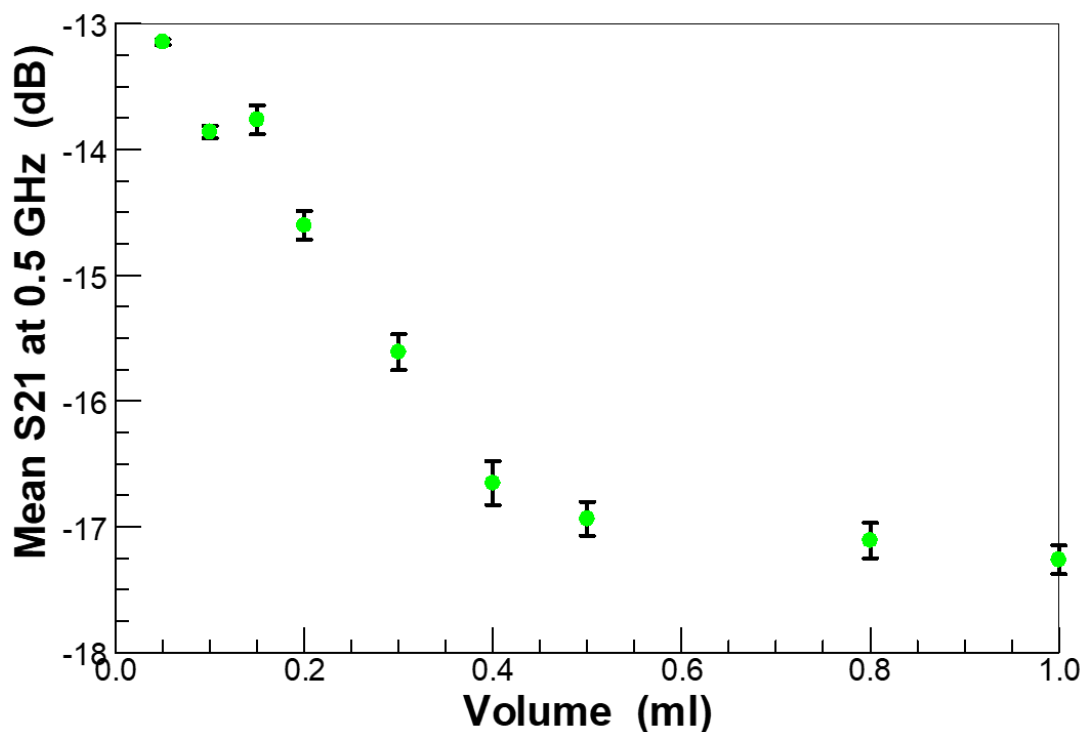


Figure 0.6. Methanol concentration dependence of the time-averaged microwave insertion loss amplitude (S_{21}) of a TCNQ-loaded HKUST-1 SURMOF film on Si substrate at 65 °C, purged with pure air, monitored at 0.5 GHz. The error bars represent the standard deviation of at least three five-minute measurements for each aliquot of methanol.

Figure 6.7 compares the time-averaged insertion loss amplitude (S_{21}) monitored at 0.5 GHz for methanol (MeOH), ethanol (EtOH), 2-propanol (2-PrOH), and acetone as a function of the volume of solvent flash vaporized into the reactor with TCNQ-doped HKUST-1 SURMOF at 65 °C and purged with pure air. Although acetone is not an aliphatic alcohol, it is an oxidation product of 2-propanol and was studied to understand the impact of adsorption/desorption kinetics of the oxidation products in the proposed BDS detection mechanism. The S_{21} amplitude response spanned a wide range, but close inspection shows that all the traces share the salient features of Figure 6.7: three segments comprised of a subcritical concentration range in which the impedance is quite high, a linear region in which the S_{21} amplitude response is proportional to the analyte

concentration, and a saturation segment above which the insertion loss does not appear to depend on the analyte concentration. Table 6.1 summarizes these features, and some pertinent physico-chemical properties for the solvents studied.

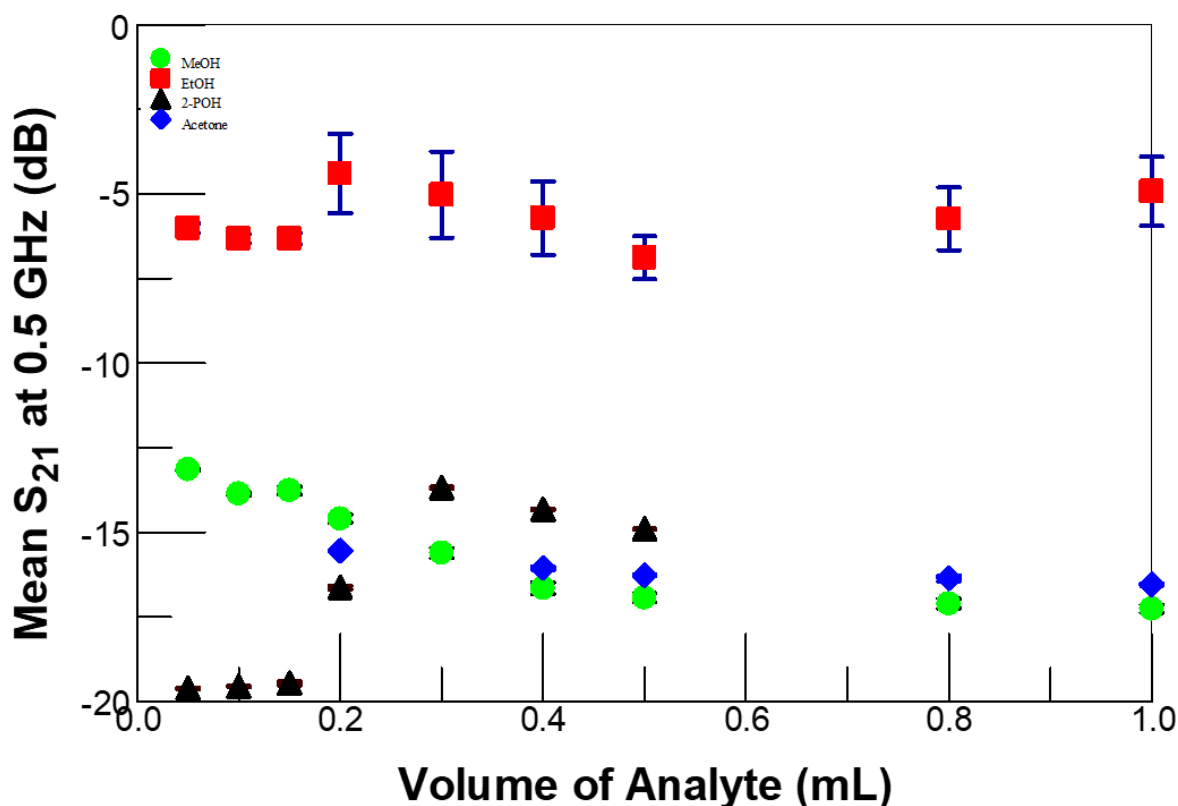


Figure 0.7. Comparison of analyte concentration dependence of microwave insertion loss amplitude (S_{21}) TCNQ-loaded HKUST-1 SURMOF on Si substrate at 65 C° in air, monitored at 0.5 GHz. The error bars represent the standard deviation of at least three measurements.

In the linear range, the insertion loss amplitude increased (i.e., S_{21}) with increasing analyte concentration, consistent with impedance increases due to the reduction on the majority carrier concentration in the TCNQ-doped HKUST-1 SURMOF [28,39], and is reminiscent of the output of coulometric gas sensors [46]. Furthermore, the linear segment can be fitted to a linear equation

(with $R_2 > 0.98$, Prob > t of at least 0.02) with a characteristic slope as summarized in Table 6.1. As discussed below, the solvent molecules enter the unoccupied subunits within the MOF cage to adsorb at the open Cu^{2+} sites and are subsequently oxidized in a charge transfer (e.g., electrons transferred from the analyte to the metal center). The net electron transfer reaction reduces the hole concentration to alter the conductivity and impedance of the sensor device. While we do not expect the analyte molecules to displace TCNQ from the host, the changes in the impedance suggest some adsorbate-induced changes in the SURMOF. We take the analyte concentration dependence of the $|S_{21}|$ (i.e., the slopes of the linear sections of the traces in Figure 6.7) as a measure of the ease of oxidation of the adsorbed analyte molecules (i.e., electron donation into the doped MOF complex). Figure 6.8 shows a correlation between the proposed ease of oxidation, i.e., the slopes of the linear sections of the traces in Figure 6.7 and representative electrooxidation potentials of the solvents molecules on an arbitral platinum-based catalyst obtained from the literature [47]. The strong correlation suggests that the insertion loss change depends on the thermodynamics of oxidation of the aliphatic alcohol analytes.

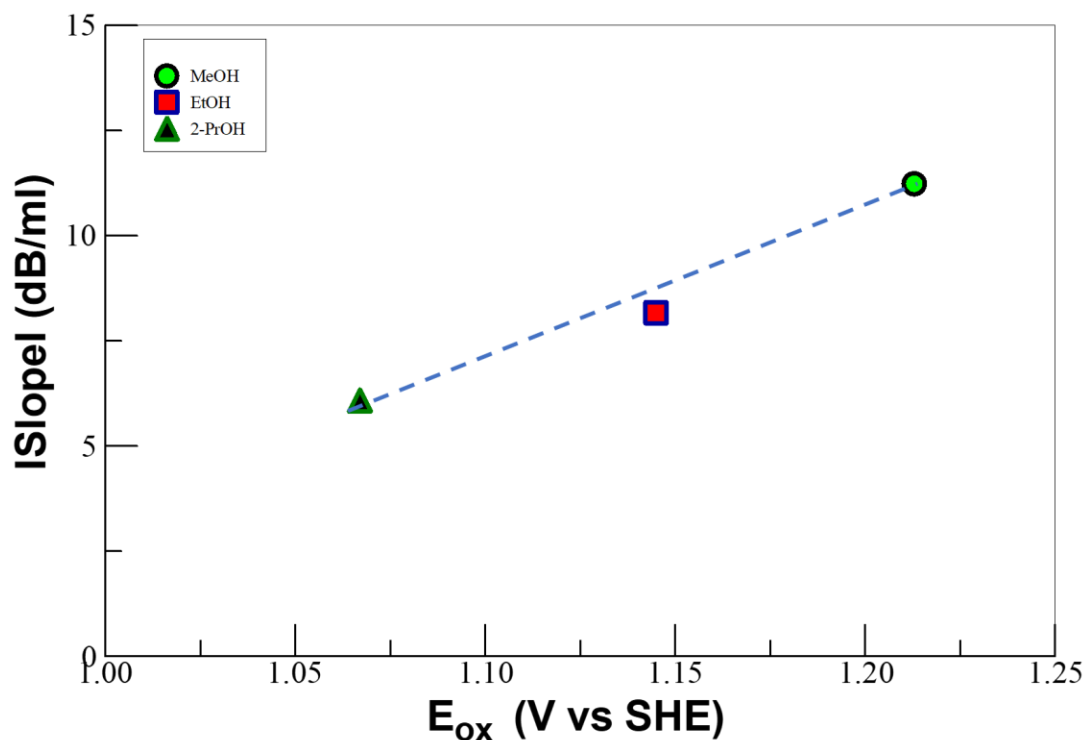


Figure 0.8. The dependence of the slope of the analyte volume dependence of insertion loss on the electrocatalytic oxidation potential of aliphatic alcohol analytes on a platinum-based catalyst, taken from Lammy et al. [47]. The blue dashed line is just a visual aid.

TABLE 0.1

Summary of $|S_{21}|$ -concentration plot features, and some salient physico-chemical properties of neat analytes.

Solvent	Dielectric Constant	Dipole Moment	Acceptor Number	Oxidation Potential (V/SHE) [45]	ΔG (kJmol ⁻¹)	Lower Detection Limit (ml)	Upper Linear Limit (ml)	Slope (dB/ml)
Methanol	32.7	1.7	41.5	0.016	-9.3	0.1	0.5	-11.228
Ethanol	24.5	1.69	37.9	0.084	-97.3	0.2	0.5	-8.160
2-Propanol	18	1.66	33.5	0.097	-168	0.3	0.5	-6.083
Acetone	20.7	2.85	12.5	-0.879		0.2	0.5	-2.440

In Figure 6.8, the S_{21} response to injected analyte volumes below 0.2 ml suggest anomalously high impedances, which seem to recover after exposing the films to higher volumes of solvent. Moreover, the $|S_{21}|$ -analyte concentration plots for 2-propanol, acetone, and methanol exhibit higher impedances than that of ethanol. These observations suggest that other factors, beyond redox thermodynamics, such as reduced mass transport, influence the VOC detection. Solvents are known to plasticize the outer layer of the MOF material, due to MOF destructuring at the film–air interface [13,48,49]. Thus, the reduced mass transport could be due to blocked pores at the film–air interface surface due to solvent-induced modifications of the outer surface of HKUST-1 SURMOF films, which impede the uptake and release of solvent by the films. Interestingly, the deconstructed surface can be regenerated when exposed to the synthesis solvents, i.e., ethanol in the case of HKUST-1 SURMOF, to allow improved analyte uptake by the film [13], as shown in Figure 6.7. Figure 6.9 shows the atomic force microscope (AFM)-measured surface roughness of HKUST-1 SURMOF films exposed to varying amounts of ethanol vapor at 65 °C. The data show that the initial surface plasticizes when exposed to small volumes of ethanol but recovers with increasing volumes of solvent exposure. The regeneration of the outer film surface in ethanol explains the observed lower impedances when ethanol is used as the analyte.

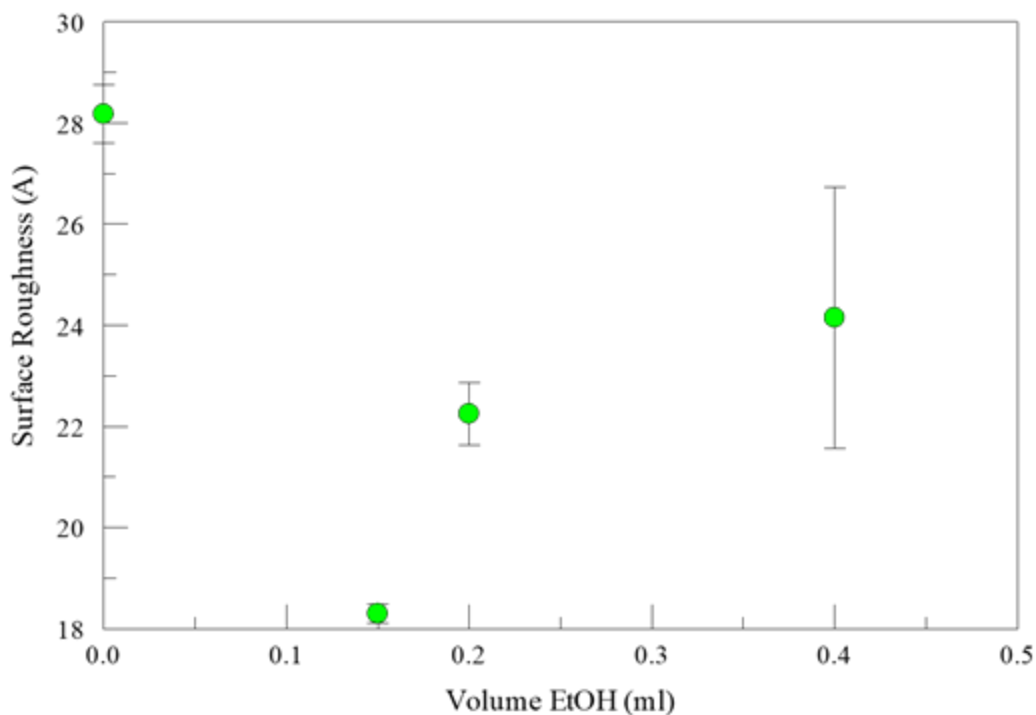


Figure 0.9. Surface roughness of HKUST-1 SURMOF films exposed to varying amounts of ethanol vapor at 65 °C showing initial surface plasticization and recovery with increasing volumes of solvent. The error bars represent the standard deviation of roughness measurements from at least three distinct areas on the sample surface.

The thermodynamic versus kinetic selectivity of the analyte oxidation was evaluated by challenging a fresh TCNQ-doped HKUST-1 SURMOF sample with a 1:1 volume mixture of methanol and ethanol at 65 °C in air. As shown in Figure 6.10, the data for the 1:1 MeOH-EtOH mixture, monitored at 0.5 GHz, completely overlap that for neat methanol (MeOH), i.e., the mixture response is identical to that of pure methanol. This indicates that the sensing agent is selective to methanol over ethanol, despite the surface deconstruction, which limits the mass transport of methanol into the pores of the SURMOF. The data also suggest that the methanol selectivity is kinetically driven, probably due to the differences in the analyte diffusion rates to the

metal sites; in turn, this is probably due to the SURMOF surface plasticization, as shown in Figure 7.

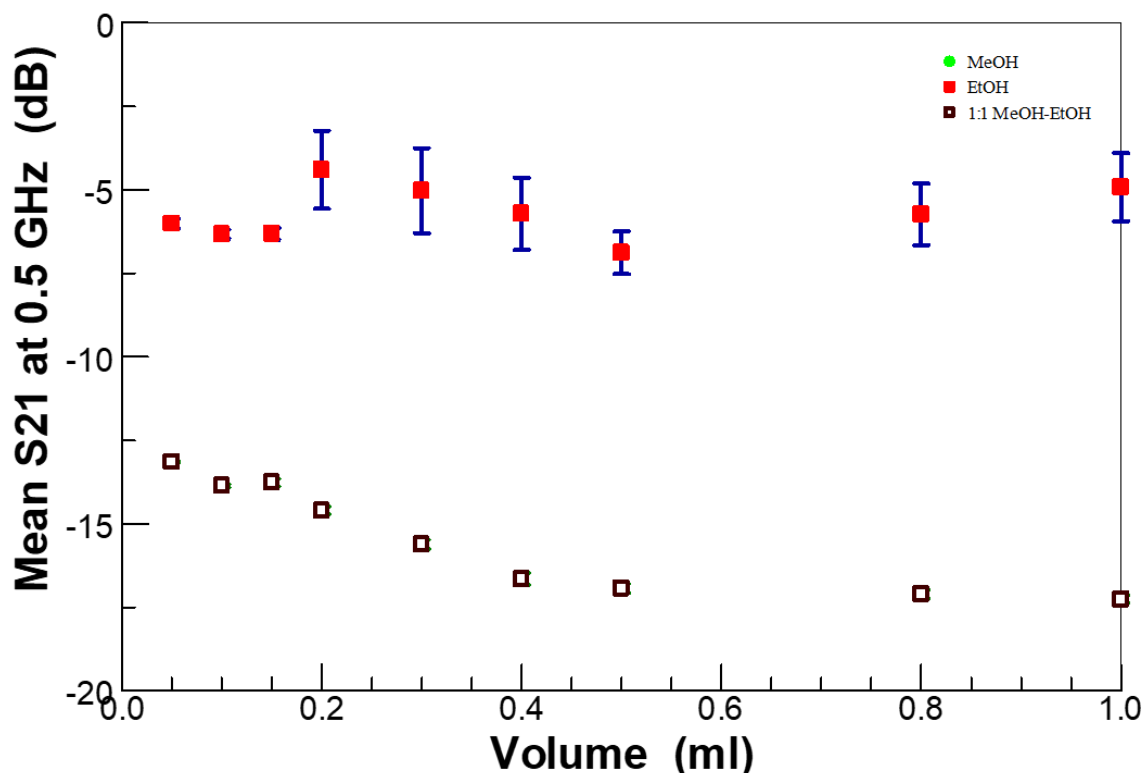


Figure 0.10. Comparison of solvent concentration dependence of microwave insertion loss amplitude (S_{21}) TCNQ-loaded HKUST-1 on Si substrate at 65 °C, in air, for methanol (MeOH), ethanol (EtOH), and 1:1 mixture of ethanol and methanol, monitored at 0.5 GHz. The 1:1 mixture of MeOH-EtOH designated by black symbols completely overlap those for pure methanol (MeOH) blocking the visibility of the green symbols. The error bars represent the standard deviation of at least three measurements.

Figure 6.11 shows the relationship between the slope of the analyte volume dependence of insertion loss, i.e., the slopes of the linear sections of the traces in Figure 5, and the Gutmann Acceptor (AN) of the analyte molecules studied, where the AN is a measure of the strength of solvents as Lewis acids [50]. While the alcohol analytes show a linear dependence on the AN,

acetone is off the line. This strongly suggests that the alcohol analyte and/or the oxidation products hydrogen bond within the HKUST-1 structure [6], possibly due to the pre-existing dopants at the color centers within the film [30]. This hydrogen bonding may also explain the reduced diffusion of analyte molecules into the MOF film [51]. Taken together, the sensitivity of VOC detection depends on the diffusion rate of the analyte molecule and the ease of charge transfer at the active metal sites.

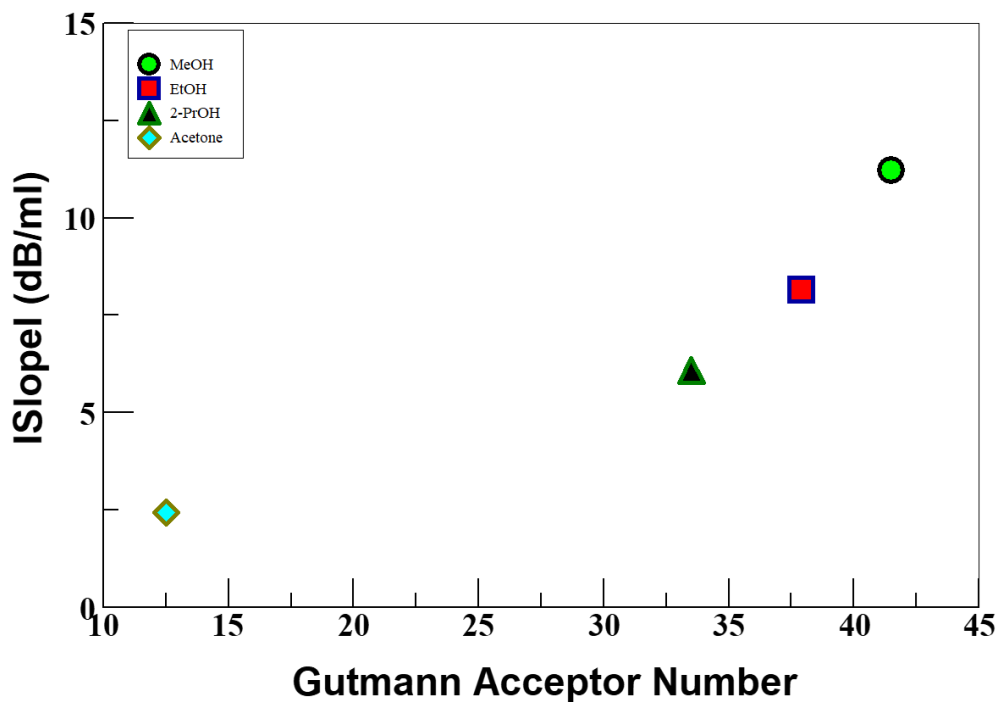


Figure 0.11. The relationship between the slope of the analyte volume dependence of insertion loss and the Gutmann Acceptor (AN). AN is a measure of hydrogen bond acidity, and the linear relationship suggests that the analyte molecules and/or the oxidation products form hydrogen bonds within the HKUST-1 structure.

6.3.3 Proposed Mechanism for BDS Detection of Aliphatic Alcohols in HKUST-1 MOF

Metal organic frameworks have been shown to be efficient electrode modifiers in the selective electro-oxidation of alcohols into carbonyl compounds [52,53] and acids [54]. Analyte ingress and subsequent confinement, within the MOF, appear to be critical to the success of these oxidation reactions. We have previously proposed the following set of conceivable elementary steps involved in the BDS detection of aliphatic alcohols with TCNQ-doped HKUST-1 SURMOF [20].

1. Analyte molecules diffuse into accessible cavities to interact with the open Cu^{2+} active sites, some of which exist as Cu^{2+} - Cu^+ - O_2 defects, in the SURMOF. These defects appear to be responsible for many of the electronic properties of the SURMOF films [12,32]. The introduction of the analyte molecules also induces distortion of the mechanical structure, as well as changes in the electronic band structure that lead to changes in the conductivity of the MOF. In a pure nitrogen ambient, the N_2 adsorbs on the metal sites [55], but in the presence of Lewis base molecules, such as aliphatic alcohols, the analyte is expected to displace pre-adsorbed N_2 molecules to form adducts from the open metal sites.
2. The aliphatic alcohol probably associates with the binuclear copper-oxo defects [32], or coordinates to the open metal center, via the hydroxyl-oxygen atom. The confined alcohol analyte is aerobically oxidized by the Cu sites [56] into carbonyl compounds (e.g., aldehydes from the primary) at room temperature [57], with electrons transferred into the MOF from the alcohol. This step is dependent on the presence of oxygen in the ambient conditions within the reactor, which is required for the reoxidation of the Cu(I) to Cu(II) . The oxidative abilities of HKUST-1 MOF films are attributable to the presence of mixed valent-Cu-oxo defects [33], which behave like aerobic functions such as in respiration

[58]. These mixed valent Cu-oxo centers in the defective MOF are critical for the spontaneous oxidation of alcohols in aerobic conditions [4,59,60].

Mechanistic studies [16,61] of Cu-catalyzed oxidation of alcohols under aerobic conditions suggest an initial hydrogen atom abstraction via a cupric-superoxide complex in which an O-coordinated alcoholate undergoes an H-abstraction reaction from the α -carbon atom of the alcoholate. This generates a bound ketyl radical which then converts intramolecularly into aldehyde, via a one-electron reduction of the Cu (II) into a Cu-I center [62]. Such redox reactions at the metal centers should be readily detected by BDS because of the expected changes in the conductivity of the device under test (DUT) [4]. The resultant carbonyl compounds are also more polarizable and will contribute to the observed increased insertion loss.

The open metal sites in the HKUST-1 MOF, formed by removing axial ligands and/or the defective metal sites, strongly coordinate to electron rich species (i.e., Lewis bases). Small molecules, such as short-chained aliphatic alcohols, reversibly adsorb at the available open metal centers in the MOF cavity inducing changes in its physicochemical properties [4,59,63]. The adsorption and reaction at the metal sites also result in changes in interfacial polarization and permittivity, which should be readily detected by microwave energy dissipation [64]. Furthermore, microwave (MW) irradiation is known to promote the rapid and selective oxidation of alcohols to carbonyl compounds as the microwave irradiation promotes faster and more efficient internal heating through direct interaction between microwave energy and the reactants [65–67]. Thus, we expect the adsorbed aliphatic alcohol analyte at the open Cu sites in the host MOF sites to be aerobically oxidized into aldehydes [68] as the basis of VOC detection with MOF thin films [18]. Furthermore, microwave (MW) irradiation is known to rapidly convert alcohols to carbonyl compounds over transition metal catalysts [69], probably due to more efficient internal heating

within the reactants [65–67], the creation of localized plasmon resonance-like “hot spots” in the metal support [70], or some specific microwave effects on chemical reactions [71].

6.4 Conclusions

By observing microwave signal attenuation in different sensor material systems, we demonstrated physics consistent with chemo-induced changes in the electrical properties of the TCNQ-doped HKUST-1 SURMOF sensing media in the detection of volatile solvents (i.e., methanol, ethanol, 2-propanol, and acetone) at 65 °C. The microwave signal attenuation, possibly due to resistance increases, is attributed to majority carrier (hole) annihilation from the electrons donated into the extended hybrid molecular orbital network of the TCNQ-HKUST-1 complex during the analyte oxidation. The VOC analyte specific detection sensitivity depends on the ease of oxidation, i.e., the oxidation potential, of the analyte. Unfortunately, the analyte degrades the surface of the SURMOF to form a plasticized skin that impedes the analyte’s diffusion into the porous medium. This results in the underutilization of a tremendous volume of the sensing media.

References

- [1] Korotcenkov, G. *Chemical Sensors: Comprehensive Sensor Technologies Volume 4: Solid State Devices*; Momentum Press: New York, NY, USA, 2011
- [2] Gopel, W. Chemisorption and charge-transfer at ionic semiconductor surfaces—Implications in designing gas sensors. *Prog. Surf. Sci.* 1985, 20, 9–103. [https://doi.org/10.1016/0079-6816\(85\)90004-8](https://doi.org/10.1016/0079-6816(85)90004-8).
- [3] Dey, A. Semiconductor metal oxide gas sensors: A review. *Mater. Sci. Eng. B* 2018, 229, 206–217.
- [4] (a) Park, C., Koo, W.-T., Chong, S., Shin, H., Kim, Y. H., Cho, H.-J., Jang, J.-S., Kim, D.-H., Lee, J., Park, S., Ko, J., Kim, J., Kim, I.-D., Confinement of Ultrasmall Bimetallic Nanoparticles in Conductive Metal–Organic Frameworks via Site-Specific Nucleation. *Adv. Mater.* 2021, 33, 2101216. <https://doi.org/10.1002/adma.202101216>. (b) Zhong, H.,

- Ghorbani-Asl, M., Ly, K.H. et al. Synergistic electroreduction of carbon dioxide to carbon monoxide on bimetallic layered conjugated metal-organic frameworks. *Nat Commun* 11, 1409 (2020). <https://doi.org/10.1038/s41467-020-15141-y>.
- [5] Ma, D.; Li, Z.; Zhu, J.; Zhou, Y.; Chen, L.; Mai, X.; Liufu, M.; Wu, Y.; Li, Y. Inverse and highly selective separation of CO₂/C₂H₂ on a thulium–organic framework. *J. Mater. Chem. A* 2020, 8, 11933–11937.
- [6] Kreno, L.E.; Leong, K.; Farha, O.K.; Allendorf, M.; Van Duyne, R.P.; Hupp, J.T. Metal–organic framework materials as chemical sensors. *Chem. Rev.* 2012, 112, 1105–1125. <https://doi.org/10.1021/cr200324t>.
- [7] Homayoonnia, S.; Zeinali, S. Design and fabrication of capacitive nanosensor based on MOF nanoparticles as sensing layer for VOCs detection. *Sens. Actuators B Chem.* 2016, 237, 776–786.
- [8] Ali, A.; Alzamly, A.; Greish, Y.E.; Bakiro, M.; Nguyen, H.L.; Mahmoud, S.T. A highly sensitive and flexible metal-organic framework polymer-based H₂S gas sensor. *ACS Omega* 2021, 6, 17690–17697. <https://doi.org/10.1021/acsomega.1c02295>.
- [9] Chowdhury, S.; Torad, N.L.; Ashok, A.; Gumilar, G.; Chaikittisilp, W.; Xin, R.; Cheng, P.; Ul Hoque, M.I.; Wahab, M.A.; Karim, M.R.; et al. Template- and etching-free fabrication of two-dimensional hollow bimetallic metal-organic framework hexagonal nanoplates for ammonia sensing. *Chem. Eng. J.* 2022, 450, 138065.
- [10] Qin, P.; Day, B.A.; Okur, S.; Li, C.; Chandresh, A.; Wilmer, C.E.; Heinke, L. VOC mixture sensing with a MOF film sensor array: detection and discrimination of Xylene Isomers and their Ternary Blends. *ACS Sensors* 2022, 7, 1666–1675. <https://doi.org/10.1021/acssensors.2c00301>.
- [11] R. Kenji Sumida, Jarad A. Mason, Thomas M. McDonald, Eric D. Bloch, Zoey R. Herm, Tae-Hyun Bae, and Jeffrey R. Long, "Carbon Dioxide Capture in Metal–Organic Frameworks," *Chemical Reviews* vol. 112 no. 2, pp. 724-781, 2012, doi: 10.1021/cr2003272.
- [12] Heinke, L.; Wöll, C. Surface-mounted metal–organic frameworks: Crystalline and porous molecular assemblies for fundamental insights and advanced applications. *Adv. Mater.* 2019, 31, 1806324.
- [13] Müller, K.; Vankova, N.; Schöttner, L.; Heine, T.; Heinke, L. Dissolving uptake-hindering surface defects in metal–organic frameworks. *Chem. Sci.* 2019, 10, 153–160. <https://doi.org/10.1039/C8SC03735C>.
- [14] K. Z. Xin Chen, Zeinab Mohamed Hassan, Engelbert Redel and Helmut Baumgart, "Charge. transport, conductivity and Seebeck coefficient in pristine and TCNQ loaded preferentially grown metal-organic framework films," *Journal of Physics: Condensed Matter*, vol. 34, no. 40, p. 404001, 2022 doi: 10.1088/1361-648X/abe72f.
- [15] Babaei, H.; DeCoster, M.E.; Jeong, M.; Hassan, Z.M.; Islamoglu, T.; Baumgart, H.; McGaughey, A.J.H.; Redel, E.; Farha, O.K.; Hopkins, P.E.; et al. Observation of reduced

- thermal conductivity in a metal-organic framework due to the presence of adsorbates. *Nat. Commun.* 2020, 11, 4010. <https://doi.org/10.1038/s41467-020-17822-0>.
- [16] DeCoster, M.E.; Babaei, H.; Jung, S.S.; Hassan, Z.M.; Gaskins, J.T.; Giri, A.; Tiernan, E.M.; Tomko, J.A.; Baumgart, H.; Norris, P.M.; et al. Hybridization from guest–host interactions reduces the thermal conductivity of metal–organic frameworks. *J. Am. Chem. Soc.* 2022, 144, 3603–3613. <https://doi.org/10.1021/jacs.1c12545>.
- [17] Babal, A.S.; Mollick, S.; Kamal, W.; Elston, S.; Castrejón-Pita, A.A.; Morris, S.M.; Tan, J.-C. Parts-per-billion (ppb) selective iodine sensors leveraging metal–organic framework nanoenvironment. *Mater. Today* 2022, <https://doi.org/10.1016/j.mattod.2022.07.001>.
- [18] Rydosz, A.; Maciak, E.; Wincza, K.; Gruszczynski, S. Microwave-based sensors with phthalocyanine films for acetone, ethanol and methanol detection. *Sens. Actuators B Chem.* 2016, 237, 876–886.
- [19] Amoah, P.K.; Lin, P.; Baumgart, H.; Franklin, R.; Obeng, Y.S. Broadband dielectric spectroscopic detection of volatile organic compounds with ZnO nanorod gas sensors. *J. Phys. D Appl. Phys.* 2020, 54, 135104. <https://doi.org/10.1088/1361-6463/abd3ce>.
- [20] Amoah, P.K.; Hassan, Z.M.; Lin, P.; Redel, E.; Baumgart, H.; Obeng, Y.S. Broadband dielectric spectroscopic detection of ethanol: A side-by-side comparison of ZnO and HKUST-1 MOFs as sensing media. *Chemosensors* 2022, 10, 241.
- [21] Li, F.; Zheng, Y.; Hua, C.; Jian, J. Gas sensing by microwave transduction: Review of progress and challenges. *Front. Mater.* 2019, 6, 101. <https://doi.org/10.3389/fmats.2019.00101>.
- [22] Broadband Dielectric Spectroscopy; Woodward, W.H.H., Ed.; American Chemical Society: Washington, DC, USA, 2021; <https://doi.org/10.1021/bk-2021-1375>.
- [23] Badalyan, A.; Stahl, S.S. Cooperative electrocatalytic alcohol oxidation with electron-proton-transfer mediators. *Nature* 2016, 535, 406–410. <https://doi.org/10.1038/nature18008>.
- [24] Kremer, F.; Schönhals, A. Broadband Dielectric Spectroscopy, 1st ed.; Friedrich Kremer, A.S., Ed.; Springer: Berlin/Heidelberg, Germany, 2003; <https://doi.org/10.1007/978-3-642-56120-7>.
- [25] Entesari, K.; Ghiri, R.E.; Kaya, E. Broadband dielectric spectroscopy: recent developments in microwave time-domain techniques. *IEEE Microw. Mag.* 2021, 22, 26–48. <https://doi.org/10.1109/MMM.2021.3064100>.
- [26] Collin, R.E. Foundations for Microwave Engineering, 2nd ed.; Wiley-Interscience, New York, NY 2001.
- [27] Wilson, P. The Circuit Designer's Companion; Newnes: Oxford, UK, 2012; <https://doi.org/10.1016/c2010-0-66361-9>.
- [28] Chen, X.; Zhang, K.; Hassan, Z.M.; Redel, E.; Baumgart, H. Charge transport, conductivity and seebeck coefficient in pristine and TCNQ loaded preferentially grown metal-organic framework films. *J. Phys. Condens. Matter* 2022, 34, abe72f.

- [29] Arslan, H.K.; Shekhah, O.; Wohlgemuth, J.; Franzreb, M.; Fischer, R.A.; Wöll, C. High-throughput fabrication of uniform and homogenous MOF coatings. *Adv. Funct. Mater.* 2011, 21, 4228–4231.
- [30] James J. Calvo, Sydney M. Angel, and Monica C. So, "Charge transport in metal–organic frameworks for electronics applications", *APL Materials* 8, 050901 (2020) <https://doi.org/10.1063/1.5143590>
- [31] Sundriyal, S.; Shrivastav, V.; Bhardwaj, S.K.; Mishra, S.; Deep, A. Tetracyanoquinodimethane doped copper-organic framework electrode with excellent electrochemical performance for energy storage applications. *Electrochim. Acta* 2021, 380, 138229.
- [32] Müller, K.; Fink, K.; Schöttner, L.; Koenig, M.; Heinke, L.; Wöll, C. Defects as color centers: The apparent color of metal–organic frameworks containing Cu²⁺-based paddle-wheel units. *ACS Appl. Mater. Interfaces* 2017, 9, 37463–37467. <https://doi.org/10.1021/acsami.7b12045>.
- [33] Wang, W.; Sharapa, D.I.; Chandresh, A.; Nefedov, A.; Heißler, S.; Heinke, L.; Studt, F.; Wang, Y.; Wöll, C. Interplay of electronic and steric effects to yield low-temperature CO oxidation at metal single sites in defect-engineered HKUST-1. *Angew. Chem. Int. Ed.* 2020, 59, 10514–10518.
- [34] Pozar, D.M. *Microwave Engineering*, 4th ed.; J. Wiley: Hoboken, NJ, USA, 2012.
- [35] Hassan, Z.M.A. *The Photophysical Properties of Chromophores Assembled into Metal–Organic Framework Thin-Films*. Ph.D. Thesis, Karlsruher Institut für Technologie (KIT), Karlsruhe, Germany, 2021.
- [36] Rivera-Torrente, M.; Filez, M.; Schneider, C.; van der Feltz, E.C.; Wolkersdörfer, K.; Taffa, D.H.; Wark, M.; Fischer, R.A.; Weckhuysen, B.M. Micro-spectroscopy of HKUST-1 metal–organic framework crystals loaded with tetracyanoquinodimethane: Effects of water on host–guest chemistry and electrical conductivity. *Phys. Chem. Chem. Phys.* 2019, 21, 25678–25689. <https://doi.org/10.1039/C9CP05082E>.
- [37] Strauss, I.; Mundstock, A.; Treger, M.; Lange, K.; Hwang, S.; Chmelik, C.; Rusch, P.; Bigall, N.C.; Pichler, T.; Shiozawa, H.; et al. Metal–organic framework Co-MOF-74-Based host–guest composites for resistive gas sensing. *ACS Appl. Mater. Interfaces* 2019, 11, 14175–14181. <https://doi.org/10.1021/acsami.8b22002>.
- [38] Talin, A.A.; Centrone, A.; Ford, A.C.; Foster, M.E.; Stavila, V.; Haney, P.; Kinney, R.A.; Szalai, V.; Gabaly, F.E.; Yoon, H.P.; et al. Tunable electrical conductivity in metal-organic framework thin-film devices. *Science* 2014, 343, 66–69. <https://doi.org/10.1126/science.1246738>.
- [39] Erickson, K.J.; Léonard, F.; Stavila, V.; Foster, M.E.; Spataru, C.D.; Jones, R.E.; Foley, B.M.; Hopkins, P.E.; Allendorf, M.D.; Talin, A.A. Thin film thermoelectric metal–organic framework with high seebeck coefficient and low thermal conductivity. *Adv. Mater.* 2015, 27, 3453–3459.

- [40] Liu, J.; Wächter, T.; Irmeler, A.; Weidler, P.G.; Gliemann, H.; Pauly, F.; Mugnaini, V.; Zharnikov, M.; Wöll, C. Electric transport properties of surface-anchored metal-organic frameworks and the effect of ferrocene loading. *ACS Appl. Mater. Interfaces* 2015, 7, 9824–9830. <https://doi.org/10.1021/acsami.5b01792>.
- [41] Janczak, J.; Prochowicz, D.; Lewiński, J.; Fairen-Jimenez, D.; Bereta, T.; Lisowski, J. Trinuclear cage-like ZnII macrocyclic complexes: Enantiomeric recognition and gas adsorption properties. *Chem. A Eur. J.* 2016, 22, 598–609.
- [42] Deegan, M.M.; Dworzak, M.R.; Gosselin, A.J.; Korman, K.J.; Bloch, E.D. Gas storage in porous molecular materials. *Chem. A Eur. J.* 2021, 27, 4531–4547.
- [43] Collier-Oxandale, A.M.; Thorson, J.; Halliday, H.; Milford, J.; Hannigan, M. Understanding the ability of low-cost MOx sensors to quantify ambient VOCs. *Atmos. Meas. Tech.* 2019, 12, 1441–1460. <https://doi.org/10.5194/amt-12-1441-2019>.
- [44] Loera-Serna, S.; Oliver-Tolentino, M.A.; de Lourdes López-Núñez, M.; Santana-Cruz, A.; Guzmán-Vargas, A.; Cabrera-Sierra, R.; Beltrán, H.I.; Flores, J. Electrochemical behavior of [Cu₃(BTC)₂] metal–organic framework: The effect of the method of synthesis. *J. Alloy. Compd.* 2012, 540, 113–120.
- [45] Hendon, C.H.; Walsh, A. Chemical principles underpinning the performance of the metal–organic framework HKUST-1. *Chem. Sci.* 2015, 6, 3674–3683. <https://doi.org/10.1039/C5SC01489A>.
- [46] Chou, J. *Hazardous Gas Monitors: A Practical Guide to Selection, Operation and Applications*, 1st ed.; McGraw-Hill: New York, NY, USA, 2000.
- [47] Lamy, C.; Belgsir, E.M.; Léger, J.M. Electrocatalytic oxidation of aliphatic alcohols: Application to the direct alcohol fuel cell (DAFC). *J. Appl. Electrochem.* 2001, 31, 799–809. <https://doi.org/10.1023/A:1017587310150>.
- [48] Heinke, L.; Gu, Z.; Wöll, C. The surface barrier phenomenon at the loading of metal-organic frameworks. *Nature Communications* 2014, 5, 4562. <https://doi.org/10.1038/ncomms5562>.
- [49] Chevalier, V.; Martin, J.; Peralta, D.; Roussey, A.; Tardif, F. Performance of HKUST-1 Metal-Organic Framework for a VOCs mixture adsorption at realistic concentrations ranging from 0.5 to 2.5 ppmv under different humidity conditions. *J. Environ. Chem. Eng.* 2019, 7, 103131.
- [50] Gutmann, V.; Gutmann, V. *The Donor-Acceptor Approach to Molecular Interactions*; Springer: New York, NY, USA, 1978; Volume 228.
- [51] Tan, K.; Jensen, S.; Zuluaga, S.; Chapman, E.K.; Wang, H.; Rahman, R.; Cure, J.; Kim, T.-H.; Li, J.; Thonhauser, T.; et al. Role of hydrogen bonding on transport of coadsorbed gases in metal–organic frameworks materials. *J. Am. Chem. Soc.* 2018, 140, 856–859. <https://doi.org/10.1021/jacs.7b09943>.
- [52] Khakyzadeh, V.; Sediqi, S. The electro-oxidation of primary alcohols via a coral-shaped cobalt metal–organic framework modified graphite electrode in neutral media. *Sci. Rep.* 2022, 12, 8560. <https://doi.org/10.1038/s41598-022-12200-w>.

- [53] Guo, P.; Froese, C.; Fu, Q.; Chen, Y.-T.; Peng, B.; Kleist, W.; Fischer, R.A.; Muhler, M.; Wang, Y. CuPd mixed-metal HKUST-1 as a catalyst for aerobic alcohol oxidation. *J. Phys. Chem. C* 2018, 122, 21433–21440. <https://doi.org/10.1021/acs.jpcc.8b05882>.
- [54] Greco, R.; Tiburcio-Fortes, E.; Fernandez, A.; Marini, C.; Vidal-Moya, A.; Oliver-Meseguer, J.; Armentano, D.; Pardo, E.; Ferrando-Soria, J.; Leyva-Pérez, A. MOF-stabilized perfluorinated palladium cages catalyze the additive-free aerobic oxidation of aliphatic alcohols to acids. *Chem. A Eur. J.* 2022, 28, e202103781.
- [55] Bordiga, S.; Regli, L.; Bonino, F.; Groppo, E.; Lamberti, C.; Xiao, B.; Wheatley, P.S.; Morris, R.E.; Zecchina, A. Adsorption properties of HKUST-1 toward hydrogen and other small molecules monitored by IR. *Phys. Chem. Chem. Phys.* 2007, 9, 2676–2685. <https://doi.org/10.1039/B703643D>.
- [56] Rubio-Giménez, V.; Almora-Barrios, N.; Escorcía-Ariza, G.; Galbiati, M.; Sessolo, M.; Tatay, S.; Martí-Gastaldo, C. Origin of the chemiresistive response of ultrathin films of conductive metal–organic frameworks. *Angew. Chem. Int. Ed.* 2018, 57, 15086–15090.
- [57] Koo, W.-T.; Jang, J.-S.; Kim, I.-D. Metal-organic frameworks for chemiresistive sensors. *Chem* 2019, 5, 1938–1963. <https://doi.org/10.1016/j.chempr.2019.04.013>.
- [58] Ho, R.Y.N.; Liebman, J.F.; Valentine, J.S. Biological reactions of dioxygen: An introduction. In *Active Oxygen in Biochemistry*, Valentine, J.S., Foote, C.S., Greenberg, A., Liebman, J.F., Eds.; Springer: Dordrecht, The Netherlands, 1995; pp. 1–36, https://doi.org/10.1007/978-94-011-0609-2_1.
- [59] Cadman, L. Multi-Component Metal-Organic Frameworks. Ph.D. Thesis, University of Bath, Bath, UK, 2017.
- [60] Sun, L.; Hendon, C.H.; Minier, M.A.; Walsh, A.; Dincă, M. Million-fold electrical conductivity enhancement in Fe₂(DEBDC) versus Mn₂(DEBDC) (E = S, O). *J. Am. Chem. Soc.* 2015, 137, 6164–6167. <https://doi.org/10.1021/jacs.5b02897>.
- [61] Dhakshinamoorthy, A.; Asiri, A.M.; Garcia, H. Tuneable nature of metal organic frameworks as heterogeneous solid catalysts for alcohol oxidation. *Chem. Commun.* 2017, 53, 10851–10869. <https://doi.org/10.1039/C7CC05927B>.
- [62] Chaudhuri, P.; Hess, M.; Müller, J.; Hildenbrand, K.; Bill, E.; Weyhermüller, T.; Wieghardt, K. Aerobic oxidation of primary alcohols (including methanol) by Copper(II)– and Zinc(II)–Phenoxyl radical catalysts. *J. Am. Chem. Soc.* 1999, 121, 9599–9610. <https://doi.org/10.1021/ja991481t>.
- [63] Huang, Y.-R.; Liu, K.-H.; Mou, C.-Y.; Sun, C.-K. Relaxation dynamics of surface-adsorbed water molecules in nanoporous silica probed by terahertz spectroscopy. *Appl. Phys. Lett.* 2015, 107, 081607.
- [64] Sachdeva, S.; Koper, S.J.H.; Sabetghadam, A.; Soccol, D.; Gravesteijn, D.J.; Kapteijn, F.; Sudhölter, E.J.R.; Gascon, J.; de Smet, L.C.P.M. Gas phase sensing of alcohols by metal organic framework-polymer composite materials. *ACS Appl. Mater. Interfaces* 2017, 9, 24926–24935. <https://doi.org/10.1021/acsami.7b02630>.

- [65] Sutradhar, M.; Alegria, E.C.B.A.; Barman, T.R.; Guedes da Silva, M.F.C.; Liu, C.-M.; Pombeiro, A.J.L. 1D Copper(II)-Aroylhydrazone coordination polymers: magnetic properties and microwave assisted oxidation of a secondary alcohol. *Front. Chem.* 2020, 8, 157. <https://doi.org/10.3389/fchem.2020.00157>.
- [66] Hazra, S.; Martins, L.M.D.R.S.; Guedes da Silva, M.F.C.; Pombeiro, A.J.L. Sulfonated Schiff base copper(ii) complexes as efficient and selective catalysts in alcohol oxidation: Syntheses and crystal structures. *RSC Adv.* 2015, 5, 90079–90088. <https://doi.org/10.1039/C5RA19498A>.
- [67] Polshettiwar, V.; Varma, R.S. Microwave-assisted organic synthesis and transformations using benign reaction media. *Acc. Chem. Res.* 2008, 41, 629–639. <https://doi.org/10.1021/ar700238s>.
- [68] Silva, T.F.S.; Martins, L.M.D.R.S. Recent advances in copper catalyzed alcohol oxidation in homogeneous medium. *Molecules* 2020, 25, 748.
- [69] Horikoshi, S.; Watanabe, T.; Narita, A.; Suzuki, Y.; Serpone, N. The electromagnetic wave energy effect(s) in microwave-assisted organic syntheses (MAOS). *Sci. Rep.* 2018, 8, 5151. <https://doi.org/10.1038/s41598-018-23465-5>.
- [70] Huang, K.; Liu, N.; Liu, C.; Yan, L. Preliminary analysis of chemical reaction under the radiation of electromagnetic wave. *Chin. Sci. Bull.* 2000, 45, 1821–1824. <https://doi.org/10.1007/BF02886276>.
- [71] Maes, B.; Marimuthu, T.; Alapour, S.; Friedrich, H.B. Microwave-assisted oxidation reaction of primary alcohols with sensitive functional groups to aldehydes using ruthenium diphosphorus complexes. *Arkivoc* 2020, 2020, 120–135. <https://doi.org/10.24820/ark.5550190.p011.197>.
- [72] Stavila, V.; Talin A.A.; Allendorf, M.D. MOF-based electronic and opto-electronic devices. *Chem. Soc. Rev.*, 2014, 43, 5994–6010. <https://doi.org/10.1039/C4CS00096J>

CHAPTER 7

SIDE BY SIDE COMPARISON - ZnO VS MOF FILMS AS SENSING MEDIA

Part of this chapter is an adaptation from a reprint from Papa K. Amoah, Zeinab M. Hassan, Pengtao Lin, Helmut Baumgart, Engelbert Redel, and Yaw S. Obeng; “Broadband Dielectric Spectroscopic Detection of Ethanol: A Side-by-Side Comparison of ZnO and HKUST-1 MOFs as Sensing Media,” *Chemosensors*, vol. 10, no. 7, p. 241, 2022, doi: 10.3390/chemosensors10070241 with permission from MDPI Publishing.

7.1 Introduction

7.1.1 Volatile Organic Compounds (VOC) Detection

Intrinsic material property changes due to analyte adsorption and reactions of the sensing materials are the basis of many conductometric chemical sensors [1-3]. In gas sensing applications, most of the sensing materials tend to be metal oxides (MO, mostly II-VI semiconductors) due to their low cost, simple design and ease of production, short response time, wide detection range, and resistance to harsh working environments [4]. For these chemical sensors to be successful, there must be (i) charge transfer between the analyte and the sensing materials, and (ii) a reversible analyte concentration dependence of the measurand [5]. Along these lines, there is a need for effective and efficient methods to monitor volatile organic compounds (VOCs). Highly sensitive analytical chemistry techniques, such as spectrophotometry, fluorometry, gas chromatography (GC) and high-performance liquid chromatography (HPLC) have been used for the accurate quantification of VOCs. However, these techniques are expensive, bulky, have low throughput, require time consuming pre-treatment steps and highly skilled operators, consume substantial amounts of power, and do not provide real-time information for risk mitigations and decision

making [6]. These limitations preclude most of the current VOC detection techniques from being used in the internet of things (IoT, internet edge) applications.

For IoT applications, the sensor should be small, inexpensive, and fast, with high sensitivity, selectivity, and stability for specific applications [7-9]. Emerging 2D-material, such as graphene, graphene oxide, phosphorene, and transition metal dichalcogenides such (e.g., MoS₂), as well as carbon nanotubes (CNTs), are being co-integrated with digital devices into viable gas sensors, mostly as chemically sensitive resistors (chemoresistors), chemically sensitive field effect transistors (chemFETs), or carbon nanotube field effect transistors (CNTFETs). For example, MoS₂ chemoresistors have been shown to be sensitive to different organic compounds including triethylamine (TEA) and acetone, with detection limits as low as 0.16 parts-per-trillion for nitric oxide gas molecules. In addition to changing the channel resistance, analyte specific changes to the low frequency 1/f noise spectra of graphene chemFETs may be used as a VOC detection measurand in these chemFETs [10]. The selectivity and sensitivity of 2D-material sensors can be tuned with chemical functionalization of the surface of the sensing-material. These devices can be further optimized with device gate bias adjustments to electrostatically change the carrier concentration in the channel to an optimal point [10]. Advances in heterogenous integration schemes are leveraging these emerging materials into three dimensional (3-D) sensors design for IoT applications; for example, a single chip CNTFET nanosystem that senses, stores the data, and classifies ambient gases has been demonstrated [11].

Unfortunately, many of these chemFETs and chemoresistors require energy-intensive internal heating for optimal operation [12]. For IoT and autonomous applications, new metrology that do not require high temperature for transduction, such as analyte-induced volume, and surface capacitance, changes are needed [12]. Metal-organic frameworks (MOFs) have emerged as a novel

class of tunable electronic nanomaterials; they combine the advantages of long-range order of inorganic conductors with the synthetic flexibility of organic semiconductors [13]. These MOF's have the potential to overcome many of the challenges of selectivity that limit other sensor materials that depend on charge transfer processes to change resistivity [14, 15]. While altering band structures in MOF-based sensors from analyte surface reactions, similar to those in the metal-oxide semiconductor, is possible [5, 16], the ultra-large surface areas, high porosity, and the ability to form coordination complex clathrates-like structures with analyte molecules make the MOFs attractive for selective gas sensing [17]. Furthermore, many of these MOF-based gas sensors work at room temperature, negating the need for heating [17, 12].

In addition, the resistivity measurements of the chemoresistor-based sensors necessarily involve making electrical contacts to the sensing materials. This can introduce non-negligible contact impedance in series with the sensing materials, especially in the two-pole measurement techniques often used with the coulometric gas sensors. In such systems, the errors from the connecting cables can be significant, especially when the resistance of the sample is lower than approximately $50\ \Omega$ [18]. Non-contact microwave gas sensing is emerging as an alternative to coulometric gas sensing; a microwave resonant cavity technique has also been used to detect and to distinguish between methanol, ethanol and acetone in the 0-200 ppm range at room temperature [19]. Capacitive sensing of VOC, with a dielectric layer comprised of compacted Cu-BTC nanoparticles has also been demonstrated [17]. However, the performance metrics of these microwave gas sensors, such as selectivity, sensitivity, reproducibility, and long-term stability are currently not yet well established. Furthermore, the impact of environmental factors such as temperature and humidity are currently not well understood. [20] Thus, there is a need to improve our fundamental knowledge of microwave gas sensors.

The mechanisms involved in chemo resistive gas sensing are not well understood. For example, while transduction in the metal oxides are temperature dependent, the mechanisms behind the temperature dependence are not well understood [21]. Similarly, the mechanisms underpinning MOF-based gas sensing are currently not fully understood [12]; presumably, the analyte molecules oxidize when they contact the sensing materials [14]. In traditional conductometric sensing, the redox reactions convert analyte-sensor interactions into measurable DC-resistance through changes in electrical resistivity because of electron injection into, or withdrawal of electrons from, the electronic conduction band structure of the sensing element [22, 23]. In this regard the electrically active defects in the MOF materials appear to behave like those in semiconducting metal oxides [16]. Here, we compare low temperature sensing of ethanol on substrate anchored ZnO nanorods and TCNQ-doped HKUST-1 MOF, through microwave impedance changes, to gain mechanistic insights into the microwave sensing of ethanol vapor. The TCNQ-doped HKUST-1 SURMOF provides a well characterized platform for such investigations [24]. The MOFs utilized in this study are referred to as HKUST-1, which is an abbreviation derived from Hong Kong University of Science and Technology-1, and is denoted by the chemical formula $\text{Cu}_3(\text{BTC})_2(\text{H}_2\text{O})_3]_n$. HKUST-1 surface-anchored MOF thin films (SURMOFs) doped with TCNQ [7,7,8,8-tetracyano-quinodimethane] are a well-established platform for investigating selective gas detection (Figure 7.1). The incorporation of TCNQ is aimed at adjusting the electrical conductivity of the HKUST-1 material [25].

We have shown elsewhere that the thermal conductivities of SURMOF films are commensurate with their single crystalline MOF analogues and decrease in the presence of adsorbates [26], due to increased vibrational scattering introduced by extrinsic guest-MOF collisions, and guest molecule-induced hybridization of low frequency modes [27]. We have also

demonstrated elsewhere that in contrast to the traditional coulometric techniques, ZnO nanotubes can sense ethanol at temperatures under 100 °C, using broadband microwave dielectric spectroscopy (BDS) [28].

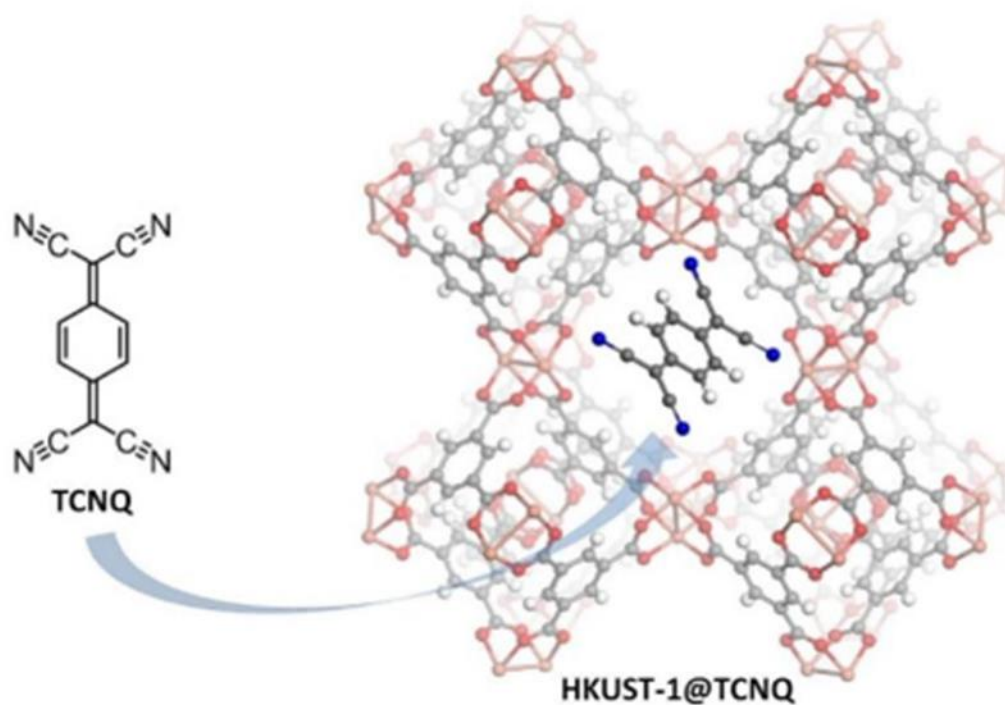


Figure 0.1. Schematic illustration depicting the structure of HKUST-1 SURMOF films, where the pores are loaded with TCNQ (TCNQ, tetracyanoquinodimethane) [25].

7.1.2 Broadband Dielectric Spectroscopy (BDS) Background

Accumulation and alignment of charged defects play significant roles in the VOC detection, as their state changes in the presence of reactive organic molecules. When exposed to electromagnetic waves, the dipolar defects oscillate to keep up with the rapidly changing external electric fields; at some critical frequency the polarizability cannot keep up with the velocity of the applied fields, resulting in dielectric loss. The displacement of the bound charges in the sensing

media in an external electric field, E , results in a dipolar moment, m , and a torque, G , as the dipolar moment orientates parallel to the electric field and in opposition to the applied field. This produces a net polarization of the material which determines the dielectric response of materials to electromagnetic radiation. In isotropic media, the volume density of polarization is directly proportional to the applied electric field intensity [29]. Thus, fundamentally, the elementary processes that underpin VOC detection with metal oxides involve changes in polarizability, and the resultant changes in electrical characteristics, of the sensing media. These changes alter the propagation characteristics of radio frequency or microwaves in such media and instigate microwave absorption / energy dissipation. We define a complex dielectric function that measures the electric displacement field due to the presence of an electric field in a dielectric material as written as Equation 1:

$$\epsilon(\omega) = \epsilon_1(\omega) + i\epsilon_2(\omega) \quad (1)$$

where, $\omega = 2c\pi/\lambda$ is the frequency, c is the speed of light and λ is the wavelength, $\epsilon_1(\omega)$ describes how much the material is polarized when an electric field is applied, and $\epsilon_2(\omega)$ is related to the absorption of the material [30, 31]. The dielectric polarizability at high frequencies sets the scale for radiation absorption, while at low frequencies, it determines the non-linear effects.

When electromagnetic waves interact with matter the incident microwave signal scatters according to the material's permittivity. During the signal scattering, a portion of the radiation is transmitted through the sample while the remainder is reflected toward the source, as described by Snell's law [29]. The ratio of transmitted to reflected energies depends in part on the impedance mismatch between the material under test (MUT) and the source. The signal scattering from the electrical interfaces is summarized as a matrix of S-parameters that quantifies how RF energy propagates through a multiport network such as a vector network analyzer (VNA). The S-

parameters can be extracted in the frequency domain (FD), time-domain (TD), or hybrid modes based on the form of the interrogating signal [31]. In this work, we used a two-port hybrid technique, in which the input excitation is convolved with the transfer function of the sensor ($h(f)$) loaded with the MUT. A typical two-port measurement contains four S-parameters (S_{11} , S_{21} , S_{12} , and S_{22}) which are vector quantities representing the magnitude and the phase of the frequency-dependent characteristics of the MUT. A portion of the incident wave is transmitted (i.e., S_{21} and S_{12}) or reflected (S_{11} and S_{22}). The portion of the transmitted signal exits the MUT with different magnitude and phase from the incident signal; thus, the S_{21} and S_{12} also encode the phase difference between a transmitted signal and an incident signal. The S-parameters can be analytically transformed to produce the characteristic circuit element of the analyte as described elsewhere [33]. Broadband microwave dielectric spectroscopy (BDS) measures the dispersive, and dissipative dielectric behavior of the analyte as a function of frequency, i.e., changes in the polarizability of the analyte. Because input excitation is convoluted by the transfer function of the sensor loaded with the MUT, i.e., ($h(f)$), to generate the output S-parameter the BDS has the advantage of rapidly interrogating a dynamic range of material characteristic [36]. Polar functional groups in organic molecules (e.g., VOCs) are electron-rich and highly polarizable, hence readily absorb microwave energy to distort as the electrons transfer from one stable state to an excited state with higher energy, forming the electron polarization, in the rapidly changing magnetic fields. Here, we use the S-parameters to evaluate the chemo-induced changes induced (CIC) in the VOC adsorbed on the MO sensing materials, by measuring the MW insertion loss characteristics (S_{21}) as a function of the experimental variables. Thus, in this work, the S-parameters are functionals of frequency and experimental stress (i.e., $F[h(f)]$).

Gas monitoring with microwave-based metrology is well known, but the technology has some performance limiting gaps. Specifically, performance metrics such as selectivity, sensitivity, reproducibility, and long-term stability are not yet well established, and the impact of environmental factors such as temperature, humidity are currently not well understood [20]. We had previously used microwave-based broadband dielectric spectroscopy (BDS) [34] to investigate the initial stages of ethanol vapor detection with ZnO nanorods [28]. The BDS detection of VOC with semiconductor metal oxides involve changes in polarizability, i.e., the repolarization of the permanent electrical dipoles which instigates micro-wave absorption / energy dissipation during the rotation and orientation of the dipoles [34, 35]. When microwaves interact with the analyte (i.e., MUT) the incident microwave signal scatters according to the material's permittivity; the signal scattering is a function of frequency and experimental stress (i.e., $F[h(f)]$). The input excitation is convoluted by the transfer function of the sensor loaded with the MUT, i.e., $(h(f))$, to generate the output S-parameter [32]. In this study, using BDS metrology, we compare ethanol vapor sensing on inorganic ZnO nanorods and hybrid surface anchored metal-organic-frameworks thin films (HKUST-1 SURMOFs) as sensing materials at temperatures under 100 °C. We have shown elsewhere that surface ZnO nanorods offer significantly increased sensing surfaces that improves the sensitivity and reduces the long response / recovery times [36]. Contactless broadband dielectric spectroscopy (BDS) is most advantageous for monitoring reactions involving some degree of charge transfer regardless of the nature of the charge carriers, i.e., electrons and holes [36]. The microwave signals are absorbed when inserted into such materials due to changes in the polarizability of the MO-adsorbate interface. We use the S-parameters to evaluate the redox behavior of ethanol molecules adsorbed on the sensing materials, by measuring the insertion loss characteristics (S_{21}) as a function of the experimental variables [38, 39]. With proper calibration,

the S_{21} amplitude can be correlated to the total impedance of the GSG waveguide, and gas sensing device. Thus, we can use the S_{21} magnitude as an index to the changes in the MUT in response to an external perturbation, as shown by equation 2, where z_r and z_0 are the instantaneous and characteristic impedances of the device under test, respectively

$$z_r = z_0 \frac{2(1-s_{21})}{s_{21}} \quad (2)$$

7.2 Experimental

7.2.1 Sensing Material Preparation

For the ZnO sensing study, the gas sensor device consisted of hydrothermally synthesized ZnO nanorods grown on a random polycrystalline fine grain ZnO seed layer which was fabricated by atomic layer deposition (ALD) on a native oxide covered p-type boron-doped silicon substrate with resistivity of about 4 Ωcm to about 6 Ωcm and a thickness of about 500 μm to about 550 μm , as we have described previously [40]. The surface anchored ZnO nanorods used in the ethanol detection are described elsewhere [39]; in our hands, the average ZnO nanorod was ~ 500 nm tall and ~ 50 nm in diameter [28]. We note that the ZnO nanorods do not all appear to align perfectly at 90 degrees with respect to the small grains of the ZnO seed layer. Whether the hydrothermal ZnO nanorods grow all at 90 degrees or display some angular variation is immaterial for the gas sensing reaction; the most important factor is the resulting large surface-to-volume ratio.

Polycrystalline HKUST-1 surface-mounted metal–organic framework thin films (SURMOFs) were grown by quasi liquid phase epitaxy (LPE surface-anchored) on plasma activated borosilicate SiO_2 glass, as described elsewhere [41]. In this work we used ≈ 35 nm thick

HKUST-1 films, formed from 30 spray-cycles [42]. The greenish color of our films is indicative of $\text{Cu}^{2+}/\text{Cu}^+$ defects [43]. Loading (doping) of fresh HKUST-1 MOF thin films is accomplished by infiltration with 7,7,8,8-tetracyano-quinodimethane (TCNQ), as described in the open literature [44]. Planar view scanning electron micrography (SEM) of the TCNQ loaded SUR-MOFs films shows uniform distribution of grain size comprised of primarily large grains separated by what appears to be wide gaps between the MOF domains [41]. The gaps are presumably formed as a result of significant unit-cell change when the pristine HKUST-1 is doped with TCNQ [41]. The substrates with the samples were diced into 1.5 cm by 2.5cm pieces and stored in a pure nitrogen atmosphere prior to use.

Analytical grade ethanol was obtained from Sigma-Aldrich (Milwaukee, St. Louis, MO, USA).

7.2.2 BDS Setup and Measurements

In this work, the SURMOF films on borosilicate SiO_2 glass substrates were placed directly on a ground-signal-ground (GSG) coplanar waveguide (CPW) housed in a controlled environment, as we have previously described [28]. The 175 ml reactor was purged with a nitrogen-air mixture; a small volume fraction of pure nitrogen was added to the air flow to dilute out any adventitious water vapor in the purging gas while maintaining an aerobic ambient for the inherent oxidation of the analyte. In the bid to prolong the life of the GSG waveguides all studies were conducted at less than 100 °C, except the initial characterization data in Figure 7.2.

Varying amounts (0.05ml to 1 ml) of analytical grade ethanol was injected into the reactor via a long-needed hypodermic syringe as needed, while maintaining the reactor at a preset temperature in an aerobic atmosphere [28].

7.3 Results and Discussion

7.3.1 BDC Detection of Ethanol Vapor with ZnO sensors

Chemoresistive metal oxide-based gas sensors, such as ZnO, rely on conductometric transduction principles [23], i.e., the electrical resistance of the active sensing structure changes in response to redox active analyte molecules. For n-type ZnO sensing materials the gas sensing mechanism involves perturbing the electron concentration in the conduction band. When the ZnO nanorods are exposed to ethanol vapor in an aerobic ambience at appropriate temperatures, the alcohol molecule is oxidized to form aldehydes in a 3-step charge transfer process [45]:

- (1) the sensor activation step involves the formation of a depletion layer at the air/ ZnO-nanorod interface from adsorbed oxygen species on the surface of the ZnO; the speciation of the adsorbed oxygen depends on temperature: O^{2-} at temperatures of less than 100 °C; O^- at temperatures between 100 and 300 °C, and O^{2-} at temperature higher than 300 °C [2],
- (2) analyte gas molecules adsorb on the oxygen rich ZnO nanorods surface to form adducts,
- (3) the adducts oxidize / reduce through charge transfer reactions, in the 200 °C – 400 °C temperature range. This perturbs the electron density in the conduction band to alter the resistivity of the sensing device.

The number of electrons (i.e., coulombs) released into the conduction band is limited by number of adsorbed analyte molecules, the surface area and chemistry of the surface. It has been demonstrated experimentally that the sensitivity and response speed of VOC detection with ZnO appears to depend on numerous factors, including but not limited to the nanoscale morphology, quality, and chemistry of the ZnO surface. For example, while ZnO microrods on SiO₂/Si substrate synthesized by low temperature (95° C) via wet chemical process showed maximum sensitivity and response time for ethanol and methanol vapor detection at 150 °C [46], we have shown elsewhere that hydrothermally synthesized ZnO nanorods grown on fine grained random nanocrystalline seed ZnO layers [40] prepared by atomic layer deposition (ALD) exhibit maximum sensitivity at around 320 °C [47].

Figure 7.2 shows the temperature dependence of microwave insertion loss (S_{21} amplitude, reported at 6 GHz) of ZnO on Si in nitrogen-enriched air (Air-N₂) and in gaseous ethanol environments, respectively, monitored at 6 GHz. While the system impedance (denoted by the insertion loss amplitude (S_{21} amplitude)) was stable below 100 °C, the system impedance increased with increasing temperature above 100 °C, which may be due the speciation changes during the sensor activation step (i.e., as discussed in step 1 above), and changes in interfacial capacitance that results from the surface potential barrier formed from the adsorption of analyte species from the environment onto the ZnO [48, 49, 28], along with the temperature dependence of the intrinsic semiconductor resistivity properties of the ZnO-nanotubes grown on silicon substrate. The contribution of the interfacial capacitance is illustrated by the introduction of ethanol vapor into the reactor as shown in Figure 7.2. It is proposed that at temperatures lower than 100 °C, the ethanol molecules adsorb to form adducts with the preexisting oxygen adsorbed species. At suitably higher temperatures, the adducts further react. This initial adduct formation alters the

electrostatics of the ZnO system, manifesting as increased impedance of the system and higher insertion losses. The BDS response to the ethanol analyte at sub-100 °C temperatures is rather remarkable since there is no conductometric response of ethanol vapor on ZnO nano-rods at temperatures below 100 °C [21].

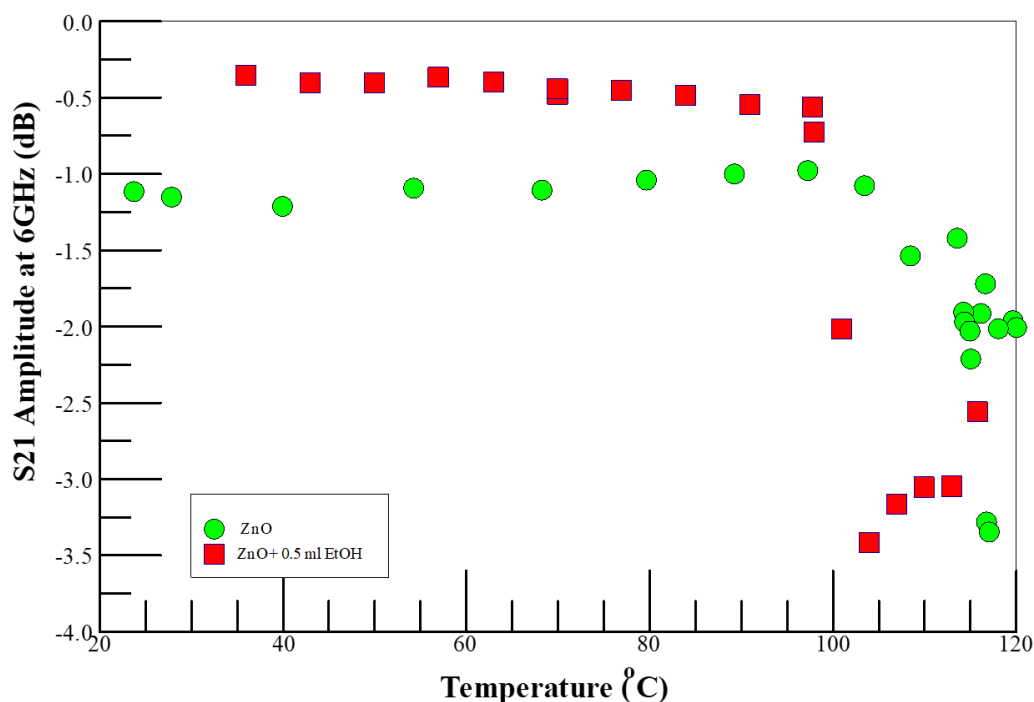


Figure 0.2. Temperature dependence of microwave insertion loss (S_{21} amplitude) of ZnO on Si substrate in nitrogen-rich air and gaseous ethanol environments, monitored at 6 GHz. Note that the symbol sizes are much larger than the error bars.

The perturbation of the conductivity of the sensing element is traditionally measured through coulometry, however, each of the elementary processes discussed above involves changes in the surface polarizability which can be discussed with chemisorption models without getting into the details of the surface reactions, and the sensing mechanism [50]. Such chemisorbed models

are easily monitored by corresponding changes in microwave S-parameters. Using BDS, we have previously investigated the three steps discussed above, and shown that ethanol can be detected on our ZnO nanorods, at temperatures well below 100 °C [28]. As we discuss below, we observed the formation of ethanol- O^{2-} adducts on the ZnO-nanorod surface which do not have to react chemically to change the impedance of the sensor. Thus, the ability to detect chemisorbed species at low temperatures with BDS negates the need for high temperature charge transfer reactions to capture the quantity of electrons transferred in to infer the number of adsorbed analyte molecules present.

7.3.2 Ethanol Vapor Detection with Pristine and TCNQ-loaded HKUST-1 SURMOF

The potential of metal-organic frameworks (MOFs) for gas mixture separation [51], and as VOC sensing agents have been discussed in the literature [14, 12]. Furthermore, copper MOFs are widely used in MOF alcohol oxidation, due to the intrinsic activity of copper as an oxidizing catalyst [52]. The HKUST-1 MOF, $[Cu_3(BTC)_2(H_2O)_3]_n$ (where BTC is benzene-1,3,5-tricarboxylate), is comprised of square Cu-Cu paddlewheel clusters connected by BTC ligands to form a rigid porous open framework with bimodal pore size distribution [53, 54], and two coordination unsaturated Cu^{2+} metal sites (open metal sites) per paddlewheel where polar groups can attach through dative bonding [55]. The open metal sites, formed by removing axial ligands, strongly coordinate to electron rich species (i.e., Lewis bases). The HKUST-1 MOF has three distinct internal pores, two of comparable size (aperture = 14 Å) and a smaller pore (aperture = 10 Å). One of the two larger pores has the Cu-Cu paddle-wheels directed into the pores making it suitable for coordinating TCNQ guest molecules. The open metal sites in the smaller pores are still available for coordinating to small molecules [55, 56]. The open Cu sites in the small cavities are

separated by 8.2 Å which limits the size, stereochemistry, and the number analyte molecules that could be adsorbed at those sites [52]. Small aliphatic alcohol molecules and similar sized polar molecules reversibly adsorb at the available open metal centers in MOF cavity causing the cavity to expand and inducing changes in its physicochemical properties, such as decreased thermal conductivity [27] and the electrical conductivity of the MOF [13, 57, 58]. Experimental data suggest that charge transfer between the adsorbed analyte and the open metal sites, occur within the pores of the MOF framework [12]. The adsorption at the metal sites also results in change in interfacial polarization and permittivity which should be readily detected by microwave energy dissipation [59].

Copper MOFs are widely used as catalysts for alcohol oxidation, due to the intrinsic activity of copper as an oxidizing catalyst [52]. For example, Guo et al have demonstrated that mixed-metal CuPd-HKUST-1 MOF exhibits superior catalytic performance compared to the pristine HKUST-1 for the selective aerobic oxidation of benzyl alcohol to benzaldehyde [60]. Defective HKUST-1 thin films [61], such as used in this work contain $\text{Cu}^{2+}/\text{Cu}^+$ dimers that form reactive adducts with dioxygen molecules which are probably responsible for the catalytic aerobic oxidative properties of the HKUST-1 MOF [62]. These oxidative abilities of defects are similar to the aerobic organisms, such as in respiration [63]. Copper(I)-dioxygen (O_2) adducts, have been proposed as intermediates in dioxygen-activating enzymes; they are capable of oxidizing substrates containing weak O–H and C–H bonds. Mechanistic studies for some enzymes and model systems have supported an initial hydrogen-atom abstraction via the cupric-superoxide complex as the first step of substrate oxidation [64, 65]. In the rate-determining step, an O-coordinated alcoholate undergoes an H-abstraction reaction from the α -carbon atom of the alcoholate to generate a bound ketyl radical which is then intramolecularly converted via a one-

electron oxidation to the aldehyde with the reduction of the Cu (II) center into a Cu-I species, which is then later deoxidized O^2 [66]. Thus, we expect the absorbed alcohol analyte to be aerobically oxidized in the host MOF to the corresponding aldehydes [67]. Such redox reactions at the metal centers should be readily detected by BDS, because of the expected changes in the conductivity of the HKUST-1 SURMOF [13]. Furthermore, microwave (MW) irradiation is known to rapidly convert alcohols to carbonyl compounds over transition metal catalysts [68]. MW irradiation of immobilized reactants on inorganic supports reduces the reaction time and promotes the yield, selectivity and purity of products, as the microwave irradiation promotes faster and more efficient internal heating through direct interaction between microwave energy and the reactants [69-71].

In analogy to the aerobic oxidation of aliphatic alcohols on ZnO, we propose conceivable elementary steps involved in the BDS detection of aliphatic alcohols in TCNQ-doped HKUST-1 SURMOF. We expect the adsorbed aliphatic alcohol analyte at the open Cu-sites in the host MOF sites to be aerobically oxidized into aldehydes [69] in a process comprised of multiple steps, each with its characteristic polarization dynamics, viz,

- (1) Analyte molecules diffuse into size accessible cavities to coordinate to the available open Cu^{2+} active sites, some of which exist as $Cu^{2+}-Cu^+-O_2$ adducts, in the HKUST-1 MOFs. This induces an impedance increase in the device under test (DUT) due to distortion of the mechanical structure, as well as changes in the electronic band structure that lead to changes in the conductivity of the MOF. In a pure nitrogen ambient, the N_2 adsorbs on the metal sites [72], but in the presence of Lewis base molecules, such as aliphatic alcohols, the analyte is expected to displace pre-adsorbed N_2 molecules from the open metal sites.

- (2) The aliphatic alcohol probably coordinates to the open metal center via the hydroxyl-oxygen atom. The absorbed alcohol analyte is aerobically oxidized by the Cu-sites [73] into carbonyl compounds (e.g., aldehydes from the primary) at room temperature [12], with electrons transferred into the MOF from the alcohol, as discussed above. This step is dependent on the presence of oxygen in the ambient within the reactor, which is required for the reoxidation of the Cu(I) to Cu(II). The resultant carbonyl compounds, because of their increased electrophilic nature, are more polarizable, and will contribute to the observed increased insertion loss.
- (3) The oxidation of the adsorbed alcohol analyte in the MOF into aldehydes, in step [2], may be aided by the probe microwave stimulus.

There are multiple dielectric mechanisms and polarization processes inherent in the HKUST-1-analyte interactions that can be triggered using different frequencies [74]; thus, careful analyses of the BDS spectra could afford deep mechanistic insights into the VOC detection as each event results in changes in polarization and has a characteristic relaxation frequency [75].

Nitrogen enriched air, without ethanol, was used in the initial characterization studies to understand the impact of Lewis base coordination to the open Cu^{2+} centers in the SURMOF films, i.e., to investigate step 1 of the proposed mechanism. Figure 7.3 shows the temperature dependence of microwave insertion loss (S_{21} amplitude) in TCNQ doped HKUST-1 SURMOF in N_2 -rich air. The insertion loss is higher in the nitrogen-rich environment than in pure air and increased with increasing temperature from 22 °C to 40 °C, then leveled off at higher temperatures. Seebeck coefficient measurements indicate holes as the majority charge carriers in TCNQ-HKUST-1 films at room temperature [76], and charge transport is only in the vertical direction in the highly oriented films [41]. The observation of the system becoming more resistive in the

nitrogen-enriched-air suggests that the N_2 molecules (Lewis base) coordinate to the open Cu^{2+} centers [77], and reduce the concentration of the majority hole carriers [76]. The behavior of the doped material is also consistent with guest induced electronic and vibrational structures changes of the SURMOF films [27, 78]. Furthermore, the temperature dependence of the impedance in the SURMOF suggests that either nitrogen adsorption at the open metal sites is gated by thermal-induced conformational changes in the MOF cage to allow access to the open metal sites [79, 80], or the DUT has temperature drifts below 50 °C [81]. Irrespective of the reason for the S_{21} saturation above 50 °C, all subsequent experiments were conducted at 65° C or higher temperatures to avoid the S_{21} drift.

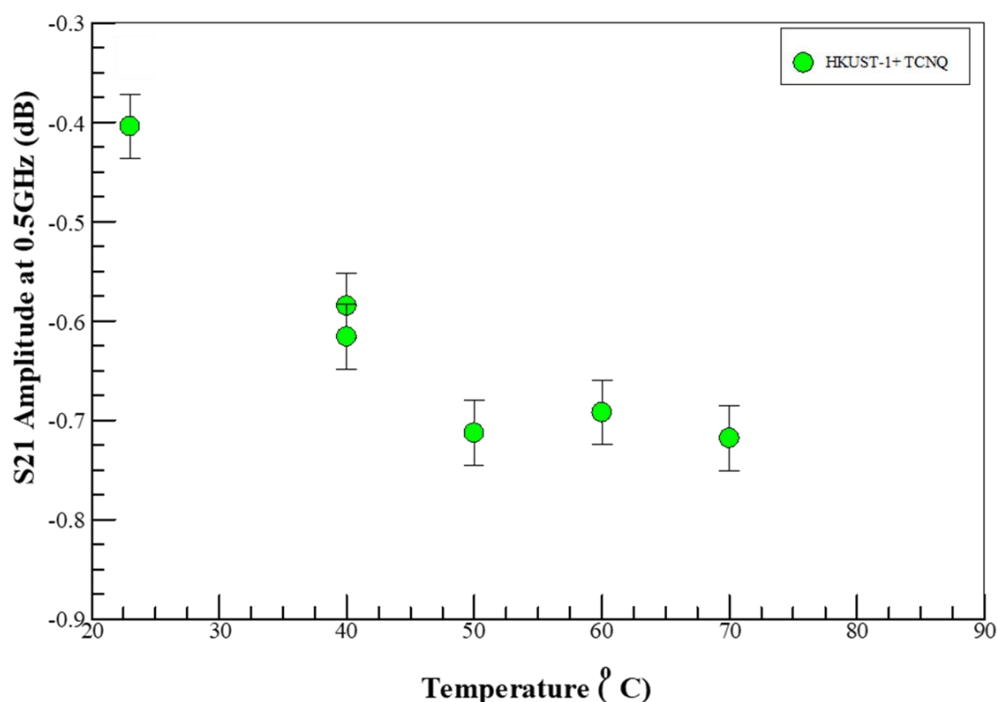


Figure 0.3. Temperature dependence of microwave insertion loss (S_{21} amplitude) in TCNQ loaded HKUST-1 MOF film on Si substrate in N_2 -rich air, The error bars represent the standard deviation of at least three measurements on the same sample.

Figure 7.4 shows the S_{21} amplitude with increasing concentration of the ethanol vapor at a fixed temperature of 80 °C in air. The S_{21} appears to saturate above 0.5 ml of injected neat ethanol. As in the nitrogen ambient, the system becomes resistive as the ethanol (Lewis base) coordinates to the open Cu^{2+} centers [77], and reduces the concentration of the majority hole carriers by donating electrons to the electron deficient metal site. As discussed above, holes are the majority carriers in TCNQ-doped HKUST-1 [76], and charge transport is only in the vertical direction in the highly oriented SURMOF films [41], such as those used here. Based on the results from currently ongoing work in our laboratory, we suggest that the ethanol molecules probably coordinate with otherwise free metal centers, as well as hydrogen bond to TCNQ dopant, to reduce the hole concentration by electron injection into the SURMOF from the oxidation of the analyte. This explains the increase in the resistance of the system with increasing analyte concentration.

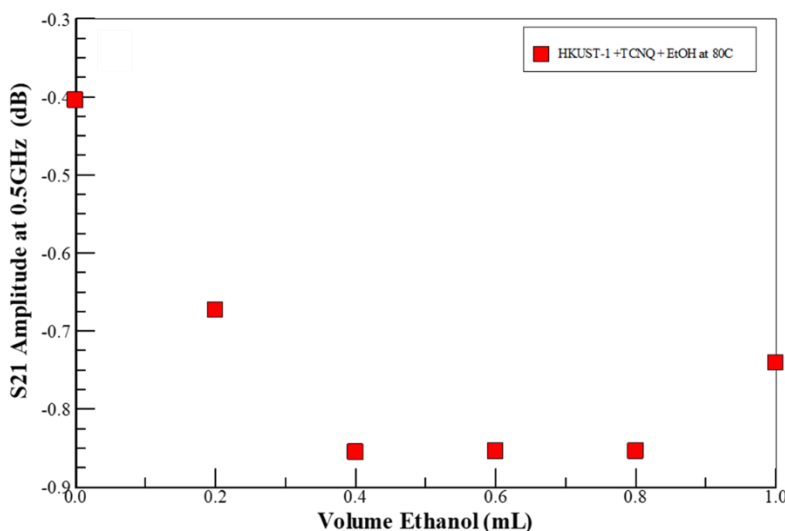


Figure 0.4. Insertion loss (S_{21} Amplitude) monitored at 0.5 GHz as a function of volume of neat ethanol injected into vapor reactor (i.e., ethanol vapor concentration) environments at 80 C° in air.

It has been demonstrated that only a single layer adsorbed analyte is formed when the SURMOF layer is exposed to ethanol. The ethanol molecules coordinate to the open Cu-centers via the hydroxyl-oxygen atom from the ethanol, and only a single layer is formed due to the weak hydrogen-bonding interactions from coordinated ethanol molecules with additional adsorbed ethanol molecules [82]. Furthermore, the ethanol analyte does not lead to the degradation of the MOF sensing material. In contrast to water, the ethanol sorption capacity of HKUST-1 remained unchanged with the sorption experiment time, at least at 303 K. In contrast to water, ethanol's weaker interaction with the open Cu(II) sites does not lead to the breaking of the Cu-carboxylate bond in the host HKUST-1 [83]. Thus, the evolution of S_{21} with ethanol volume, as shown in Figure 7.4, reflects the adsorption of the analyte into the SURMOF sensing layer. Up to 0.4 ml (i.e., ~ 1.1 times the volume of the re-actor, or 1.5×10^{13} times the volume of the SURMOF at 80 °C) of ethanol is adsorbed into the SURMOF sensing layer, which is reminiscent of the adsorption of small molecules into MOF materials [83]. Beyond analyte saturation of the sensing element additional ethanol volumes do not contribute to the sensor performance; the additional molecules are trapped between the SURMOF substrate and the waveguide or condense on the waveguide end-launch connectors to reduce the system impedance.

7.3.3 Comparison of BDS detection of Ethanol on MOF and ZnO Sensing Media

Figure 7.5 compares the microwave insertion loss (S_{21}) dependence on volume of neat ethanol flash vaporized into the reactor at 80 °C for the two sensing materials ZnO and TCNQ-doped HKUST-1 SUR-MOF in nitrogen-enriched air, monitored at 0.1 GHz. The error bars represent the standard deviation of at least 3 replicate measurements. In the case of TCNQ doped MOFs, the charge transfer reactions inject electrons into the metal center to reduce the hole

majority carrier and increase the device resistance. In contrast, ethanol adsorption on ZnO induced relatively small concentration dependent changes in the device impedance. Thus, the TCNQ doped-HKUST-1 SURMOF films were shown to be more sensitive in detecting ethanol at temperatures below 100 °C than their ZnO analogs. As discussed above, while the ZnO was detected through capacitance changes due to the ethanol-O²⁻ adducts formed on the nanorod's surface, the detection with the MOF is through direct electron injection into the conduction band. Clearly, the MOF system is more sensitive to ethanol concentration than the ethanol detection on ZnO. We admit that 80 °C is substantially below the optimum VOC detection temperature of around 300 °C for ZnO nanorods but have shown elsewhere that the BDS can detect a VOC at such low temperatures [28]. Analysis of the BDS data (at specific frequencies) provides electrical information that can be correlated to elementary processes, such as the adduct formation on oxidized ZnO, and charge-transfer reactions in the doped HKUST-1 SURMOF sensing material [84]. Clearly, the BDS technique affords the capability to distinguish between different impedance changing mechanisms and provides new mechanistic insights into the elementary events that occur on the ZnO surface during the initial activation step for ethanol detection.

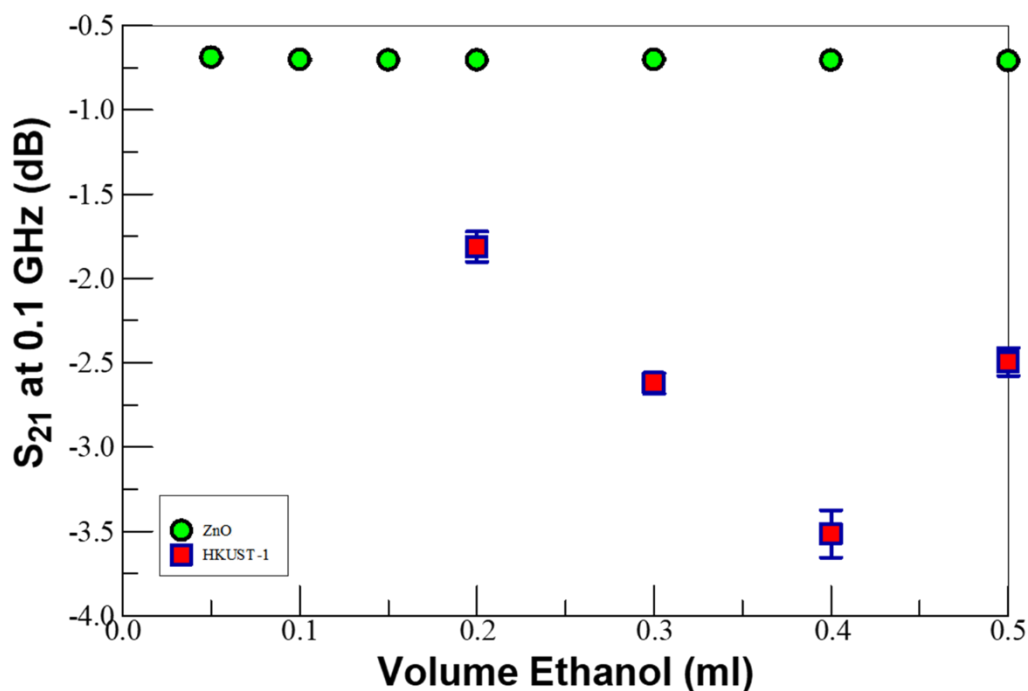


Figure 0.5. Comparison of the microwave insertion loss (S_{21}) dependence on ethanol concentration on ZnO versus TCNQ-doped HKUST-1 MOF sensing media on Si in gaseous ethanol environments, monitored at 0.1 GHz. Note the error bars represent the standard deviation of at least 3 replicate measurements.

7.4 Conclusions

Using microwave signal attenuation, we have demonstrated physics consistent with analyte-induced physicochemical changes of the sensing media consistent at a temperature as low as 80 °C on both ZnO and TCNQ-doped HKUST-1 SURMOF sensing media. In the case of TCNQ-doped HKUST SURMOFs, the charge transfer reactions inject electrons into the metal center to reduce the hole majority carrier and increased device resistance. In contrast, ethanol adsorption on ZnO induced relatively small concentration dependent changes in the device impedance, mostly through changes in surface electrostatics. The doped-HKUST-1 SURMOF films were shown to be more sensitive in detecting ethanol at temperatures below 100 °C than their ZnO analogs. Also,

the BDS technique affords new mechanistic insights into the elementary events that occur on the ZnO surface during the initial activation step for ethanol detection.

References

- [1] G. Korotcenkov, *Chemical Sensors: Comprehensive Sensor Technologies Volume 4: Solid State Devices*. (Momentum Press, New York, NY 10017 |, 2011).
- [2] F. Meng, X. Shi, Z. Yuan, H. Ji, W. Qin, Y. Shen and C. Xing, *Sensors and Actuators B: Chemical* 350, 130867 (2022).
- [3] G. Korotcenkov, V. Brinzari and B. K. Cho, *Microchimica Acta* 183 (3), 1033-1054 (2016).
- [4] A. Dey, *Materials Science and Engineering: B* 229, 206-217 (2018).
- [5] W. Gopel, *Progress in Surface Science* 20 (1), 9-103 (1985).
- [6] A. Mirzaei, S. G. Leonardi and G. Neri, *Ceramics International* 42 (14), 15119-15141 (2016).
- [7] S. R. Mobasser, J.; Zhang, Y.; Shi, W.; Dittrich, T.M.; Miller, C.J. , in 2019 Superfund Research Program (SRP) Annual Meeting (Seattle, WA, USA, 2019).
- [8] J. Ahn, H. Kim, E. Kim and J. Ko, *Ad Hoc Networks* 113, 102360 (2021).
- [9] F. U. M. Chowdhury, J. Gardner, in *Fourth Scientific Meeting EuNetAir* (Linkoping University, Linkoping, Sweden 2015), pp. 40 - 43.
- [10] A. Nourbakhsh, L. Yu, Y. Lin, M. Hempel, R.-J. Shiue, D. Englund and T. Palacios, in *Beyond-CMOS Technologies for Next Generation Computer Design*, edited by R. O. Topaloglu and H. S. P. Wong (Springer International Publishing, Cham, 2019), pp. 43-84.
- [11] M. M. Shulaker, G. Hills, R. S. Park, R. T. Howe, K. Saraswat, H. S. P. Wong and S. Mitra, *Nature* 547 (7661), 74-78 (2017).
- [12] W.-T. Koo, J.-S. Jang and I.-D. Kim, *Chem* 5 (8), 1938-1963 (2019).
- [13] J. J. Calvo, S. M. Angel and M. C. So, *APL Materials* 8 (5), 050901 (2020).
- [14] L. E. Kreno, K. Leong, O. K. Farha, M. Allendorf, R. P. Van Duyne and J. T. Hupp, *Chemical Reviews* 112 (2), 1105-1125 (2012).
- [15] W.-Q. Xu, S. He, C.-C. Lin, Y.-X. Qiu, X.-J. Liu, T. Jiang, W.-T. Liu, X.-L. Zhang and J.-J. Jiang, *Inorganic Chemistry Communications* 92, 1-4 (2018).
- [16] Y. Min, *Massachusetts Institute of Technology*, 2003.
- [17] S. Homayoonnia and S. Zeinali, *Sensors and Actuators B: Chemical* 237, 776-786 (2016).
- [18] M. Sophocleous, in *Electrical Resistivity and Conductivity* (2017).

- [19] A. Rydosz, E. Maciak, K. Wincza and S. Gruszczynski, *Sensors and Actuators B: Chemical* 237, 876-886 (2016).
- [20] F. Li, Y. Zheng, C. Hua and J. Jian, *Frontiers in Materials* 6 (101) (2019).
- [21] F. Xu, C. Zhou and H.-P. Ho, *Journal of Alloys and Compounds* 858, 158294 (2021).
- [22] A. M. Lord, T. G. Maffei, A. S. Walton, D. M. Kepaptsoglou, Q. M. Ramasse, M. B. Ward, J. Köble and S. P. Wilks, *Nanotechnology* 24 (43), 435706 (2013).
- [23] I.-D. Kim, A. Rothschild and H. L. Tuller, *Acta Materialia* 61 (3), 974-1000 (2013).
- [24] K. Müller, N. Vankova, L. Schöttner, T. Heine and L. Heinke, *Chemical Science* 10 (1), 153-160 (2019).
- [25] K. Z. Xin Chen, Zeinab Mohamed Hassan, Engelbert Redel and Helmut Baumgart, "Charge. transport, conductivity and Seebeck coefficient in pristine and TCNQ loaded preferentially grown metal-organic framework films," *Journal of Physics: Condensed Matter*, vol. 34, no. 40, p. 404001, 2022 doi: 10.1088/1361-648X/abe72f.
- [26] H. Babaei, M. E. DeCoster, M. Jeong, Z. M. Hassan, T. Islamoglu, H. Baumgart, A. J. H. McGaughey, E. Redel, O. K. Farha, P. E. Hopkins, J. A. Malen and C. E. Wilmer, *Nature Communications* 11 (1), 4010 (2020).
- [27] M. E. DeCoster, H. Babaei, S. S. Jung, Z. M. Hassan, J. T. Gaskins, A. Giri, E. M. Tiernan, J. A. Tomko, H. Baumgart, P. M. Norris, A. J. H. McGaughey, C. E. Wilmer, E. Redel, G. Giri and P. E. Hopkins, *Journal of the American Chemical Society* 144 (8), 3603-3613 (2022).
- [28] P. K. Amoah, P. Lin, H. Baumgart, R. Franklin and Y. S. Obeng, *Journal of Physics D: Applied Physics* (2020).
- [29] R. Zamorano Ulloa, M. Guadalupe Hernandez Santiago and V. L. Villegas Rueda, in *Electromagnetic Fields and Waves* (IntechOpen, London, United Kingdom: , 2019).
- [30] D. T. s. t. S. o. I. E. a. M. Rongzhen Chen, Department of Materials Science and Engineering, KTH Royal Institute of Technology, Sweden, , , KTH Royal Institute of Technology, 2017.
- [31] C. Ambrosch-Draxl and J. O. Sofo, *Computer Physics Communications* 175 (1), 1-14 (2006).
- [32] K. Entesari, R. E. Ghiri and E. Kaya, *IEEE Microwave Magazine* 22 (6), 26-48 (2021).
- [33] N. B. Obeng YS, Reyes DR, Poster DL, Postek MT, *J Res Natl Inst Stan* 126: (2021).
- [34] F. K. a. A. Schönhals, *Broadband Dielectric Spectroscopy*. (Springer, Berlin, Heidelberg, 2003).
- [35] M. Marghany, in *Synthetic Aperture Radar Imaging Mechanism for Oil Spills*, edited by M. Marghany (Gulf Professional Publishing, 2020), pp. 73-92.
- [36] P. Lin, 2019 (unpublished).

- [37] A. M. Wernbacher, M. Eichelbaum, T. Risse, S. Cap, A. Trunschke and R. Schlögl, *The Journal of Physical Chemistry C* 123 (13), 8005-8017 (2019).
- [38] H.-J. Kim and J.-H. Lee, *Sensors and Actuators B: Chemical* 192, 607-627 (2014).
- [39] P. Lin, X. Chen, K. Zhang and H. Baumgart, *ECS Journal of Solid State Science and Technology* 7 (12), Q246-Q252 (2018).
- [40] E. Biehler, R. Whiteman, P. Lin, K. Zhang, H. Baumgart and T. Abdel-Fattah, *ECS Journal of Solid State Science and Technology* 9, 121008 (2020).
- [41] X. Chen, K. Zhang, Z. M. Hassan, E. Redel and H. Baumgart, *Journal of Physics: Condensed Matter* (2021).
- [42] H. K. Arslan, O. Shekhah, J. Wohlgemuth, M. Franzreb, R. A. Fischer and C. Wöll, *Advanced Functional Materials* 21 (22), 4228-4231 (2011).
- [43] K. Müller, K. Fink, L. Schöttner, M. Koenig, L. Heinke and C. Wöll, *ACS Applied Materials & Interfaces* 9 (42), 37463-37467 (2017).
- [44] A. A. Talin, A. Centrone, A. C. Ford, M. E. Foster, V. Stavila, P. Haney, R. A. Kinney, V. Szalai, F. El Gabaly, H. P. Yoon, F. Léonard and M. D. Allendorf, *Science* 343 (6166), 66-69 (2014).
- [45] L. Wang, Y. Kang, X. Liu, S. Zhang, W. Huang and S. Wang, *Sensors and Actuators B: Chemical* 162 (1), 237-243 (2012).
- [46] M. Sinha, R. Mahapatra and R. Ghosh, *Materials Today: Proceedings* 11, 708-713 (2019).
- [47] P. Lin, X. Chen, K. Zhang and H. Baumgart, *ECS Journal of Solid State Science and Technology* 7, Q246-Q252 (2018).
- [48] A. Bejaoui, J. Guerin, J. A. Zapien and K. Aguir, *Sensors and Actuators B: Chemical* 190, 8-15 (2014).
- [49] A. Bejaoui, J. Guerin and K. Aguir, *Sensors and Actuators B: Chemical* 181, 340-347 (2013).
- [50] S. Steinhauer, *Chemosensors* 9 (3), 51 (2021).
- [51] D. Ma, Z. Li, J. Zhu, Y. Zhou, L. Chen, X. Mai, M. Liufu, Y. Wu and Y. Li, *Journal of Materials Chemistry A* 8 (24), 11933-11937 (2020).
- [52] A. Dhakshinamoorthy, A. M. Asiri and H. Garcia, *Chemical Communications* 53 (79), 10851-10869 (2017).
- [53] S. S.-Y. Chui, S. M.-F. Lo, J. P. H. Charmant, A. G. Orpen and I. D. Williams, *Science* 283 (5405), 1148-1150 (1999).
- [54] Q. Min Wang, D. Shen, M. Bülow, M. Ling Lau, S. Deng, F. R. Fitch, N. O. Lemcoff and J. Semanscin, *Microporous and Mesoporous Materials* 55 (2), 217-230 (2002).
- [55] C. H. Hendon and A. Walsh, *Chemical Science* 6 (7), 3674-3683 (2015).

- [56] K. Dedecker, E. Dumas, B. Lavédrine, N. Steunou and C. Serre, in *Metal-Organic Frameworks (MOFs) for Environmental Applications*, edited by S. K. Ghosh (Elsevier, 2019), pp. 141-178.
- [57] L. Cadman, University of Bath, *Multi-Component Metal-Organic Frameworks*
- [58] L. Sun, C. H. Hendon, M. A. Minier, A. Walsh and M. Dincă, *Journal of the American Chemical Society* 137 (19), 6164-6167 (2015).
- [59] S. Sachdeva, S. J. H. Koper, A. Sabetghadam, D. Soccol, D. J. Gravesteijn, F. Kapteijn, E. J. R. Sudhölter, J. Gascon and L. C. P. M. de Smet, *ACS applied materials & interfaces* 9 (29), 24926-24935 (2017).
- [60] P. Guo, C. Froese, Q. Fu, Y.-T. Chen, B. Peng, W. Kleist, R. A. Fischer, M. Muhler and Y. Wang, *The Journal of Physical Chemistry C* 122 (37), 21433-21440 (2018).
- [61] L. Heinke and C. Wöll, *Advanced Materials* 31 (26), 1806324 (2019).
- [62] W. Wang, D. I. Sharapa, A. Chandresh, A. Nefedov, S. Heißler, L. Heinke, F. Studt, Y. Wang and C. Wöll, *Angewandte Chemie International Edition* 59 (26), 10514-10518 (2020).
- [63] R. Y. N. Ho, J. F. Liebman and J. S. Valentine, in *Active Oxygen in Biochemistry*, edited by J. S. Valentine, C. S. Foote, A. Greenberg and J. F. Liebman (Springer Netherlands, Dordrecht, 1995), pp. 1-36.
- [64] J. Shearer, C. X. Zhang, L. N. Zakharov, A. L. Rheingold and K. D. Karlin, *Journal of the American Chemical Society* 127 (15), 5469-5483 (2005).
- [65] D. A. Quist, D. E. Diaz, J. J. Liu and K. D. Karlin, *JBIC Journal of Biological Inorganic Chemistry* 22 (2), 253-288 (2017).
- [66] P. Chaudhuri, M. Hess, J. Müller, K. Hildenbrand, E. Bill, T. Weyhermüller and K. Wieghardt, *Journal of the American Chemical Society* 121 (41), 9599-9610 (1999).
- [67] T. F. S. Silva and L. M. D. R. S. Martins, *Molecules* 25 (3), 748 (2020).
- [68] B. Maes, T. Marimuthu, S. Alapour and H. B. Friedrich, *Arkivoc* 2020 (3), 120-135 (2020).
- [69] M. Sutradhar, E. C. B. A. Alegria, T. R. Barman, M. F. C. Guedes da Silva, C.-M. Liu and A. J. L. Pombeiro, *Frontiers in Chemistry* 8 (157) (2020).
- [70] S. Hazra, L. M. D. R. S. Martins, M. F. C. Guedes da Silva and A. J. L. Pombeiro, *RSC Advances* 5 (109), 90079-90088 (2015).
- [71] V. Polshettiwar and R. S. Varma, *Accounts of Chemical Research* 41 (5), 629-639 (2008).
- [72] S. Bordiga, L. Regli, F. Bonino, E. Groppo, C. Lamberti, B. Xiao, P. S. Wheatley, R. E. Morris and A. Zecchina, *Physical Chemistry Chemical Physics* 9 (21), 2676-2685 (2007).
- [73] V. Rubio-Giménez, N. Almora-Barrios, G. Escorcia-Ariza, M. Galbiati, M. Sessolo, S. Tatay and C. Martí-Gastaldo, *Angewandte Chemie International Edition* 57 (46), 15086-15090 (2018).

- [74] A. S. Babal, L. Donà, M. R. Ryder, K. Titov, A. K. Chaudhari, Z. Zeng, C. S. Kelley, M. D. Frogley, G. Cinque, B. Civalieri and J.-C. Tan, *The Journal of Physical Chemistry C* 123 (48), 29427-29435 (2019).
- [75] A. M. Bottreau, Y. Dutuit and J. Moreau, *The Journal of Chemical Physics* 66 (8), 3331-3336 (1977).
- [76] K. J. Erickson, F. Léonard, V. Stavila, M. E. Foster, C. D. Spataru, R. E. Jones, B. M. Foley, P. E. Hopkins, M. D. Allendorf and A. A. Talin, *Advanced Materials* 27 (22), 3453-3459 (2015).
- [77] I. Strauss, A. Mundstock, M. Treger, K. Lange, S. Hwang, C. Chmelik, P. Rusch, N. C. Bigall, T. Pichler, H. Shiozawa and J. Caro, *ACS Applied Materials & Interfaces* 11 (15), 14175-14181 (2019).
- [78] J. Liu, T. Wächter, A. Irmeler, P. G. Weidler, H. Gliemann, F. Pauly, V. Mugnaini, M. Zharnikov and C. Wöll, *ACS Applied Materials & Interfaces* 7 (18), 9824-9830 (2015).
- [79] J. Janczak, D. Prochowicz, J. Lewiński, D. Fairen-Jimenez, T. Bereta and J. Lisowski, *chemistry – A European Journal* 22 (2), 598-609 (2016).
- [80] M. M. Deegan, M. R. Dworzak, A. J. Gosselin, K. J. Korman and E. D. Bloch, *Chemistry – A European Journal* 27 (14), 4531-4547 (2021).
- [81] A. M. Collier-Oxandale, J. Thorson, H. Halliday, J. Milford and M. Hannigan, *Atmos. Meas. Tech.* 12 (3), 1441-1460 (2019).
- [82] N. C. Jeong, B. Samanta, C. Y. Lee, O. K. Farha and J. T. Hupp, *Journal of the American Chemical Society* 134 (1), 51-54 (2012).
- [83] J. R. Álvarez, E. Sánchez-González, E. Pérez, E. Schneider-Revueltas, A. Martínez, A. Tejeda-Cruz, A. Islas-Jácome, E. González-Zamora and I. A. Ibarra, *Dalton Transactions* 46 (28), 9192-9200 (2017).
- [84] A. Serghei, J. R. Sangoro and F. Kremer, in *Electrical Phenomena at Interfaces and Biointerfaces* (2012), pp. 241-273.

CHAPTER 8

SUMMARY AND FUTURE WORK

8.1 Summary

8.1.1 ZnO as Sensing Media

The following section summarizes the achievements attained for the investigation of ZnO nanorods as sensing media utilizing microwave Broadband Spectroscopy BDS. This thesis has explored the use of zinc oxide (ZnO) as a detection element in gas sensing applications, particularly focusing on its properties and interactions in detecting aliphatic alcohols (e.g., ethanol). ZnO nanostructures offer advantages such as high sensitivity, short response time, and resistance to harsh environments, and high surface-to-volume ratios making them suitable for gas sensing. The previous chapters highlighted the challenges associated with traditional electrical characterization techniques due to tool-measurand interactions and introduced broadband dielectric spectroscopy (BDS) as a non-contact metrology method to probe the intrinsic properties of ZnO. By synthesizing ZnO nanorods, the surface-to-volume ratio is increased considerably, enhancing the sensing surfaces and addressing shortcomings like insufficient sensitivity and long response times observed in thin film ZnO gas sensors. Mechanistically, the interaction of ZnO with oxygen-rich ambient and reducing target gases like ethanol leads to changes in the majority carrier density and electrical resistance, which can be monitored using BDS.

Experimental setup involved ZnO nanorods grown on silicon substrates, with measurements conducted using broadband dielectric spectroscopy (BDS) to study gas-sensor activation steps for VOC detection. The setup allowed for non-contact monitoring, minimizing artifacts introduced by electrical contacts. Temperature control was critical, with steady-state measurements revealing temperature and time-dependent changes in ZnO impedance. Microwave insertion loss and attenuation constant measurements provided insights into ZnO's response to different environments, such as air and ethanol vapor. Notably, impedance changes observed during sensor activation at temperatures above 100°C suggested complex charge transfer events on ZnO surfaces.

Results indicate that BDS offers detailed insights into ZnO gas sensing mechanisms, highlighting the advantages over traditional direct current resistivity measurements. By distinguishing charge transfer reactions and identifying reaction intermediates, BDS provides a deeper understanding of ZnO's behavior during gas sensing. However, further optimization and exploration of BDS detection limits are necessary. Overall, this work demonstrates the potential of ZnO nanorods coupled with BDS for improved gas sensing applications, paving the way for enhanced detection of volatile organic compounds like ethanol.

8.1.2 Metal-doped ZnO as Sensing Media

This study provided an overview of doping in ZnO, highlighting its advantages in various applications. The focus of this chapter is on studying doped transition-metal ZnO nanorods, specifically with Cobalt (Co), as well as coinage metals silver (Ag) and gold (Au) to enhance gas sensor responses. Doping modifies ZnO's electronic characteristics by adjusting its bandgap and affecting charge carrier density, thus influencing its conductivity. Transition metals on MOS

surfaces serve various roles, enhancing stability and altering properties. Co-doping with Co^{2+} ions, known for enhancing gas sensing, introduces active sites and morphology regulation, offering desirable properties. Similarly, Ag and Au doping introduce notable distinctions due to their unique behavior within the lattice, affecting optical, electrical, and structural properties.

Experimental details included a hydrothermal process to produce doped ZnO nanorods, with Co, Ag, and Au doping solutions applied separately. Characterization involved SEM/EDS for morphological and elemental analysis and Raman spectroscopy for structural examination. Co-doping induced a reduction in peak intensity, indicating disrupted packing or amorphization, while Au doping increased intensity, suggesting Surface-enhanced Raman Scattering (SERS), supported by a red-shift in frequency and indicative of Au nanoparticle agglomeration on the ZnO nanorod surface. However, we were unable to obtain Raman spectra of Ag-doped because of laser induced damage the material. Doping / alloying the ZnO nanorods with various transition metal resulted in disparate gas sensing results, viz, Ag-doped ZnO exhibited chemically reactive (possibly catalytic decomposition of analyte) behavior, while Au-doped ZnO showed increasing impedance with increasing analyte concentration, while Co-doped ZnO showed a behavior similar to undoped ZnO. This observation shows how metal doping changes the chemical properties of the sensing agents in VOC detection, such as different detection mechanism for Ag and Au doping, possibly involving catalytic decomposition of analytes.

8.1.3 Metal-Organic Framework MOF Films as Sensing Media

The following section summarizes the experimental achievements and analytical insights attained for the investigation of Metal-Organic Framework MOF Films as sensing media utilizing microwave Broadband Spectroscopy BDS. In this chapter, we investigated the chemo-induced

changes (CIC) resulting from volatile organic compounds (VOCs), particularly aliphatic alcohols, adsorbed on HKUST-1 SURMOF sensing materials. We used BDS S-parameters to evaluate these changes by measuring the microwave insertion loss (S21) as a function of experimental variables. The experimental setup utilized a ground-signal-ground (GSG) coplanar waveguide (CPW) to interact with the sensing material, allowing for the approximation of electric fields as planar. Through proper calibration, the S21 amplitude and phase were correlated with the impedance of the waveguide and sensing device.

The SURMOF sensing materials, specifically TCNQ-doped HKUST-1 films were prepared using a layer-by-layer growth technique on substrates, followed by TCNQ loading. BDS measurements were conducted using a CPW setup, with temperature control and vaporized analyte injection. Results showed that the insertion loss amplitude increased with analyte concentration, indicating changes in impedance due to electron donation to open Cu^{2+} centers. The study explored the response to various aliphatic alcohols and acetone, revealing distinctive features in the insertion loss response, including a linear region proportional to analyte concentration and a saturation point.

A proposed mechanism for BDS detection involved analyte diffusion into the MOF structure, coordination with metal sites, and subsequent oxidation, leading to changes in conductivity and impedance. The presence of electron-rich species at open metal centers induced changes in physicochemical properties, detectable through microwave energy dissipation. Furthermore, microwave irradiation was suggested to facilitate rapid oxidation of adsorbed alcohols, supporting the basis for VOC detection using MOF thin films. The study provided insights into the sensitivity and selectivity of BDS for aliphatic alcohols, shedding light on potential applications in gas sensing technologies.

8.1.4 Advantages of MOF Films versus ZnO as Sensing Media

In this research section, we used contactless broadband dielectric spectroscopy (BDS) to compare the advantages and disadvantages of ethanol vapor sensing capabilities of ZnO nanorods versus surface-anchored metal-organic-frameworks thin films (HKUST-1 SURMOF) at temperatures below 100 °C. BDS is particularly advantageous for monitoring reactions involving charge transfer, such as gas-surface interactions. By measuring the microwave insertion loss characteristics (S21) as a function of experimental variables, we evaluated the redox behavior of ethanol molecules adsorbed on the sensing materials. BDS was shown to be able to detect ethanol on ZnO nanorods at temperatures below 100 °C, providing insights into the sensing mechanism without relying on high-temperature charge transfer reactions.

For the ZnO sensing study, ZnO nanorods were grown on silicon substrates, while HKUST-1 SURMOF thin films were grown on borosilicate glass. Experimental setups involved exposing these materials to varying concentrations of ethanol vapor, and BDS measurements were conducted to monitor changes in the insertion loss. The results suggested that ethanol molecules adsorbed on the ZnO nanorods formed adducts, leading to changes in surface polarizability and impedance. Similarly, in the case of HKUST-1 SURMOF films, ethanol molecules coordinated with open metal sites, inducing changes in conductivity and impedance. These findings highlight the potential of both ZnO nanorods and MOF thin films for ethanol vapor detection at relatively low temperatures.

Comparative analysis revealed that the TCNQ doped HKUST-1 SURMOF films exhibited higher sensitivity to ethanol vapor compared to ZnO nanorods at temperatures below 100°C providing a distinct advantage for TCNQ doped HKUST-1 MOF films at low detection

temperatures. While ZnO nanorods detected ethanol through changes in surface capacitance due to adduct formation, the MOF system detected ethanol via direct electron injection into the conduction band. This study demonstrates the effectiveness of BDS in elucidating the sensing mechanisms of different materials and provides insights into optimizing gas sensing devices for practical applications.

8.2 Contributions to Science

This thesis presents groundbreaking research in the field of gas sensing by introducing a novel non-contact broadband dielectric spectroscopy (BDS) method for detecting volatile organic compounds (VOCs), particularly aliphatic alcohols like ethanol, at significantly reduced temperatures. This innovative approach not only offers a non-invasive means of monitoring gas-surface interactions but also provides detailed insights into the intricate mechanisms underlying gas sensing processes. By utilizing BDS, the study achieves a deeper understanding of how zinc oxide (ZnO) nanostructures interact with target gases, elucidating the complex changes in electrical properties that occur during VOC detection. Moreover, the investigation into metal-doped ZnO nanorods extends our understanding of how dopants influence the conductivity and sensing capabilities of ZnO, paving the way for the development of tailored sensing materials with enhanced performance. Additionally, the exploration of metal-organic frameworks (MOFs), specifically HKUST-1 SURMOF thin films, for ethanol vapor detection represents a significant advancement in the field, highlighting their sensitivity and selectivity in gas sensing applications. Overall, this research not only pushes the boundaries of gas sensing technology but also lays a solid foundation for the future development of improved sensing materials and techniques across a wide range of applications.

8.3 Outlook and Future work

8.3.1 Effect of doping via Ion implantation versus Diffusion Doping in solution during hydrothermal synthesis.

Selective doping plays a crucial role in the production of electronic devices [263]. At the forefront of doping technology lies ion-implantation, which offers precise adjustment of surface properties while maintaining bulk characteristics. This method introduces intermediate energy levels within a semiconductor's bandgap, providing flexibility unparalleled by conventional methods like gas phase diffusion or diffusion doping in solution. Unlike these methods, ion-implantation allows any element to be bombarded onto the near-surface region of a solid substrate without introducing additional phases or impurities.

During ion-implantation, dopants are embedded into the target material, creating interstitial point defects within the crystal lattice as energetic ions collide with target atoms, disturbing their lattice positions in the pathway of lattice defect cascades. Consequently, ion-implanted materials may initially display poor conductivity due to lattice damage, which can be remedied through dopant activation annealing. Annealing involves infusing energy into the crystal system to repair lattice damage and to activate impurity atoms onto substitutional lattice sites, significantly enhancing conductivity, critical for improving efficiency in state-of-the-art MOSFET and photovoltaic applications.


Sub-Surface material modification through ion-beam impartation induces nuclear and electronic disorder, initiating nucleation and growth processes. Control parameters such as implant energy, ion beam current density, energy, flux, fluence, time, substrate temperature, and ambient

conditions influence the Gaussian peak depth and range and dose of the implanted dopant species [264].

In the study of metal-doped ZnO, as detailed in Chapter 5, hydrothermal synthesis methods were used to dope nanorods using diffusion doping in solution techniques. Ion-beam implantation stands out as a superior doping method due to its ability to custom tailor precisely the penetration depth and dose of dopants into the sample, resulting in controlled higher electrical activity compared to other methods. Furthermore, it allows for precise control over dopant concentration and depth profiles, enabling tailored doping profiles to be achieved.

Collaborative efforts with Hugo Bouteiller, Jean-François Barbot, and their team at PPRIME Institute CNRS, University of Poitiers, France, have commenced preliminary work in this area. Titanium (Ti) and Chromium (Cr) were selected as dopants at 1% levels for our ZnO samples, with additional samples implanted with Ti at 2% to investigate the impact of doping levels. Future research aims to compare the microwave sensing characteristics of ZnO samples doped via hydrothermal methods versus ion-beam implantation with Ti and Cr. The implantation parameters utilized in this study are illustrated in Figures 8.1-8.33. These figures represent variables such as ion energy, ion dose, and implantation temperature which influence the depth distribution and concentration of chromium atoms within the ZnO lattice. Moreover, first simulated depth profiles depicted in Figure 8.1 and 8.2 offer valuable insights into the peak position and range distribution extent of implanted chromium atoms within the ZnO material.

Implantation Cr 1%



10:16:54
23/01/2024

PARAMETRES IMPLANTEUR

	Mini	Maxi	V Moy
AMU	51.80	53.17	52.27
Energie [kV]	19.70	20.67	19.99
Beam Current [µA]	0.00	9.73	1.36
Temp Substrat [°C]	0.00	0.00	0.00
Filament V [V]	8.78	9.30	8.93
Filament I [A]	67.12	70.00	68.55
Arc V [V]	58.00	59.00	58.82
Arc I [A]	9.33	12.24	10.46
Temp Vapo [°C]	0.00	0.00	0.00
Sputtering V [V]	789.86	869.17	822.28
Sputtering I [mA]	105.31	132.59	117.65
Sample Pos	188.00	188.00	188.00
Ar [sccm]	0.00	0.00	0.00
Xe [sccm]	0.30	0.30	0.30
O2 [sccm]	0.00	0.00	0.00
Baratron [torr]	0.00	0.00	0.00
Magnet I [A]	32.34	32.56	32.47
Bfield [kG]	4.96	7.61	6.13
Extraction V [kV]	20.45	20.83	20.77
Extraction I [mA]	4.21	5.61	4.81
Post Accel V [kV]	0.00	0.00	0.00
Post Accel I [mA]	0.00	0.00	0.00
Post Decel V [kV]	0.00	0.00	0.00
Post Decel [mA]	0.00	0.00	0.00
Vide Beam Line [mBar]	3.29E-6	3.61E-6	3.41E-6
Vide Chambre [mBar]	9.51E-7	1.32E-6	9.92E-7

Operateur:

Demandeur:

Recette:

Dose cible:

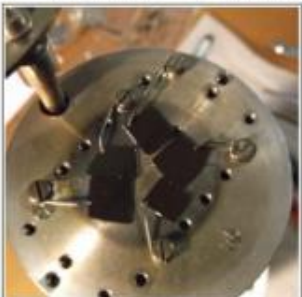
Temps écoulé:

Espèce:

Nom du substrat:

Focus A: Offset X: Ampl. X:

Focus B: Offset Y: Ampl. Y:



USER COMMENT RT

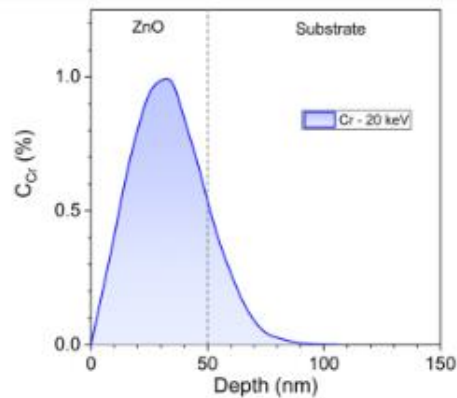



Figure 0.1. Illustrates the ion implantation of ZnO with Cr at a concentration of 1%, delineating the associated parameters and the simulated Gaussian depth profile of Cr at 20 keV.

Implantation Ti 1%



10:30:07
16/01/2024

PARAMETRES IMPLANTEUR

	Mini	Maxi	V Moy
AMU	47.71	110.85	48.27
Energie [kV]	5.80	20.22	19.87
Beam Courant [μA]	0.00	2.55	1.79
Temp Substrat [°C]	0.00	0.00	0.00
Filament V [V]	7.82	8.80	7.95
Filament I [A]	68.05	69.42	68.46
Arc V [V]	25.22	63.22	62.87
Arc I [A]	4.42	10.30	8.98
Temp Vapo [°C]	0.00	0.00	0.00
Sputtering V [V]	485.71	494.14	490.32
Sputtering I [mA]	44.36	130.99	117.45
Sample Pos	185.00	185.00	185.00
Ar [sccm]	0.00	0.00	0.00
Xe [sccm]	0.20	0.20	0.20
O2 [sccm]	0.00	0.00	0.00
Balatron [torr]	0.00	0.00	0.00
Magnet I [A]	30.99	31.21	31.10
Bfield [μG]	4.78	7.70	6.61
Extraction V [kV]	8.99	20.78	20.86
Extraction I [mA]	1.31	11.17	3.33
Post Accel V [kV]	0.00	0.00	0.00
Post Accel I [mA]	0.00	0.00	0.00
Post Decel V [kV]	0.00	0.00	0.00
Post Decel [mA]	0.00	0.00	0.00
Vide Beam Line [mBar]	2.48E-6	3.01E-6	2.88E-6
Vide Chambre [mBar]	8.62E-7	1.14E-6	9.07E-7

Operateur: Marc

Demandeur: Hugo+ Bab

Recette: Ti+

Dose cible: 1.45E+15 Ion/cm2

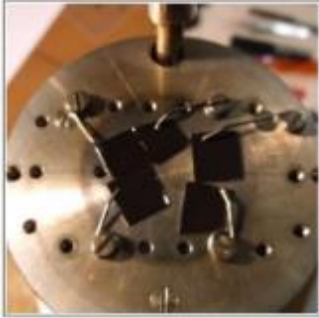
Temps écoulé: 00:23:17.99

Espèce: Ti+

Nom du substrat:

Focus A: 700 Offset X: 62 Ampl. X: 0.29

Focus B: 692 Offset Y: 500 Ampl. Y: 0.3



USER COMMENT RT

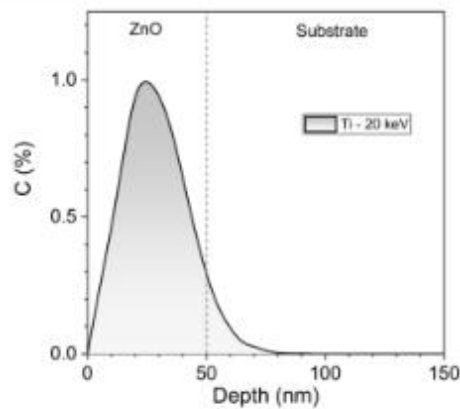



Figure 0.2. Illustrates the implantation of ZnO with Ti at a concentration of 1%, delineating the associated parameters and the simulated Gaussian depth profile Ti at 20 keV.

Implantation Ti 2%



16:26:01
16/01/2024

PARAMETRES IMPLANTEUR

	Min	Maxi	V Moy
AMU	47.88	78.58	46.35
Energie [KV]	7.51	20.20	19.84
Beam Courant [µA]	0.00	1.66	1.38
Temp Substrat [°C]	0.00	0.00	0.00
Filament V [V]	7.64	8.55	8.25
Filament I [A]	68.67	68.97	68.05
Arc V [V]	54.56	70.78	55.17
Arc I [A]	7.86	12.29	10.06
Temp Vapo [°C]	0.00	0.00	0.00
Sputtering V [V]	394.32	592.56	502.34
Sputtering I [mA]	110.38	148.45	126.66
Sample Pos	185.00	187.00	185.98
Ar [sccm]	0.00	0.00	0.00
Xe [sccm]	0.20	0.30	0.20
O2 [sccm]	0.00	0.00	0.00
Balatron [torr]	0.00	0.00	0.00
Magnet I [A]	30.96	31.25	31.12
Bfield [kG]	3.83	7.56	5.71
Extraction V [kV]	12.72	20.74	20.64
Extraction I [mA]	3.09	8.94	3.54
Post Accel V [kV]	0.00	0.00	0.00
Post Accel I [mA]	0.00	0.00	0.00
Post Decel V [kV]	0.00	0.00	0.00
Post Decel [mA]	0.00	0.00	0.00
Vide Beam Line [mBar]	2.73E-6	3.26E-6	2.95E-6
Vide Chambre [mBar]	9.37E-7	1.29E-6	9.80E-7

Operateur

Demandeur

Recette

Dose cible

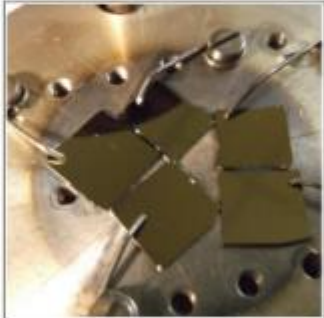
Temps écoulé

Espèce

Nom du substrat

Focus A Offset X Ampl. X

Focus B Offset Y Ampl. Y



USER COMMENT

Figure 0.3. Illustrates the ion implantation of Ti into ZnO with Ti at a concentration of 2%. Completing an in-depth study of ion implantation doping effects on the sensing properties of ZnO presents a rich research field for the next generation of graduate students.

8.3.2 Advancing Broadband Dielectric Spectroscopy

Environmental Influences: Understanding how environmental factors affect BDS-based gas sensors is crucial for ensuring their reliable performance in real-world scenarios. Future research could explore the effects of temperature, humidity, pressure, and ambient gas composition on sensor response and stability. Crafting methods to minimize the impact of environmental changes using techniques like temperature compensation algorithms or encapsulation can improve sensor longevity and reliability across different operating conditions.

Analyzing Uncertainties in Errors: It's crucial to thoroughly analyze uncertainties when it comes to measuring and reducing errors in gas sensors based on BDS technology. Future studies could focus on systematically identifying different sources of error, such as changes in temperature, variations in humidity, and sensor drift. Using more advanced calibration methods and models for error propagation can enhance the precision and dependability of gas concentration measurements. Moreover, investigating methods for calibrating sensors on-site and allowing them to diagnose themselves could further improve measurement accuracy across different environmental conditions.

8.3.3 Exploring the Potential of BDS in Solvent Detection

Analyzing Dielectric Response: Studying the dielectric response of BDS sensors when exposed to various solvent vapors could be a potential area for future research. This would involve examining how the dielectric permittivity of the sensing material is affected by methanol, isopropyl alcohol, and acetone. By analyzing the frequency-dependent dielectric spectra, valuable information can be obtained regarding the molecular interactions between the solvents and the detection element.

Understanding Adsorption Kinetics: To improve sensor response time, it's crucial to look into how methanol, isopropyl alcohol, and acetone are taken up by the sensing material surface. Further investigations could focus on how these solvents are absorbed and released, considering aspects like absorption speeds, balance times, and release energies. This understanding can help enhance the design of BDS sensors for quick and effective detection.

Characterizing Environmental Effects: Studying how environmental factors affect BDS sensor performance in detecting methanol, isopropyl alcohol, and acetone is crucial for practical use. Further research could look into the impact of temperature, humidity, and ambient gas composition on sensor response and stability.

8.3.4 VOC Interaction with Active Metal Centers in MOFs through Metal Center Analysis

Investigation of VOC Adsorption Mechanisms: Understanding the mechanisms of VOC adsorption onto the active metal centers in MOFs is crucial for elucidating gas sensing behavior. Future research could investigate the kinetics, thermodynamics, and molecular interactions during the uptake of VOC molecules by MOFs. Computational modeling methods like density functional theory (DFT) calculations and molecular dynamics simulations can support experimental studies by forecasting adsorption energies, binding geometries, and diffusion pathways of VOC molecules within MOF structures.

Effect of Active Metal Centers on microwave response: The impact of active metal centers on BDS signals in MOF-based gas sensors is essential for improving sensor design. Future studies could explore how changes in metal composition, coordination geometry, and

oxidation state influence the dielectric properties of MOFs and their reaction to VOCs. This may include creating diverse metal node MOFs and methodically assessing their BDS response to VOCs to understand structure-property connections and boost sensor effectiveness.

Correlation between analyte's hydrogen bonding ability (as parametrized through solvents Acceptor Number (AN)) and VOC Sensitivity/Selectivity: Exploring how acceptor number (AN) affects gas sensing properties can offer valuable insights into MOF design. Future research could examine how modifying analyte's *hydrogen bonding ability* impact the sensitivity and selectivity of MOF-based gas sensors for various VOCs. By methodically adjusting AN and analyzing the resulting BDS response, we can uncover how acceptor sites influence VOC adsorption and recognition, potentially leading to improved sensing capabilities in tailored MOF materials.

Optimization of MOF-Based Gas Sensors: Optimizing MOF-based gas sensors for VOC detection requires a thorough understanding of the interaction between VOC molecules and active metal centers, as probed by BDS. Future research can focus on customizing MOF properties to maximize VOC adsorption and sensor response, as well as improving sensor stability, reproducibility, and reversibility for practical applicability in environmental monitoring, industrial safety, and healthcare.

8.3.5 Redox Potential Relationship in Solvent Detection with MOFs via BDS

Characterization of Redox Properties: Future studies could focus on thoroughly examining the redox characteristics of MOFs, encompassing their potential for oxidation and the speed of electron transfer. Methods like cyclic voltammetry and electrochemical impedance spectroscopy can offer important understandings into how MOFs behave electrochemically and react to various

solvent molecules. Exploring the connection between redox properties and solvent recognition can unveil insights into sensing mechanisms, which can inform the development of more effective MOF-based sensors.

Investigation of Solvent Oxidation Reactions: Understanding the kinetics and mechanisms of solvent oxidation reactions on the surface of MOFs is crucial for optimizing sensor performance. Future work could explore pathways, intermediates, and the influence of MOF structure, composition, and surface functionalization on these reactions. This may involve using in situ spectroscopic techniques to monitor solvent oxidation processes in real time and correlate them with BDS measurements.

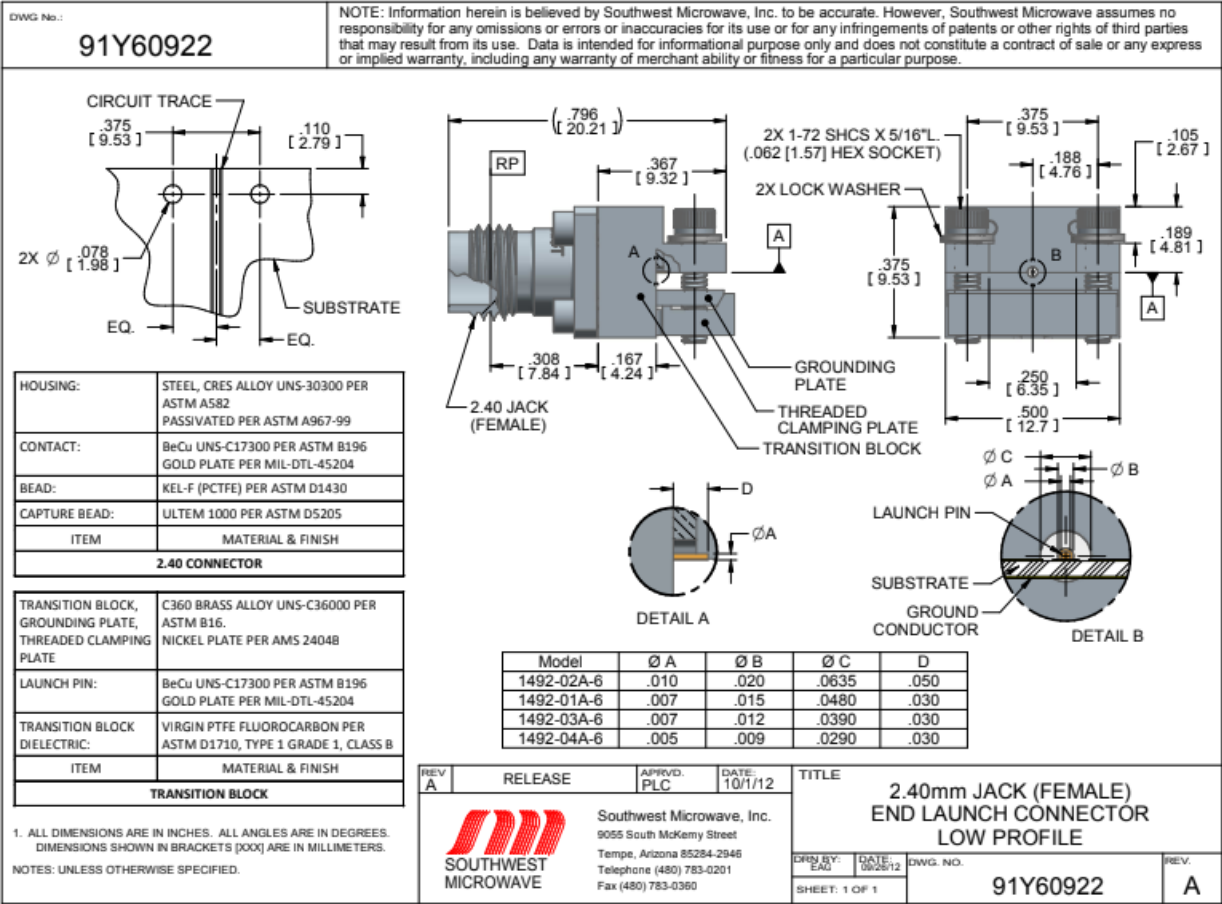
Effect of Solvent Rate and Oxidation Potential on Sensor Response: Examining the impact of solvent rate and oxidation potential on sensor response is crucial for enhancing MOF-based gas sensors. Further studies could explore the connection between solvent concentration, oxidation potential, and BDS signals obtained from MOF sensors. This may include researching how changes in dielectric properties of MOFs correlate with the kinetics of solvent oxidation reactions, along with examining how solvent diffusion rates affect sensor response time and sensitivity.

References

- [1] Silicon VLSI Technology: Fundamentals, Practice and Modeling by James D. Plummer, Michael D. Deal and Peter B. Griffin; Chapter 8: Ion Implantation (Prentice Hall Electronics and VLSI Series)
- [2] F. G. Fabrizio Roccaforte, and Giuseppe Greco, "Ion Implantation Doping in Silicon Carbide and Gallium Nitride Electronic Devices," *Micro*, vol. 2, no. 1, pp. 23-53, 2022, doi: 10.3390/micro2010002.
- [3] S. G. Mandeep Kaur, Navdeep Goyal, "Ion-implantation and photovoltaics efficiency: A review," *Materials Letters*, vol. 309, p. 131356, 2022, doi: 10.1016/j.matlet.2021.131356.

APPENDIX

Appendix A: End Launch Connectors Data Sheet



Appendix B: End Launch Connectors Specifications Sheet

SPECIFICATIONS

End Launch Connectors DC to 110 GHz

ELECTRICAL

- ▶ Mode free through 110 GHz
- ▶ Low VSWR
- ▶ Low Insertion Loss

MATERIALS / CONSTRUCTION

- ▶ **Connector housing:** CRES Alloy UNS S30300 per ASTM A582, Passivated per ASTM A967
- ▶ **Contact:** BeCu, UNS C17300 per ASTM B196, Au plated per ASTM B488
- ▶ **Dielectric:** SMA only – PTFE per ASTM D1710
- ▶ **Contact Capture Bead:**
 - SMA - Ultem 1000 per ASTM D5205
 - 2.92 and 2.40 mm - Ultem 1000 per ASTM D5205 and Kel-F per ASTM D1430
 - 1.85 mm – Ultem 1000 per ASTM D5205 and PTFE per ASTM D1710
 - 1.0 mm – Ultem 1000 per ASTM D5205
- ▶ **Connector interfaces:**
 - SMA – per MIL-STD-348, figs. 310-1 and 310-2
 - 2.92 mm – per MIL-STD-348, figs 323-1 and 323-2
 - 2.40 mm – per MIL-STD-348, figs 324-1 and 324-2
 - 1.85 mm – per IEEE 287
 - 1.0 mm – per IEEE 287
- ▶ **Transition Block and clamping plates:** Brass Alloy UNS C36000 per ASTM B16, Ni plated per ASTM 2404B
- ▶ **Transition Pin:** BeCu per UNS C17300 per ASTM B196, Au plate per ASTM B488
- ▶ **Transition Dielectric:** PTFE per ASTM D1710
- ▶ **Connector fasteners:** (4 each): # 0-80 SHCS
- ▶ **Transition block/PCB fasteners:** (2 each): # 1-72 SHCS (2 in lbs max. torque)

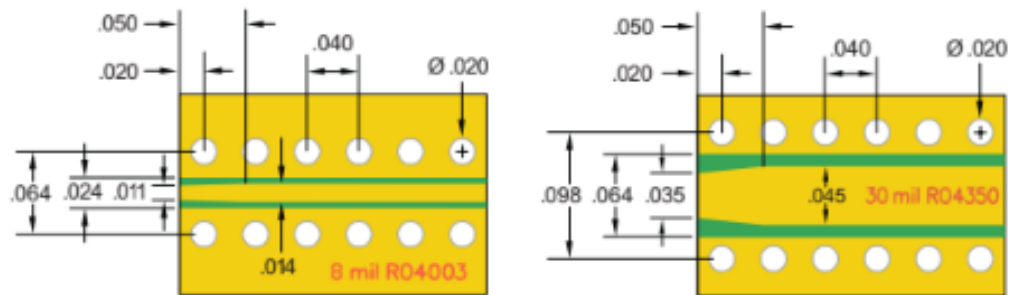
ENVIRONMENTAL

- ▶ Temperature:
 - SMA -65 to +165 °C
 - 2.92 mm and 2.40 mm -55 to +135 °C
 - 1.85 mm and 1.0 mm -55 to +165 °C

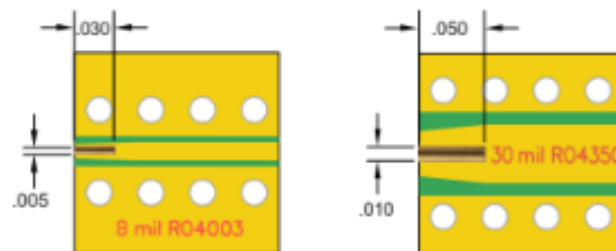
Appendix C: Coplanar Waveguide Board Layout

GCPWG Layouts

The 8 mil GCPWG board again has a slight taper to account for the pin of the connector. The 30 mil board is slightly more difficult to match and has a moderate taper to account for the pin of the connector. This 30 mil design was optimized with software as seen in the example earlier in the paper.



8 mil and 30 mil Straight Microstrip final board layout dimensions.



8 mil & 30 mil Straight Microstrip pin sizes relative to the board thickness.

Appendix D: Patent Application Receipt



UNITED STATES
PATENT AND TRADEMARK OFFICE

Page 1 of 2

P.O. Box 1450
Alexandria, VA 22313 - 1450
www.uspto.gov

ELECTRONIC ACKNOWLEDGEMENT RECEIPT

APPLICATION #	RECEIPT DATE / TIME	ATTORNEY DOCKET #
63/566,444	03/18/2024 11:04:57 AM Z ET	24-022P1

Title of Invention

A METHOD TO DETERMINE THE CONCENTRATION OF VOLATILE ORGANIC COMPOUNDS (VOCs) IN AIR WITH METAL OXIDE SENSOR MATERIALS BY EMPLOYING THE IMAGINARY PHASE COMPONENT OF THE MICROWAVE INSERTION LOSS FROM BROADBAND DIELECTRIC SPECTROSCOPY


Application Information

APPLICATION TYPE	Utility - Provisional Application under 35 USC 111(b)	PATENT #	-
CONFIRMATION #	2378	FILED BY	Dana Bowins
PATENT CENTER #	64719985	FILING DATE	-
CUSTOMER #	78798	FIRST NAMED INVENTOR	Yaw Samuel Obeng
CORRESPONDENCE ADDRESS	-	AUTHORIZED BY	Richard Bis

Appendix E: Copyright Permission granted by the Publisher

The material presented in Chapters Four, Six, and Seven of this dissertation is sourced from works published in the following journals. The copyright holders have granted permission for the following publications:

Papa K. Amoah, Pengtao Lin, Helmut Baumgart, Rhonda R. Franklin, Yaw S. Obeng; “Broadband Dielectric Spectroscopic Detection of Volatile Organic Compounds with ZnO Nanorod Gas Sensors,” Journal of physics D: Applied physics, vol. 53, no. 13, p. 135104, 2021, doi: 10.1088/1361-6463/abd3ce


Permissions <permissions@iopublishing.org>
to me ▾

Mon, Feb 12, 8:29 AM

★ ↶ ⋮

Dear Papa Kojo Amoah,

Thank you for your email and for taking the time to seek this permission.

When you transferred the copyright in your article to IOP, we granted back to you certain rights, including the right to include all or part of the [Final Published Version](#) of the article within any thesis or dissertation provided it is not then shared or deposited online. Full details can be found in our [Author Rights Policy](#).

If you are required by your institution to share your thesis/dissertation publicly (such as in an institutional repository), the Final Published Version would need to be removed prior to publication online or in print. Your institution should be able to withhold the IOP article section of your thesis from this version. However, you should still reference the article, include the abstract and provide a DOI link to it on IOPscience so that people know that it has been published.

Please include citation details, “© IOP Publishing. Reproduced with permission. All rights reserved” and for online use, a link to the Version of Record.

Please note you may need to obtain separate permission for any third party content you included within your article.

If you do not wish to remove the IOP article section of your thesis, you also have the following alternative options:

- 1) Our Author Rights Policy allows authors to post the [Accepted Manuscript](#) in certain places **after** the embargo period has elapsed. This includes your institutional repository, subject to certain restrictions (please see the full terms and conditions in our Author Rights Policy linked in the signature of this email.). Therefore, an option may be to include your Accepted Manuscript article version in your thesis or dissertation, as it would allow you to place the unaltered dissertation onto your repository after the embargo period.
Please note that your article is outside of its embargo period. An Embargo Period is 'a period of 12 months from the Date of Publication'.
- 2) A further option would be to include the [Author's Original or Preprint](#) version of the article, provided that you do so in line with our [Preprint pre-publication policy](#).

I wish you the best of luck with the completion of your thesis/dissertation.

Kind regards,

Sophie
Copyright & Permissions Team
 Sophie Brittain - Rights & Permissions Assistant
 Cameron Wood - Legal & Rights Adviser
 Contact Details
 E-mail: permissions@iopublishing.org

Papa K. Amoah, Zeinab M. Hassan, Rhonda R. Franklin, Helmut Baumgart, Engelbert Redel, and Yaw S. Obeng; “Broadband Dielectric Spectroscopic Detection of Aliphatic Alcohol Vapors with Surface-Mounted HKUST-1 MOFs as Sensing Media,” *Chemosensors*, vol. 53, no. 13, p. 135104, 2022, doi: 10.1088/1361-6463/abd3ce

Papa K. Amoah, Zeinab M. Hassan, Pengtao Lin, Helmut Baumgart, Engelbert Redel, and Yaw S. Obeng; “Broadband Dielectric Spectroscopic Detection of Ethanol: A Side-by-Side Comparison of ZnO and HKUST-1 MOFs as Sensing Media,” *Chemosensors*, vol. 10, no. 7, p. 241, 2022, doi: 10.3390/chemosensors10070241



chemosensors

to me ▼

Dear Dr. Amoah,

Thanks for your letter. As an open access publisher, we do not hold copyright to articles. I just checked these two articles, please feel free to use the figures in the first article as long as you add the correct citation. For Figures 2 and 6 in the second article, you need to contact the publisher of the original pictures to obtain the copyright.

If you have any questions, please feel free to contact us.

Kind regards,
Ms. Shirley Yun
Managing Editor

Chemosensors Editorial Office
E-Mail: chemosensors@mdpi.com
<https://www.mdpi.com/journal/chemosensors>

Impact Factor 2022: 4.2
CiteScore 2022: 3.9

Articles recommendation:

Gas Sensors Based on Copper Oxide Nanomaterials: A Review

<https://www.mdpi.com/2227-9040/9/3/51>

Molecularly Imprinted Polymers for Chemical Sensing: A Tutorial Review

<https://www.mdpi.com/2227-9040/9/6/123>

A Comprehensive Review on Raman Spectroscopy Applications

<https://www.mdpi.com/2227-9040/9/9/262>

Twitter: https://twitter.com/chemosens_MDPi

LinkedIn: <https://www.linkedin.com/company/70496380>

Facebook: <https://www.facebook.com/people/Chemosensors-MDPi/100086682738712/>

Disclaimer: The information and files contained in this message are

Appendix F: Copyright Permission granted by the Publisher

Figure 5.5 of this dissertation is sourced from Figure 6 of the journal article “Highly Uniform Self-Assembled Gold Nanoparticles over High Surface Area ZnO Nanorods as Catalysts”. The copyright holders have granted permission to use the material in this dissertation.

A. W. Tarek M. Abdel-Fattah, Kai Zhang, Wei Cao, and Helmut Baumgart, "Highly Uniform Self-Assembled Gold Nanoparticles over High Surface Area ZnO Nanorods as Catalysts," ECS Journal of Solid State Science and Technology, vol. 3, no. 10, 2014, doi: 10.1149/2.0211410jss.



Permissions

to me ▾

Apr 12, 2024, 10:49AM (5 days ago) ★ ↶ ⋮

Good afternoon,

Thank you for your request to reproduce material published by IOP Publishing in your dissertation, "BROADBAND DIELECTRIC SPECTROSCOPIC DETECTION OF VOLATILE ORGANIC COMPOUNDS WITH ZINC OXIDE AND METAL-ORGANIC FRAMEWORKS AS SOLID-STATE SENSOR MATERIALS"

Regarding:

- Figure 6 from "Highly Uniform Self-Assembled Gold Nanoparticles over High Surface Area ZnO Nanorods as Catalysts"

We are happy to grant [permission](#) for the use you request on the terms set out below.

License to publish material published by IOP Publishing

Conditions

Non-exclusive, non-transferrable, revocable, worldwide, [permission](#) to use the material in print and electronic form will be granted **subject to the following conditions**:

- [Permission](#) will be cancelled without notice if you fail to fulfil any of the conditions of this letter.
- You will make reasonable efforts to contact the author(s) to seek consent for your intended use. Contacting one author acting expressly as authorised agent for their co-authors is acceptable.
- You will reproduce the following prominently alongside the material:
 - the source of the material, including author, article title, title of journal, volume number, issue number (if relevant), page range (or first page if this is the only information available) and date of first publication. This information can be contained in a footnote or reference note; or
 - a link back to the article (via DOI); and
 - *if practical and IN ALL CASES for works published under any of the Creative Commons licences the words "© The Electrochemical Society. Reproduced by [permission](#) of IOP Publishing. All rights reserved"*
- The material will not, without the express [permission](#) of the author(s), be used in any way which, in the opinion of IOP Publishing, could distort or alter the author(s)' original intention(s) and meaning, be prejudicial to the honour or reputation of the author(s) and/or imply endorsement by the author(s) and/or IOP Publishing and/or The Electrochemical Society.
- Payment of £0 is received in full by IOP Publishing prior to use.

This [permission](#) does not apply to any material/figure which is credited to another source in our publication or has been obtained from a third party. Express [permission](#) for such materials/figures must be obtained from the copyright owner.

Kind regards,

Sophie

Copyright & [Permissions Team](#)

Sophie Brittain - Rights & [Permissions Assistant](#)

Cameron Wood - Legal & Rights Adviser

Contact Details

E-mail: permissions@iopublishing.org

VITA

Papa Kojo Amoah
amoapapa8@outlook.com

Education

Old Dominion University, Norfolk, VA August 2019 – May 2024
Doctor of Philosophy in Electrical and Computer Engineering

Frostburg State University, Frostburg, MD August 2013 – December 2016
Bachelor of Science in Electrical Engineering

Professional Experience

Applied Research Center at Jefferson Lab-ODU, Newport News, VA, Aug 2019 - May 2024
Graduate Research Assistant

National Institute of Standards and Technology, Gaithersburg, MD Jan 2015 – July 2019
Guest Researcher

5 Journal Publications and (13 Conference Proceedings With 4 Listed)

Papa K. Amoah, Zeinab M. Hassan, Pengtao Lin, Helmut Baumgart, Engelbert Redel, Yaw S Obeng. “Broadband Dielectric Spectroscopic Detection of Ethanol: A Side-by-Side Comparison of ZnO and HKUST-1 MOFs as Sensing Media” Chemosensors. 2022. Volume 10, issue 7, 241, doi: 10.3390/chemosensors10070241. Impact Factor IF 4.229

Papa K. Amoah, Zeinab M. Hassan, Rhonda R. Franklin, Helmut Baumgart, Englebert Redel, Yaw S. Obeng. “Broadband Dielectric Spectroscopic Detection of Aliphatic Alcohol Vapors with Surface-Mounted HKUST-1 MOFs as Sensing Media” Chemosensors. 2022 Volume 10, issue 10, 408, doi: 10.3390/chemosensors10100408. Impact Factor IF 4.229

Yaw S. Obeng, Nhan V. Nguyen, **Papa K. Amoah**, Jungjoon Ahn, Mikhail Y. Shalaginov, Juejun Hu, and Kathleen A. Richardson. “Dielectric spectroscopic investigation of reversible photo-induced changes in amorphous Ge₂Sb₂Se₅ thin films” J. Appl. Phys. 2022. Volume 131, 075102, doi: 10.1063/5.0080142. Impact Factor 2.29.

Papa K. Amoah, Christopher E. Sunday, Chuckwudi A. Okuro, Jungjoon Ahn, Lin You, Dmitry Veksler, Joseph Kopanski, Yaw S. Obeng. “Towards the Physical Reliability of 3D-Integrated Systems: Broadband Dielectric Spectroscopic (BDS) Studies of Material Evolution and Reliability in Integrated Systems” ECS Transactions. 2022 volume 109, issue 2, 41, doi: 10.1149/10902.0041ecst. Impact Factor 3.90.

Papa K. Amoah, Pengtao Lin, Helmut Baumgart, Rhonda Franklin, Yaw S. Obeng, “Broadband Dielectric Spectroscopy Detection of Volatile Organic Compounds with ZnO Nanorod Gas Sensors”, Journal Physics D, 54, 135104 (2021) Institute of Physics IOP <https://doi.org/10.1088/1361-6463/abd3ce> ; Impact Factor 3.169

Presentations & International Conferences (13 Proceedings With 4 Listed)

Papa K. Amoah, Helmut Baumgart, Yaw S. Obeng, et al., “Detection of VOCs Using Doped ZnO Nanorods,” 244th Electrochemical Society (ECS) Meeting. Gothenburg, Sweden, October 8-12, 2023.

Papa K. Amoah, Helmut Baumgart, Yaw S. Obeng, et al., “Broadband Dielectric Spectroscopic Detection of VOCs with ZnO & MOFs,” 244th Electrochemical Society (ECS) Meeting. Gothenburg, Sweden, October 8-12, 2023.

Papa K. Amoah, Helmut Baumgart, Yaw S. Obeng, “Morphology changes in Transition Metal Doped-ZnO Nanorods,” 23rd annual Tidewater Student Research Poster Session. Newport News, Virginia, US, November 18, 2022.

Papa K. Amoah, Helmut Baumgart, Yaw S. Obeng, “Characterization of Noble and Transition Metal Doped-ZnO Sensing of VOC Analytes Using Broadband Dielectric Spectroscopy,” 242nd Electrochemical Society (ECS) Meeting. Atlanta, Georgia, US, October 9-13, 2022.

Patent

Papa K. Amoah, Helmut Baumgart, Yaw S. Obeng, “A Method to Determine the Concentration of Volatile Organic Compounds (VOCs) in Air with Metal Oxide Sensor Materials by Employing the Imaginary Phase Component of the Microwave Insertion Loss from Broadband Dielectric Spectroscopy”. SN: 63/566,444. US Provisional Patent Application filed March 18, 2024.